On-line nuclear orientation studies of neutron deficient Te, I and Cs isotopes

Timothy Lee Shaw
The Queen's College

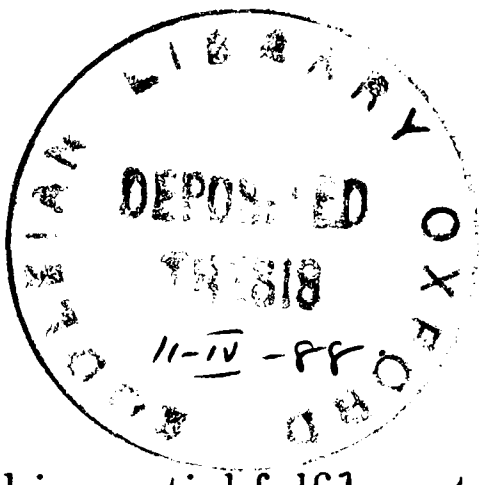

A thesis submitted in partial fulfilment of the requirements
for the degree of Doctor of Philosophy
in the University of Oxford

Trinity term 1987

to my parents

On-line nuclear orientation studies of neutron deficient Te, I and Cs isotopes

Timothy Lee Shaw
The Queen's College

A thesis submitted in partial fulfilment of the requirements
for the degree of Doctor of Philosophy
in the University of Oxford

Trinity term 1987

Abstract

On-line nuclear orientation at low temperature has become an important technique for the study of nuclei far from stability, through measurements of nuclear moments and other quantities of spectroscopic interest.

The theory of low temperature nuclear orientation and its application to the study of nuclear structure are reviewed. Of particular importance to the *on-line* measurement, in which a wide range of short-lived nuclei are available for study, is the question of how fast these nuclei can be cooled to the lattice temperature, and thus oriented. To address this, the theory of nuclear spin-lattice relaxation, relevant to the on-line technique, is outlined. In particular, quantitative methods to deal with cases in which the spin-lattice relaxation time is comparable with the isotope half-life have been developed and applied.

One of the major current interests in nuclear structure physics is to investigate how the neutron-proton interaction influences the structure of nuclei that are *transitional*, between well established regions of spherical and deformed nuclei. In such nuclei, *intruder* excitations, which signal the onset of deformation, are observed low in energy. Using the Daresbury on-line isotope separator, an extensive study of the decay of ^{118}I to ^{118}Te has been performed using nuclear orientation techniques, combined with $\gamma - \gamma$ and conversion electron spectroscopy measurements. Interpretation of the results obtained for ^{118}Te within the framework of IBM-2, gives strong evidence for the existence of such an *intruder* configuration in this nucleus.

On-line experiments have also been performed in which a range of neutron-deficient Cs nuclei has been oriented for the first time. In these measurements the hyperfine field of Cs*Fe* has been determined as (+)40.8(7) T, and also the Korringa constant for the system ^{121}Cs^{m}*Fe* has been measured (using a *new* technique) to be $C_k = 0.059(16)$sK. These results have been applied to the case of ^{118}Cs^{m}, for which the magnetic moment has been measured to be 5.4(1.1)nm. This large value clearly indicates the presence of the [404]9/2 orbital, which provides further evidence for the existence of *intruder* states in this region.

ACKNOWLEDGEMENTS

It is my pleasure to be able to express my thanks to those who have supported and assisted me during the course of this work, making this thesis possible:

Firstly, I would like to thank Professor E.W.J.Mitchell for making available the facilities of the Clarendon Laboratory, and also Professor D.H. Perkins and Professor K.W. Allen for allowing me use the Nuclear Physics Laboratory over the last four years. I would also like to thank the Science and Engineering Research Council for a postgraduate studentship, and for the use of the Nuclear Structure Facility at Daresbury.

In particular, I would like to thank my supervisor Dr. Nick Stone for his help, guidance and encouragement in all aspects of this work. I am also grateful to Dr. Jirina Rikovska for many varied and interesting discussions (ranging from IBM-2 to ice skating), and for providing an invaluable *cutting and pasting* service towards the end of the writing of this thesis.

In addition, I would like to thank all my collaborators, both in the Nuclear Orientation group and elsewhere; Vincent Green and Chris Leyland for looking after the Daresbury refrigerator, Phil Walker, Ian Grant, Janet Groves and Dave Toltree for running the isotope separator, and Bill Walters who joined us for a year, and provided me with such generous hospitality on my recent visit to the University of Maryland. I would also like to acknowledge the other students in the group, Jeremy, Chris and Austyn for providing a very pleasant working atmosphere. Finally, my thanks go to the various summer students who have worked with the group over the past three years, Jenny, Danny, Karen and David.

In addition I must thank the NSF crew members for providing beams, and also Peter Noake for patiently answering many trivial qustions about the Daresbury GEC system. Thanks are also due to Ian McArthur for looking after the OEG computer facilities so well.

On a more personal note I would like to thank Stanley Ooi and Phil Evans for providing such good company on frequent visits to the local hostelries. A word of thanks also to Louise for her generous hospitality, during many trips to Daresbury.

Finally, I am very grateful to my parents for providing me with the opportunities that led to this work.

Tim Shaw
The Queen's College, Oxford
October 1987

Contents

List Of Figures

page

List Of Tables

Chapter 7. Nuclear Orientation and Relaxation of Cs Isotopes

Chapter 1

Low Temperature Nuclear Orientation

1.1 Introduction

For a radiating system of angular momentum **J**, the probability of emission of electromagnetic radiation depends, in general, on the angle between **J** and the direction **k** of emission of the radiation. For an ordinary source of radiation, consisting of an ensemble of many radiating systems, the **J** vectors are oriented at random, i.e. the expectation value for the spin of the ensemble, $\langle \mathbf{J} \rangle$ is zero. This results in the distribution of radiation being isotropic. If, however, $\langle \mathbf{J} \rangle$ is finite, the ensemble will favour a particular direction in space, which will, in general, lead to an anisotropic radiation pattern. Such a system is said to be *oriented*.

In low temperature nuclear orientation (LTNO), the degeneracy of the nuclear spin sub-levels is removed by the interaction of the nuclei with magnetic or electric fields at the nuclear site. These fields are often those found in the solid state enviroment of the nucleus, and their interactions with the nucleus are known as hyperfine interactions. The advantage of such hyperfine fields is that they can be much larger than fields produced in the laboratory. For example, the hyperfine field seen by I nuclei in a substitutional site in a polarized iron host is 115 Tesla.

To achieve orientation of the spin system, it is necessary to create a population difference between the different sub-levels. This is done by cooling the nuclear spins to a temperature T_L, such that the the randomizing thermal energy kT_L is of order the sub-level splitting. The nuclear spins will now have a spatial orienatation, the orientation axis being defined by the direction of the magnetic (or electric) field. To illustrate the sort of temperatures necessary to achieve LTNO, take a nucleus of spin 2, a moment of 1nm and a hyperfine field of 100 Tesla. The energy splitting of the $(2I+1)$ sub-levels can be written in the form $\Delta E = kT_{int}$, where T_{int} is the interaction temperature, which is 18mK for this system.

In this thesis, the angular distribution of γ-rays emitted following the β-decay of oriented samples (produced by on-line implantation) has been studied. The intensity distribution observed depends on several main factors,

(i) the degree of orientation of the β-emitting parent state,

(ii) the proportion of the implanted nuclei which see the full hyperfine field,

(iii) the multipole character of the emitted radiation and properties of levels in the daughter nucleus.

The following sections will deal with how the distribution of radiation is related to these points. At the end of the chapter there will be a short discussion on the origin of the hyperfine interaction itself.

1.2 Angular distribution of radiation from an oriented source

1.2.1 General formalism

The sub-levels of a state of spin I may be described by a wavefunction $|\psi_j\rangle$, which is an eigenfunction of the nuclear Hamiltonian

$$\hat{H}_N|\psi_j\rangle = \epsilon_j|\psi_j\rangle \tag{1.1}$$

The wavefunctions $|\psi_j\rangle$ may be expanded in terms of a complete set of wavefunctions $|Im\rangle$, where m is the projection of the spin I onto the z-axis.

$$\begin{aligned} |\psi_j\rangle &= \sum_{m=-I}^{I} \langle Im|\psi_j\rangle \, |Im\rangle \\ &= \sum_{m=-I}^{I} a_m^j |Im\rangle \end{aligned} \tag{1.2}$$

In all representations I is a good quantum number, but m is only a good quantum number for systems possessing axial symmetry about the z-axis. Such a condition is satisfied for the interaction of the nuclear ensemble with a magnetic field (or an axially symmetric electric field gradient). Thus, a nuclear state may be described by a wavefunction $|\psi_j\rangle = |\alpha, Im\rangle$, where α denotes additional quantum numbers describing the state. These are unimportant in determining the intensity distribution and will be omitted for the following discussion.

The golden rule transition probability, in first order perturbation theory, for a transition from a discrete state $|i\rangle$ to a continuum state $|f\rangle$, is given by

$$P_{i\to f} = \frac{2\pi}{\hbar}|\langle f|\hat{H}_a|i\rangle|^2\rho_f \tag{1.3}$$

where $\hat{H}_a$ is the absorption interaction Hamiltonian and ρ_f is the final density of states. Brink and Rose [1] show, using a time reversal argument, that $2\pi\rho_f/\hbar = k/2\pi\hbar$.

Consider a transition between an initial nuclear state $|I_i m_i\rangle$, and a final nuclear state $|I_f m_f\rangle$, with the emission of a photon of wavenumber $\mathbf{k}$ and polarization $\boldsymbol{\sigma}$. This may be represented by $|i\rangle = |I_i m_i\rangle$ and $|f\rangle = |I_f m_f; \mathbf{k}\boldsymbol{\sigma}\rangle$. Now, the transition probability for this process may be written

$$P_{nucleus}(I_i m_i \rightarrow I_f m_f; \mathbf{k}\boldsymbol{\sigma}) = \frac{k}{2\pi\hbar} |\langle I_f m_f; \mathbf{k}\boldsymbol{\sigma}|\hat{H}_a|I_i m_i\rangle|^2 \qquad (1.4)$$

This is the transition probability for a single nucleus. For the entire ensemble, the total transition probability is obtained by taking an incoherent sum (because each nucleus decays independently) over the initial states, weighted according to the occupation probability, $g(m_i)$, for each state. Hence,

$$P_{ensemble}(I_i \rightarrow I_f; \mathbf{k}\boldsymbol{\sigma}) = \frac{k}{2\pi\hbar} \sum_{m_i, m_f} g(m_i)\ |\langle I_f m_f; \mathbf{k}\boldsymbol{\sigma}|\hat{H}_a|I_i m_i\rangle|^2 \qquad (1.5)$$

The summation over m_f is because the final state is unobserved. If the polarization of the detected radiation is not observed, then a summation over $\boldsymbol{\sigma}$ must also be performed. Introducing the shorthand notation $|f\rangle \equiv |I_f m_f; \mathbf{k}\boldsymbol{\sigma}\rangle$ and $|n\rangle \equiv |I_n m_n\rangle$, with a summation over n representing a summation over m_n, equation (1.5) may be expanded as follows

$$\begin{aligned} P_{ensemble}(i \rightarrow f) &= \frac{k}{2\pi\hbar} \sum_{i,f} g(i)\ |\langle f|\hat{H}_a|i\rangle|^2 = \frac{k}{2\pi\hbar} \sum_{i,f} g(i)\ \langle f|\hat{H}_a|i\rangle \langle f|\hat{H}_a|i\rangle^* \\ &= \frac{k}{2\pi\hbar} \sum_{i,f} g(i) \left(\sum_n \langle f|\hat{H}_a|n\rangle\langle n|i\rangle \right) \left(\sum_{n'} \langle f|\hat{H}_a|n'\rangle^* \langle n'|i\rangle^* \right) \\ &= \frac{k}{2\pi\hbar} \sum_{i,n,n'} \langle n|i\rangle\ g(i)\ \langle i|n'\rangle \\ &\qquad \times \sum_f \langle f|\hat{H}_a|n\rangle \langle f|\hat{H}_a|n'\rangle^* \end{aligned} \qquad (1.6)$$

This expression is in fact quite general, being valid for both axially and non-axially symmetric systems. The first term, which describes the orientation of the initial state, can be written in a simple form only for an axially symmetric

system. The second term essentially deals with the γ-transition to the final state. These two terms will now be considered separately.

1.2.2 The orientation coefficients, B_λ

Using the same notation as in the previous subsection, the expectation value of an observable $\hat{A}$ in a pure state, $|i\rangle$, is simply

$$\langle \hat{A} \rangle = \langle i|\hat{A}|i\rangle = \sum_{n',n} \langle i|n'\rangle\langle n'|\hat{A}|n\rangle\langle n|i\rangle \tag{1.7}$$

Now consider a mixed state, consisting of an ensemble of several elements, where each element is in one N possible different pure states $|i\rangle$. This mixed state can be described by an incoherent sum over the N pure states, each weighted with a factor $g(i)$, which is the number of elements in the ensemble in the state $|i\rangle$. The expectation value of $\hat{A}$ for the mixed state will be a weighted average of the individual expectation values for the pure states

$$\begin{aligned}\langle \hat{A} \rangle &= \sum_i g(i)\langle i|\hat{A}|i\rangle \\ &= \sum_{i,n,n'} \langle n|i\rangle g(i)\langle i|n'\rangle \ \langle n'|\hat{A}|n\rangle \\ &= \sum_{n,n'} \langle n|\hat{\rho}|n'\rangle \ \langle n'|\hat{A}|n\rangle \end{aligned} \tag{1.8a}$$

where

$$\langle n|\hat{\rho}|n'\rangle = \sum_i \langle n|i\rangle \ g(i) \ \langle i|n'\rangle \tag{1.8b}$$

The matrix ρ is known as the density matrix, and it characterizes the state of the ensemble. It is clear that the first term in equation (1.6) is just the density matrix defined above and, in shorthand notation, equation (1.6) may be written

$$P_{ensemble}(i \to f) = \frac{k}{2\pi\hbar} \sum_{n,n',f} \langle n|\hat{\rho}|n'\rangle \ \langle f|\hat{H}_a|n\rangle\langle f|\hat{H}_a|n'\rangle^* \tag{1.9}$$

By considering the properties of the density matrix under rotation [2], it is possible to define statistical tensors, ρ_q^λ (of rank λ), as linear combinations of the density matrix elements. Converting back from shorthand notation with $|n\rangle = |j_1 m_1\rangle$, and $|n'\rangle = |j_2 m_2\rangle$, the statistical tensors can be written

$$\rho_q^\lambda(j_1 j_2) = \sqrt{2\lambda+1} \sum_{m_1} \langle j_1 m_1 | \hat{\rho} | j_2 m_2 \rangle (-1)^{j_2+m_2} \begin{pmatrix} j_2 & j_1 & \lambda \\ -m_2 & m_1 & q \end{pmatrix} \qquad (1.10)$$

The statistical tensors contain exactly the same information as the density matrix, but are much more convenient to use in studying the rotational properties of a system. An important, but non-trivial result may be derived for an ensemble of nuclei at room temperature which has, in general, no preferred axis in space, and hence must be invariant under a three dimensional rotation. Because of this, all the statistical tensors, ρ_q^λ, describing a *random ensemble* vanish, except for ρ_0^0. This corresponds to the sub-level populations being uniformly distributed among the $|Im\rangle$ states.

For axial symmetry, the density matrix operator may be simply be written as

$$\hat{\rho} = \sum_m |Im\rangle \; g(m) \; \langle Im| \qquad (1.11)$$

with the result that the density matrix is diagonal,

$$\langle Im_1 | \hat{\rho} | Im_2 \rangle = \delta_{mm_1} \delta_{mm_2} \; g(m) \qquad (1.12)$$

with the weighting factors, $g(m)$, being simply the relative populations of the $|Im\rangle$ states. A further constraint is that the statistical tensors must now be invariant under rotations about the z-axis. This means that all statistical tensors with $q \neq 0$ vanish. Equation (1.10) now reduces to

$$\rho_0^\lambda(0) = \sqrt{2\lambda+1} \sum_m (-1)^{I+m} \begin{pmatrix} I & I & \lambda \\ -m & m & 0 \end{pmatrix} g(m) \qquad (1.13)$$

As there is no dependence on q, a set of orientation parameters, $B_\lambda(I)$, may be defined by

$$\begin{aligned} B_\lambda(I) &= \sqrt{2I+1}\,\rho_0^\lambda(I) \\ &= \sqrt{(2\lambda+1)(2I+1)}\sum_m (-1)^{I+m}\begin{pmatrix} I & I & \lambda \\ -m & m & 0 \end{pmatrix} g(m) \end{aligned} \tag{1.14}$$

The orientation parameters are normalized such that $B_0(I) = 1$.

The B_λ are functions of the oriented state populations, and the oriented state spin, as seen above. In on-line experiments, nuclei are implanted warm and take a certain time to *relax* to the lattice temperature, T_L. If this relaxation time is short compared to the half-life, then the nuclear spins will reach full thermal equilibrium with the lattice before decay. In this case, the normalized sub-level populations are given by the Boltzmann distribution

$$g(m) = \mathrm{e}^{-E_m/kT_L} \Big/ \sum_{m'} \mathrm{e}^{-E_{m'}/kT_L} \tag{1.15}$$

where E_m is the energy of the state $|Im\rangle$. Cases where the relaxation time cannot be ignored will be dealt with in the next chapter.

For an interaction between a magnetic field, B_{hf}, and a nuclear magnetic dipole moment, μ, the sub-level energies are given by

$$E_m = -\frac{\mu B_{hf}}{I}\, m \tag{1.16}$$

Such a system, which has $g(m) \neq g(-m)$ (i.e. it is not invariant under reversal of the symmetry axis), is said to be *polarized*. Systems for which $g(m) = g(-m)$ are said to be *aligned* (this is the case for the interaction of an axially symmetric electric field gradient with a quadrupole moment). From the properties of the 3-j symbols, the highest non-vanishing multipole is $B_{\lambda_{max}}$, where $\lambda_{max} = 2I$. Assuming a magnetic interaction, all the non-zero even multipoles of B_λ are plotted in [Fig 1.1] for spins 2 and 5 as a function of T_{int}/T_L.

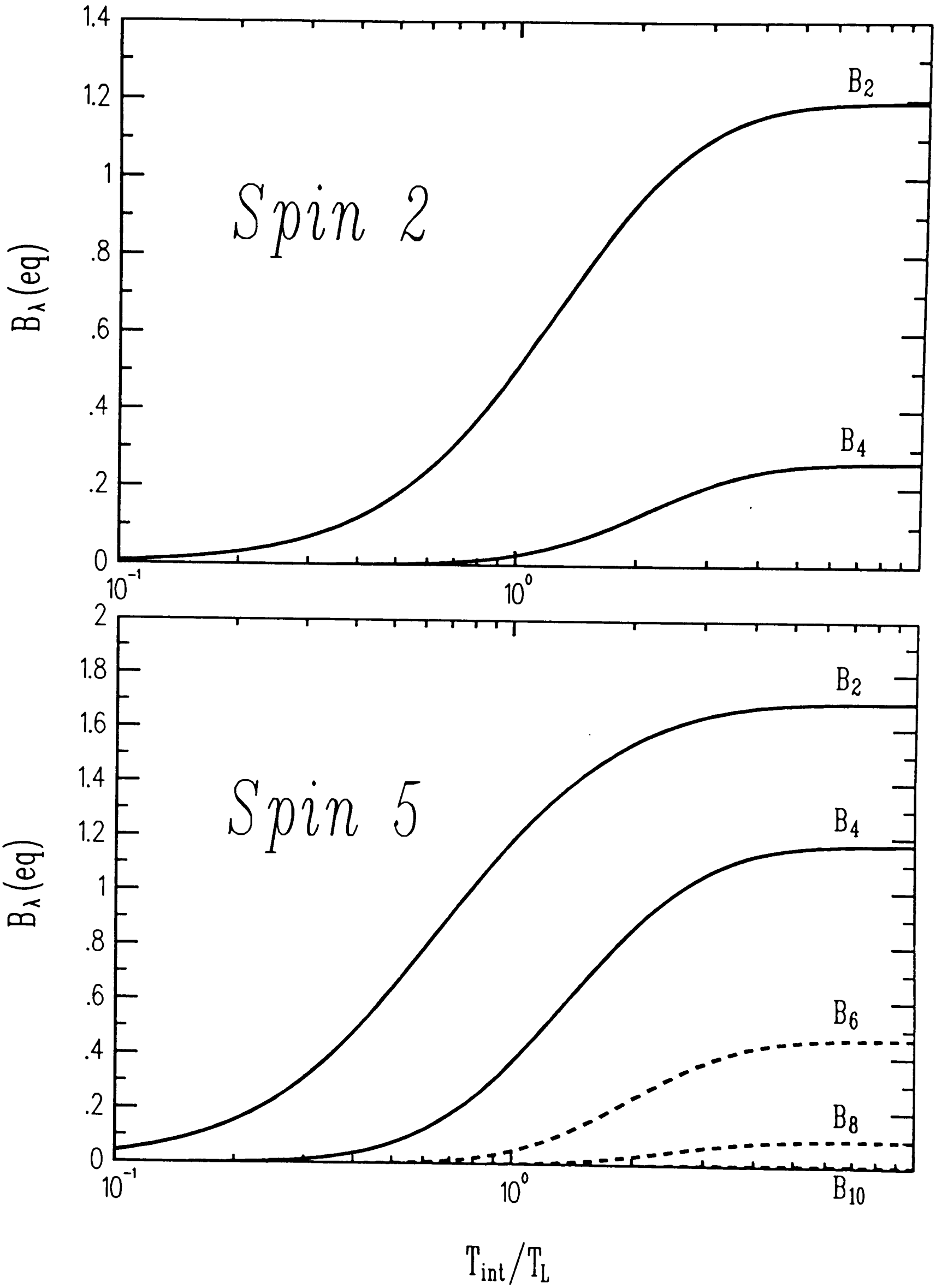

Figure 1.1. The non-zero orientation coefficients, B_λ, for even multipoles, for spins 2 and 5 as a function of T_{int}/T_L.

Symmetry properties for the orientation coefficients may be deduced by considering the contribution from the $+m$ and $-m$ terms in equation (1.14). By writing

$$f(m) = (-1)^{I+m} \begin{pmatrix} I & I & \lambda \\ -m & m & 0 \end{pmatrix} g(m) \tag{1.17}$$

then, using properties of the 3-j symbols, the sum $f(m) + f(-m)$ becomes

$$\begin{aligned} f(m) + f(-m) &= (-1)^{I+m} \begin{pmatrix} I & I & \lambda \\ -m & m & 0 \end{pmatrix} g(m) + (-1)^{I-m} \begin{pmatrix} I & I & \lambda \\ m & -m & 0 \end{pmatrix} g(-m) \\ &= (-1)^{I+m} \begin{pmatrix} I & I & \lambda \\ -m & m & 0 \end{pmatrix} [g(m) + (-1)^{\lambda} g(-m)] \end{aligned} \tag{1.18}$$

This reveals the following result for a *polarized* system

$$B_\lambda(I, +\mu B_{hf}) = (-1)^{\lambda} B_\lambda(I, -\mu B_{hf}) \tag{1.19}$$

hence even multipoles (which, as shown in the next subsection, are the only ones observed in γ-ray angular distributions) are not sensitive to the sign of the magnetic interaction.

For an *aligned* system, it can similarly be shown that odd multipoles vanish, with the even multipoles being sensitive to the sign of the electric interaction. An extensive tabulation of orientation parameters, both for magnetic-dipole and electric-quadrupole splittings, has been given by Krane [3].

1.2.3 The angular distribution coefficients, A_λ

In a semi-classical treatment of the interaction of radiation with matter, the absorption interaction Hamiltonian, $\hat{H}_a$, is given by

$$\hat{H}_a = -\int \mathbf{j}_N(\mathbf{r}) \cdot \mathbf{A}(\mathbf{r}, t)\, d\tau \tag{1.20}$$

where $\mathbf{j}_N(\mathbf{r})$ is the nuclear current density operator, and $\mathbf{A}(\mathbf{r}, t)$ is the vector field potential describing the electromagnetic radiation. The vector field, $\mathbf{A}(\mathbf{r}, t)$, can

be decomposed into a series of multipole fields, $A_{LM}^{(\pi)}$, where π represents the character of the radiation (electric or magnetic), and L, M are the total angular momentum and its z-component. The multipolarity of the emitted radiation, described by the $A_{LM}^{(\pi)}$, is 2^L and the parity is $(-1)^L$ for electric and $(-1)^{L+1}$ for magnetic transitions. Explicit expressions for these multipole fields are given by Krane [4]. For a transition between an initial state, $|I_i m_i\rangle$ of parity π_i, to a final state, $|I_f m_f\rangle$ of parity π_f, the emission matrix element may be written [5]

$$\begin{aligned}\langle I_f m_f | j_N A_{LM}^{(\pi)*} | I_i m_i \rangle &= (-1)^{L-M+1} \langle I_f m_f | j_N A_{L-M}^{(\pi)} | I_i m_i \rangle \\ &= (-1)^{L-M+1+I_f-m_f} \begin{pmatrix} I_f & L & I_i \\ -m_f & -M & m_i \end{pmatrix} \\ &\quad \times \langle I_f || j_N A_L^{(\pi)} || I_i \rangle \qquad (1.21)\end{aligned}$$

using the Wigner-Eckart theorem. The Wigner 3-j symbol illustrates the conservation of angular momentum (and its z-component) for electromagnetic transitions. In addition, parity is also conserved, leading to the following selection rules

$$\begin{aligned} |I_f - I_i| \leq L \leq I_f + I_i \quad (L > 0) \\ m_i = M + m_f \qquad (1.22) \\ \pi_i \pi_f = \begin{cases} (-1)^L & \text{(electric)} \\ (-1)^{L+1} & \text{(magnetic)} \end{cases} \end{aligned}$$

with the restriction that $L \neq 0$ for a real photon of intrinsic angular momentum $1\hbar$.

The above conditions imply that more than one multipolarity can contribute to a transition. For radiation of a fixed character, the probability of emission of radiation $\pi(L+1)$ is retarded over that for $\pi(L)$ by a factor of order $(a/\lambda)^2$, where λ is the wavelength of radiation emitted and a is the nuclear size. For a γ-ray of energy 1MeV, and a nuclear size of 5.9fm, corresponding to nucleus with $A = 120$, this factor is of order 2×10^{-5}. Similarly, radiation M(L) is retarded compared to E(L) by a factor of order $(v/c)^2$, where v is the mean

nucleon velocity. This factor is typically $\sim 10^{-2}$. Generally speaking, M(L) and E(L+1) may compete, and it is rare for more than two multipolarities to make an appreciable contribution to the electromagnetic decay of a nuclear state. The relative amplitude of two multipole orders is given by a mixing ratio, $\delta(L'/L)$ (the relative intensity of the two components is given by $\delta(L'/L)^2$). This mixing ratio is defined in terms of the reduced matrix elements from equation (1.21)

$$\delta(\pi' L'/\pi L) = \frac{\langle I_f || j_N A_{L'}^{(\pi')} || I_i \rangle}{\langle I_f || j_N A_L^{(\pi)} || I_i \rangle} \tag{1.23}$$

The Steffen phase convention[2] is used for mixing ratios in this thesis.

If the polarization of the emitted radiation is not observed, then, by making use of the multipole expansion of the interaction Hamiltonian, it is possible to show that, for axial symmetry[2]

$$\sum_{m_f,\sigma} |\langle I_f m_f; \mathbf{k}\sigma | \hat{H}_a | I_i m_i \rangle|^2 = \sum_{m_f,\sigma} \langle I_f m_f; \mathbf{k}\sigma | \hat{H}_a | I_i m_i \rangle \langle I_f m_f; \mathbf{k}\sigma | \hat{H}_a | I_i m_i \rangle^*$$

$$= \sum_{\lambda=0,2,\ldots}^{\lambda_{max}} (-1)^{I_f - m_i} A_\lambda \begin{pmatrix} I_i & I_i & \lambda \\ -m_i & m_i & 0 \end{pmatrix}$$

$$\times \sqrt{2\lambda+1}\, P_\lambda(\cos\theta) \tag{1.24}$$

where $P_\lambda(\cos\theta)$ is the Legendre polynomial of order λ, and θ is angle between the emitted γ-ray and the axis of symmetry. Due to the conservation of parity in the electromagnetic interaction, the expansion is over even values of λ as the parity of the Legendre polynomials is $(-1)^L$.

A_λ is a coefficient depending on the observed γ-ray , that is on the initial and final spins, and the relative mixing of multipole radiations contributing to the transition. For two competing multipolarities, L and L', the A_λ coefficient is given by

$$A_\lambda = \frac{F_\lambda(LLI_fI_i) + 2\delta F_\lambda(LL'I_fI_i) + \delta^2 F_\lambda(L'L'I_fI_i)}{1+\delta^2} \tag{1.25}$$

where the mixing ratio, δ, is defined by equation (1.23). The F_λ coefficients are given by

$$F_\lambda(LL'I_fI_i) = (-1)^{I_i+I_f-1}\sqrt{(2L+1)(2L'+1)(2I_i+1)(2\lambda+1)} \times \begin{pmatrix} L & L' & \lambda \\ 1 & -1 & 0 \end{pmatrix} \begin{Bmatrix} L & L' & \lambda \\ I_i & I_i & I_f \end{Bmatrix} \qquad (1.26)$$

From the properties of the Wigner 3-j and 6-j symbols, the highest non-vanishing multipole is $A_{\lambda_{max}}$, where $\lambda_{max} = \min(2L_{max}, 2I_i)$, and L_{max} is the highest multipolarity contributing to the transition. Hence for E1 and M1 transitions there is only an A_2 term, and for E2 transitions there are only A_2 and A_4 terms. Also, for transitions involving spin 0 or spin 1/2 levels there is no A_2 term, and hence no γ-ray anisotropy.

Values of A_2 and A_4 have been calculated for spin $2 \rightarrow 2$ and $3 \rightarrow 2$ sequences, and are plotted in [Fig 1.2] as a function of $\delta^2/(1+\delta^2)$, where δ is the mixing ratio (with $L = 1$ and $L' = 2$). When plotted in this way, the values of A_2 trace out an ellipse, and the A_4 values form a straight line.

Considering equation (1.9) for the case of axial symmetry, and using equations (1.12) and (1.24),

$$P_{ensemble}(i \rightarrow f) = \sum_{m_i,\lambda=0,2,\ldots}^{\lambda_{max}} (-1)^{I_f-m_i} g(m_i) \begin{pmatrix} I_i & I_i & \lambda \\ -m_i & m_i & 0 \end{pmatrix} \sqrt{2\lambda+1}\, A_\lambda P_\lambda(\cos\theta)$$

$$= \frac{(-1)^{I_f-I_i}}{\sqrt{2I_i+1}} \sum_{\lambda=0,2,\ldots}^{\lambda_{max}} B_\lambda A_\lambda P_\lambda(\cos\theta) \qquad (1.27)$$

using equation (1.14).

If the $\lambda = 0$ term in this equation is normalized to unity, then the normalized count rate, $W(\theta)$, may be written as

$$W(\theta) = 1 + \sum_{\lambda=2,4,\ldots}^{\lambda_{max}} B_\lambda A_\lambda P_\lambda(\cos\theta) \qquad (1.28)$$

where $\lambda_{max} = \min(2L_{max}, 2I_i)$. For an unoriented source all the B_λ coefficients are zero ($\lambda \neq 0$), and the angular distribution is isotropic, being described by $W(\theta) = 1$.

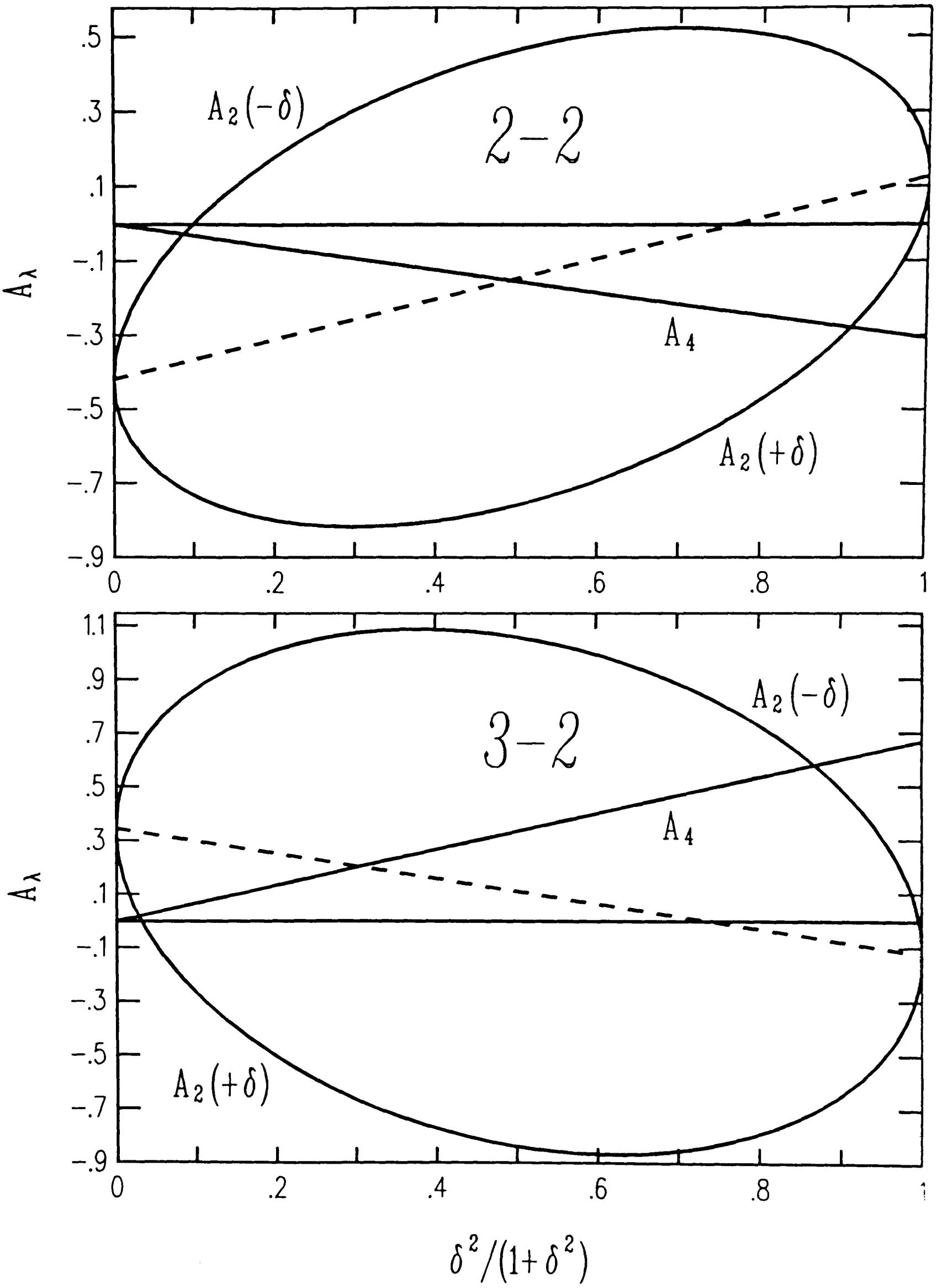

Figure 1.2. Values of A_2 and A_4 plotted for transitions between spins $2 \rightarrow 2$ and $3 \rightarrow 2$ as a function of $\delta^2/(1+\delta^2)$. In both plots the A_2 values above the dotted line correspond to negative values of δ, and to positive values below it.

1.2.4 The de-orientation coefficients, U_λ

Equation (1.28) describes the situation where the observed γ-ray comes directly from the initial oriented state. This, however, does not represent the usual situation in LTNO. In order to achieve full thermal equilibrium orientation, the requirement is that the lifetime of the oriented state must be longer than the time taken for it to reach equilibrium (the relaxation time). The lifetime of a state decaying by an E2/M1 transition ($E_\gamma > 50$keV) is typically $10^{-12} - 10^{-6}$ seconds. This is to be compared with possible relaxation times for nuclei in metals which vary from 10^{-3} to 10^{4} seconds. In general, γ-decaying states are too short-lived for this method of orientation. Instead, the initial oriented states are chosen to be β-decaying states, with long enough lifetimes to satisfy the thermal equilibrium requirement.

The γ-radiation observed is that emitted by the daughter nucleus, following the β-decay of the oriented parent. When the observed radiation is preceeded by a γ-transition of multipolarity L, or a β-transition for which $j_\beta = L$, as shown in [Fig 1.3] , then the sub-level populations of the state preceeding the transition are given by the Clebsch-Gordon transformation

$$g(m_i) = \sum_{m_0} \begin{pmatrix} I_i & L & I_0 \\ m_i & M & -m_0 \end{pmatrix}^2 g(m_0) \tag{1.29}$$

assuming that no re-orientation can occur due to the short lifetime of the γ-emitting state.

The angular momentum coupling through this *unobserved* transition attenuates the orientation of the initial β-emitting state (only for the case where $L = M = 0$ is there no attenuation). This coupling is described in a multipole basis by a de-orientation coefficient $U_\lambda(I_n I_{n+1} L^n_{n+1})$, where L^n_{n+1} is the multipolarity of the *unobserved* transition between states of spin I_n and I_{n+1}, such that

$$B_\lambda(I_{n+1}) = U_\lambda(I_n I_{n+1} L^n_{n+1})\, B_\lambda(I_n) \tag{1.30}$$

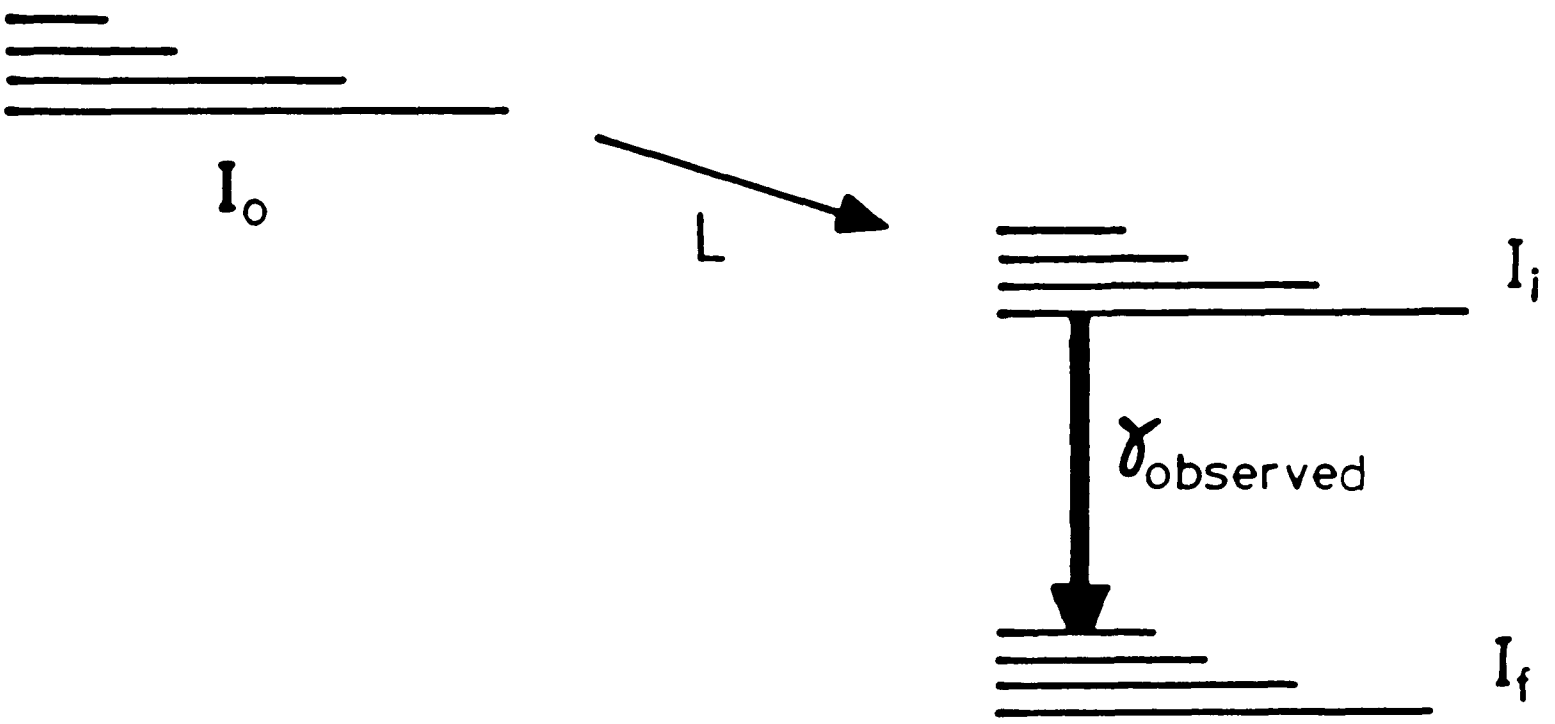

Figure 1.3. The observed γ-ray , preceeded by a γ-transition or β-transition of multipolarity L from the initial oriented state.

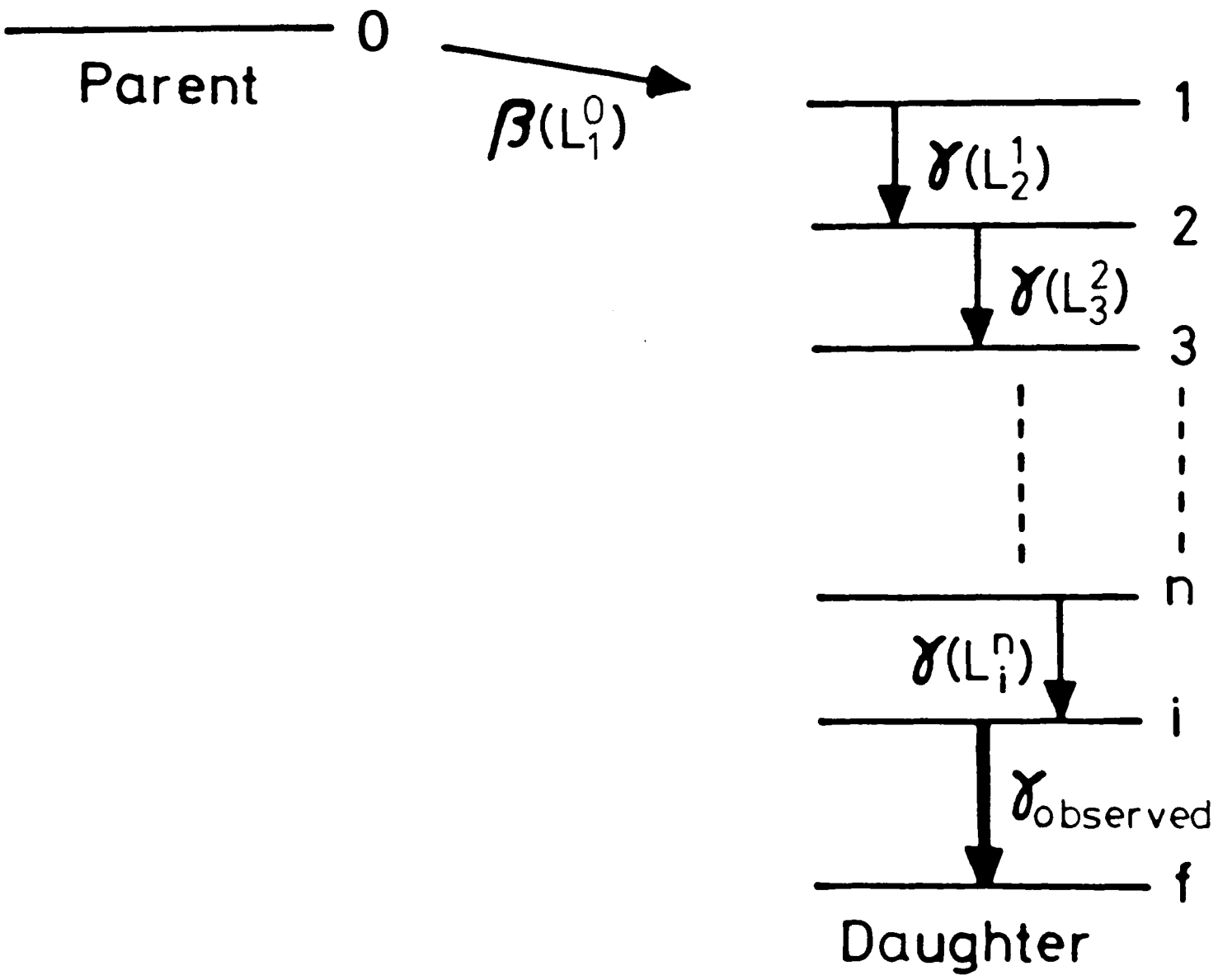

Figure 1.4. The observed γ-ray , fed by a β-transition from the oriented parent, followed by n γ-transitions in the daughter.

or for several preceeding transitions

$$B_\lambda(I_{n+1}) = U_\lambda(I_n I_{n+1} L^n_{n+1})\, U_\lambda(I_{n-1} I_n L^{n-1}_n) \ldots$$
$$\ldots U_\lambda(I_1 I_2 L^1_2)\, U_\lambda(I_0 I_1 L^0_1)\; B_\lambda(I_0) \qquad (1.31)$$

where $B_\lambda(I_0)$ is the orientation coefficient of the parent, which decays to the *observed* γ-ray by a β-decay, and n *unobserved* γ-rays in the daughter nucleus. This is shown in [Fig 1.4] . These de-orientation coefficients for a transition of multipolarity L between initial and final states of spin I_{n+1} and I_n, are given by

$$U_\lambda(I_n I_{n+1} L) = (-1)^{I_n + I_{n+1} + \lambda + L} \sqrt{(2I_{n+1}+1)(2I_n+1)}$$
$$\times \begin{Bmatrix} I_n & I_n & \lambda \\ I_{n+1} & I_{n+1} & L \end{Bmatrix} \qquad (1.32)$$

If two multipolarities L and L' compete, then

$$U_\lambda(I_n \rightarrow I_{n+1}) = \frac{U_\lambda(I_n I_{n+1} L) + \delta^2 U_\lambda(I_n I_{n+1} L')}{1+\delta^2} \qquad (1.33)$$

where δ is defined by equation (1.23). The highest non-vanishing multipole is determined by $\lambda_{max} = \min(2I_n, 2I_{n+1})$.

For a typical decay scheme, there is more than one independent path from the oriented parent to the initial state I_i, from which the *observed* γ-ray is emitted. The total de-orientation coefficient $U^{tot}_\lambda(I_0 \rightarrow I_i)$ for this state is obtained by taking an *average* over all the possible paths, weighted with the intensities of the transitions involved. If $\Im_{nm}$ is the intensity of a transition between states of spin I_n and I_m, and $U_\lambda(I_n \rightarrow I_m)$ is the corresponding de-orientation coefficient, then the total de-orientation coefficients become

$$U^{tot}_\lambda(I_0 \rightarrow I_0) = 1$$

$$U^{tot}_\lambda(I_0 \rightarrow I_1) = U_\lambda(I_0 \rightarrow I_1)$$

$$U^{tot}_\lambda(I_0 \rightarrow I_2) = \frac{\Im_{02} U_\lambda(I_0 \rightarrow I_2) + U^{tot}_\lambda(I_0 \rightarrow I_1)\left[\Im_{12} U_\lambda(I_1 \rightarrow I_2)\right]}{\Im_{02} + \Im_{12}}$$

leading to...

$$U^{tot}_\lambda(I_0 \rightarrow I_i) = \sum_{n=0}^{i-1} U^{tot}_\lambda(I_0 \rightarrow I_n)\left[\Im_{ni} U_\lambda(I_n \rightarrow I_i)\right] \Big/ \sum_{n=0}^{i-1} \Im_{ni} \qquad (1.34)$$

1.2.5 The solid angle correction factors, Q_λ

The angular distribution of γ-radiation can now be written as

$$W(\theta) = 1 + \sum_{\lambda=2,4,\ldots}^{\lambda_{max}} B_\lambda U_\lambda A_\lambda P_\lambda(\cos\theta) \tag{1.35}$$

However, this cannot be compared directly with the measured distribution because Ge(Li) detectors subtend a finite solid angle at the source. To account for this, $W(\theta)$ must be integrated over this solid angle, with a weighting factor for the detector efficiency, which is a function of angle.

The *useful* absorption of γ-rays incident on a Ge(Li) detector is proportional to $(1 - e^{-\tau(\gamma)x(\theta)})$ where $\tau(\gamma)$ is the full energy absorption coefficient, and $x(\theta)$ is the distance travelled in the active depletion region of the detector. The measured distribution is given by the average $\overline{W(\theta)}$, given by

$$\overline{W(\theta)} = \frac{\int W(\theta)(1 - e^{\tau x})\, d\Omega}{\int (1 - e^{\tau x})\, d\Omega} \tag{1.36}$$

where the integration is performed over the solid angle subtended by the detector at the source. Substituting for $W(\theta)$ from equation (1.35), this becomes

$$\overline{W(\theta)} = 1 + \sum_{\lambda=2,4,\ldots}^{\lambda_{max}} B_\lambda U_\lambda A_\lambda \left(\frac{\int P_\lambda(\cos\theta)(1 - e^{\tau x})\, d\Omega}{\int (1 - e^{\tau x})\, d\Omega} \right) \tag{1.37}$$

These integrals can be simplified by assuming that the detector is a right circular cylinder, with its base directly facing the source. This is shown in [Fig 1.5] , where the angles θ,θ_0 and β are defined. Using the spherical harmonic theorem it is possible to show that [6]

$$P_\lambda(\cos\theta) = P_\lambda(\cos\theta_0) P_\lambda(\cos\beta) + \text{azimuthal terms} \tag{1.38}$$

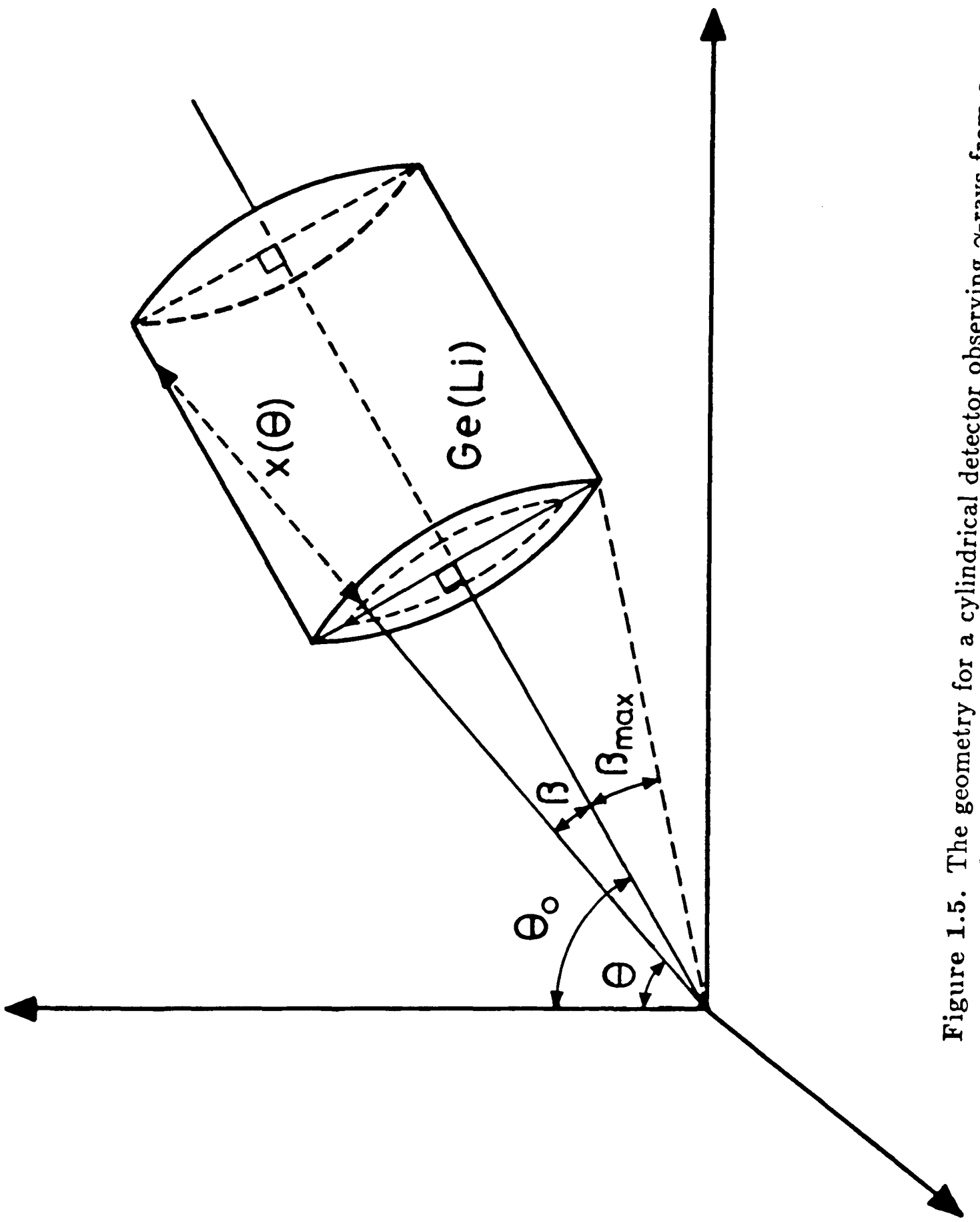

Figure 1.5. The geometry for a cylindrical detector observing γ-rays from a source at the origin, at an angle θ_0 to the orientation axis.

Due to the axial symmetry of the detector, the azimuthal terms do not contribute to the integral over solid angle (i.e. integrating over β instead of θ), which may be written as

$$\int P_\lambda(\cos\theta)(1-e^{\tau x})\,d\Omega = P_\lambda(\cos\theta_0)\int_0^{\beta_{max}} P_\lambda(\cos\beta)(1-e^{\tau x})2\pi\sin\beta\,d\beta \tag{1.39}$$

By defining

$$J_\lambda = \int_0^{\beta_{max}} P_\lambda(\cos\beta)(1-e^{\tau(\gamma)x(\beta)})\sin\beta\,d\beta \tag{1.40}$$

and substituting (1.39) into equation (1.37), the measured angular distribution becomes

$$\begin{aligned}\overline{W(\theta)} &= 1+\sum_{\lambda=2,4,\ldots}^{\lambda_{max}} B_\lambda U_\lambda A_\lambda\left(P_\lambda(\cos\theta_0)\frac{J_\lambda}{J_0}\right)\\ &= 1+\sum_{\lambda=2,4,\ldots}^{\lambda_{max}} B_\lambda U_\lambda A_\lambda Q_\lambda P_\lambda(\cos\theta_0)\\ &= W(\theta_0)\end{aligned} \tag{1.41}$$

where the solid angle correction factor Q_λ is defined by

$$Q_\lambda = \frac{J_\lambda}{J_0} \tag{1.42}$$

Evaluation of these factors requires a knowledge of $\tau(\gamma)$ and the detector construction. This will be discussed further in chapter 4.3.3.

1.2.6 The fraction in good sites

All the experiments described in this thesis have used samples prepared by implantation of the β-decaying parent nucleus into the host lattice, by means of an isotope separator. When a heavy ion is implanted with a kinetic energy of $\sim$ 100keV into a metal, it loses most of its energy by elastic collisions with metal ions (and electrons). Energetic recoil ions are produced, that subsequently

produce a branching series of further recoil ions, giving rise a region of radiation damage (vacancies, interstitials, etc.) over a volume of order $(100 \times L)^3$, where L is the lattice spacing.

If the implanted ions are associated with damage (e.g. one or more vacancies), then they will experience a range of *different* hyperfine fields. An NMR/ON experiment (where the orientation is destroyed by application of an rf field of frequency ν, with $h\nu$ equal to the sub-level splitting) on such a system would show a series of *resonances* at different frequencies, corresponding to the different hyperfine fields. The magnitude of the each resonance signal would be an indication of the proportion of nuclei in that particular field site. A static LTNO experiment, however, with its dependence on B_λ, is not sensitive to a distribution of field sites, and would just measure an *average* hyperfine interaction for the system.

Monte Carlo calculations, and many experiments show that the incident ion has a large probability of stopping in a substitutional site, without damage nearby. The hyperfine interaction experienced by these substitutional nuclei is unique, and the simplest model for a field site distribution is to assume that a fraction, f of the implants see the full substitutional hyperfine field, and the remainder, $(1 - f)$, experience zero field. With this assumption the angular distribution of γ-rays may be written as

$$W(\theta) = 1 + f \sum_{\lambda=2,4,\ldots}^{\lambda_{max}} B_\lambda U_\lambda A_\lambda Q_\lambda P_\lambda(\cos\theta_0) \qquad (1.43)$$

For many cases of room temperature implantation of ions which are soluble in the host lattice, it has been found that this simple assumption is justified, with fractions f of order 90% possible. For insoluble implants, it is possible for vacancies (which are mobile at room temperature) to be attracted and be bound to the implants, which will then lose their substitutional hyperfine field. Pattyn *et al* [7] have shown for implanted Xe ions that f rises from $\sim$ 30% at a dose of 10^{15} ions/cm^2 to close to 100% when the dose is reduced to 10^{11} ions/cm^2.

This is plausible on the following very simple argument. The average penetration of a heavy ion (such as Xe) at an energy of $\sim$ 100keV is of order 10nm in an iron lattice, which is also roughly the diameter of the damage cascade it produces. Hence, for an implantation dose below $\sim 10^{12}$ ions/cm^2, each ion will enter an undamaged portion of the host, with a high likelihood of entering a substitutional site. However, for higher dose rates, the damage cascades from neighbouring implants will begin to overlap, thus increasing the probability of the implants being associated with damage in the host lattice, which will lower the hyperfine field seen by the implant.

For on-line LTNO, there are two very good reasons to expect a high substitutional fraction,

(i) the implantation is performed at 4K or below, and at such temperatures vacancies and interstitials lose their mobility. Hence, they cannot be trapped by the implanted ions as easily as at room temperature.

(ii) the flux of implanted ions is very low, as the nuclei are produced far from stability. For a high flux of 10^6 ions/sec, it would take 1-2 shifts (of 8 hours) to reach a total dose of 10^{11} ions/cm^2.

In this thesis, the simple 2-site model described above has been used to analyse the experimental data, and, for example, values of $f \sim 80 - 90\%$ have been observed for I*Fe*.

1.2.7 Conclusions

In most circumstances, only the $\lambda = 2$ and $\lambda = 4$ terms in equation (1.43) are necessary to describe the angular distribution. The main reason for this is simply that A_λ is zero for $\lambda > 2L$, where L is the highest multipole contributing to the transition. For terms with $\lambda > 4$ to be non-zero requires that the *observed* γ-ray has multipole components with $L \geq 3$ (i.e. an E3/M3 γ-ray). There are

also constraints on B_λ and U_λ which limit λ_{max} to $2I_0$, and, $\min(2I_i, 2I_f)$ respectively. Cases where there are non-zero $\lambda > 4$ terms are uncommon, and even where they exist, they are likely to be small as the orientation coefficients B_λ fall off rapidly above $\lambda = 4$, as seen from [Fig 1.1].

The final expression for the directional distribution of γ-rays from a magnetically oriented system is

$$W(\theta) = 1 + f \sum_{\lambda=2,4} B_\lambda(\mu B_{hf}/kT_L)\, U_\lambda^{tot}(L_n^{unobs}, L_{n-1}^{unobs} \ldots L_0^{unobs}) \times A_\lambda(L_i^{obs})\, Q_\lambda^{det} P_\lambda(\cos\theta) \qquad (1.44)$$

This expression is functionally very simple, and can be separated into terms which depend on the initial parent state and the daughter,

(i) *the parent* – the fraction in good sites, f, is the fraction of the parent nuclei which see the full hyperfine field. The B_λ coefficients, which describe the orientation, are functions only of the hyperfine interaction and the lattice temperature.

(ii) *the daughter* – the U_λ^{tot} coefficients involve intermediate *unobserved* transitions, and the A_λ coefficients depend on the properties of *observed* γ-ray in the daughter.

As the temperature dependence of $W(\theta)$ is contained in the B_λ coefficients, a measurement of $W(\theta, T_L)$ can yield, both the hyperfine interaction (from the *shape* of the temperature dependence) and $fU_\lambda A_\lambda$ (from the saturation value). If this is done for a transition with known U_λ and A_λ values, then f may also be extracted.

A knowledge of f and $B_\lambda(\mu B_{hf}/kT_L)$ for a system allows information on spins, multipolarities and mixing ratios to be deduced from measurement of the $U_\lambda A_\lambda$ coefficients. If both nuclear and solid state properties are understood, measurement of the orientation allows the temperature to be determined. In LTNO this is how temperatures (in the mK region) are usually measured.

1.3 Angular distribution of linearly polarized γ-rays

In the last section the directional distribution of γ-rays from an oriented source was discussed, which is not sensitive to the type of radiation (electric or magnetic). However, this is not true if the linear polarization of the emitted γ-rays can be measured. Such a measurement can yield the relative parity of nuclear states and also uniquely determine the mixing ratio of a transition, in combination with the A_λ coefficients. It can be shown that[2] the linear polarization angular distribution of γ-rays emitted from an axially symmetric state is given by

$$W(\theta,\psi) = 1 + 0.5f \sum_{\lambda=2,4} B_\lambda U_\lambda Q_\lambda \left[A_\lambda P_\lambda(\cos\theta) + 2A'_{\lambda 2} P^2_\lambda(\cos\theta)\cos 2\psi\right] \quad (1.45)$$

where B_λ,U_λ,A_λ, Q_λ and $P_\lambda(\cos\theta)$, have the same meaning as in equation (1.44). The terms $A'_{\lambda 2}$ depend on the same characteristics of the γ-transition as do the A_λ terms, but they also depend on the parity of the radiation through a factor $(-1)^{\Lambda(\pi)}$, where $\Lambda(electric) = 0$ and $\Lambda(magnetic) = 1$. For two mixed multipoles $A'_{\lambda 2}$ may be written

$$\begin{aligned} A'_{\lambda 2}(L\pi, L'\pi') = -0.5\{&(-1)^{\Lambda(\pi)} C_\lambda(LLI_f I_i) \\ &+ \delta\left[(-1)^{\Lambda(\pi')} + (-1)^{\Lambda(\pi)+L+L'+\lambda}\right] C_\lambda(LL'I_f I_i) \\ &+ \delta^2(-1)^{\Lambda(\pi')} C_\lambda(L'L'I_f I_i)\}/(1+\delta^2) \end{aligned} \quad (1.46)$$

where the $C_\lambda(LL'I_f I_i)$ coefficients are defined by

$$C_\lambda(LL'I_f I_i) = \sqrt{\frac{(\lambda-2)!}{(\lambda+2)!}} \left[\begin{pmatrix} L & L' & \lambda \\ 1 & 1 & -2 \end{pmatrix} \Big/ \begin{pmatrix} L & L' & \lambda \\ 1 & 1 & 0 \end{pmatrix}\right] F_\lambda(LL'I_f I_i) \quad (1.47)$$

The angular dependence of the distribution is determined by the Legendre polynomials $P_\lambda(\cos\theta)$, the unnormalized associated Legendre polynomials $P^2_\lambda(\cos\theta)$ and $\cos 2\psi$. The direction of the linear polarization of γ-rays from an oriented source, emitted at an angle θ to the orientation axis, is specified by ψ,

the angle between the **E** (electric) vector of the γ-ray and the reaction plane (defined by the orientation axis and direction of emission of the γ-ray).

The degree of linear polarization can be defined as[2]

$$P(\theta) = \frac{W(\theta, \psi = 0°) - W(\theta, \psi = 90°)}{W(\theta, \psi = 0°) + W(\theta, \psi = 90°)} \tag{1.48}$$

where the normalization is such that $-1 \leq P(\theta) \leq +1$. The angles $\psi(= 0°, 90°)$ are chosen as they *maximize* the function $P(\theta)$, due to the to $\cos 2\psi(= \pm 1)$ term in the above expression for $W(\theta, \psi)$. The term $P_2^2(\cos\theta)$ has its maximum value at $\theta = 90°$, and this angle commonly produces the largest magnitude of $P(\theta)$. For $\theta = 90°$ and the case of a mixed dipole-quadrupole transition it can be shown that [8]

$$P^{\mathrm{NO}}(90) = \frac{\pm\{1.5M_2F_2^{11} - \delta M_2F_2^{12} + \delta^2[1.5M_2F_2^{22} + 0.625M_4F_4^{22}]\}}{1 - 0.5M_2F_2^{11} - \delta M_2F_2^{12} + \delta^2[1 - 0.5M_2F_2^{22} + 0.375M_4F_4^{22}]} \tag{1.49}$$

where $M_\lambda = fB_\lambda U_\lambda Q_\lambda$ and $F_\lambda^{12} = F_\lambda(LL'I_fI_i)$ $(L = 1$ and $L' = 2)$. The sign $+(-)$ corresponds to a transition without(with) a parity change.

Evaluation of this expression requires a knowledge of f, B_λ and U_λ. The f, B_λ parameters are normally extracted from the γ-ray directional distribution for a transition with known U_λ and A_λ. The U_λ for a particular level can either be calculated (if the decay scheme is sufficiently well known), or deduced from a transition from the level with known A_λ.

There are cases where the U_λ coefficients are very difficult to extract, and for such cases the linear polarization data can be analysed in a different way, with the directional distribution being written as

$$W(\theta) = 1 + \sum_{\lambda=2,4} A_{\lambda\lambda} P_\lambda(\cos\theta) \tag{1.50}$$

where $A_{\lambda\lambda} = fB_\lambda U_\lambda A_\lambda Q_\lambda$. The $A_{\lambda\lambda}$ coefficients are simply deduced from a measurement of $W(\theta)$, and do not require separation of the factors f, B_λ and U_λ. In LTNO, A_{22} and A_{44} are deduced from a measurement of $W(0)$ and

$W(90)$. Using this notation it is possible to show that the degree of linear polarization for $\theta = 90°$ (and $\lambda \leq 4$) may be written as

$$P(90) = \frac{\pm\{3A_{22}H_2 - 7.5\ A_{44}H_4\}}{2 - A_{22} + 0.75A_{44}} \tag{1.51}$$

where the $+(-)$ sign is as defined above, and the H_λ coefficients for a mixed dipole-quadrupole transition are

$$H_2^{12} = \frac{F_2^{11} - (2\delta/3)F_2^{12} + \delta^2 F_2^{22}}{F_2^{11} + 2\delta F_2^{12} + \delta^2 F_2^{22}} \tag{1.52a}$$

and

$$H_4^{12} = -1/6 \tag{1.52b}$$

Both equations (1.49) and (1.51) are used in the analysis of linear polarization data, which will be discussed in more detail in chapter 4.4.

1.4 The origin of the magnetic hyperfine interaction

1.4.1 Introduction

All the experiments described in this thesis have been performed on atomic nuclei implanted into a ferromagnetic host. Such nuclei can experience very large magnetic fields, of order 10–100 Tesla, which can result in large degrees of nuclear polarization at temperatures of 10mK. The magnetic hyperfine field of Cs*Fe* has been measured in this work, and some discussion as to origin of these fields will now be given.

The nuclear hyperfine Hamiltonian for an impurity nucleus of spin I in a ferromagnetic host may be written

$$\hat{H}_{hf} = \hat{H}_{Fermi} + \hat{H}_{OD} + \hat{H}_{SD} + \hat{H}_{ext} \tag{1.53}$$

neglecting electric quadrupole interactions. The first of these terms is known as the Fermi contact interaction

$$\hat{H}_{Fermi} = -\frac{\mu_0}{4\pi} g_s \mu_B g_N \mu_N \left[\frac{8\pi}{3}\delta(\mathbf{r})\right] \tag{1.54}$$

and arises from the magnetism of the electrons *inside* the nucleus. These electrons are mainly of s-character, although there is a small $p_{1/2}$ contribution due to relativistic effects.

The next two terms are the long range orbital and spin dipolar terms, defined by

$$\hat{H}_{OD} = -\frac{\mu_0}{4\pi} g_s \mu_B g_N \mu_N \left[\frac{\mathbf{I}\cdot\mathbf{L}}{r^3}\right] \tag{1.55a}$$

and

$$\hat{H}_{SD} = -\frac{\mu_0}{4\pi} g_s \mu_B g_N \mu_N \left[\frac{3(\mathbf{I}\cdot\hat{\mathbf{r}})(\mathbf{S}\cdot\hat{\mathbf{r}})}{r^3} - \frac{\mathbf{I}\cdot\mathbf{S}}{r^3}\right] \tag{1.55b}$$

These arise from the interaction of the nuclear moment with the electronic orbital motion and with the *external* spin density. In many cases the strong crystal fields present at the impurity ion in a ferromagnet quench the electronic orbital angular momentum $L\hbar$, so that the orbital contribution $\hat{H}_{OD}$ is often small. For a cubic system, such as iron, the spin-dipolar term $\hat{H}_{SD}$ is equal to zero. As a consequence, these terms are usually very small compared with the Fermi contact interaction, for impurities in a ferromagnetic host.

The final term in equation (1.53) represents the interaction of the nuclear moment with the external magnetic field and the demagnetizing field. This and the Fermi contact interaction will now be discussed in more detail.

1.4.2 The external field

In order to define a unique quantization axis, the ferromagnetic sample must be magnetically saturated, which is done by applying an external magnetic field to the sample. Polarizing fields of ~ 0.7 Tesla are sufficient to almost completely align the domains in an iron host (to within 2%). The nuclear interaction with this externally applied field ($\mathbf{B}_{app}$) may be written as

$$\hat{H}_{ext} = -g_N \mu_N \mathbf{I} \cdot [(1+K)\mathbf{B}_{app} - D\mathbf{M}] \tag{1.56}$$

where $D\mathbf{M}$ the demagnetizing field and K is the Knight shift. For good sample shape (e.g. a thin foil magnetized in its plane) the demagnetizing field is small and the Knight shift is also usually small ($\sim 1\%$). Also $\mathbf{B}_{hf} \gg \mathbf{B}_{app}$, and it is usually adequate to take the effective magnetic field $\mathbf{B}_{eff}$ at an impurity nucleus in a ferromagnetic host to be

$$\mathbf{B}_{eff} = \mathbf{B}_{hf} + \mathbf{B}_{app} \tag{1.57}$$

1.4.3 The Fermi contact interaction

This is the interaction of the nuclear dipole moment with a net electron spin density at the nucleus. There are two mechanisms which can give rise to this contact field,

(i) *Conduction electron polarization* – In a ferromagnet, the $s-d$ exchange interaction between magnetic $3d$ electrons of the host and the s-like conduction electrons removes the degeneracy of the $\mathbf{s}_\uparrow$ and $\mathbf{s}_\downarrow$ conduction bands. This results in a net surplus of spin-up $\mathbf{s}_\uparrow$ electrons,

$$|\psi_e(0)_\uparrow|^2 = \sum_i |\psi_i(0)_\uparrow|^2 - \sum_j |\psi_j(0)_\downarrow|^2 \tag{1.58}$$

(ii) *Exchange core polarization* – The overlap between the polarized conduction electrons of the magnetic host with and the inner *s*-electrons of the non-magnetic impurity atoms effectively induces a polarization of the impurity ion core. These polarized core *s*-electrons then contribute to the hyperfine field.

References

[1] . D.M.Brink and H.J.Rose, Rev. Mod. Phys. **39**(1967)309.

[2] . K.Alder and R.M.Steffen, in The Electromagnetic Interaction in Nuclear Spectroscopy, ed. W.D.Hamilton (North Holland,Amsterdam,1975) Ch 12.

[3] . K.S.Krane, Nuclear Data Tables **11**(1973)407.

[4] . K.S.Krane, Los Alamos Laboratory Report, LA-4677(1971)

[5] . K.S.Krane and R.M.Steffen, Phys. Rev. C**2**(1970)724.

[6] . M.E.Rose, Phys. Rev. **91**(1953)610.

[7] . H.Pattyn, R.Coussement, J.Odeurs, E.Schoeters, R.E.Silverans and L.Vanneste, Hyp. Int. **2**(1976)362.

[8] . J.Rikovska, Hyp. Int. **26**(1985)963.

Chapter 2

Nuclear Spin-Lattice Relaxation

2.1 Introduction

Conventional nuclear orientation (with top loading) allows the study of nuclei with half-lives down to about one hour. This half-life limitation is simply due to the time taken to load and cool a newly prepared sample from room temperature down to $\sim$ 10 mK. With on-line nuclear orientation (ONLO) the activity is made and then implanted into the cooled host at $\sim$ 10 mK, with a typical delay of order 10ms [1] between production and implantation. Hence, with the on-line technique it becomes possible to study nuclei with with much shorter half-lives, allowing the systematic study of nuclei further from stability than is possible with conventional source preparation.

To achieve equilibrium nuclear orientation on-line, two basic requirements must be met,

(i) a static interaction to split the nuclear sub-levels, and a low enough temperature so that kT $\sim$ the sub-level splitting,

(ii) a sufficiently strong interaction between the *hot* implanted nuclei and the *cold* host lattice so that the nuclei relax to the lattice temperature in a time short compared to their half-life.

This second condition is of particular importance for ONLO, where the half-life can be short enough to be comparable with the relaxation time. As a result, any *observed* orientation will be attenuated compared to the full thermal equilibrium effect. For such nuclei, a detailed knowledge of the relaxation mechanism is essential for a complete analysis.

The theory of nuclear spin-lattice relaxation (SLR) has been developed with reference to nuclear orientation by several authors, for example see, Spanjaard *et al* [2] , Bacon *et al* [3] , Turrell [4] and Klein [5] . In particular, Klein [6] has recently given a very complete treatment of the problem. This chapter is intended to deal with those aspects of SLR which are important for on-line work.

2.2 Transition probabilities in the single impurity limit

2.2.1 General assumptions

The angular distribution of γ-rays emitted from an ensemble of nuclei oriented by means of an axially symmetric static (hyperfine) interaction is given by

$$W(\theta) = 1 + f \sum_{\lambda=2,4} B_\lambda(p_m(t)) A_\lambda U_\lambda Q_\lambda P_\lambda(\cos\theta) \qquad (2.1)$$

where all the terms have their usual meanings. The $p_m(t)$ refer to the nuclear sub-level populations (at time t), which, in the absence of external perturbations and for constant lattice temperature T_L, will always tend towards the Boltzmann distribution characteristic of that temperature. Relaxation theories which predict the behaviour of the $p_m(t)$ can be formulated for two idealized limiting cases,

(i) *single impurity limit* – each nucleus is coupled only to the host lattice and mutual interactions within the nuclear spin system can be neglected. This is valid for a highly dilute spin system (a few ppm or less).

(ii) *spin temperature limit* – the interactions between the nuclei are strong enough to establish a Boltzmann distribution corresponding to a spin temperature. This approach becomes valid when there is a moderate concentration of impurity nuclei in the host (at the % level).

For on-line implantation the impurity concentrations are generally so low that the single impurity limit is assumed to be valid at all times. The nuclei are simply too far apart (on average, many tens to hundreds of lattice spacings), for the spin-spin interactions to produce a spin temperature. In this limit the nuclei all relax independently and the level populations will not, in general, obey a Boltzmann distribution (i.e. the system cannot be described in terms of a temperature).

Sher and Primakoff [7] have studied the time evolution of the density matrix of a small system of interest (the nuclear spin system S) coupled to a thermal reservoir (the lattice L, meaning the conduction electrons in most cases). Under a number of conditions,

(i) weak coupling of S and L,

(ii) small heat capacity of S compared to L,

(iii) a diagonal density matrix of $S+L$ at t=0.

they show that the spin density matrix S remains diagonal at all times. These diagonal elements, which simply correspond to the sub-level populations, can be shown to obey a gain-loss equation of the form

$$\frac{dp_m}{dt} = \sum_n (W_{n,m}p_n - W_{m,n}p_m) \tag{2.2}$$

where $W_{m,n}$ is the time independent transition probability between sub-levels $|m\rangle \rightarrow |n\rangle$.

2.2.2 Derivation of the transition probabilities

In order to determine the transition probabilities, the Hamiltonian of the system must be considered. Weak coupling of the nuclear spin system and the lattice means that the Hamiltonian for the combined system may be written as

$$\hat{H}_{S+L} = \hat{H}_S + \hat{H}_L + \hat{H}_{SL} \tag{2.3}$$

where $\hat{H}_S$ is the Zeeman splitting of the sub-levels and $\hat{H}_{SL}$ is small enough to be treated in perturbation theory. The transitions between sub-levels are caused by the non-diagonal elements of the hyperfine interaction Hamiltonian

$$\hat{H}_{SL} = A\hat{\mathbf{I}} \cdot \hat{\mathbf{S}} = AI_zS_z + \frac{1}{2}A(S_+I_- + S_-I_+) \tag{2.4}$$

where $\hat{I}$ is the nuclear spin operator and $\hat{S}$ is the effective spin operator, which can be related to the orbital or spin operator of the conduction electrons (or both).

Using an interaction of this form transition probabilities may be derived, requiring only that the nuclei relax by exchanging energy with a degenerate Fermi gas (the conduction electrons in the host lattice), via magnetic dipole transitions. The conduction electrons are represented by eigenfunctions $|\mathbf{k}s\rangle$ with k the wave-vector and s the spin orientation. A nuclear transition $|m\rangle$ to $|n\rangle$ will be associated with a corresponding electron transition, which is treated as a scattering process from an occupied state $|\mathbf{k}s\rangle$ to an unoccupied state $|\mathbf{k}'s'\rangle$. The transition probability from an initial state $|m\mathbf{k}s\rangle$ to a final state $|n\mathbf{k}'s'\rangle$ is given by Fermi's Golden rule

$$W_{m\mathbf{k}s,n\mathbf{k}'s'} = \frac{2\pi}{\hbar}|\langle n\mathbf{k}'s'|\frac{1}{2}A(S_+I_- + S_-I_+)|m\mathbf{k}s\rangle|^2 \times \delta(E_m + E_{\mathbf{k}s} - E_n - E_{\mathbf{k}'s'}) \tag{2.5}$$

where the delta function ensures energy conservation.

Because of the weak coupling of the nuclear spin system to the conduction electrons the nuclear and electronic parts of the matrix element can be treated separately. The nuclear part may be deduced from the properties of the raising and lowering operators $I_{\pm}$

$$\langle n|I_{\pm}|m\rangle = \sqrt{I(I+1) - m(m \pm 1)}\ \delta_{n,m\pm1} \tag{2.6}$$

The electronic part of the matrix element requires a summation over allowed initial and final electron states. The total transition probability $W_{m,n}$ is given by

$$\begin{aligned} W_{m,n} &= \sum_{\substack{\mathbf{k}'s' \text{ unoccupied} \\ \mathbf{k}s \text{ occupied}}} W_{m\mathbf{k}s,n\mathbf{k}'s'} \\ &= \sum_{\substack{\mathbf{k}'s' \\ \mathbf{k}s}} W_{m\mathbf{k}s,n\mathbf{k}'s'} f(E_{\mathbf{k}s})[1 - f(E_{\mathbf{k}'s'})] \end{aligned} \tag{2.7}$$

where $f(E_{\mathbf{k}s})$ is the Fermi distribution function.

This summation over electron states may be replaced by an integration over the electron energies $E_{\mathbf{k}s}$ and $E_{\mathbf{k}'s'}$. If this is done the only non-zero transition probabilities are found to be

$$W_{m+1,m} = \frac{\Delta E_m}{2kC_k} \frac{[I(I+1) - m(m+1)]}{1 - e^{-\Delta E_m/kT_L}} \tag{2.8a}$$

$$W_{m,m+1} = \frac{\Delta E_m}{2kC_k} \frac{[I(I+1) - m(m+1)]}{e^{\Delta E_m/kT_L} - 1} \tag{2.8b}$$

where $\Delta E_m = (E_{m+1} - E_m)$ and C_k, the Korringa constant, is a system dependent constant arising from the integral over electron states.

For equidistant sub-level splittings (i.e. magnetic splitting), an interaction temperature $T_{int} = |\Delta E_m|/k$ may be defined, which gives an appropriate scale for both nuclear orientation and relaxation.

2.2.3 Discussion

It is instructive to write the above transition probabilities in the following way. For $E_{m+1} > E_m$,

$$W_{m+1,m} = \frac{\Delta E_m}{2kC_k}[I(I+1) - m(m+1)]\left[1 + \frac{1}{e^{\Delta E_m/kT_L} - 1}\right]$$
$$= W_{m,m+1} + \frac{\Delta E_m}{2kC_k}[I(I+1) - m(m+1)] \qquad (2.9)$$

The downward transition probability $W_{m+1,m}$ contains a temperature dependent part, equal to the upward transition probability $W_{m,m+1}$ (analogous to stimulated emission and absorption of radiation), and a temperature independent part (analogous to spontaneous emission).

As Bacon *et al*[3] pointed out, the appearance of stimulated and spontaneous transition probabilities is a consequence of the excitations (electron-hole pairs, corresponding to nuclear transitions) obeying Bose-Einstein statistics. From this general observation, it is expected that any approximations made in calculating the electronic part of the matrix element will influence only C_k, and not the general form of the equations.

2.3 Relaxation equations

2.3.1 Solution of the master equation

The time dependence of the $(2I+1)$ sub-level populations that describe the nuclear spin system is governed by the master equation (2.2). Using the fact that the system relaxes via magnetic dipole transitions, the master equation reduces to

$$\begin{aligned} \frac{dp_m}{dt} = & \sum_n (W_{n,m}p_n - W_{m,n}p_m) \\ = & \; W_{m+1,m}\, p_{m+1} \\ & - (W_{m,m+1} + W_{m,m-1})\, p_m \\ & + \; W_{m-1,m}\, p_{m-1} \end{aligned} \tag{2.10}$$

This set of $(2I+1)$ coupled equations may be written in matrix form

$$\frac{d\mathbf{p}}{dt} = \mathbf{R}\mathbf{p} \tag{2.11a}$$

where $\mathbf{p}$ is a $(2I+1)$ dimensional column vector and $\mathbf{R}$ is the time independent relaxation matrix. In component form this is simply

$$\frac{dp_m}{dt} = \sum_n R_{mn}p_n \tag{2.11b}$$

As seen from (2.8) and (2.10) the relaxation matrix $\mathbf{R}$ is tri-diagonal with non-zero elements

$$R_{mn} = \begin{cases} W_{n,m} & \text{for } n \neq m \\ -(W_{n,m+1} + W_{n,m-1}) & \text{for } n = m \end{cases} \tag{2.12}$$

Following the approach adopted by Klein[6], the diagonal matrix $\mathbf{D}$ with $D_{mn} = \delta_{mn}\mathrm{e}^{-E_m/2kT_L} = d_m$ is used to produce an equivalence transformation of $\mathbf{R}$ to a symmetric matrix $\mathbf{R^s} = \mathbf{D^{-1}RD}$ (see appendix I.1 for details). Equation

(2.11) is now solved by diagonalization of $\mathbf{R^s}$, which essentially decouples the $(2I+1)$ equations. If $\mathbf{U^s}$ is the matrix of eigenvectors for $\mathbf{R^s}$, and $\mathbf{K}$ the matrix of eigenvalues (with $K_{lj} = \delta_{lj} k_l$), then

$$\mathbf{p}(t) = \mathbf{D}\mathbf{U^s}\mathrm{e}^{\mathbf{K}t}(\mathbf{U^s})^{-1}\mathbf{D}^{-1}\,\mathbf{p}(0) \tag{2.13a}$$

or in component form

$$p_m(t) = \sum_l d_m U^s_{ml} \mathrm{e}^{k_l t} \left(\sum_n U^s_{nl} d_n^{-1} p_n(0) \right) \tag{2.13b}$$

It should be pointed out that this method of solution requires the eigenvalues to be non-degenerate so that $\mathbf{U}$ is not singular and can be inverted. However, for $T_L \ll T_{int}$ the eigenvalues may be written as

$$k_l = -\frac{T_{int}}{C_k}\, l\,[(2I+1) - l] \tag{2.14}$$

where $l = 0, 1 \ldots 2I$.

From this it can be seen that the eigenvalues k_l and k_j are degenerate for $l + j = (2I + 1)$. Hence, equation (2.13) is not a general solution, and as a consequence the algorithms used to solve this equation may show convergence problems, and also be subject to rounding errors, in the extreme low temperature limit $(T_L < 0.1\, T_{int})$.

2.3.2 Relaxation times

In conventional NMR the spin-lattice relaxation time T_1 is regarded as a fundamental quantity because all observable quantities relax as e^{-t/T_1}. The Hebel-Slichter equation [8] defines T_1 in terms of the transition probabilities $W_{m,n}$ as

$$\frac{1}{T_1} = \frac{1}{2} \sum_{m,n} W_{m,n} (E_m - E_n)^2 \Big/ \sum_n E_n^2 \tag{2.15}$$

Substituting for the transition probabilities from (2.8) gives,

$$T_1 = \frac{2C_k}{T_{int}} \tanh \frac{T_{int}}{2T_L} \tag{2.16}$$

which, in the high temperature limit reduces to the Korringa relation

$$T_1 T_L = C_k \tag{2.17}$$

To determine whether these results can be applied to nuclear orientation, it is necessary to look at a few of the assumptions underlying the NMR theory,

(i) the observed quantity (the magnetization) is a rank one tensor,

(ii) experiments are performed in the high temperature limit,

(iii) the Hebel-Slichter equation is based upon the existence of a spin temperature.

In fact, none of these conditions is satisfied in nuclear orientation. Firstly, the observables (B_2 and B_4) are not rank one tensors and consequently their behaviour is more complicated. Secondly, and more important, neither the high temperature nor the spin temperature limits are valid in LTNO.

In order to get a feel for relaxation in LTNO it is useful to write equation (2.13*b*) in the form

$$p_m(t) = \sum_l r_{ml} e^{k_l t} \tag{2.18a}$$

where

$$r_{ml} = d_m U^s_{ml} \sum_n U^s_{nl} d_n^{-1} p_n(0) \tag{2.18b}$$

This emphasizes the fact that the time evolution of the populations is described by a multi-exponential function, and in general, it is a bad approximation to treat relaxation in terms of a single exponential. However, if the initial conditions, $p_n(0)$ are known, then this multi-exponential function is completely determined by the Korringa constant, C_k.

There are two limiting cases where the relaxation time constants, given by $\tau_l = 1/k_l$, approach limiting values,

(i) *high temperature limit (h.t.l.)* – for $T_L \gg T_{int}$ all the transition probabilities become equal and also are proportional to T_L. The corresponding time constants become

$$\tau_l = \frac{C_k}{T_L}, \frac{1}{3}\frac{C_k}{T_L}, \cdots \frac{2}{l(l+1)}\frac{C_k}{T_L} \cdots \tag{2.19}$$

High temperature NMR relaxation curves contain one exponential with a time constant $\tau_1 = T_1$ corresponding to the Korringa relation (2.17).

(ii) *low temperature limit (l.t.l.)* – for $T_L \ll T_{int}$ the upward transition probabilities tend to zero and the downward transition probabilities become proportional to T_{int}. The associated time constants are

$$\tau_l = \frac{1}{I}\frac{C_k}{T_{int}}, \frac{1}{2I-1}\frac{C_k}{T_{int}} \cdots \frac{2}{l[(2I+1)-l]}\frac{C_k}{T_L} \cdots \tag{2.20}$$

For a quantitative understanding, this multi-exponential approach must be used. Single exponential behaviour applies only in very specialized and often unrealistic cases as far as LTNO is concerned.

However, despite the complex true time dependence it is possible to define an effective time constant, which will qualitatively describe the approach of the sub-level populations to equilibrium. Such a time constant, τ_{SLR}, may be defined in the following way

$$B_2(\tau_{SLR}) - B_2(\infty) = [B_2(0) - B_2(\infty)]/\mathrm{e} \tag{2.21}$$

where B_2 is the orientation coefficient and e is the base of the natural logarithm. For ONLO it is appropriate to consider the nuclei to relax from warm (i.e. on implantation at $t = 0$) to thermal equilibrium with the lattice, as $t \to \infty$. Hence, $B_2(0)$ is zero and τ_{SLR} is the time after which the deviation of B_2 from $B_2(\infty)$ is equal to $B_2(\infty)/\mathrm{e}$.

Now, the transition probabilities given by (2.8) are proportional to T_{int}/C_k multiplied by some function of I and T_{int}/T_L. The term T_{int}/C_k is just a scaling factor, and any relaxation time, τ, may be written as

$$\tau = \frac{C_k}{T_{int}} f(I, T_{int}/T_L) \tag{2.22}$$

where $f(I, T_{int}/T_L)$ specifies some functional dependence on I and T_{int}/T_L. Hence, the product of $\tau T_{int}/C_k$ is just dependent on the spin and the ratio T_{int}/T_L. The ratio $\tau_{SLR}T_{int}/C_k$ has been calculated as a function of T_{int}/T_L for spins 2 and 5, and is shown in [Fig 2.1] .

A simple empirical estimate for τ_{SLR} can be made by

$$\tau_{emp} = \min(\tau_{htl}, \tau_{ltl}) \tag{2.23a}$$

where

$$\tau_{htl} = \frac{4}{3}\frac{C_k}{T_L} \qquad \text{and} \qquad \tau_{ltl} = \frac{3.3}{I+\frac{1}{2}}\frac{C_k}{T_{int}} \tag{2.23b}$$

The dashed lines in [Fig 2.1] represent τ_{emp}. For all spins, the simple estimates, τ_{htl} and τ_{ltl}, agree very well with τ_{SLR}, in the high and low temperature limits respectively. For $T_{int} \sim T_L$, τ_{emp} tends to overpredict τ_{SLR}. To stress again, this effective relaxation time is only valid for the case where the nuclei start warm and relax to the lattice temperature, without any external perturbation. The dot-dashed line in [Fig 2.1] represents T_1, defined by equation (2.16), which, not surprisingly, is an inappropriate measure of low temperature relaxation.

2.3.3 Discussion

From a knowledge of the initial populations and C_k (as well as T_{int}), it is possible to completely determine the time evolution of the sub-level populations. For on-line work nuclei are implanted *hot* (defining all the $p_n(0)$ to be equal), so that the relaxation is characterized just by C_k. A knowledge of C_k is obviously essential for the calculation of the full time dependence as well as for simple estimates of relaxation times. A comprehensive tabulation of measured C_k values is given by Klein[6] for various impurity-host combinations. However, if C_k is not known for the particular impurity-host combination of interest, there are several to ways to estimate it,

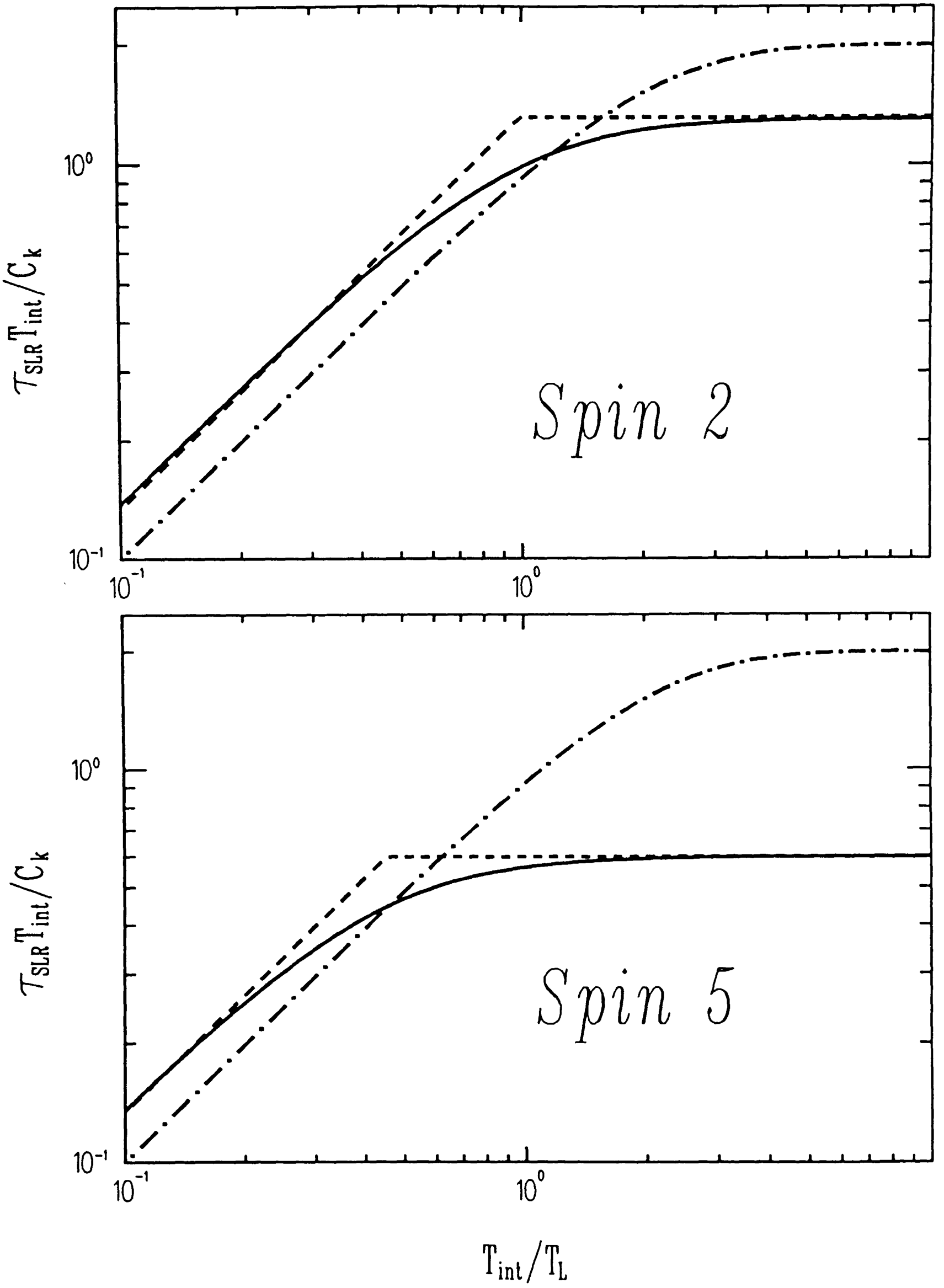

Figure 2.1. $\tau_{SLR}T_{int}/C_k$ for spins 2 and 5 as a function of T_{int}/T_L. The dotted line represents τ_{emp} given by equation (2.23), and the dot-dashed line represents T_1 given by equation (2.16), which are shown for comparison.

(i) as long as the relaxation proceeds via magnetic dipole interactions and single boson excitations (electron-hole pairs) it is possible to write

$$\gamma_n^2 C_k = \text{constant} \tag{2.24}$$

for different isotopes in the same host, as far as hyperfine anomalies are neglected (γ_n, the gyromagnetic ratio, is defined by $\gamma_n = \mu\mu_n/I\hbar$). Hence, C_k values may be estimated for a whole range of isotopes, provided that at least one has been measured.

(ii) empirically, for impurities in an iron host, it is found that the fluctuating field causing SLR is approximately proportional to the hyperfine field [9]. This leads to a generalization of (2.24) to give

$$\nu_0^2 C_k = 6.0 \times 10^{16}\ \text{Ks}^{-1} \tag{2.25a}$$

where ν_0 is the zero field NMR frequency, or alternatively,

$$T_{int}^2 C_k = 1.4 \times 10^{-4}\ \text{sK}^3 \tag{2.25b}$$

With the exception of Mn, which relaxes ten times faster than expected, experimental results deviate from equation (2.25) by less than a factor of 4 (and in a lot of cases 2). This is to be compared with $\gamma_n^2 C_k$, which varies by nearly three orders of magnitude. This result coupled with equation (2.23) make it possible to estimate a relaxation time from a knowledge just of T_{int}. Such a tabulation of estimated relaxation times for isotopes in an iron host has been given by Stone [10].

A feature of equation (2.25) is that C_k is proportional to T_{int}^{-2}, so the higher the interaction temperature, the smaller C_k. Since the transition probabilities, $W_{m,n} \propto 1/C_k \propto T_{int}^2$, nuclei with a higher interaction temperature relax faster. In particular, in the low temperature limit $\tau_{SLR} \propto C_k/T_{int} \propto 1/T_{int}^3$, and the effective relaxation time is strongly dependent on the interaction temperature.

2.4 Relaxation with finite lifetime and implantation

2.4.1 The modified master equation

The last section dealt with situations in which the half-life, $t_{1/2}$, of the relaxing state could be taken as infinite with respect to the time constants determining the relaxation. For on-line experiments, however, this is not always the case. For example, for impurities in iron at LTNO temperatures τ_{SLR} can vary from 10^{-3}s to 10^{4}s, depending on the system. For the case where $\tau_{SLR} \sim \tau$ ($\tau = t_{1/2}/\ln 2$) the sub-level populations are no longer given by a Boltzmann distribution, in the absence of external perturbations to the spin system or of the lattice temperature. For a sample at a temperature T_L, with an isotope of lifetime τ, the observed anisotropy $\overline{W(\theta)}$ of those nuclei which started to relax at a time t before the detected γ-ray was emitted, is

$$\overline{W(\theta)} = \frac{1}{\tau}\int_0^\infty W(\theta,t)\mathrm{e}^{-t/\tau}\,dt \qquad (2.26)$$

$W(\theta,t)$ is calculated by solution of equation (2.11) with initial populations determined by the orientation of the parent state and re-orientation through preceeding decays.

In order to take into account external perturbations to the spin system or of the lattice temperature, it is desirable to use a modified form of master equation, instead of trying to generalize equation (2.26). The general formalism for this has been derived [11] and the modified master equation may be written as

$$\frac{d\mathbf{p}}{dt} = (\mathbf{R}+\mathbf{T})\,\mathbf{p} + \mathbf{P}\,\mathbf{p_p} \qquad (2.27)$$

where $\mathbf{p}$ and $\mathbf{p_p}$ represent the sub-level populations of the *relaxing* and *populating* states respectively and $\mathbf{R}$ is the relaxation matrix, defined in equation

(2.12). The matrix **T**, corresponding to the radioactive decay of the *relaxing* sub-levels, is diagonal with

$$T_{mn} = -\frac{1}{\tau}\,\delta_{mn} \tag{2.28}$$

where τ is the nuclear lifetime. The terms in equation (2.27) are shown schematically in [Fig 2.2] .

The matrix **P** refers to the population of the *relaxing* sub-levels, which may either be by direct implantation, or by radioactive decay of a parent nucleus. For the latter case, assuming population by a single transition from $|I_p m_p\rangle$ to $|Im\rangle$ with emission of pure radiation $|LM\rangle$ the population matrix $(I_p \times I)$ becomes (see equation (1.29))

$$P_{mm_p} = \frac{2I_p+1}{\tau}\begin{pmatrix} I & L & I_p \\ m & M & -m_p \end{pmatrix}^2 \tag{2.29}$$

where $M = m_p - m$.

The solution of equation (2.27) is greatly simplified for cases where $\mathbf{p_p}$ is constant, or nearly so. For population by nuclear decay such cases include,

(i) the parent spin, $I_p = 0$,

(ii) $T_{int,p} \ll T_L$ at all times,

(iii) very fast or very slow relaxation of the parent state relative to the daughter state.

For population by direct implantation, all the sub-levels will be populated equally and constant $\mathbf{p_p}$ simply refers to a constant implantation rate. The solution of equation (2.27) for constant $\mathbf{p_p}$ is straightforward (see appendix I.2.2) and is analogous to the solution of the unmodified master equation (2.11), giving

$$\mathbf{p}(t) = \mathrm{e}^{-t/\tau}\,\mathbf{D}\mathbf{U}^{\mathbf{s}}\mathrm{e}^{\mathbf{K}t}(\mathbf{U}^{\mathbf{s}})^{-1}\mathbf{D}^{-1}\,[\mathbf{p}(0) - \mathbf{p}(\infty)] + \mathbf{p}(\infty) \tag{2.30a}$$

or in component form

$$p_m(t) = \mathrm{e}^{-t/\tau}\sum_l d_m U^s_{ml}\mathrm{e}^{k_l t}\left(\sum_n U^s_{nl} d_n^{-1}\,[p_n(0) - p_n(\infty)]\right) + p_m(\infty) \tag{2.30b}$$

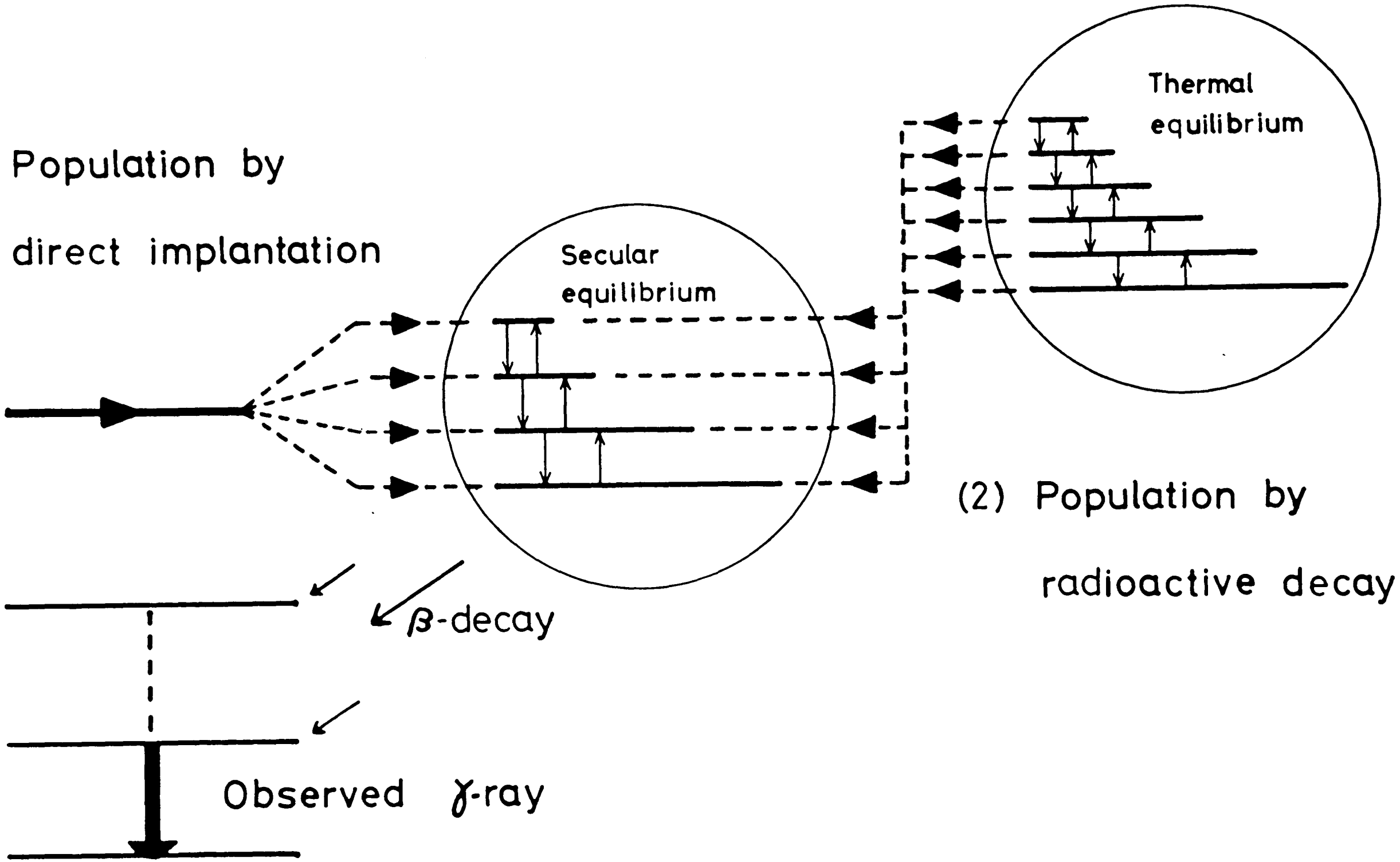

Figure 2.2. An illustration of the three terms in equation (2.27), corresponding to the relaxation, decay and population of the sub-levels **p**.

where

$$\mathbf{p}(\infty) = -(\mathbf{R}+\mathbf{T})^{-1}\,\mathbf{p_p}(0) \tag{2.31}$$

As long as the $\mathbf{T} \neq 0$ the matrix $(\mathbf{R}+\mathbf{T})$ is non-singular, and consequently has an inverse.

2.4.2 Initial conditions and source strength

In order to evaluate equation (2.30) it is necessary to know the initial sub-level populations of the *relaxing* and *populating* states, $\mathbf{p}(0)$ and $\mathbf{p_p}$ respectively. For the population terms, the simplest assumption to make is that I_0 nuclei/second are produced, which are equally distributed amongst the *relaxing* sub-levels. This will be the case if the population is by continuous implantation, or by nuclear decay of a parent that does not orient. For all cases in this thesis for which $\tau_{SLR} \sim t_{1/2}$, this assumption is valid, and will be used for the following discussion. Cases where the relaxing sub-levels are not equally populated may be treated as a simple extension of the theory outlined below.

Equation (2.27) may now be written in component form

$$\frac{dp_m}{dt} = \sum_n (W_{n,m}p_n - W_{m,n}p_m) - \frac{1}{\tau}\,p_m + \frac{I_0}{2I+1} \tag{2.32}$$

If this equation is now summed over m, the source strength as a function of time may be deduced as follows

$$\begin{aligned}\frac{d}{dt}\left(\sum_m p_m(t)\right) &= \left(\sum_{m,n} W_{n,m}p_n - \sum_{n,m} W_{m,n}p_m\right) - \frac{1}{\tau}\sum_m p_m(t) + I_0 \\ &= -\frac{1}{\tau}\sum_m p_m(t) + I_0 \end{aligned} \tag{2.33}$$

This is easily solved to give

$$\sum_m p_m(t) = \mathrm{e}^{-t/\tau}\sum_m p_m(0) + I_0\tau(1-\mathrm{e}^{-t/\tau}) \tag{2.34}$$

If $I_0 = 0$, corresponding to no implantation, then equation (2.32) is the same as equation (2.11), but with the addition of a term due to the finite half-life of the source. The only consequence of this is that the resultant populations, defined by equation (2.13), should be multiplied by a factor $e^{-t/\tau} \sum_m p_m(0)$ to take account of their decay.

For a non-zero I_0, equation (2.34) shows that as $t \to \infty$ the source strength $\sum_m p_m(\infty) \to I_0\tau$. If a normalization condition $I_0\tau = 1$ is applied, the above equations may be further simplified to

$$\frac{dp_m}{dt} = \sum_n (W_{n,m}p_n - W_{m,n}p_m) - \frac{1}{\tau}\, p_m + \frac{1}{\tau(2I+1)} \tag{2.35}$$

and

$$\sum_m p_m(t) = 1 - e^{-t/\tau}\left(1 - \sum_m p_m(0)\right) \tag{2.36}$$

The solution of equation (2.35) is discussed in appendix I.2, and the resultant sub-level populations are evaluated using the subroutine TRELAX. In addition, the source strength, $n(t) = \sum_m p_m(t)$, given by equation (2.36), is also calculated.

2.4.3 Secular equilibrium

For experiments without external perturbation of the system, the sub-level populations will attain *secular* equilibrium values, somewhere between the initial (i.e. equal) and the thermal equilibrium populations. In this steady state situation $d\mathrm{p}/dt \to 0$, and the sub-level populations may may be obtained from (2.27) as a series of linear equations. The solution of these equations simply yields $\mathrm{p}(\infty)$ as defined by (2.31).

It is possible to show that, starting with the same initial conditions,

$$\frac{1}{\tau}\int_0^\infty p_m(t)e^{-t/\tau}\, dt = p_m(\infty) \tag{2.37}$$

where $p_m(t)$ is given by (2.13) and $p_m(\infty)$ by (2.31). This has in fact been done using the subroutines given in appendix I, and serves as a consistency check for their validity. This equation also shows that the solution of (2.31) will give the same results as (2.27), but with much less computation required. The solution of equation (2.31) is described in appendix $I.3$.

Assuming equal population of the sub-levels, the secular equilibrium solution of equation (2.35) may be written

$$\frac{dp_m}{dt} = 0 = \sum_n R_{mn} p_n - \frac{1}{\tau}\, p_m + \frac{1}{\tau(2I+1)} \qquad (2.38a)$$

Now, as the transition probabilities given by (2.8) are proportional to T_{int}/C_k, it is possible to write $R_{mn} = (T_{int}/C_k)\, R'_{mn}$, where R'_{mn} is a function of I and T_{int}/T_L). The above equation may now be written as

$$0 = \sum_n \left[\left(\frac{\tau T_{int}}{C_k} \right) R'_{mn} - \delta_{mn} \right] p_n + \frac{1}{(2I+1)} \qquad (2.38b)$$

The factor $\tau T_{int}/C_k$ is essentially a measure of the ratio of the nuclear lifetime to the relaxation time, with the other relevant parameters being the spin I and T_{int}/T_L. It is useful to introduce a reduction factor r defined by

$$B_2(\text{secular}) = r\, B_2(\text{thermal}) \qquad (2.39)$$

where B_2(thermal) is the orientation coefficient for full thermal equilibrium. This reduction factor is shown in [Fig 2.3] for spins 2 and 5 as a function of T_{int}/T_L, for different values of $\tau T_{int}/C_k$.

It is clear that for $\tau \ll C_k/T_{int}$, $r \to 0$ and for $\tau \gg C_k/T_{int}$, $r \to 1$, as would be expected from the form of (2.38). Another feature is that in the low temperature limit the ratio r becomes temperature independent. This is simply a consequence of the effective relaxation time τ_{SLR} becoming temperature independent, as may be seen from [Fig 2.1]. This will be discussed further in chapter 7.2.1 with reference to Cs isotopes.

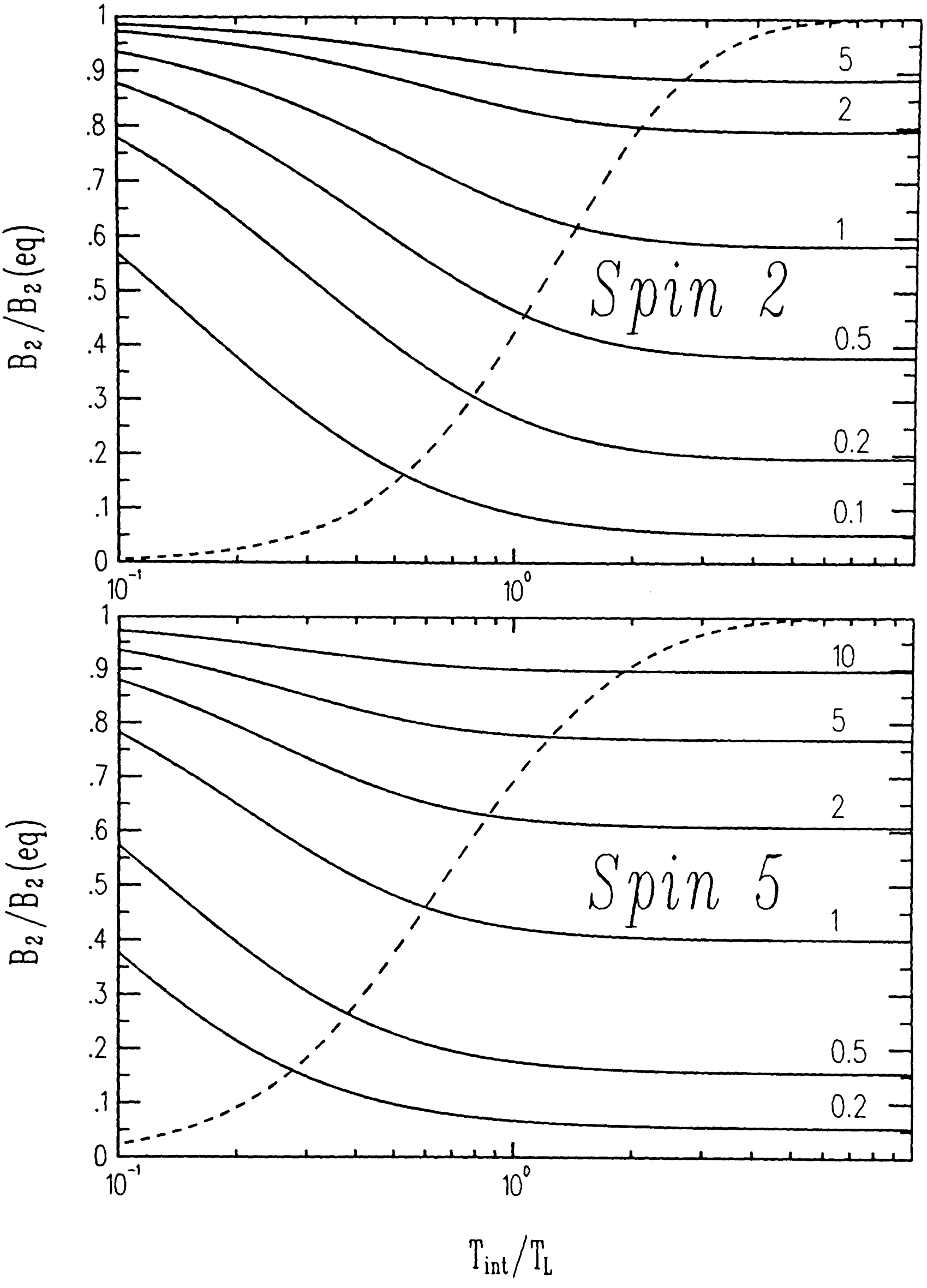

Figure 2.3. $B_2/B_2(eq)$ for spins 2 and 5 as a function of T_{int}/T_L. The curves correspond to different values of the parameter $\tau T_{int}/C_k$ (which are shown for each curve). The dashed line represents the temperature dependence of $B_2(eq)$ (the full thermal equilibrium value), normalized to its saturation value.

References

[1] . R.Kirchner, K.H.Burchard, W.Hüller and O.Klepper, Nucl. Instr. and Meth., **186**(1981)295.

[2] . D.Spanjaard and F.Hartmann-Boutron, Solid State Comm. **8**(1970)233.

[3] . F.Bacon, J.A.Barclay, W.D.Brewer, D.A.Shirley and J.E.Templeton, Phys.Rev. **B5**(1972)2397.

[4] . B.G.Turrell, Hyp. Int. **7**(1980)429.

[5] . E.Klein, Hyp. Int. **15/16**(1983)557.

E.Klein, Hyp. Int. **22**(1985)111.

[6] . E.Klein, in Low-Temperature Nuclear Orientation, eds. N.J.Stone and H.Postma (North Holland,Amsterdam,1987) Ch 12.

[7] . A.Sher and H.Primakoff, Phys. Rev. **119**(1960)178.

[8] . C.P.Slichter, in Principles of Magnetic Resonance (Springer-Verlag,Berlin,Heidelberg,New York,1978)143.

[9] . N.J.Stone, in Hyperfine Interaction in Excited Nuclei, eds. G.Goldring and C.Kalish (Gordon and Breach,New York,1971)237.

[10] . N.J.Stone, Hyp. Int. **22**(1985)3.

[11] . M.Kopp, B.Kazemi-Far and E.Klein, Z. Phys. **B44**(1981)73.

Chapter 3

Experimental apparatus and techniques

3.1 Introduction

All the work described in this thesis has been performed at the SERC Daresbury Laboratory, using mass-separated beams provided by the Daresbury On-Line Isotope Separator (DOLIS), which is *on-line* to the Nuclear Structure Facility (NSF) Van der Graff generator. The NSF is a conventional vertical tandem, which currently operates at terminal voltages of up to 20MV, with a wide range of ion beams available.

The basic idea behind the operation of a *tandem* accelerator is relatively simple. Initially, a beam of negative ions is produced, and then accelerated to the centre terminal by its positive high voltage, where it is stripped of electrons. The resulting positive ion beam is re-accelerated through the lower half of the beam tube to an energy, which depends upon the terminal voltage, and also the atomic number of the ion. For example, at 20MV the most probable charge state for a beam of S^- ions passing through a thin carbon foil stripper is S^{10+}. Thus, the resultant energy of the beam would be $(1 + 10) \times 20 = 220$ MeV. If a gas stripper were to be used instead of the foil, the quality of the emergent beam would be improved, but at the expense of less efficient stripping (as the

spacing between molecules in the gas stripper is much greater than that in the foil).

For masses below $A \sim 50$, beams of the most probable charge state may be accelerated to energies above 5 MeV/nucleon at the NSF. A wide range of neutron-deficient isotopes far from stability may be produced using such beams, and as the energy is relatively easy to change in a tandem, the optimum conditions for production of a particular isotope may usually be found. A description of the *full* range of experimental facilities available at the NSF has been given in a review by Gelletly [1], and only the apparatus associated with the isotope separator will be discussed here.

In heavy-ion fusion reactions, the yields are always modest, typically leading to separated beams of $10^3 - 10^6$ ions/second. However, these are more than sufficient to enable a full range of experiments to be performed with DOLIS, and its associated equipment (to be described later). A pictorial diagram of the separator and associated equipment is shown in [Fig 3.1] .

The DOLIS facility was designed in order that as much information as possible could be obtained on the decay schemes of mass-separated isotopes. To this end a variety of spectroscopic techniques are available,

(i) low temperature nuclear orientation, and γ-ray linear polarization measurements using a ^{3}He/^{4}He dilution refrigerator,

(ii) electron conversion spectroscopy, using a mini-orange electron spectrometer,

(iii) $\gamma - \gamma$ coincidence and correlation measurements,

(iv) laser spectroscopy for the study of atomic hyperfine structure.

In this chapter, some of the above experimental techniques, which are relevant to experiments detailed later, will be described. A photograph of DOLIS during an on-line experiment is shown in [Fig 3.2] , illustrating some of the above techniques.

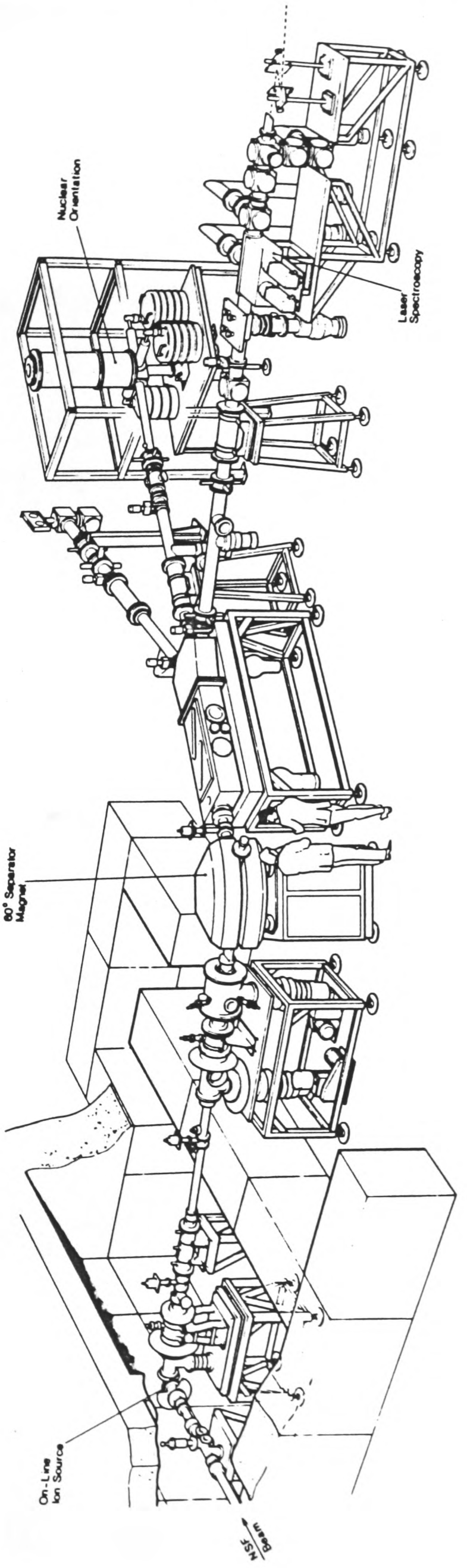

Figure 3.1. A pictorial view of the Daresbury On-Line Isotope Separator (DOLIS).

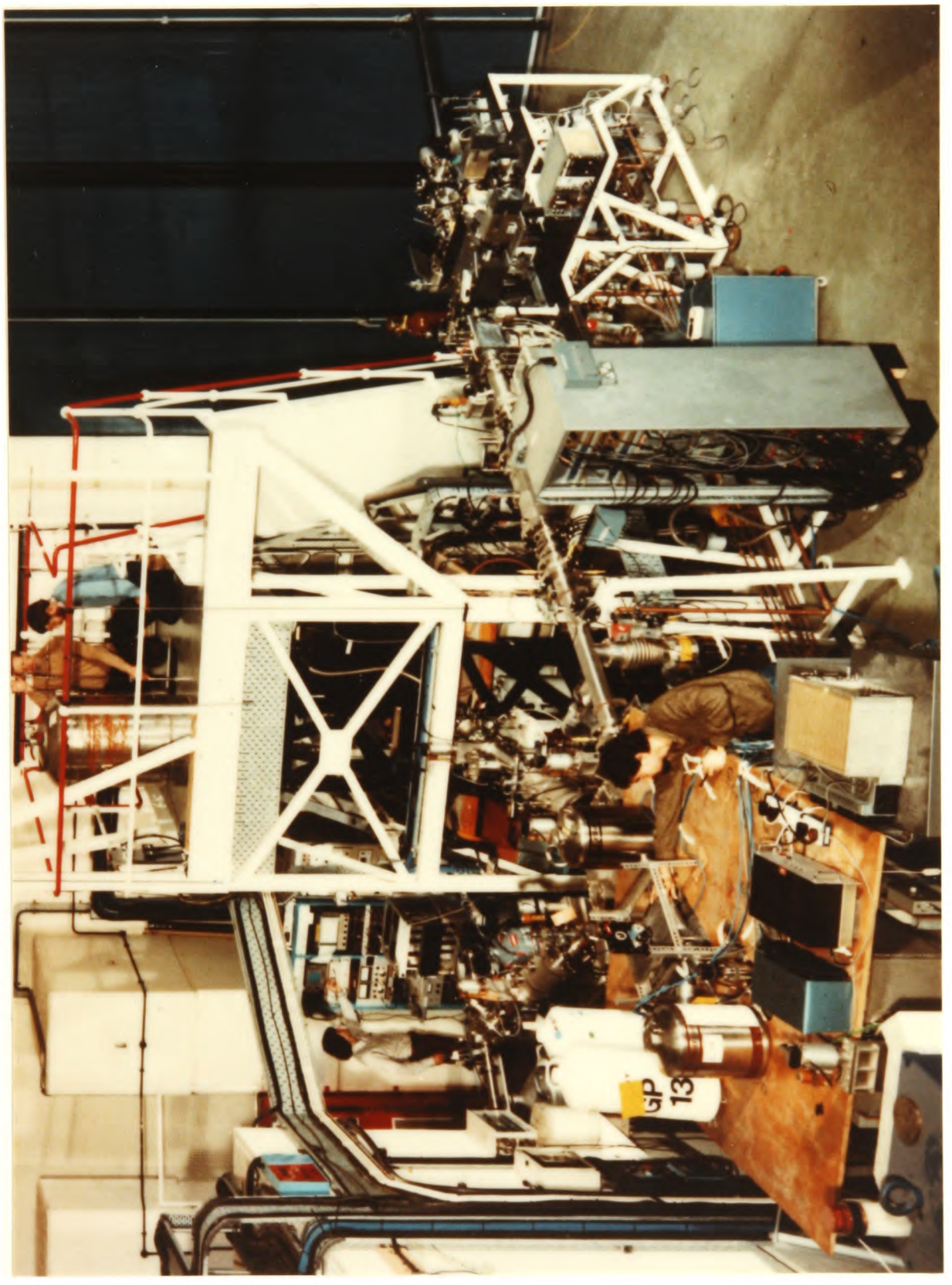

Figure 3.2. A photograph of the Daresbury On-Line Isotope Separator during an on-line run. Experimenters may be seen loading a sample into the refrigerator, checking detectors on the focal plane of the separator, and checking the settings of the separator.

3.2 The Daresbury On-Line Isotope Separator

3.2.1 Introduction

To study the products of heavy-ion reactions, the basic principle of on-line separation is to stop the reaction products inside an ion source, and following ionization, to extract them into an isotope separator, which separates ions by momentum using a dipole magnet. The Daresbury isotope separator was designed to meet the following requirements,

(i) dispersion and resolution good enough to separate nuclei with mass numbers up to $A \sim 250$,

(ii) simultaneous collection of a range of different isotopes in the focal plane,

(iii) the possibility of both on-line and off-line use, with the flexibility to allow the use of ion sources in different positions,

(iv) post-acceleration of the separated beam up to 60keV, to allow implantation into a host lattice suitable for nuclear orientation studies.

A detailed account of the operation of the separator has recently been given [2] , and the following discussion is only intended to cover some of the more important points. The layout of the separator, along with its associated equipment, can be seen in [Fig 3.3] , showing the on-line source in a shielded cave, and a separate position for the off-line sources, outside the radiation shielding.

The experiments to be described in this thesis have all been performed *on-line*, with the beam from the NSF striking a target adjacent to a FEBIAD [3] ion source. Nuclear recoils from the target pass through a thin ($\sim$ 1 mg/cm^2) window (alternatively, the window itself may form the target, depending on whether it is refractory or not), and are stopped on a graphite (or tantalum) catcher. This is maintained at a high temperature ($\sim$ 2000°C), so that the nuclei stopped in the surface will diffuse out quickly into a small, low pressure plasma

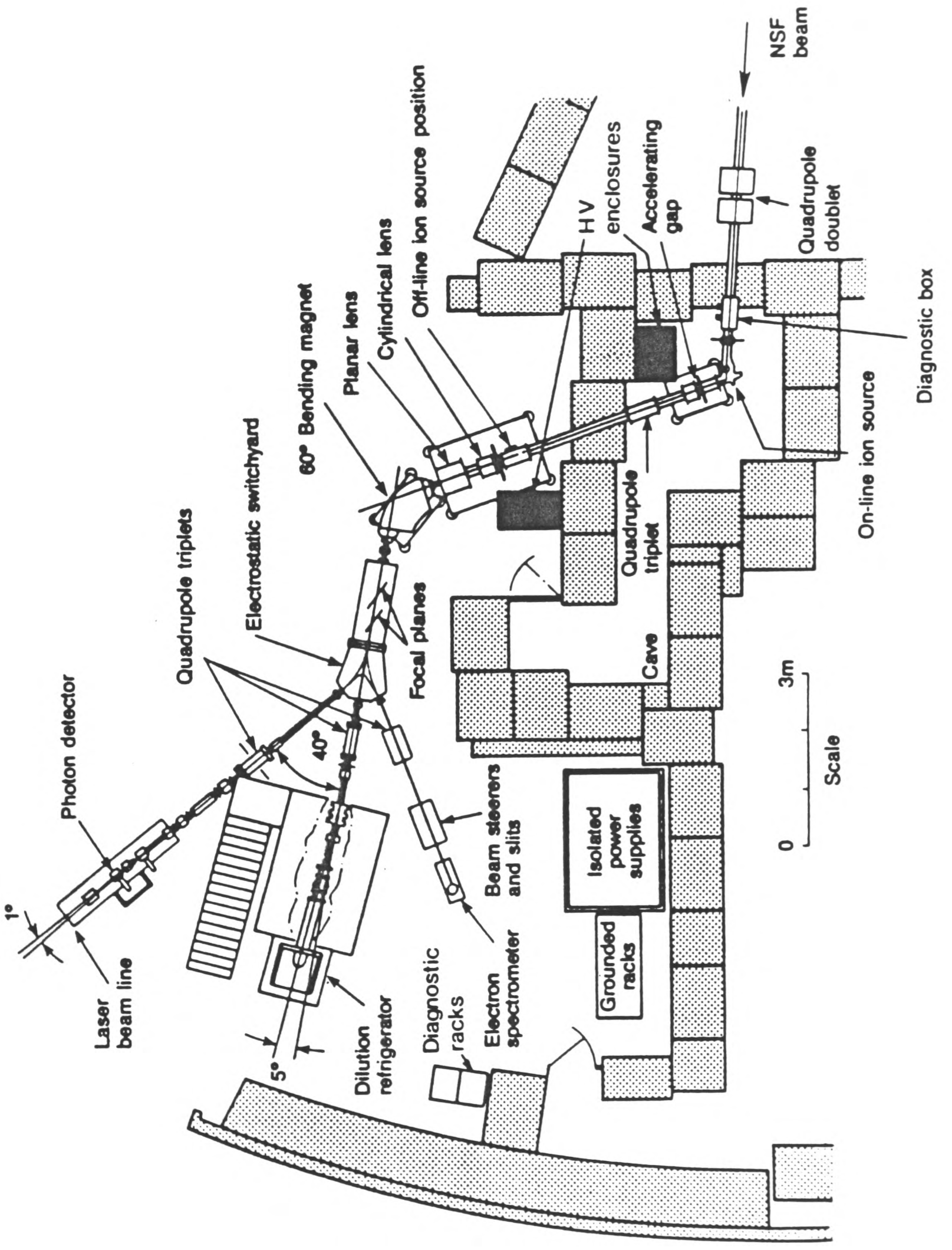

Figure 3.3. Plan view of the Daresbury On-Line Isotope Separator (DOLIS).

region, where an arc discharge is maintained by Forced Electron Bombardment. The nuclei are subsequently ionized and extracted at a potential of up to 30KV. This *secondary* beam is then accelerated and focussed so that it re-forms at the off-line source position to act as the *effective* source at that point. Mass separation is then achieved using a 60° sector dipole magnet, with a 60mm pole gap. The dispersion is adequate to separate neighbouring masses (a 1% change in mass will shift the image position 10mm).

As indicated earlier, the beam optics have been arranged so that ions within 10% of the central mass may be collected in the focal plane box. In particular, there is a tape transport system that can be moved to any position along the focal plane, and the tape positioned to catch any nearby non-central mass. A source collected in this way may then be transported up to a platform above the focal plane box, where $\gamma - \gamma$ coincidence and correlation studies may be performed. The minimum time for transport of the source to the counting position is 2 seconds.

After the focal plane is an electrostatic switchyard, which directs the central beam to one of three secondary beam lines. One of these leaves the switchyard along the axis of the focal plane box which leads to the dilution refrigerator. The other two beam lines are at ±40° to the central line, one of which is used for laser spectroscopy, and the other is a general purpose beam line (referred to later as the Mini-Beam Line – MBL), which has been used primarily for conversion electron studies in this work.

For the central beam line, the beam enters the refrigerator via a cooled side access tube (to be discussed in the next section), before which a 5° *bend* has been incorporated, which serves a dual purpose,

(i) to eliminate any neutral atoms, which would contribute to the heat load of the refrigerator,

(ii) to allow the cold finger of the refrigerator to face a plate cooled to 77K.

Another important feature of the beam optics is that while the central mass beam is being *implanted* into the refrigerator, it is also possible to direct a beam of neighbouring mass down the mini-beam line. Under favourable conditions, it is thus possible to carry out two independent experiments *simultaneously*. This is obviously of considerable importance in making maximum use of available beam time.

3.2.2 CASCADE calculations

In order to select suitable reactions to produce the nuclei studied in this thesis, cross-sections for fusion-evaporation reactions were calculated using the code CASCADE [4] (modified to run on a VAX11/780†). The program was used for the reactions of ^{32,34}S beams on ^{93}Nb targets, for incident beam energies up to 200MeV. Cross-sections for the production of a range of Cs, Xe and I isotopes are shown in [Fig 3.4] . In these calculations, only the atomic numbers, masses and spins of the target and projectile were specified, with default values being taken for the other parameters.

The beam energy may thus be chosen to optimize the production of a given isotope, bearing in mind that the incident beam loses $\sim$ 7MeV per mg/cm^2 of the ^{93}Nb target [5] (e.g. for a 3mg/cm^2 target the *effective* beam energy would span a range of $\sim$ 20MeV in the target).

The Coulomb barrier (in the laboratory frame) may be written as [6]

$$V_c = \frac{1.44(A_t + A_p)Z_t Z_p}{A_t\left[r_0(A_t^{1/3} + A_p^{1/3}) + d\right]} \quad \text{[MeV]} \tag{3.1}$$

where $Z_{t,p}$, $A_{t,p}$ are the atomic numbers and masses of the target and projectile respectively, and the values $r_0 = 1.225$ and $d = 1.5-2.0$ are taken. The Coulomb barriers for the reactions shown in [Fig 3.4] are $\sim$ 115MeV (taking $d = 1.8$), and

† E.F.Garman, Nuclear Physics Laboratory, Oxford (1982).

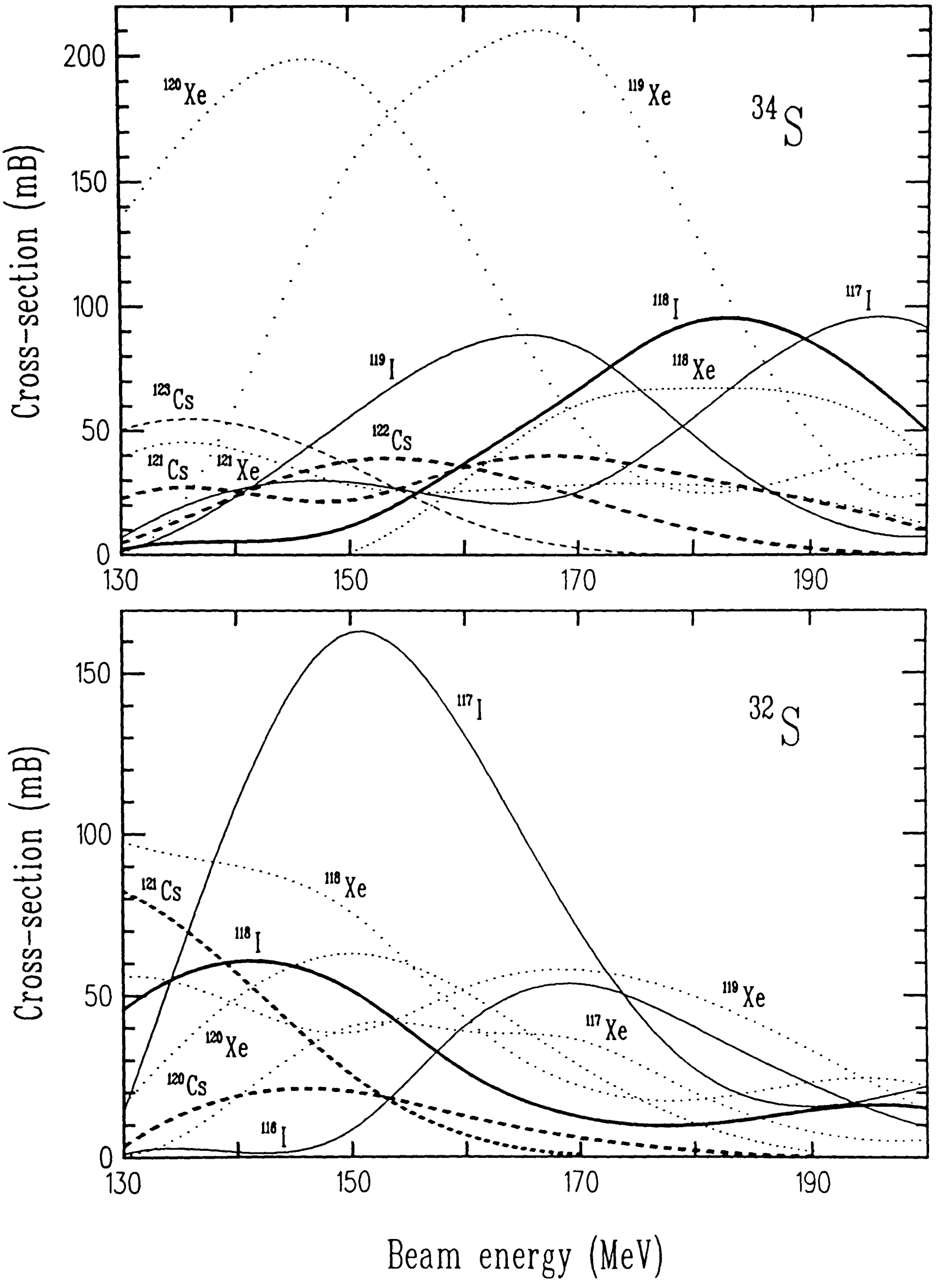

Figure 3.4. CASCADE cross-sections for ^{32,34}S beams on a ^{93}Nb target. The solid lines indicate I isotopes, dashed lines Cs isotopes and dotted lines Xe isotopes. Those isotopes that have been studied in this thesis are shown by *thick* lines.

hence for the beam energies available at the NSF, a wide range of nuclei far from stability may be produced (as shown by CASCADE).

These calculations give a good indication of the reaction products likely to be produced in the ion source of the separator. However, the ion source efficiency for extraction of these reaction products depends strongly on their atomic properties (i.e. how easily they diffuse out of the catcher and can be ionized). This is illustrated by the fact that Cs^+ ion beams are much easier to produce than Xe^+ beams, and although the predicted Xe cross-sections are somewhat larger, this is far outweighed in practice by the difference in ion source efficiency for the two elements.

3.3 The dilution refrigerator

3.3.1 The ^{3}He/^{4}He cooling process

The operation of the dilution refrigerator relies upon the special properties of liquid ^{3}He/^{4}He mixtures at low temperatures. Below a temperature of 0.87K, a mixture of ^{3}He/^{4}He separates into two phases, one being rich in ^{3}He (*concentrated* phase) and the other rich in ^{4}He (*dilute* phase). The concentrated phase floats on top of the dilute phase, because of its lower density.

At lower temperatures, below 0.1K, the two phases consist, one of almost pure ^{3}He, and the other a rather dilute solution of ^{3}He in ^{4}He. The ^{4}He obeys Bose-Einstein statistics, and at such low temperatures it is effectively in its quantum mechanical ground state, and is essentially *inert*. As a result, the ^{4}He in the dilute phase may be considered as a quantum mechanical vacuum *supporting* the ^{3}He particles. If ^{3}He now passes from the concentrated to the

dilute phase, heat is absorbed from the surroundings. This cooling process may be visualized in terms of the ^{3}He in the concentrated phase *evaporating* into the *vacuum* provided by the ^{4}He in the dilute phase. This is analogous to the cooling observed upon evaporation of many liquids.

In the operation of a dilution refrigerator, cooling is achieved by removing ^{3}He from the dilute phase, which in turn draws ^{3}He across the phase boundary from the concentrated phase to replace the ^{3}He lost. After pre-cooling, the ^{3}He removed from the dilute phase is re-condensed into the concentrated phase, thus producing a *continuous* cooling cycle.

The reason why such low temperatures can be obtained in this way is due to the fact that the equilibrium concentration of ^{3}He in the dilute phase remains finite, and rather high (6.4%) as $T \rightarrow 0$. By comparison, for a conventional liquid, the vapour pressure tends exponentially to zero as $T \rightarrow 0$, and as a result, any evaporation induced cooling will disappear as the temperature falls. A full discussion of the properties of ^{3}He/^{4}He mixtures is given by Lounasmaa [7] .

3.3.2 Continuous operation below 10mK

A schematic view showing the the main features of a conventional continuous operation ^{3}He/^{4}He dilution refrigerator is given in [Fig 3.5] (the side access tube is not shown at this stage, but will be described later). The Daresbury 300μW dilution refrigerator (and side access) were manufactured by the Oxford Instrument Company [8]. In stable operation, the concentrated-dilute phase boundary lies in the *mixing chamber*, which is the coldest part of the system. The dilute phase in the mixing chamber is connected to the *still* via *heat exchangers*. When the still is pumped, ^{3}He is removed from the dilute phase, driving ^{3}He across the phase boundary in the mixing chamber, causing cooling.

For optimum circulation rates, an electric heater maintains the still at a temperature of $\sim$ 0.8K. Although the concentration of ^{3}He in the still at this

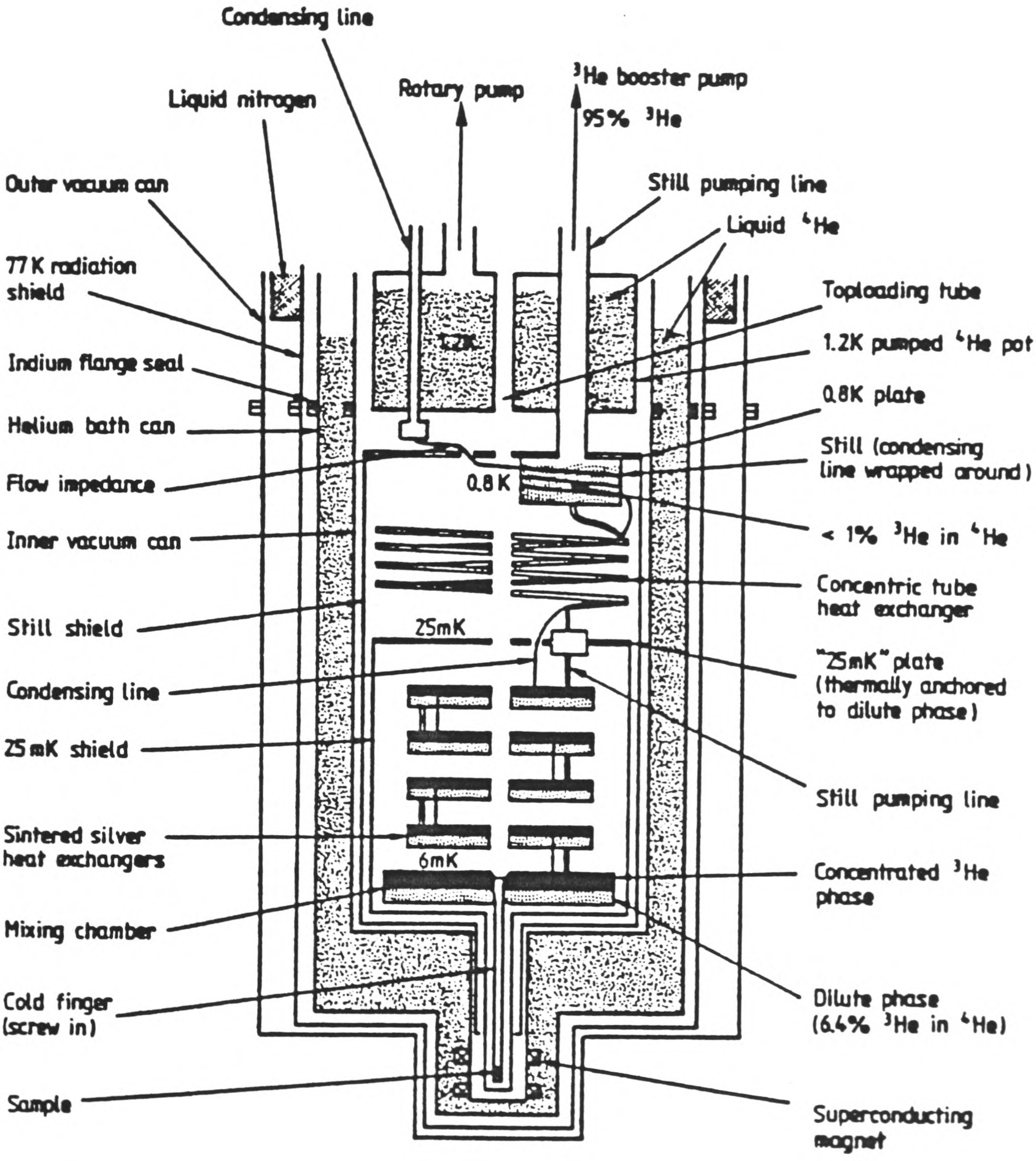

Figure 3.5. Schematic view of a conventional ^{3}He/^{4}He dilution refrigerator, showing the main features necessary for continuous operation at temperatures down to 6mK.

temperature is only 0.7%, about 95% of the vapour removed is ^{3}He, because of its large vapour pressure. Under normal conditions, the still is pumped by a large 9″ diffusion pump, backed by a sealed rotary pump. The ^{3}He from the rotary pump exhaust re-enters the cryostat, and is re-cooled to 1.2K by thermal contact with a pumped ^{4}He *pot*. The ^{3}He is then condensed in the *condenser*, which comprises a fine capillary tube of high impedance. Any air that may have leaked into the room temperature part of the circuit is removed by passing the mixture through liquid nitrogen *cold traps*, before it re-enters the cryostat.

The re-condensed ^{3}He is now returned to the concentrated phase, after it has first been cooled by way of a *wrap around* heat exchanger attached to the still, followed by a *concentric tube* continuous heat exchanger and four sintered silver step heat exchangers, where pre-cooling is performed by the out-going dilute phase. The efficiency with which the returning ^{3}He can be pre-cooled before entering the mixing chamber is one of the limitations to the minimum (or *base*) temperature attainable.

The conventional cryostat design consists of an Inner Vacuum Can (IVC), a main helium bath (of capacity $\sim$ 30 litres), and an Outer Vacuum Can (OVC). Within the OVC is a radiation shield maintained at 77K by a liquid nitrogen cooled jacket. The dilution unit lies inside the IVC, where pressures of $< 10^{-6}\tau$ are maintained during stable operation. The IVC is also in contact with the helium bath, and thus acts as a 4.2K radiation shield. In addition, there is also a 0.8K radiation shield (attached to the still), and a 25mk shield (thermally anchored to the dilute phase), both of which are to reduce the radiative and conductive heat leaks to the dilution unit.

The still, 25mk plate and the mixing chamber temperatures may all be monitored during refrigerator start-up by Speer carbon resistors. In normal operation, the temperature ($<$ 100mK) is measured by use of a standard nuclear orientation thermometer (e.g. ^{57}Co$\underline{Fe}$) soldered to a copper cold finger, which is screwed to the base of the mixing chamber to ensure good thermal contact.

In attaining the minimum base temperature in this continuous mode, a balance must be struck between the cooling induced by ^{3}He crossing the phase boundary, and the heating caused by the returning ^{3}He. For the Daresbury refrigerator, the ^{3}He circulation rate for *optimum* performance is $\sim 400\mu$mol/s, and the base temperature thus obtainable is $\sim$ 7mK (when all external heat leaks have been minimized).

It is useful to be able to *vary* the temperature of the mixing chamber, and hence that of the sample. This can be done by passing current through a 462Ω resistor, thermally attached to the mixing chamber. If the external heating of the mixing chamber is denoted by $\dot{Q}_i (= i^2 R_{mc})$, then from the cooling power of the refrigerator as a function of temperature[7], it can be shown that

$$\dot{Q}_i = C(T_{mc}^2 - T_{base}^2) \tag{3.2}$$

where T_{mc} is the temperature of the mixing chamber, and T_{base} is the minimum temperature that can be attained. C is a constant for a particular set of fridge operating conditions. This equation may be re-written in the following form

$$\begin{aligned} T_{mc} &= \sqrt{\frac{\dot{Q}_i}{C} + T_{base}^2} \\ &= T_{base}\sqrt{\frac{R_{mc}}{C}\left(\frac{i}{T_{base}}\right)^2 + 1} \\ &\approx \sqrt{\frac{R_{mc}}{C}}\, i \qquad \text{for} \quad \left(\frac{T_{mc}}{T_{base}}\right)^2 \gg 1 \end{aligned} \tag{3.3}$$

The cooling curve for the Daresbury refrigerator has been measured for a flow rate of 400μmol/s, and a plot of T_{mc} (mK) against current i (μA) is shown in [Fig 3.6] . The experimental points have been fitted using equation (3.3), giving the values

$$\begin{aligned} C &= 0.0191(5)\ \mu\text{W} \\ T_{base} &= 7.3(1)\ \text{mK} \end{aligned} \tag{3.4}$$

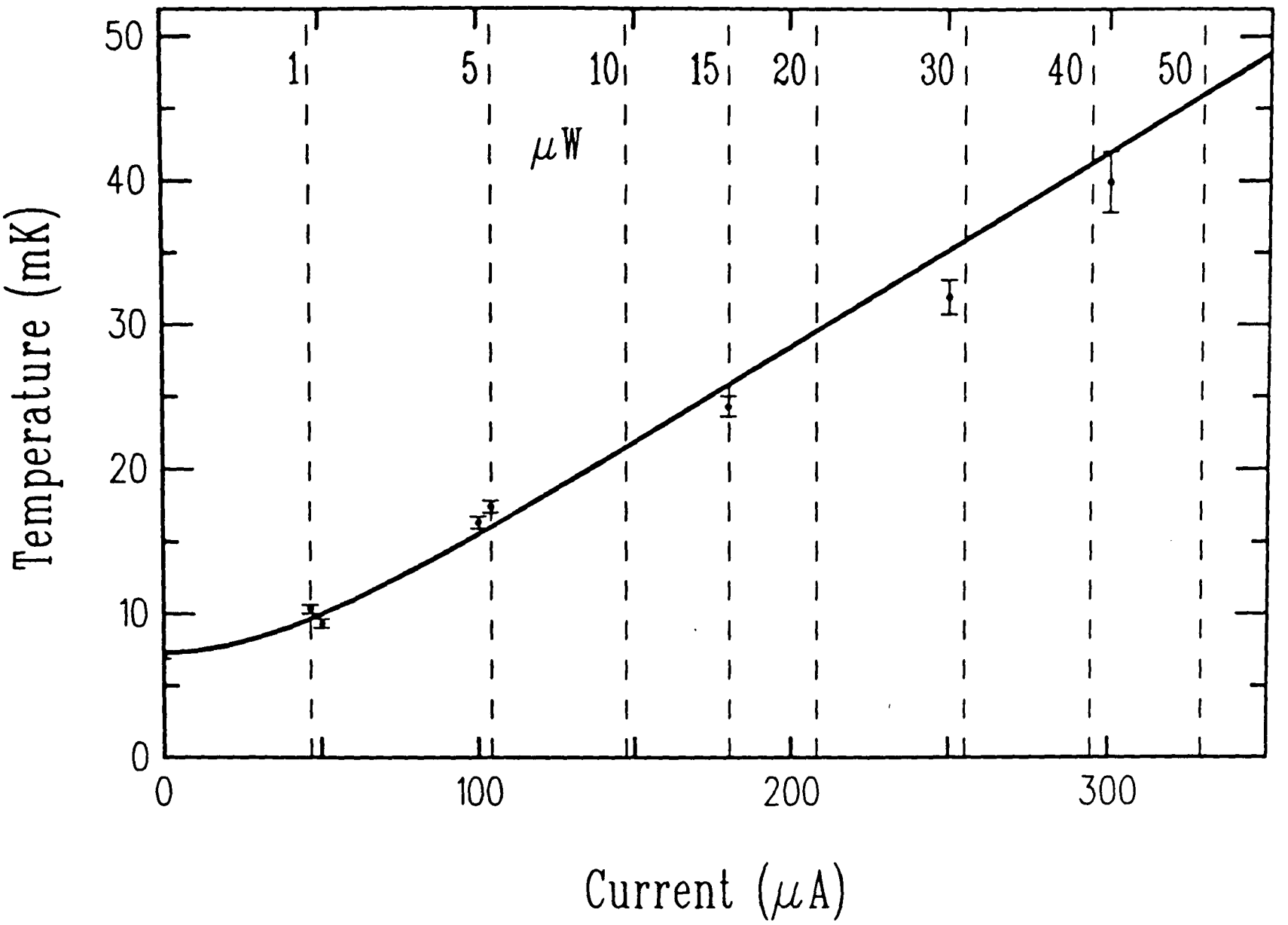

Figure 3.6. Cooling power of the Daresbury refrigerator. The mixing chamber temperature (mK) is plotted against the current (μA) in the mixing chamber resistor. The vertical dashed lines indicate cooling powers (μW).

It can be seen that the cooling power at 25mK is $\sim 15\mu$W using the above parameters, which agrees with the specifications quoted by Oxford Instruments. From these results, it is possible to select a required temperature, by supplying the appropriate current to the mixing chamber heater. This is how all the temperature dependence data in this thesis have been acquired.

3.3.3 Sample preparation and orientation

The cold fingers for the refrigerator are made from a solid bar of high purity copper and have a 9mm wide × 20mm long × 1mm thick *flat* onto which the targets and also nuclear orientation thermometers are attached (usually by soldering onto opposite faces of the *flat*). The cold finger screws into a copper adaptor attached to the mixing chamber of the dilution unit. In on-line experiments, the mass-separated beam is *implanted* at an energy of 60keV into a target foil (or crystal), cooled by thermal contact with the cold finger.

In this work the hosts used have all been poly-crystalline iron foils, of $> 99.998\%$ purity. These are prepared by first cold-rolling an initial iron sheet down to a thickness of ~ 0.15mm, and then annealing under an atmosphere of dry hydrogen at a temperature of $\sim 900°C$ for a period of $6-9$ hours. Finally, just before use, the foil is chemically etched in a solution of 54 vol % H_3PO_4 (80%), 36 vol % H_2O_2 (30%), 8.5 vol % distilled water and 1.5 vol % butoxy-ethanol [9] . After $30-60$ seconds in such an etch, followed by washing with a plentiful supply of water, the resulting foil is ready to be soldered to the cold finger.

The depth profile of the implants may be calculated using the theoretical treatment of Lindhard [10] and is approximately Gaussian in shape for amorphous materials. For ^{118}I implanted into iron at 60keV, the mean range has been calculated as 11.7nm, with a width or *straggling* of ± 4.8nm [11] . As most of the implanted ions come to rest essentially in the surface of the foil, the surface quality is thus very important. For ^{118}I a noticable improvement in the fraction in good sites has been observed using this chemical *polishing* technique. Indeed, it has recently been shown that further improvements are possible if in addition the foil is *mechanically* polished to a very small grain size [12] .

The nuclear orientation thermometers that have been used for on-line work have all been ^{57}Co*Fe*. The two main transitions in the decay of this isotope

are at 122.1 and 136.5 keV, and hence the thermometer produces no Compton scattered background above these energies (unlike ^{60}Co for example). This is particularly important in experiments where the implanted source is weak compared to the thermometer. A ^{57}Co*Fe* thermometer is prepared by high temperature diffusion of ^{57}Co into a suitably prepared Fe foil [13] . After etching the foil to remove surface activity, fractions in good sites of 100% can consistently be achieved, due to the high *solubility* of Co in Fe. All of the thermometers used for on-line experiments have checked been checked against a ^{60}Co*Co* thermometer down to the base temperature of the refrigerator.

The refrigerator has a *top-load* facility which enables experimental samples to be changed while the refrigerator is running. This is important because the target foil may need to be changed during a run to remove longer lived activities built up in the sample during implantation. A complete sample change, involving the removal of an old sample and the loading of a new one with the attainment of temperatures below 10mK takes $\sim$ 3 hours.

In the top-loading process, the cold finger is screwed by reverse thread onto the end of the loading syphon, which is designed to allow the cold finger to be pre-cooled with ^{4}He from the main bath before insertion into the mixing chamber. The top of the cold finger has a portion of right-handed thread, and by turning clockwise it screws into the mixing chamber. Further rotation in this sense causes the syphon to unscrew, leaving the cold finger firmly attached to the mixing chamber. It is important that the orientation of the cold finger is such that the target foil lies in a plane perpendicular to the beam direction. In practice, this is achieved by attaching the cold finger to the top-load syphon using a calibrated torque wrench, preset to a standard value.

The loaded target foil lies at the centre of a 1.5T superconducting split coil magnet which is used to polarize the iron target foils and nuclear orientation thermometers used in these experiments (typically polarizing fields of 0.7T are used which are quite sufficient to ensure magnetic saturation). The magnetic

field also ensures that the solder is not superconducting, and hence good thermal contact to the cold finger is achieved. The magnet is fitted with a heat switch which enables it to be run in persistent mode. The magnetic field direction, and hence the axis of nuclear orientation, is horizontal and is perpendicular to the direction of the implanted beam (i.e. it is parallel to the surface of the iron target foil). Also, the field produced by the magnet has a homogeneity of 1% over the sample volume.

With such a field direction four γ-ray detectors can be placed in optimum counting positions around the refrigerator. Two detectors can be placed along the field direction (*axial*) and two perpendicular to it (*equatorial*). Additional detectors can be placed at other angles but with an increase both in their distance from the sample and in the amount of absorbing material between sample and detector. The distance of closest approach of the axial and equatorial detectors to the sample is 7.5cm. The design of the square lower tails of the refrigerator and the stainless steel magnet case is such that the only absorbing materials between the sample and these detectors are 1mm of stainless steel and 3mm of aluminium.

3.3.4 The cooled side access

In order to maintain temperatures below 10mK during implantation the *total* heat load on the sample, from equation (3.2) must be kept below $\sim 1\mu$W (assuming good thermal contact between the cold finger and mixing chamber). The total heat load comes from,

(i) the radioactive decay of nuclei implanted into the target foil,

(ii) thermal radiation, mainly from the side access tube,

(iii) the 60keV mass separated beam.

The radioactive decay heat load comes mainly from the absorption of β-radiation in the target foil and cold finger. For a 10^5Bq source in which a mean

2MeV of energy is deposited in the target/decay, the corresponding heat load is only $\sim$ 30nW.

In order to reduce the radiation heat load from (ii) to the μW level the cryostat is supplied with a one metre long *cooled* side access tube. The refrigerator and the side access tube are illustrated in [Fig 3.7] . The inner wall of the side-access is a copper tube, cooled to 4K by thermal contact with ^{4}He from the main bath.

At 7cm from the sample position there is a moveable radiation baffle, also thermally anchored at 4K. This baffle has been modified to allow ion current measurements, and is the final position for beam diagnostics, since the host itself should not be irradiated with intense stable beams (because of radiation damage that would occur). Under normal conditions the current on the 4K baffle is optimized (e.g. using stable ^{129}Xe from the FEBIAD ion source) when setting up and checking the separator beam transmission through to the refrigerator, before switching to the unstable mass of interest. The transmission is normally checked at regular intervals during an experiment.

At one metre from the sample there is a variable diameter iris at 77K which limits the thermal radiation heating when the 4K baffle is open. Through the iris aperture (normally set at a diameter of 6mm) the sample sees a room temperature surface (which may be cooled to 77K using liquid nitrogen if necessary). In addition there is also a fixed aperture 40cm from the sample position, consisting of a 1cm thick lead *plug* encapsulated in a copper sheath, with a slot 2.5mm wide and 5mm high. This is cooled to 4K by thermal contact with the side access tube. The function of these two apertures is not only to act as radiation baffles, but also to ensure that unscattered beam entering the refrigerator strikes the sample.

Activity on the lead plug is monitored, and beam transmission of $> 90\%$ has consistently been achieved, with a limit on the fraction of ions *missing* the target foil of $< 0.5\%$. The detectors around the sample in the

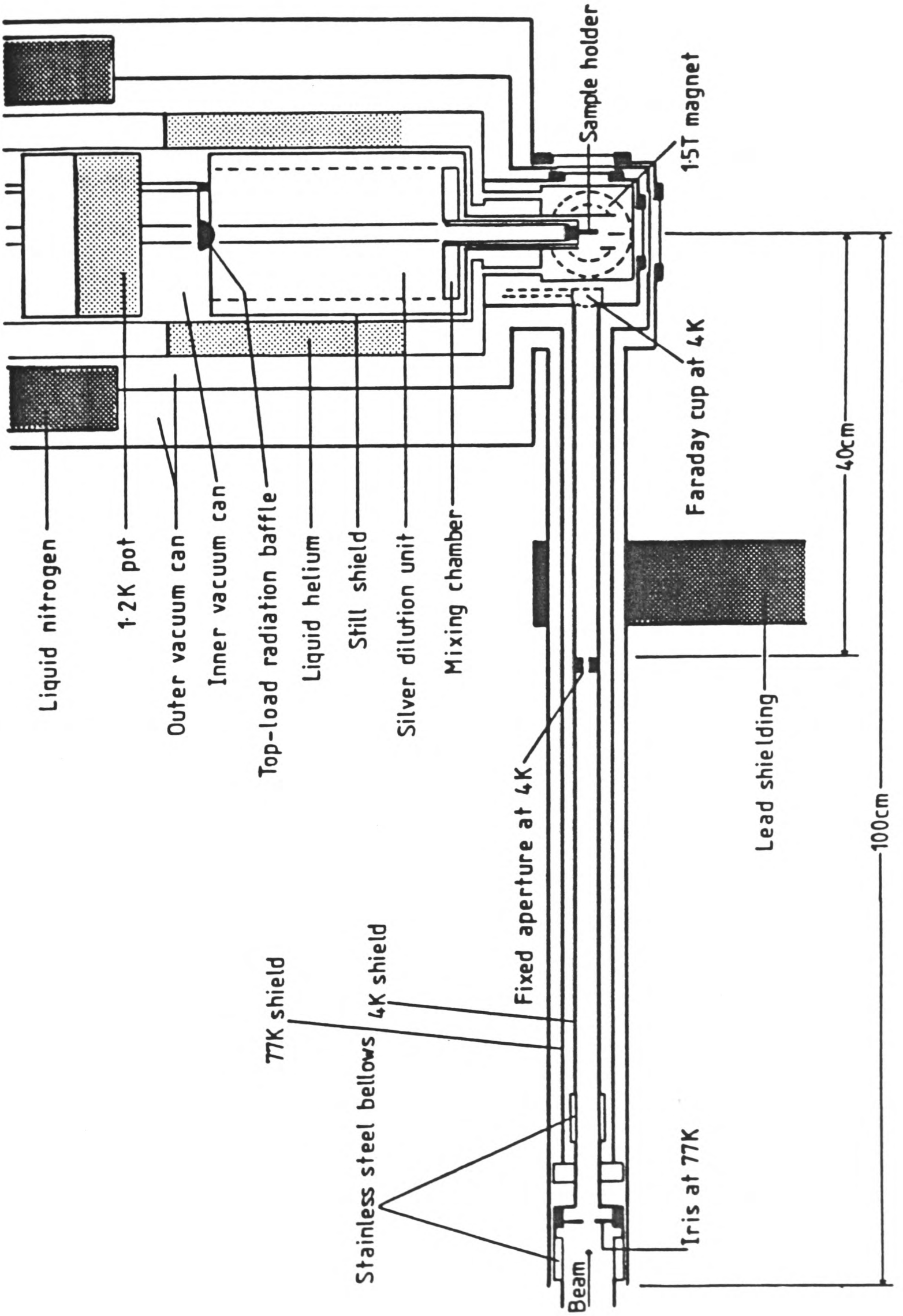

Figure 3.7. The Daresbury dilution refrigerator and cooled side-access tube.

refrigerator are shielded from any activity collected on the lead plug by a *wall* of 7.6cm thick lead blocks.

Both the radioactive decay and thermal radiation heating of the sample are generally low enough not to significantly affect the temperature of the sample (e.g. with no beam little change is observed when the 4K baffle is opened), and the dominant heat load on the sample during implantation frequently comes from the separator beam itself. The beam heating comes not from radioactive ions (10^6 ions s^{-1} at 60keV gives 10nW), but from stable ions present at most masses in the 1-10pA range (1pA at 60keV gives 60nW). This heating depends on the type of ion source, its operating conditions and the selected mass. For experiments with a FEBIAD ion source in the mass $110-120$ region base temperatures for continuous implantation of 10mK have been obtained, representing beam heating of $\sim 1\mu$W.

3.4 The mini-beam line

The mini-beam line is a general purpose beam line, which has mainly been used for conversion electron studies. This allows the parities of transitions to be determined through electron conversion coefficients, and also allows the *discovery* of E0 transitions.

There are two cubes set up on the end of the beam line, with one situated above the other. The separated beam enters the upper cube, and is collected on a tape transport system (similar to that used in the focal plane). A source collected in the upper cube may thus be moved down to the lower cube. A Si(Li) electron spectrometer may be attached to either cube, both of which have re-entrant covers to allow photon detectors to be positioned near the tape. It is therefore possible to measure $\gamma-\gamma$, or even $\gamma-e^-$ coincidences. This

arrangement offers considerable flexibility, and the set up may be chosen to best suit the particular requirements of the experiment. For instance, if the spectrometer is mounted on,

(i) *the upper cube* – this is suited to measuring short-lived isotopes, where unwanted longer-lived activities may periodically be removed by moving the tape.

(ii) *the lower cube* – this is suited to measuring longer-lived isotopes, where it is desirable to filter out shorter-lived activities. The tape can be set to move a collected source down to the lower cube at regular periods (a period of $1.8 \times t_{1/2}$ will maximize the observed number of counts for the isotope of interest).

The electron spectrometer, shown in [Fig 3.8] , consists of a mini-orange magnetic filter, which serves to *focus* conversion electrons onto the face of a cooled Si(Li) detector [14] .

The mini-orange filter consists of 5 rectangular Sm/Co permanent magnets, giving a broad acceptance above 200keV. β^+ particles are defocussed by the magnets, and a lead plug at the centre of the magnet array shields the Si(Li) detector from direct γ-rays , thus enabling very clean conversion electron spectra to be taken. A diagram illustrating the main features of the spectrometer is shown in [Fig 3.9] .

The Si(Li) detector is attached to a horizontal copper rod, which slides within a fixed cylindrical copper sleeve maintained at liquid nitrogen temperature. The detector is cooled partly by radiation, and partly through spring finger contacts, enabling operating temperatures of $-40°$C to be obtained. This is low enough to ensure adequate performance (FWHM $\sim$ 3keV), and the system has proved quite satisfactory.

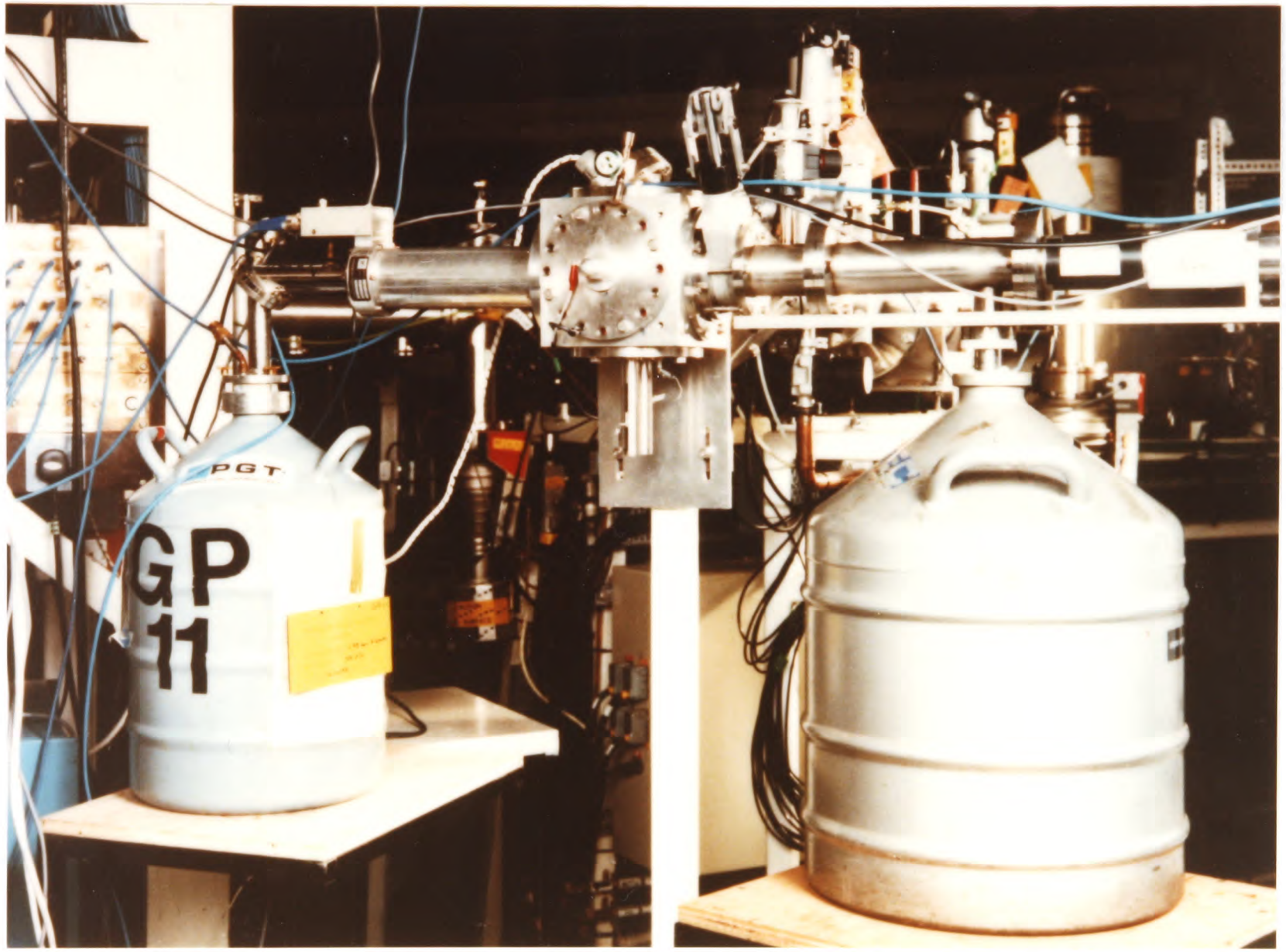

Figure 3.8. An early photograph of the Si(Li) electron spectrometer, attached to what is now the *upper* of two cubes (the tape drive has also been added since this photograph). On the left hand side side of the cube there is a Ge(Li) detector, enabling on-line conversion electron measurements to be performed.

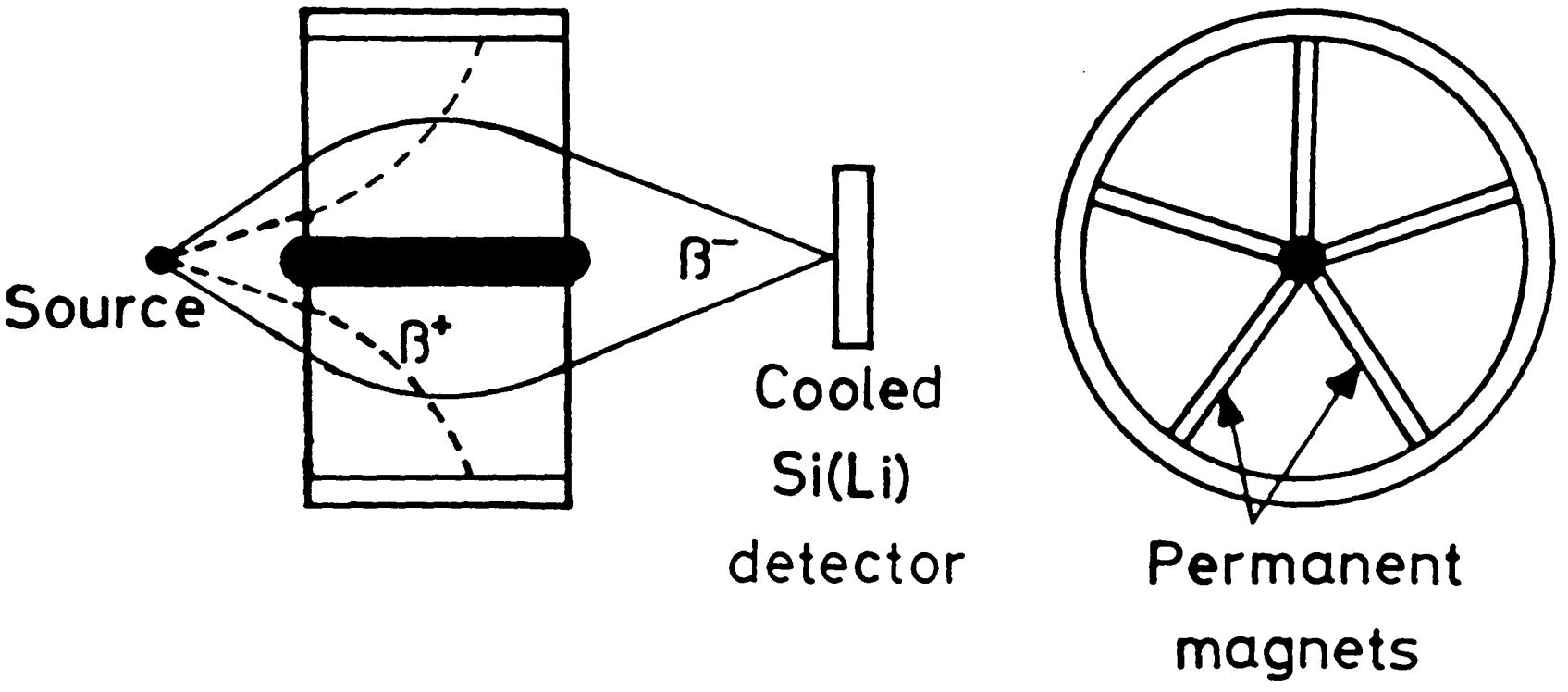

Figure 3.9. Schematic view of the mini-orange electron spectrometer.

3.5 Data acquisition system

3.5.1 Introduction

The data acquisition system is based on a network of GEC 4000 series computers, with three data collection interfaces, commonly referred to as *event managers*. The philosophy behind the system is to separate the more demanding tasks into separate processors, where performance will not be impaired by other less important tasks.

There are three GEC–4190 and two GEC–4090 computers, all running an enhanced version of the GEC OS–4000 operating system. They are used in the following ways,

(i) NNGA is a 4190 and is the main *resource* machine, which controls system peripherals, such as printers, plotters and tape drives. It also has a

network connection to other experimental establishments via JANET (the Joint Academic NETwork).

(ii) NNGB is a 4190 with five graphics stations, which are used to define and control individual experiment configurations. Four of the graphics stations are in the control room, and the fifth is situated by the refrigerator (which has proved invaluable in on-line experiments).

(iii) NNGC,D,E are known as *accumulation* machines. NNGC and NNGE are 4090's and NNGD is a 4190. These machines are accessed only via NNGB from the graphics stations, and are dedicated to controlling the three racks of counting electronics. Each can (by instruction from NNGB) enable specific pieces of counting equipment (e.g. to start/stop counting), and also transfer the data collected direct to NNGA for storage on magnetic tape.

Detector signals from the experimental areas are transmitted via low-loss cables to the racks of counting electronics, where they are counted, timed and digitized using ADC's (Analogue to Digital Converters) and scalers. The results are then transferred to *local* memory under control of the event manager, which is in turn controlled by the appropriate accumulation machine. The event manager will *flag* the accumulation machine when its data buffer is full, and the data is then transferred for further manipulation, or for permanent storage. The event manager can accommodate a total system of 64 ADC's, although in practice smaller systems are normally used to reduce the amount of hardware required.

The data acquisition system provides a full range of facilities for both multi-parameter and singles data collection, as well as for replay and analysis. The aim of this section is to give a brief overview of the system. For further details, comprehensive documentation is provided in the following Daresbury User Guides:-

(i) Introduction to the system,

(ii) Data acquisition hardware,

(iii) Data acquisition software,

(iv) Data analysis,

(v) Multi-parameter event monitoring.

3.5.2 Singles and routed spectra

The energy signal from a detector pre-amplifier, having been further amplified and shaped, is digitized by an ADC (Analogue to Digital Converter). There are three types of ADC available at Daresbury, two of which offer a maximum of 4K channels (LABEN and Daresbury), whereas the other has a maximum range of 8K channels (Silena). When connected up to the event manager, each of these types of ADC may be used to accumulate singles spectra.

Singles spectra are held in CAMAC store modules associated with the each event manager, and spectra may be taken with a precision of 16 or 32 bits per channel (corresponding to maximum channel counts of 65 535 and 4 294 967 295 respectively). Provision is made for incrementing more than one spectrum per ADC by the use of *routing bits*, referred to as auxiliary data bits in the description of the event manager. Before data from an ADC is passed to the CAMAC module, it is combined with the bit pattern present on the relevant auxiliary data input panel. An ADC word consists of 16 bits, and the upper 8 bits are *OR*'ed with the first 8 bits of the auxiliary data. This is shown schematically in [Fig 3.10] .

If all 8 routing bits are used then this allows 256 routed spectra to be defined, each consisting of 256 channels. The relationship between the maximum number of routed spectra possible for an ADC defined to have 2^N channels is given in Table 3.1.

A conventional singles spectrum is known by the name of ADn, where $n = 1, 2, \ldots$. If more than one spectrum per ADC is created by routing, then

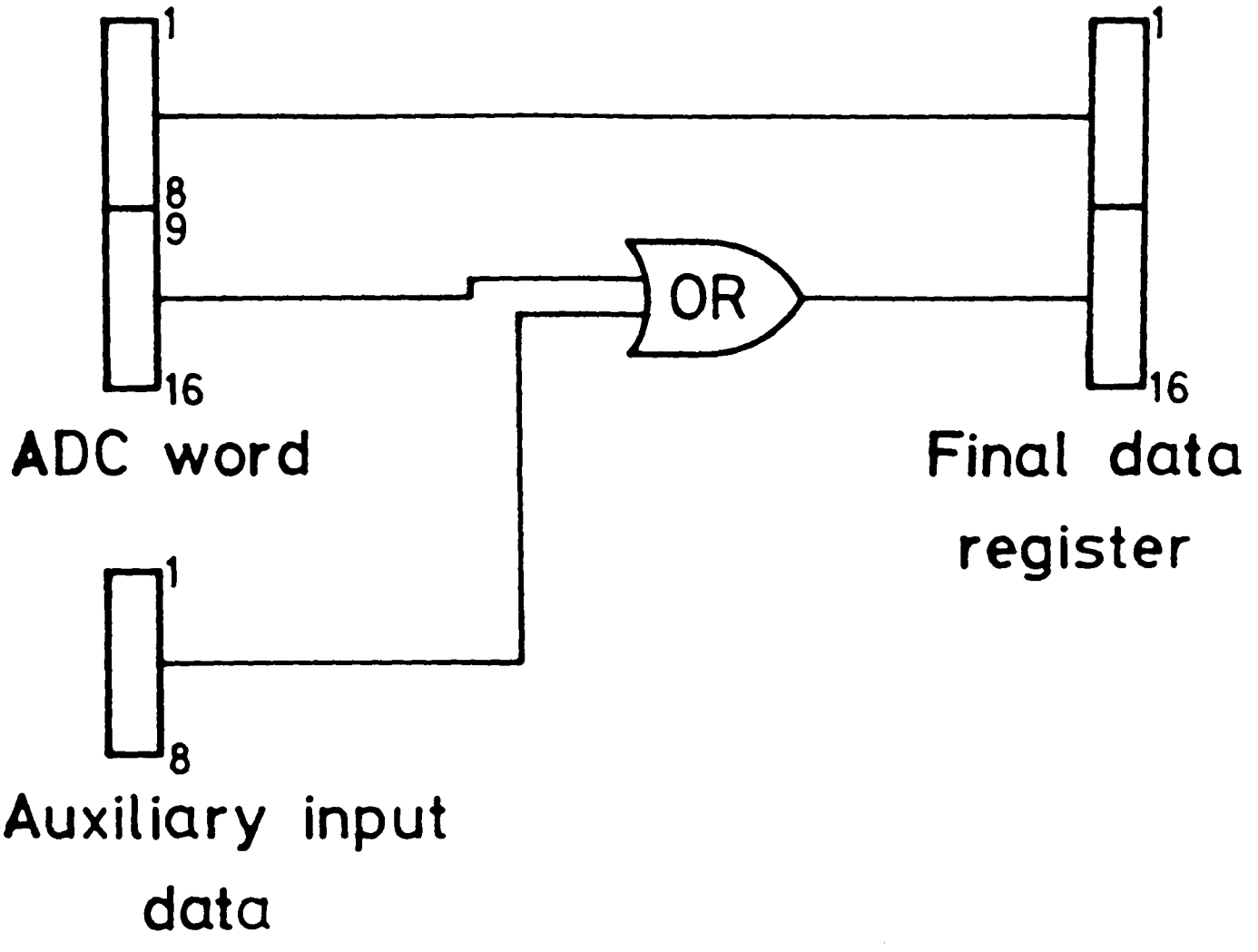

Figure 3.10. Modification to ADC data by event manager routing.

N	Number of channels	Number of routed spectra
8	256	256
9	512	128
10	1024	64
11	2048	32
12	4096	16
13	8192	8

Table 3.1 Number of routed spectra for a 2^N channel spectrum.

it is specified by a further suffix in the form ADnRm, where $m = 0, 1, \ldots$. For on-line experiments a number of JCL (Job Control Language) macros have been written to facilitate both the acquisition of singles spectra (with on-line analysis

options), and the subsequent storage on magnetic tape for later off-line analysis.

3.5.3 Event-by-event data

When an interaction in an experiment causes signals to be produced in more than one detector, it is necessary to record not only the values of the *coincident* signals, but also the fact that they are associated with one another. This is what is meant by a multi-parameter event, and it is recognized by the user's fast electronics (see next section) in the form of discriminators and coincidence units. Thus, with each such event there is an associated *trigger* signal which is fed into the event manager.

In all such experiments to be described, the external indirect trigger (*trigger 24*) has been used. In this particular mode, a pattern of coincident input signals defining those ADC's to comprise the event is connected to the Externally Defined Trigger Pattern Input Panel. If for each event there is always an input signal present on all the relevant external inputs, then all those ADC's which had signals present at the leading edge of the trigger input will appear in the event (this may simply be achieved by connecting up trigger 24 via all the external inputs of the appropriate ADC's). In this mode it is possible to acquire singles spectra at the same time as event-by-event data, for the same ADC.

Each event is written to tape in a variable block structure, where the first word consists of the trigger identifier and the number of words per event. The second word identifies those ADC's which participate in the event, and the following words contain the digital signals from the ADC's. The *event-by-event* data thus written to tape may subsequently be *replayed* and analysed off-line.

3.6 γ-ray measurements

3.6.1 Introduction

For all the work to be described, γ-rays have been observed using germanium detectors, as they combine reasonable photopeak efficiency (typically $\sim$ 25% relative to a $3'' \times 3''$ NaI detector) with good resolution (typically $\sim$ 2.5keV at 1333keV). For the majority of experiments, the detectors used have been taken from the *pool* of germanium detectors, which are stored and maintained in the Germanium Detector Laboratory at the NSF. The available detectors consist of lithium drifted germanium (Ge(Li)) and hyperpure germanium crystals mounted in liquid nitrogen cooled cryostats, which are constructed in a variety of configurations, which can be

(i) closed-end or true *co-axial*,

(ii) planar,

(iii) annular.

Most of the detectors used have been of the Ge(Li) co-axial variety. However, for measurements on the mini-beam line hyperpure Ge detectors (with thin Be windows) have sometimes been used, because of their very good efficiency for detection of low energy γ-rays (and even X-rays). Dimensional and technical information on individual detectors is available [15] (e.g. for the calculation of solid angle correction factors).

The detector pre-amplifiers have a power supply input, a *test* input (to which a pulser may be connected for dead-time corrections) and two signal outputs (one for energy and the other for timing). These outputs are connected to the various pieces of electronics needed for the particular kind of experiment, and data is accumulated and stored using the data acquisition system outlined in the previous section. Examples of typical experimental set ups for the acquisition

of singles and event-by-event data are given in [Fig 3.11] . The various boxes of electronics shown in [Fig 3.11] correspond to

459 E.H.T	:	±5kV high voltage power supply	Ortec 459
572 Amp	:	Spectroscopy amplifier	Ortec 572
BNC Pulser	:	Pulse generator	BNC 8020
474 TFA	:	Timing Filter Amplifier	Ortec 474
473A CFD	:	Constant Fraction Discriminator	Ortec 473A
ns Delay	:	Delay box	Canberra 2058
467 TAC	:	Time to Amplitude Converter	Ortec 467
416A GDG	:	Gate and Delay Generator	Ortec 416A

For standard nuclear orientation experiments the data are collected in singles mode. In order to correct for dead-time losses in the system (see next chapter) a pulser is connected to the pre-amplifier of each detector. The pulser rate is normally set at $\sim$ 10 counts/second and the pulser peak placed at a convenient position towards the top of the γ-ray spectrum.

The block diagram illustrating event-by-event data collection in [Fig 3.11] is set to detect $\gamma - e^-$ coincidences between a Ge(Li) and a Si(Li) detector (the Si(Li) detector could equally be another Ge(Li) detector, as the outputs from their pre-amplifiers are treated in the same way). The TAC is set up to measure the time relationship between coincident events in the two detectors. The signals from the two detectors, as well as the output of the TAC are connected to separate ADC's. For each coincident event, the SCA (Single Channel Analyser) output from the TAC provides the trigger to the event manager (via Trigger 24),

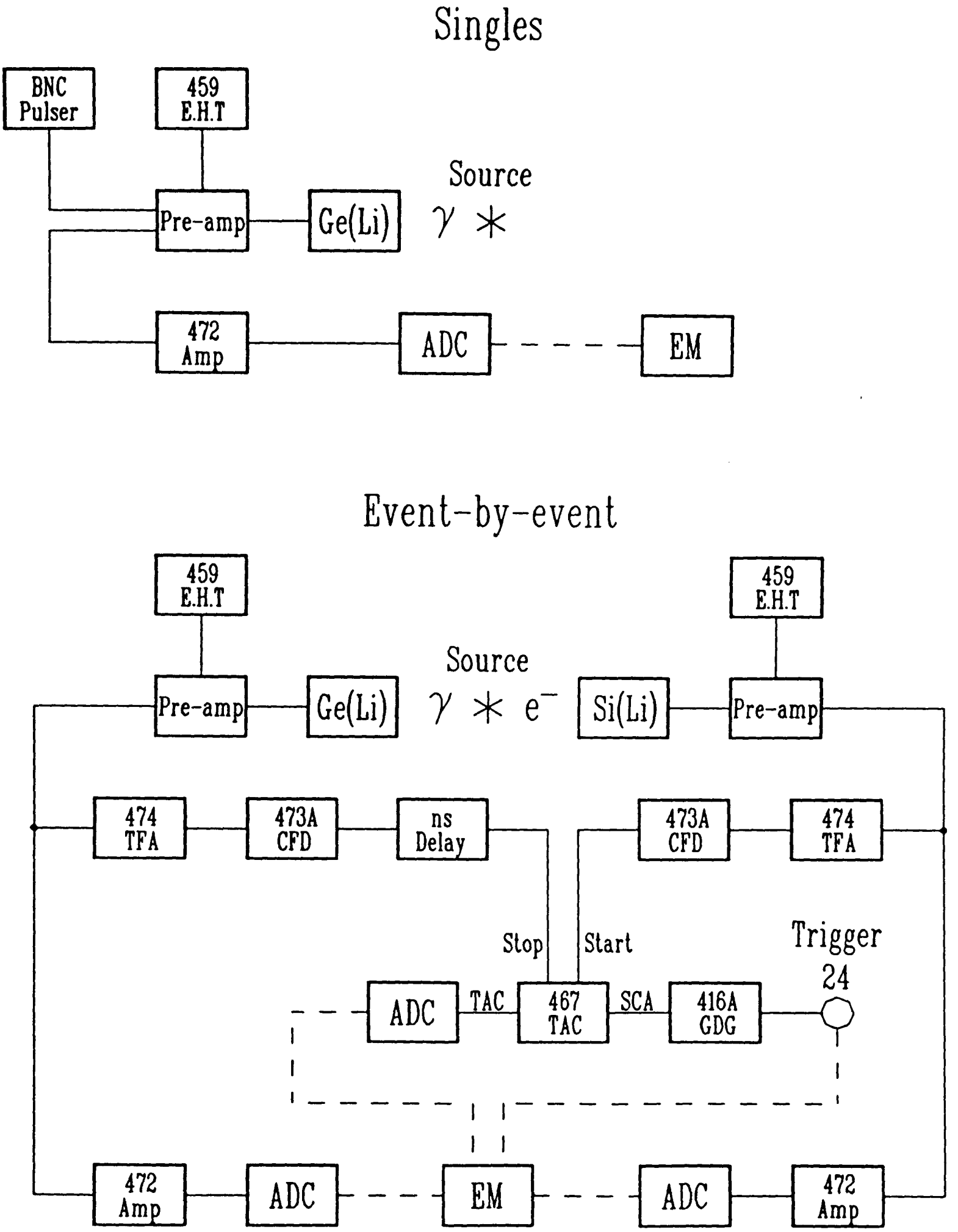

Figure 3.11. Typical block diagrams for the acquisition of *singles* data (for one Ge(Li) detector) and *event-by-event* data (for $\gamma - e^-$ coincidence). A key to the notation used is given in the text. The dashed lines indicate connections *internal* to the Event Manager (EM).

and the values of the detector signals are recorded, along with the timing (TAC) information (enabling *true* coincidences to be distinguished from *random* ones).

A simple sort program for the accumulation of event-by-event data for the set up shown in [Fig 3.11] is given below

```
*ADCS
 AD1 GELI
 AD2 SILI
*TRIGGERS
 24 GELI SILI
*SPECTRA
 GELI 4096 32
 SILI 4096 32
*COMMANDS
*DATA
*FINISH
```

The *COMMANDS section is where any on-line (or off-line) sorting commands may be placed. For details of these commands see the Daresbury User Guides (mentioned in 3.5.1).

It is of course possible to connect up more than two detectors in multi-parameter mode. This may be done by extending the set up shown in [Fig 3.11] . However, if more than three detectors are required, then it is more usual to use coincidence units instead of TAC's to provide the necessary coincidence trigger signals.

3.6.2 Detection of linearly polarized γ-rays

The basic process that is used in this work to detect linearly polarized γ-rays is Compton scattering, where the scattering cross-section is dependent on the direction of the electric vector of the incident γ-ray . The Compton polarimeter that has been used in on-line experiments [16] consists of three detectors, one of which (the *scatterer*) is vertical, and the other two (the *analysers*) are horizontal.

A typical experimental set up including this type of polarimeter can be seen in [Fig 3.12] .

The scatterer is placed at an angle of $\theta = 90°$ to the orientation axis (and also serves as an *equatorial* detector for LTNO measurements). This angle is chosen as it frequently maximixes the polarization $P(\theta)$ as defined in equation (1.48) [17] . A proportion of the γ-radiation incident upon the scatterer is not completely absorbed, and is Compton scattered out of the detector in a direction dependent upon its initial polarization. The two analysers are placed around the scatterer parallel and perpendicular to the orientation axis, in order to detect γ-rays that have been Compton scattered through an angle $\nu \sim 90°$. The analysers are shielded with $\sim$ 5mm thick lead sheet to reduce the flux of *direct* γ-rays from the source.

Fast electronics are set up to detect coincident events between the scatterer and each of the two analysers individually, and data is collected in event-by-event mode. Timing information for the relevant scatterer-analyser pair is recorded along with the values of the coincident signals. Data taken in this way is subsequently analysed by setting digital gates on the time (TAC) spectra, and also by setting kinematic gates. The analysis procedure will be described in the next chapter.

3.6.3 Time dependent measurements

It is possible to collect spectra as a function of time by use of a Time Frame Generator (TFG), in conjunction with routed spectra (described in 3.5.2). The TFG may be set up for 2^N *frames* ($N = 1, \ldots, 8$), each of which corresponds to a counting period t_{TFG}, which must be specified. When the TFG is set running, the number of the current frame is incremented by one after the set counting period t_{TFG} elapses. This cycle continues until the specified number of

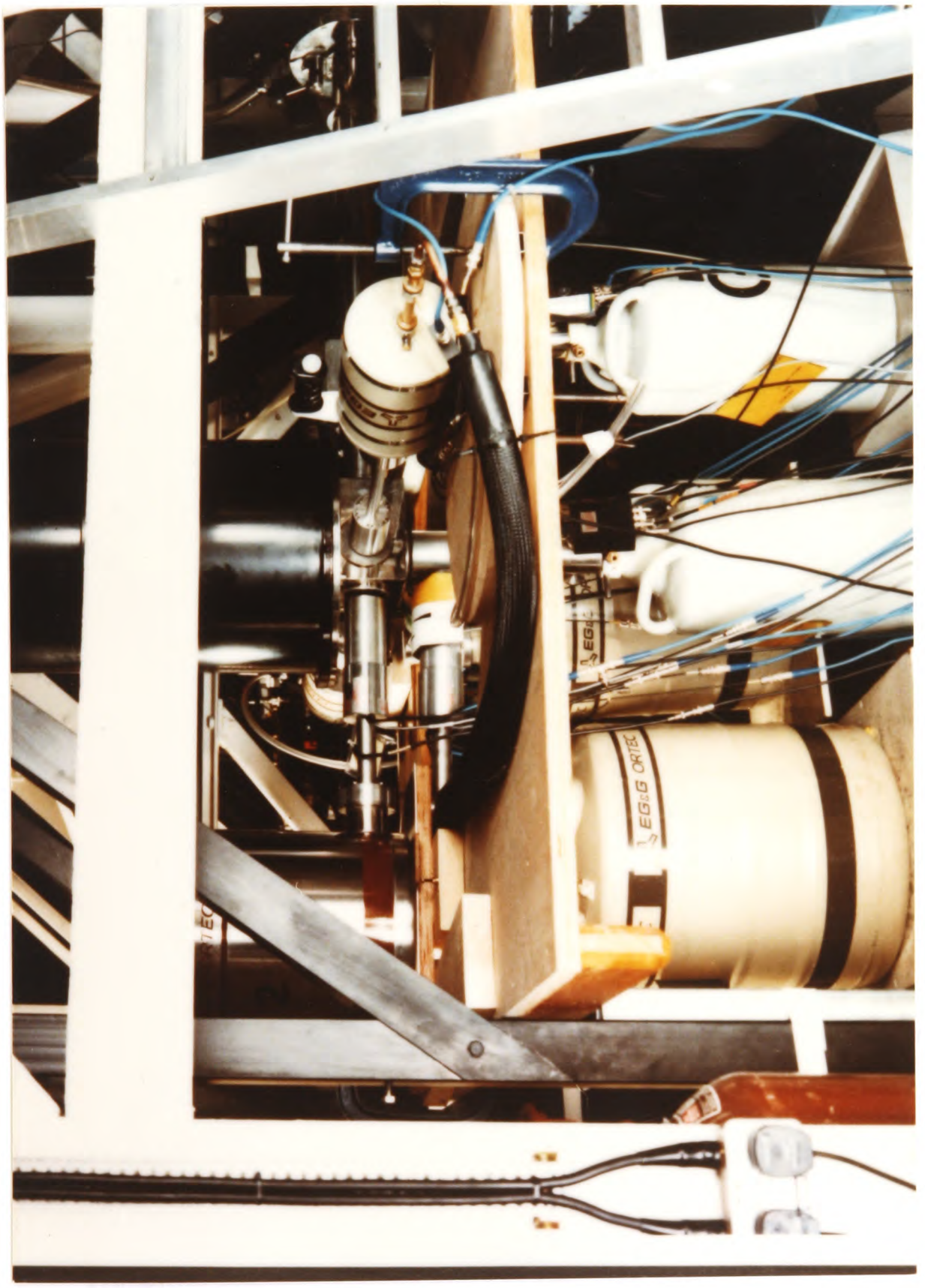

Figure 3.12. Arrangement of γ-detectors around the refrigerator for LTNO and γ-ray linear polarization measurements.

frames has been reached. The number of the current frame is transferred to the event manager in *binary* form by connecting the relevant outputs of the TFG to corresponding inputs on the auxiliary data input panel. Thus, for a particular ADC, the spectrum ADnRm will correspond to the $(m-1)^{th}$ time frame.

In this work, the TFG has been used to route spectra to perform a measurement of time dependent relaxation (see chapter 7.3). The technique employed involves periodically implanting a source into the refrigerator for a short time, and observing the time dependent count rate by use of spectra routed in the above way. The main features of the experimental set up used to perform this measurement are shown in [Fig 3.13] .

The arrangement shown in [Fig 3.13] works in the following way,

(i) the system is set running by a manual start of the *implant* timer, which sets the TFG running. This enables the event manager and data collection into the routed spectra commences. For the duration of the set implant time a Faraday cup is moved out of the path of the beam, allowing a source to be implanted into the refrigerator.

(ii) at the end of the implant time the Faraday cup is put in and implantation stops. Data collection (controlled by the TFG) continues.

(iii) at the end of the TFG counting cycle the event manager is disabled and the TFG reset. The *wait* timer is now started and runs for a preset time to allow the implanted source to decay away.

(iv) at the end of the wait time, the implant timer and TFG are set running again, i.e. now back to (i).

Once the above sequence has been started, it proceeds in a continuous loop, and data from successive cycles are added together for the appropriate routed spectra. When the statistical quality of the data is adequate, the loop may be terminated.

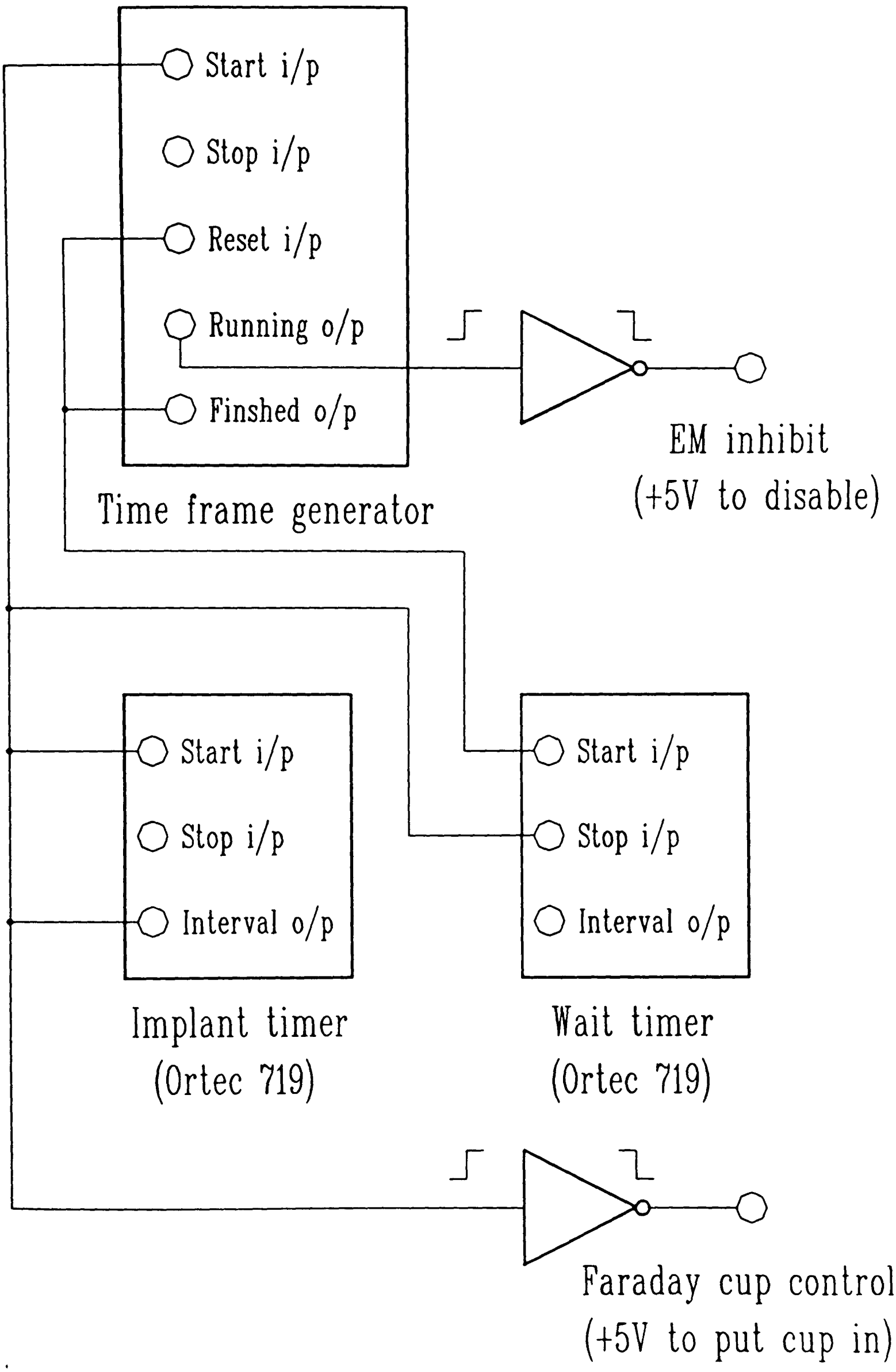

Figure 3.13. Block diagram showing the main components used to periodically provide a short beam pulse into the refrigerator, used in the measurement of time dependent relaxation.

References

[1] . W.Gelletly, Nucl. Instr. and Meth., **211**(1983)89.

[2] . I.S.Grant, D.A.Eastham, J.Groves, D.W.L.Tolfree, P.M.Walker, V.R.Green, J.Rikovska, N.J.Stone, W.D.Hamilton and J.A.R.Griffith, Nucl. Instr. and Meth., **26B**(1987)95.

[3] . R.Kirchner, K.H.Burchard, W.Hüller and O.Klepper, Nucl. Instr. and Meth., **186**(1981)295.

[4] . F.Pühlhofer, Nucl. Phys **A280**(1977)267.

[5] . L.C.Northcliffe and R.F.Schilling, Nuclear Data Tables **A7**(1970)233.

J.F.Ziegler, in Handbook of stopping cross-sections for energetic ions in all elements, (Pergamon,New York,1980) vol 5.

[6] . S.Cohen, F.Plasil and W.J.Swiatecki, Annals of Physics **82**(1974)557.

[7] . O.V.Lounasmaa, in Experimental principles and methods below 1K, (Academic Press,London,1974) Ch 3.

[8] . Oxford Instruments Ltd., Osney Mead, Oxford OX2 0DX, England.

[9] . D.Visser, Ph.D. Thesis (University of Groningen,1981) Ch 3.

[10] . J.Lindhard, M.Scharff and H.W.Schiott, Kgl. Danske Vid. Selsk. Mat. Fys. Medd. **33**(1963) no 14.

[11] . D.Shaw, private communication (1986).

[12] . E. van Walle, D.Vandeplassche, J.Wouters, N.Severijns and L.Vanneste, Phys. Rev. **B34**(1986)2014.

[13] . H.Marshak, in Low-Temperature Nuclear Orientation,
eds. N.J.Stone and H.Postma
(North Holland,Amsterdam,1987) Ch 16.

[14] . P.M.Walker, V.R.Green and I.S.Grant, Daresbury Annual
Report(1984/85)112.

[15] . D.W.L.Tolfree, C.Johnson and H.G.Price, Daresbury Technical
Memorandum, DL/NUC/TM56E(1981).

[16] . J.Rikovska, N.J.Stone and V.R.Green,
Nucl. Instr. and Meth., **241**(1985)461.

[17] . J.Rikovska, N.J.Stone, Low-Temperature Nuclear Orientation,
eds. N.J.Stone and H.Postma
(North Holland,Amsterdam,1987) Ch 4.

Chapter 4

Data analysis

4.1 Introduction

A full on-line experiment at the NSF can last typically 2–4 days, during which many hundreds of singles spectra may easily be acquired. Some on-line analysis is done to monitor the progress of the experiment, but the bulk of the analysis is performed off-line in Oxford. Spectra are written to magnetic tape as *text* files, and are subsequently read and translated into a form appropriate for the spectrum analysis programs on the Oxford Nuclear Structure VAX11/780. Sorting of event-by-event data has mainly been done on the Daresbury system, and the resultant *sorted* spectra transferred to Oxford in the same way as singles spectra. The program MTCOPY† used to translate Daresbury spectra has been modified to read the spectrum header information, which facilitates the subsequent analysis. The modified version is called MTCOP1.

In this chapter an account will be given of the procedures used to analyse experimental data (comprising both singles and event-by-event data), in order to extract quantities that are relevant for the later experimental chapters.

---

† T.Fox, Nuclear Physics Laboratory, Oxford (1983).

4.2 Spectrum analysis

4.2.1 GENDAT

Analysis of spectra on the Oxford Nuclear Structure VAX11/780 is performed using a GENeral DATa analysis program, known as GENDAT† . Spectra are displayed on graphics terminals and users may interact with the program by means of a light pen (for the two monochrome HP1310 terminals) or a joystick (for the two colour VS11 terminals), as well as by typing commands at the keyboard.

In this thesis, GENDAT has been used solely for the analysis of singles spectra, which are stored as individual files on disk and are read into program memory when required. Up to 40 such spectra may be defined at any one time. Regions of interest may be indicated by the use of *markers*. A marker is a *tag* which can be entered either from the display or from the keyboard. A total of 20 markers $(0,\ldots,19)$ may be stored in the current version of the program.

The original version of GENDAT has been considerably augmented by Ooi [1], with much improved plotting routines and a more tolerant and versatile user interface. This version has in turn been considerably modified and adapted for the analysis of LTNO experiments. The current version now in use is called NJS46, into which the following features have been incorporated,

(i) auto-scaling of the displayed region of a spectrum,

(ii) the *simple* GENDAT two-point energy calibration has been superseded by a comprehensive least-squares fitting option (similar to that in use on the Daresbury system). Calibration points are supplied by the user, which are fitted with a choice of a linear, quadratic or cubic calibration function. The

† D.Sinclair and T.Fox, Nuclear Physics Laboratory, Oxford (1983).

fit performed is a multiple linear regression fit, and uses a version of the subroutine REGRES (modified to eliminate rounding errors), listed in the book by Bevington [2] (page 172).

(iii) it is often necessary to add spectra in order to improve the statistics of weak lines observed. However, over the course of an experiment the gain of a particular detector may alter (either in a discontinuous jump or with a gradual drift), due to a variety of possible causes (e.g. temperature fluctuations in the counting electronics). To account for this a *gain-shifting* routine has been written to shift a spectrum with a certain calibration to *match* another spectrum with a slightly different calibration. Care has been taken that only the positions of the peaks change, and not their peak areas. When gain-shifted spectra are added, the resolution of the resultant summed spectrum may deteriorate, but only slightly if the unshifted spectra are well calibrated before being gain-shifted.

(iv) up to 200 sets of peak markers may be created for peak area analysis (see next subsection), which may be saved on disk for later use. Peak areas for a given number of peaks (per spectrum) for a specified number of spectra may be calculated automatically using these sets of peak markers. The peak areas may also be written to disk output files in a form compatible with subsequent analysis programs (see next section).

(v) in the same way that spectra may be gain-shifted, it is also possible to gain-shift a set of peak markers from one detector to another. Slight changes may be necessary to the *shifted* markers for the new detector (e.g. if the resolution is different), but this procedure allows a consistent set of peak markers to be applied to each detector in turn. This is important in LTNO, where it is not absolute γ-ray peak areas that are required, but rather the ratio of peak areas for different detectors (see equation (4.8)).

For further information a comprehensive *help* facility is provided within the program (by typing HLP or ? in response to the * prompt), giving details of all the available commands.

4.2.2 Peak area determination

In a typical γ-ray spectrum there are many $\gamma-$peaks (some unresolved), and a non-constant and often large Compton scattered background under each peak. Using GENDAT there are two methods of extracting peak areas from such spectra, using the commands CEN and FIT.

The first of these (CEN) simply adds up the counts in the channels composing the peak, and subtracts a background linearly interpolated between lower and upper background regions, which should be free of any discrete lines. The lower and upper background regions are specified between markers $0-1$ and $4-5$ respectively. The peak window is defined by markers $2-3$. This routine has been amended to show the interpolated background on the display.

The second method (FIT) is a multiple Gaussian fitting program† , allowing unresolved multiplets to be analysed. The function that is fitted to the observed channel counts N_k (for channel k) is of the form

$$y_{fit}(k) = (b_1 + b_2 k + b_3 k^2) + \sum_{i=1}^{n} A_i \exp\left[-\frac{1}{2}\left(\frac{k - C_i}{\sigma_i}\right)^2\right] \qquad (4.1)$$

where $b_{1,2,3}$ are linear, quadratic and cubic background terms, and each of the n Gaussian peaks has 3 parameters, A_i, C_i (centroid) and σ_i (FWHM). A region of up to 256 channels may be fitted using a combination of the above parameters. In all, a maximum of 25 parameters may be varied. For example, using a linear background and only fitting the area of each peak, 23 peaks may be handled.

† D.W.O.Rogers, Nuclear Physics Laboratory, Oxford (1973).

However, if all parameters are varied for each peak, then only a total of 7 peaks can be fitted (taking a linear background).

The program performs a least-squares minimization, and as input requires initial guesses for the centroids (C_i) and FWHM (σ_i). The way in which this is done has been changed from the original version. The centroids for the n peaks to be included in the fit are now specified by markers $1,\ldots,n$, and the markers 0 and $n+1$ specify the beginning and end of the region to be fitted.

An additional option has been added in which the FWHM is assumed to be a linear function of the γ-ray energy, and is calculated by linear interpolation using the *fitted* centroids and FWHM of two *single* peaks, one near the beginning and the other near the end of the spectrum. In practice, this assumption has been found to be a good approximation by comparison of interpolated and fitted values of the FWHM for other single peaks in the spectrum. To obtain physically meaningful results, the FWHM are usually not varied in the fit, but held at their interpolated values.

An example of the use of the two commands CEN and FIT is shown in [Fig 4.1] . As the peaks *a* and *b* are not resolved in [Fig 4.1] the peak window for the CEN command has been set on both of them. The resulting peak area is seen to be consistent with the sum of the peak areas $a+b$, determined by the FIT command, which fits the triplet of lines a, b, c very nicely. In this example, the results of the CEN command are not very meaningful, but for single peaks CEN is generally to be preferred over FIT, as it offers much more freedom in the choice of background regions.

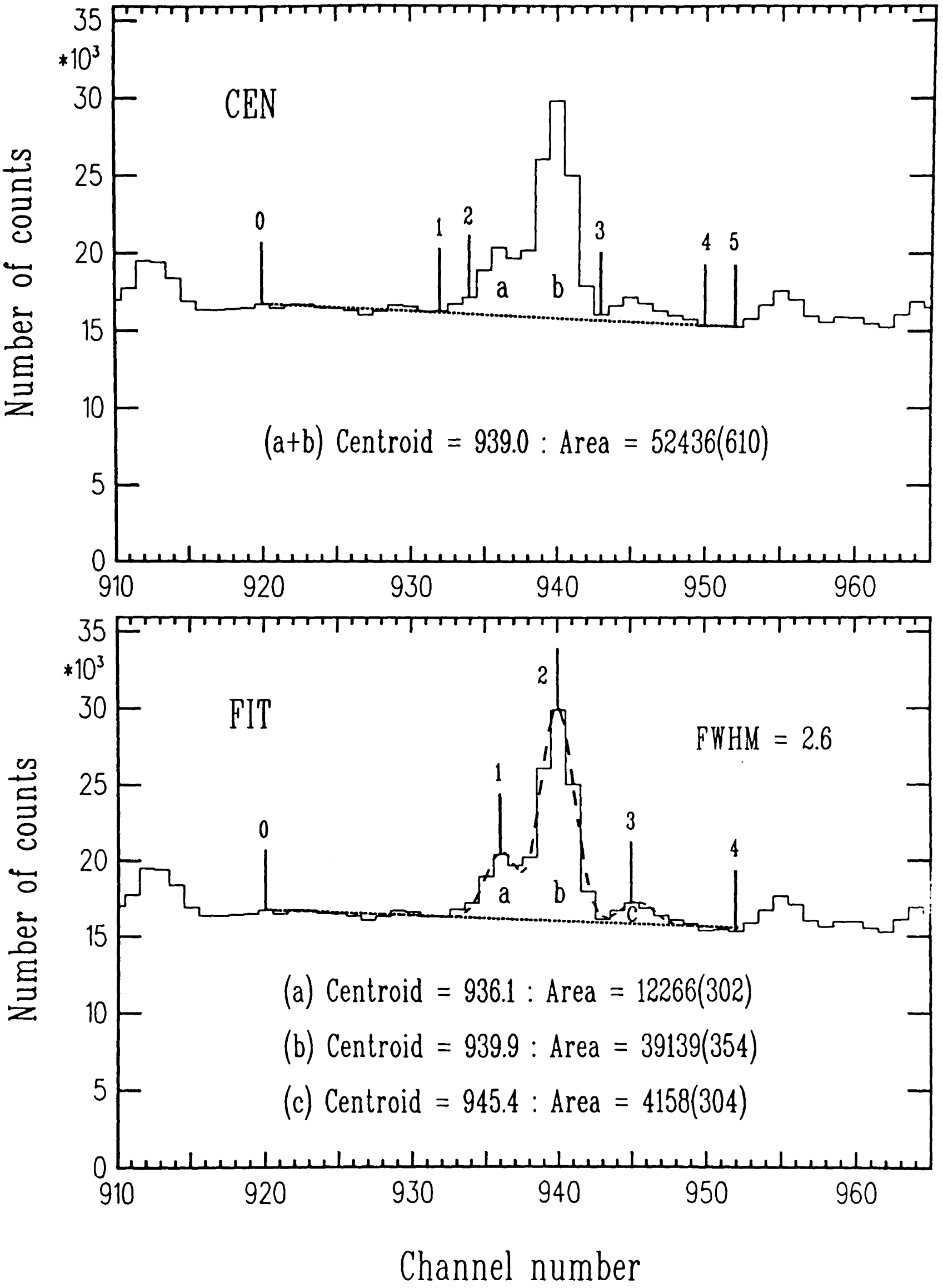

Figure 4.1. Examples of sets of peak markers used for the CEN and FIT commands in NJS46. In each case the dotted line shows the background that has been taken. For the FIT command, the dashed line shows the fitted function, given by equation (4.1).

4.3 Anisotropy measurements

4.3.1 Experimental determination of $W(\theta)$

In chapter 1, the normalized γ-ray count rate from an oriented source, at an angle θ to the orientation axis, is given by equation (1.44) as

$$W(\theta) = 1 + f \sum_{\lambda=2,4} B_\lambda U_\lambda A_\lambda Q_\lambda P_\lambda(\cos\theta) \tag{4.2}$$

In a typical LTNO experiment, spectra are taken at angles $\theta = 0°$ and $90°$ and areas extracted from peaks of interest using the analysis routines described in the previous section. The observed peak area, $N_\gamma^{obs}(\theta)$, may be related to the normalized count rate by

$$N_\gamma^{obs}(\theta) = I_\gamma D_\tau \left(\frac{t_{live}}{t_{real}}\right) \epsilon_\gamma(\theta)\Omega\, W(\theta) \tag{4.3}$$

where D_τ is the total number of nuclei that decay during the counting period t_{real}, I_γ is the γ-ray intensity/decay of each parent nucleus, $\epsilon_\gamma(\theta)$ is the γ-ray detection efficiency at an angle θ, and Ω is the solid angle subtended by the detector at the source (normally assumed to be a point source).

The factor t_{live}/t_{real} is a *dead* time correction factor. When the ADC is processing a signal it is unable to accept further data, and for a given counting period t_{real}, the ADC is only *open* to receive signals for a *live* time $t_{live}(< t_{real})$. The difference between t_{real} and t_{live} is referred to as *dead* time and is typically 5−25% of the counting time, depending on count rate. In this work the *live* time is determined by the pulser method, first suggested by Anders [3] and Bolotin *et al* [4], where an artificial line is introduced into the measured γ-ray spectrum by a stable pulse generator, whose signals are fed into the pre-amplifier input of the Ge(Li) detector. Thus, the pulser signal will undergo the same pulse processing

as the nuclear events, and will be subject to almost the same counting losses as the observed nuclear spectrum. The area of the pulser peak (N_p) divided by the repetition rate (f_p) yields the *live* time, $t_{live} = N_p/f_p$, corrected for pile-up. The *dead* time correction is thus given by the ratio of the *live* time to the *real* time.

However, as pointed out by Bolotin *et al*[4] and Wiernik [5], there are some systematic errors associated with the use of a normal pulse generator for the correction of *dead* time losses. The main problem is due to the non-randomness of each pulser signal, which can only interfere with the processing of a nuclear event, but not with the processing of the next pulser event. Thus, the losses suffered by the pulser signals will correspond to the *dead* time produced by the nuclear events only, whereas the nuclear events will be lost at a rate determined by the combined *dead* time produced by themselves and the pulser. To avoid these problems the pulser rate must be kept low, such that the ratio of the pulser *dead* time to that produced by the detected nuclear events is kept below 0.1[5]. Under the experimental conditions encountered in this work, the pulser correction technique has been found to be very reliable, as demonstrated by,

(i) *axial/equatorial anisotropies* – for low count rates the pulser correction term in equation (4.8) has always been very close to unity. For higher count rates where this was not so, consistent anisotropies were obtained from two independent pairs of detectors.

(ii) *separate axial and equatorial anisotropies* – the properties of the normalization transitions used to calculate the relative source strength from equation (4.9) were deduced using axial/equatorial ratios from (i). These source strengths were consistent for each detector and also for different normalization transitions (see chapter 5.5.2).

In order to eliminate the efficiency, solid angle and relative intensity terms, *warm* counts N_γ^w are taken at a sufficiently high temperature (usually a few

hundred mK) such that $W(\theta) = 1$, with the γ-ray distribution being isotropic. This gives

$$N_\gamma^w(\theta) = I_\gamma D_\tau^w \left(\frac{t_{live}^w}{t_{real}^w}\right) \epsilon_\gamma(\theta)\Omega$$
$$= I_\gamma D_\tau^w \left(\frac{N_p^w(\theta)}{f_p t_{real}^w}\right) \epsilon_\gamma(\theta)\Omega \qquad (4.4)$$

For a corresponding *cold* count, the *cold/warm* ratio may now be written as

$$\frac{N_\gamma^c(\theta)}{N_\gamma^w(\theta)} = W(\theta) \left(\frac{D_\tau^c t_{live}^c}{t_{real}^c}\right) \Big/ \left(\frac{D_\tau^w t_{live}^w}{t_{real}^w}\right)$$
$$= W(\theta) \left(\frac{D_\tau^c N_p^c}{t_{real}^c}\right) \Big/ \left(\frac{D_\tau^w N_p^w}{t_{real}^w}\right) \qquad (4.5)$$

which may be re-written in the form

$$W(\theta) = \frac{N_\gamma^c(\theta)}{N_\gamma^w(\theta)} \times R_c^w(\theta) \qquad (4.6a)$$

where

$$R_c^w(\theta) = \left(\frac{D_\tau^w N_p^w}{t_{real}^w}\right) \Big/ \left(\frac{D_\tau^c N_p^c}{t_{real}^c}\right) \qquad (4.6b)$$

$R_c^w(\theta)$ is essentially a factor which corrects for different integrated source strengths and *dead* times between the cold and warm counts. The ratio D_τ/t_{real} is the *average* decay rate over the counting period, with D_τ given by

$$D_\tau = \frac{1}{\tau} \int_0^{t_{real}} D(t)\, dt \qquad (4.7)$$

where $D(t)$ is the number of nuclei present at time t. If the source decays without any external perturbation, then $D(t) = D(0)\mathrm{e}^{-t/\tau}$, and D_τ may easily be evaluated. However, for on-line experiments where the source is continually being produced, both by implantation and through the decay of parent nuclei, fluctuating implantation rates generally make it impractical to calculate the source strength using equation (4.7). One way to eliminate the problem of

unknown source strengths is to form the ratio $W(0)/W(90)$, as follows

$$\begin{aligned} W(0)/W(90) &= \left(\frac{N_\gamma^c(0)}{N_\gamma^w(0)}\right) \Big/ \left(\frac{N_\gamma^c(90)}{N_\gamma^w(90)}\right) \times \frac{R_c^w(0)}{R_c^w(90)} \\ &= \left(\frac{N_\gamma^c(0)}{N_\gamma^w(0)}\right) \Big/ \left(\frac{N_\gamma^c(90)}{N_\gamma^w(90)}\right) \times \left(\frac{N_p^w(0)}{N_p^c(0)}\right) \Big/ \left(\frac{N_p^w(90)}{N_p^c(90)}\right) \\ &= \frac{\left(\frac{N_\gamma^c(0)}{N_p^c(0)}\right) \Big/ \left(\frac{N_\gamma^w(0)}{N_p^w(0)}\right)}{\left(\frac{N_\gamma^c(90)}{N_p^c(90)}\right) \Big/ \left(\frac{N_\gamma^w(90)}{N_p^w(90)}\right)} \end{aligned} \tag{4.8}$$

The pulser correction in the above equation is often very small, and only for noticable differences in *dead* times between the cold and warm counts for the axial and equatorial detectors does it make a significant contribution. A program ANAL2 has been written to calculate anisotropies given by $\{W(0)/W(90) - 1\}\%$, using equation (4.8). As input, the program requires two *warm* data files containing peak areas for N peaks from *one* axial and *one* equatorial summed warm spectrum. Two corresponding *cold* peak area files are also required, each of which may contain peak areas for more than one spectrum (e.g. for different temperatures) as long as there are N peaks/spectrum. Peak area files in the correct format to be read by ANAL2 are produced by the spectrum analysis program NJS46.

For all the temperature dependence measurements described in this work, the anisotropies used are calculated from the relation $\{W(0)/W(90) - 1\}\%$. However, for spectroscopic studies it is necessary to extract *separate* $\lambda = 2$ and $\lambda = 4$ terms, which requires measurement of *separate* $W(0)$ and $W(90)$. In order to do this, the ratio $R_c^w(\theta)$ needs to be evaluated, and this can be done using a *normalizing* transition, with properties sufficiently well known to be able to deduce the axial and equatorial effects $W_{norm}(\theta)$, as a function of $1/T_L$. For such a *normalization* line the relative source strength is simply given by

$$R_c^w(\theta) = \frac{N_{norm}^w(\theta)}{N_{norm}^c(\theta)} \times W_{norm}(\theta) \tag{4.9}$$

Using this ratio, separate axial and equatorial anisotropies may be evaluated for other γ-rays , which are populated in the decay of the same nucleus as the *normalization* transition. A program WTHETA has been written to perform this kind of normalization, and is used in chapter 5.5 in the the analysis of the ^{118}Te level scheme. The program reads peak areas in the same way as ANAL2, but also prompts for information about the normalization transition.

4.3.2 Anisotropy determination for contaminated lines

The previous section dealt with the extraction of $W(\theta)$ from the experimental peak areas. There are circumstances where the particular transition of interest is contaminated, either by another transition of the same energy placed elsewhere in the decay scheme (or in another nucleus), or due to the transition having feeds from two oriented parent states (for example, the lower levels in ^{118}Te are populated by decay of both ^{118}I^{g} and ^{118}I^{m}).

Adopting the notation of the previous section, and denoting terms which are due to the *contaminant* with a bar, the individual anisotropies for each component may be written according to equation (4.6) as

$$W(\theta) = \frac{N_\gamma^c}{N_\gamma^w} R_c^w = 1 + f \sum_{\lambda=2,4} B_\lambda U_\lambda A_\lambda Q_\lambda P_\lambda(\cos\theta) \qquad (4.10)$$

and

$$\overline{W}(\theta) = \frac{\overline{N}_\gamma^c}{\overline{N}_\gamma^w} \overline{R}_c^w = 1 + \overline{f} \sum_{\lambda=2,4} \overline{B}_\lambda \overline{U}_\lambda \overline{A}_\lambda Q_\lambda P_\lambda(\cos\theta) \qquad (4.11)$$

Experimentally, the two components cannot be separated in this way, and what is measured is the ratio ($\mathcal{W}_{meas}$) of the total cold to the total warm count for the two components combined, where

$$\begin{aligned} \mathcal{W}_{meas} &= \frac{N_\gamma^c + \overline{N}_\gamma^c}{N_\gamma^w + \overline{N}_\gamma^w} \\ &= \frac{W(\theta)}{R_c^w(1+\alpha)} + \frac{\overline{W}(\theta)}{\overline{R}_c^w(1+1/\alpha)} \end{aligned} \qquad (4.12a)$$

with

$$\alpha = \frac{\overline{N}_\gamma^w}{N_\gamma^w} \tag{4.12b}$$

α is the ratio of the strength of the contaminant line compared to that of the line of interest, as observed in the warm counts. Substituting for $W(\theta)$ and $\overline{W}(\theta)$ in equation (4.12) gives

$$\begin{aligned}
\mathcal{W}_{meas} &= \frac{1}{R_c^w(1+\alpha)}\left(1 + f\sum_{\lambda=2,4} B_\lambda U_\lambda A_\lambda Q_\lambda P_\lambda(\cos\theta)\right) \\
&\quad + \frac{1}{\overline{R}_c^w(1+1/\alpha)}\left(1 + \overline{f}\sum_{\lambda=2,4} \overline{B}_\lambda \overline{U}_\lambda \overline{A}_\lambda Q_\lambda P_\lambda(\cos\theta)\right) \\
&= \frac{1}{R_c^w(1+\alpha)} + \frac{1}{\overline{R}_c^w(1+1/\alpha)} \\
&\quad + \sum_{\lambda=2,4}\left(\frac{f\, B_\lambda U_\lambda A_\lambda}{R_c^w(1+\alpha)} + \frac{\overline{f}\,\overline{B}_\lambda \overline{U}_\lambda \overline{A}_\lambda}{\overline{R}_c^w(1+1/\alpha)}\right) Q_\lambda P_\lambda(\cos\theta)
\end{aligned} \tag{4.13}$$

This is a general expression, and if all the parameters about the contamination line are known, then its effect may be subtracted from $\mathcal{W}_{meas}$ to give the required parameters for the line of interest.

For the special case where the two normalization ratios are the same, $R_c^w = \overline{R}_c^w$, then the above equation greatly simplifies to

$$\begin{aligned}
\mathcal{W}_{meas} &= \frac{1}{R_c^w}\left(1 + \sum_{\lambda=2,4}\left(\frac{f\, B_\lambda U_\lambda A_\lambda}{(1+\alpha)} + \frac{\overline{f}\,\overline{B}_\lambda \overline{U}_\lambda \overline{A}_\lambda}{(1+1/\alpha)}\right) Q_\lambda P_\lambda(\cos\theta)\right) \\
&= \frac{1}{R_c^w}\left(1 + \sum_{\lambda=2,4}\langle f\, B_\lambda U_\lambda A_\lambda\rangle_{av} Q_\lambda P_\lambda(\cos\theta)\right) \\
&= \frac{\langle W(\theta)\rangle_{av}}{R_c^w}
\end{aligned} \tag{4.14a}$$

where

$$\langle f\, B_\lambda U_\lambda A_\lambda\rangle_{av} = \frac{f\, B_\lambda U_\lambda A_\lambda}{(1+\alpha)} + \frac{\overline{f}\,\overline{B}_\lambda \overline{U}_\lambda \overline{A}_\lambda}{(1+1/\alpha)} \tag{4.14b}$$

$\langle W(\theta)\rangle_{av}$ is the observed anisotropy using the normalization ratio R_c^w, which can be seen as essentially an *average* over the two components, weighted

according to their relative proportions. Both equations (4.13) and (4.14) are used in chapter 5.5 in the analysis of the data taken in the decay of $^{118}I^{g+m}$.

4.3.3 Calculation of the solid angle correction terms, Q_λ

In order to extract quantities of interest from the observed anisotropies, it is first necessary to know the solid angle correction factors Q_λ for the relevant detectors. The origin of these terms has been discussed in chapter 1.2.5, and their evaluation from equations (1.40) and (1.42) requires a knowledge of the *full* γ-peak attenuation coefficient $\tau(\gamma)$, as well as the detector geometry.

Most γ-rays are multiply Compton scattered in the detector before the total energy is absorbed, and energy is thus more likely to be lost from the detector if the γ-ray is incident near an edge. This means that $\tau(\gamma)$ will depend on the detector geometry, and a rigourous evaluation of this term requires Monte-Carlo type calculations of the effect of multiple Compton scattering. Such calculations have been performed by Camp and van Lehn [6] for certain detector geometries, and they found the resultant Q_λ values were not particularly sensitive to the values of $\tau(\gamma)$ used.

Based on this result, Krane [7] has calculated $\tau(\gamma)$ by just considering one Compton scattering event, and in an energy region where pair production can be neglected, this may be written as

$$\tau(\gamma) = \tau_{PE}(\gamma) + P_{PE}(\bar{\gamma}_c)\left[\tau_C^S(\gamma) + \tau_C^E(\gamma)\right] \tag{4.15}$$

where $\tau_{PE}(\gamma)$ is the attenuation coefficient for photoelectric absorption, and $\tau_C^{E,S}(\gamma)$ are the attenuation coefficients for the amount of energy transferred in a Compton scattering event to the scattered electron, and scattered photon respectively. The mean energy $\bar{\gamma}_c$ of the scattered γ-ray is given by [8]

$$\bar{\gamma}_c = \gamma\left[\frac{\tau_C^S(\gamma)}{\tau_C^S(\gamma) + \tau_C^E(\gamma)}\right] \tag{4.16}$$

The quantity $P_{PE}(\overline{\gamma}_c)$ is the probability that the Compton scattered photon will be photoelectrically absorbed, and it is via this term that Krane introduces the detector geometry dependence into $\tau(\gamma)$, by setting

$$P_{PE}(\overline{\gamma}_c) = \frac{J_0(\overline{\gamma}_c)}{2\Omega} \tag{4.17}$$

where Ω is the solid angle subtended by the detector at the source, and J_0 is calculated from equation (1.40) taking $\tau(\gamma_c) \equiv \tau_{PE}(\gamma_c)$. This value of P_{PE} chosen is approximately equal to the *intrinsic* detector efficiency[6] .

Using the above $\tau(\gamma)$ values, Krane calculates Q_λ factors for true co-axial Ge(Li) detectors, using a 100 point Simpson rule integration program which evaluates the integral J_λ for three regions of the detector, each having different geometries. This program has been modified by Murray [9] to enable calculations for closed-end co-axial detectors to be performed. This version considers four different regions of the detector, and can also take into account γ-ray absorption in the Al windows of the cryostat, which are part of a typical LTNO set up.

The ICL version of Murray's program has been adapted for use on the VAX11/780, and Q_λ coefficients for detectors used at the NSF have been calculated using appropriate attenuation coefficients [10] . With due care it is normally possible to calculate Q_λ values to an uncertainty of $\sim$ 1% or less, which is only a small contribution to the total uncertainty in a measurement.

Spin	B_{hf} (T)	μ(nm)	E_γ	I_γ	U_2A_2	U_4A_4
$7/2^-$	-28.8	4.71	122.1	87.7	0.1240(34)	0.0058(2)
			136.5	12.2	-0.4676	-0.3582

Table 4.1 Nuclear orientation parameters for the ^{57}Co*Fe* thermometer.

4.3.4 Temperature determination

As discussed in chapter 3.3.3 temperature measurements during on-line experiments have been performed using a ^{57}Co*Fe* thermometer, soldered to the back of the cold finger. The parameters for this thermometer ($t_{1/2} = 270.9$ days) that are relevant for nuclear orientation measurements are given in Table 4.1, for the main γ-transitions observed in its decay [11] .

The 136.5 keV ($5/2^- \rightarrow 1/2^-$) E2 transition is usually preferred over the ($5/2^- \rightarrow 3/2^-$) M1/E2 transition at 122.1 keV for several reasons,

(i) it has the greater *sensitivity*, because its larger $U_\lambda A_\lambda$ values outweigh the fact that it is less intense,

(ii) it is more *precise* because of uncertainties in the mixing ratio of the 122.1 keV transition. Also, peak area determination for the 122.1 keV transition is often complicated by the presence of a low energy Compton tail.

From the values quoted in Table 4.1, a value $T_{int} = 14.2$mK may be calculated for the system, and temperature measurements can typically be made over a range 7 to $\sim$ 50mK in on-line experiments.

Another parameter that is worth consideration is the relaxation time, which can easily be estimated. The Korringa constant has been measured for this system to be $C_k = 0.67(10)$ [12] (this gives a value of $C_k T_{int}^2$ which is consistent with the corresponding scaled values for other Co*Fe* systems). At a lattice temperature $T_L = T_{int}$, a relaxation time $\tau_{emp} \sim 40$s may be calculated from

equation (2.23). This *response* time has not proved a limitation in on-line experiments, as counting intervals have usually been at least an order of magnitude greater than this (e.g. $\sim$ 900s).

Once the Q_λ values are known for the particular experimental configuration, it is possible to calculate thermometer anisotropies (usually as a function of inverse temperature, $1/T_L$), which may then be compared with the experimental values, and the temperature thus determined. A temperature *finding* program TFIND has been written to do this using a Newton-Raphson iteration procedure. If A_{exp} and $A(1/T_L)$ denote the experimental and calculated anisotropies respectively, then the following loop is performed, starting with $1/T_L^1 = 20$,

$$1/T_L^{i+1} = 1/T_L^i - \frac{A(1/T_L^i) - A_{exp}}{\frac{\partial A(1/T_L^i)}{\partial(1/T_L)}} \qquad (4.18a)$$

The iteration continues until the following convergence criterion is reached

$$\frac{A(1/T_L^i) - A_{exp}}{A_{exp}} < 0.0001 \qquad (4.18b)$$

The program TFIND can handle anisotropies either of the form $\{W(\theta)-1\}$, or alternatively as $\{W(0)/W(90)-1\}$. The latter of these expressions has usually been used to determine temperatures in on-line experiments.

4.3.5 Least-squares fitting of temperature dependent data

It has been shown in the preceeding subsections how experimental data for a particular γ-transition can be reduced to a set of *measured* anisotropies against (inverse) temperature. At a particular value of $1/T_L$ the anisotropy of the γ-ray depends on,

(i) *continuous parameters* – such as the fraction is good sites f, U_2 and U_4 of the initial level, the mixing ratio of competing multipolarities, and the hyperfine interaction.

(ii) *discrete parameters* – such as the level spins and multipole components of the γ-ray .

The expression for the anisotropy (see chapter 1.2.7) is functionally relatively simple, but is non-linear in the above parameters. The procedure adopted to interpret anisotropy versus $1/T_L$ data is to perform a least-squares fit in which one or more of the *continuous* parameters is varied, keeping the *discrete* values fixed (these may be changed for subsequent fits). How this is done will now be described.

The experimental anisotropies, denoted by A_i $(i = 1, \ldots, N)$ may be expressed as a function of m independent parameters P_k (i.e. peak areas, etc. with corresponding errors σ_k) by

$$A_i = F(P_1, \ldots, P_m) \tag{4.19a}$$

with an associated error σ_i calculated using the standard *propagation of errors* formula (e.g. see Bevington[2] , chapter 4)

$$\sigma_i^2 = \sum_{k=1}^{m} \sigma_k^2 \left(\frac{\partial A_i}{\partial P_k} \right)^2 \tag{4.19b}$$

The various peak area analysis programs all calculate errors on the resulting anisotropies in this way.

If now the function to be fitted to these anisotropies is denoted by $A(1/T_L^i)$, which depends on the parameters a_j, then a measure of the *goodness* of fit χ^2 may be defined by

$$\chi^2 = \sum_{i=1}^{N} \frac{1}{\sigma_i^2} \left[A(1/T_L^i) - A_i \right]^2 \tag{4.20}$$

In the method of least-squares, optimum values for the parameters a_j are found by *minimizing* χ^2 with respect to each of the n parameters in the fit,

$$\frac{\partial \chi^2}{\partial a_j} = \frac{\partial}{\partial a_j} \left(\sum_{i=1}^{N} \frac{1}{\sigma_i^2} \left[A(1/T_L^i) - A_i \right]^2 \right) = 0 \tag{4.21}$$

Only for linear functions is there an analytic solution to this set of equations, and for non-linear functions the general procedure is to perform an n-dimensional search over the χ^2-hypersurface to find the minimum value of χ^2.

Two programs have been written to perform this kind of minimization, the main difference between them being that they use different fitting routines,

(i) *BEVFIT* – this is based on a modified version of the subroutine CURFIT (renamed FITCUR) of Bevington[2] (page 237). This combines the best features of a gradient search (suited to approaching the minimum from a distance) and the analytical method of linearizing the fitting function (which works well near the minimum). In most cases, this routine has been found to converge rapidly to the minimum value of χ^2.

(ii) *MINFIT* – this program uses the fitting program package MINUIT [13] from the CERN library. A large number of different techniques may be invoked by use of command cards, which are placed in a file that the program subsequently reads. A full description of all the commands available is given by James *et al*[13], the most frequently used being the MINIMIZE, HESSE, MINOS and CONTOUR(see below) commands. The minimization is found not to be as fast as Bevington's routine, but the power of the package lies in its versatility and ease of use.

There are a total of six parameters that may be varied using either of these programs, which are outlined in Table 4.2 (the quadrupole frequency option is included for completeness, but has not been used in this work).

Other parameters supplied are θ, Q_2 and Q_4 for a fit to $\{W(\theta)-1\}(\%)$, or $\theta_{ax,eq}$, $Q_2^{ax,eq}$ and $Q_4^{ax,eq}$ for fitting $\{W(\theta_{ax})/W(\theta_{eq})-1\}(\%)$. Also supplied are the oriented state spin, and the initial and final spins of the γ-transition (for which the multipole order L is assumed to be the lowest possible). If the initial and final spins are set to zero then the condition $A_2 = A_4 = 1$ is applied, and the U_λ terms effectively become $U_\lambda A_\lambda$ in the fit. Finally, the N data points $(1/T_L^i,\ A_i,\ \sigma_i)$ are required.

Number	Description
1	fraction in good sites, f (%)
2	magnetic hyperfine interaction, μB_{hf} (nm.Tesla)
3	quadrupole interaction frequency, P (MHz)
4	multipole mixing ratio, $\delta(L+1/L)$ (fitted as $\tan^{-1}\delta$)
5	de-orientation coefficient, U_2
6	de-orientation coefficient, U_4

Table 4.2 Parameters for the the fitting programs BEVFIT and MINFIT.

Usually fits are performed either for two or three parameters, and these two types of fit should be distinguished,

(i) *two parameter fit* – common examples are a fit for f and μB_{hf} where the $U_\lambda A_\lambda$ terms are known, or a fit to μB_{hf} and fU_2A_2 if the $\lambda = 4$ term is zero. Both BEVFIT and MINFIT will rapidly converge upon the best fit for these cases.

(ii) *three parameter fit* – a typical example is a fit to μB_{hf}, fU_2A_2 and fU_4A_4, and care must be taken to ensure that a physically meaningful fit is obtained. This commonly requires *constraining* the parameter fU_4A_4 to lie within physically reasonable limits (e.g. its sign may be known). Parameters can only be *constrained* using MINFIT.

† [PTO]

It is important to be able to assign errors to individual parameters determined in these non-linear least-squares fits. This is usually done by changing the fitted value of a parameter a_m by an amount Δa_m, then minimizing χ^2 for all the other parameters $a_{j\neq m}$, and observing the variation in χ^2 as a function of Δa_m. In this thesis, errors on fitted parameters have been determined according to the χ^2+1 rule [14]

$$\chi^2(a_m \pm \Delta a_m) = \chi^2_{min}(a_m) + 1 \qquad (4.22)$$

In this equation Δa_m corresponds to a one standard deviation error on the fitted parameter a_m. For linear functions, the variation in χ^2 about the minimum is parabolic in a_m, and the errors quoted by BEVFIT and MINFIT (using the MINIMIZE and HESSE commands) are calculated from the curvature of χ^2 at the minimum, using this assumption of linearity. Although the fitting function is non-linear, these error estimates are still valid as long as the function is *approximately* linear in the region of the minimum.

A consequence of the *parabolic* errors introduced above is that they must be symmetric about the fitted value. This can be checked using either the MINOS or CONTOUR commands within MINFIT. The MINOS command follows χ^2 out from the minimum to find both the *positive* and *negative* errors at which the $\chi^2_{min} + 1$ criterion is reached. Alternatively, function contours of constant χ^2 may be plotted for two variables at a time, using the CONTOUR command. This gives a detailed description of the shape of the function, and any serious non-linearities may easily be detected.

The input card for the CONTOUR[13] command has been modified to the following form,

`CONTOUR` N_x N_y δ_{xy} δ_x δ_y

where N_x and N_y are the parameter numbers (from Table 4.2) to be plotted along the x and y axes. If δ_x and δ_y are non-zero, then contours of χ^2 are plotted over the ranges, $x_{fit} \pm \delta_x$ and $y_{fit} \pm \delta_y$. If $\delta_x = \delta_y = 0$, then the x and y ranges ($\pm\delta_{x,y}$) for the plot are taken to be the parabolic errors deduced from the preceeding fitting command (usually MINIMIZE), scaled by the the factor δ_{xy}.

† Values of chi-squared values in this work are quoted as *reduced* chi-squared values, defined as $\chi^2_\nu = \chi^2/\nu$, where ν is the number of free parameters $(N - n)$ in the fit.

4.3.6 Extraction of the A_2 and A_4 terms

In the preceeding subsections it has been shown how the quantities $W(0)$ and $W(90)$ may be extracted from the experimental peak areas (see equations (4.6) and (4.9)). As discussed in chapter 1.2.7 only the $\lambda = 2$ and $\lambda = 4$ terms are usually necessary to describe the angular distribution $W(\theta)$. Hence, from equation (4.2), $W(0)$ and $W(90)$ may be written as

$$\begin{aligned} W(0) &= 1 + fB_2U_2A_2\,Q_2^{ax}P_2^{ax} + fB_4U_4A_4\,Q_4^{ax}P_4^{ax} \\ W(90) &= 1 + fB_2U_2A_2\,Q_2^{eq}P_2^{eq} + fB_4U_4A_4\,Q_4^{eq}P_4^{eq} \end{aligned} \tag{4.23}$$

where $Q_\lambda^{ax,eq}$ and $P_\lambda^{ax,eq}[= P_\lambda(\cos 0, 90)]$ refer to the solid angle correction and Legendre polynomial terms for the *axial* ($\theta = 0$) and *equatorial* ($\theta = 90$) detectors. The above constitute a pair of simultaneous linear equations which may be easily be solved for the variables $fB_2U_2A_2$ and $fB_4U_4A_4$, as follows

$$\begin{aligned} fB_2U_2A_2 &= \frac{Q_4^{eq}P_4^{eq}[W(0)-1] - Q_4^{ax}P_4^{ax}[W(90)-1]}{Q_2^{ax}P_2^{ax}Q_4^{eq}P_4^{eq} - Q_2^{eq}P_2^{eq}Q_4^{ax}P_4^{ax}} \\ &= \frac{3[W(0)-1] - 8\left(\frac{Q_4^{ax}}{Q_4^{eq}}\right)[W(90)-1]}{Q_2^{ax}\left[3 + 4\left(\frac{Q_4^{ax}}{Q_4^{eq}}\right)\Big/\left(\frac{Q_2^{ax}}{Q_2^{eq}}\right)\right]} \end{aligned} \tag{4.24a}$$

and

$$\begin{aligned} fB_4U_4A_4 &= \frac{Q_2^{ax}P_2^{ax}[W(90)-1] - Q_2^{eq}P_2^{eq}[W(0)-1]}{Q_2^{ax}P_2^{ax}Q_4^{eq}P_4^{eq} - Q_2^{eq}P_2^{eq}Q_4^{ax}P_4^{ax}} \\ &= \frac{4[W(0)-1] + 8\left(\frac{Q_2^{ax}}{Q_2^{eq}}\right)[W(90)-1]}{Q_4^{ax}\left[3\left(\frac{Q_2^{ax}}{Q_2^{eq}}\right)\Big/\left(\frac{Q_4^{ax}}{Q_4^{eq}}\right) + 4\right]} \end{aligned} \tag{4.24b}$$

where the values $P_2^{ax} = P_4^{ax} = 1$, $P_2^{eq} = -1/2$ and $P_4^{eq} = 3/8$ have been taken. For the case where $Q_\lambda^{ax} \equiv Q_\lambda^{eq} = Q_\lambda$ then equation (4.24) simplifies to,

$$\begin{aligned} fB_2U_2A_2Q_2 &= \frac{1}{7}\big(3[W(0)-1] - 8[W(90)-1]\big) \\ fB_4U_4A_4Q_4 &= \frac{4}{7}\big([W(0)-1] + 2[W(90)-1]\big) \end{aligned} \tag{4.25}$$

A program K24 has been written to solve equation (4.24), given $W(0)$, $W(90)$ and $Q_\lambda^{ax,eq}$. If the orientation parameters of the parent are known then the program can also calculate the orientation coefficients B_λ. If in addition f and U_λ are supplied, the values of the angular distribution coefficients A_2 and A_4 are then calculated.

The de-orientation coefficients for a particular level may be obtained in two ways,

(i) *experimentally* – by measuring the anisotropy for a transition from the level with known A_λ terms (assuming the orientation parameters f, B_λ of the parent are known).

(ii) *theoretically* – by calculating the weighted average of the U_λ coefficients for all the possible feeding paths to the level, according to equation (1.34). For a decay scheme of even modest complexity, this calculation (for all levels) requires a very large number of parameters. A program UACALC (also see chapter 5) has been written to perform this. It incorporates the feature that if the mixing ratio of a particular transition is unknown, then limiting values U_λ^{max} and U_λ^{min} are taken, thus allowing some of the uncertainties in the decay scheme to be taken into account.

4.4 γ-ray linear polarization

4.4.1 Event-by-event sorting

The experimental setup of a three detector Compton polarimeter has been outlined in chapter 3.6.2. For coincident signals between the scatterer and either of the two analysers, the energy deposited in the scatterer and the relevant analyser is recorded along with the associated TAC signal. For each such event it is possible to,

(i) separate *true* coincidences from *random* ones by placing a digital gate on the TAC spectrum,

(ii) select those coincident events which obey the Compton scattering formula within the range of Compton scattering angles θ, allowed by the geometry of the detectors.

The second option is known as *kinematic* selection [15] , and the discrimination between different types of coincident event that this can provide, will now be discussed.

The energy E_1 (in keV) of a γ-ray of initial energy E_0, that has been Compton scattered through an angle θ_1 is given by,

$$\frac{1}{E_1} = \frac{1}{E_0} + \frac{1}{511}(1 - \cos\theta_1) \tag{4.26}$$

It useful to define a quantity F such that

$$F = 511\left[\frac{E_s}{E_a(E_a + E_s)}\right] \tag{4.27}$$

where E_s and E_a are the energies (in keV) absorbed in the scatterer and analyser respectively. For a *normal* process, in which a single Compton scatter takes place

in the scatterer, and the scattered γ-ray is absorbed in one of the analysers, $E_s = E_0 - E_1$ and $E_a = E_1$. Hence from the above two equations it follows that

$$F_{norm} = 511\left[\frac{E_0 - E_1}{E_1 E_0}\right] = 511\left(\frac{1}{E_1} - \frac{1}{E_0}\right)$$
$$= 1 - \cos\theta_1 \qquad (4.28)$$

However, in addition to normal processes there are other processes which must also be considered,

(i) *multiple* scattering processes in which primary γ-rays are scattered more than once in the scatterer. If E_2 is the energy of the γ-ray after a second Compton scatter, at an angle θ_2 to the direction of the first Compton scatter, then from equation (4.26)

$$\frac{1}{E_2} = \frac{1}{E_1} + \frac{1}{511}(1 - \cos\theta_2)$$
$$= \frac{1}{E_0} + \frac{1}{511}\sum_{i=1}^{2}(1 - \cos\theta_i) \qquad (4.29)$$

Hence, it follows that the energy of the n^{th} Compton scattered γ-ray will be given by

$$\frac{1}{E_n} = \frac{1}{E_0} + \frac{1}{511}\sum_{i=1}^{n}(1 - \cos\theta_i) \qquad (4.30)$$

with the result that,

$$F_{mult} = 511\left[\frac{E_0 - E_n}{E_n E_0}\right]$$
$$= \sum_{i=1}^{n}(1 - \cos\theta_i) \qquad (4.31)$$

(ii) *inverse* processes, in which primary γ-rays are Compton scattered n times in one of the analysers before being absorbed by the scatterer. Now, $E_s = E_n$ and $E_a = E_0 - E_n$, which leads to,

$$F_{inv} = 511\left[\frac{E_n}{(E_0 - E_n)E_0}\right] = \frac{511}{E_0^2}\left(\frac{1}{E_n} - \frac{1}{E_0}\right)^{-1}$$
$$= \frac{511}{E_0^2}\left(\sum_{i=1}^{n}(1 - \cos\theta_i)\right)^{-1} \qquad (4.32)$$

(iii) ***escape*** processes, in which pair production occurs in the scatterer and one of the 511 keV annihilation quanta is absorbed in one of the analysers. Here $E_a = 511$ and $E_s = E_0 - 511$, giving rise to

$$F_{esc} = \frac{E_0 - 511}{E_0} \tag{4.33}$$

which is independent of the scattering angle.

The function F is useful in that it gives a value characteristic of each process. For a normal process, $0 < F_{norm} < 2$, but the *effective* scattering angle can typically lie in the range $90° \pm (30 - 50)°$, depending on the detector geometry. This corresponds to the range $F_{norm} = 1 \pm (0.5 - 0.75)$. F_{mult} can be larger than 2 for a multiple process, and consequently normal processes are easy to distinguish from *large* F multiple processes. For inverse processes, F_{inv} rapidly becomes small as E_0 increases, and values of F_{inv} which might clash with realistic values of F_{norm} only occur for low energy γ-rays (which are shielded from the analysers by lead sheet).

Kinematic selection performed by gating on the F spectrum enables both good signal/background ratios and also high polarization efficiency (see next subsection) to be achieved. An example of a sort program that performs TAC and kinematic gating is shown below.

```
*ADCS
 AD1 AXIAL
 AD2 EQUAT
 AD3 SCAT
 AD4 AXTIME
 AD5 EQTIME
*TRIGGERS
 24 AXIAL EQUAT SCAT AXTIME EQTIME
*SPECTRA
 AXTIME 1024 32
 EQTIME 1024 32
 AXCOS 1024 32
 EQCOS 1024 32
 AXIALG 4096 32
 EQUATG 4096 32
*COMMANDS
 TRIGGER 24
!
!  AXIAL SORT WITH TAC/KINEMATIC GATING
!
```

```
FILTER AXIAL 1 4096
FILTER SCAT 1 4096
INC AXTIME AXTIME
FILTER AXTIME 400 600
CALMATCH AXIAL AD1 SCAT AD3
DOSUM F = [SCALE] * ( SCAT * [MMO] ) / ( AXIALG * AXIAL )
INC F AXCOS
FILTER F 100 300
DOSUM AXIALG = AXIAL + SCAT
INC AXIALG AXIALG
SEQUENCE
!
!  EQUAT SORT WITH TAC/KINEMATIC GATING
!
FILTER EQUAT 1 4096
FILTER SCAT 1 4096
INC EQTIME EQTIME
FILTER EQTIME 400 600
CALMATCH EQUAT AD2 SCAT AD3
DOSUM F = [SCALE] * ( SCAT * [MMO] ) / ( EQUATG * EQUAT )
INC F EQCOS
FILTER F 100 300
DOSUM EQUATG = EQUAT + SCAT
INC EQUATG EQUATG
*DATA
VARSET SCALE 100
VARSET MMO 1024
*FINISH
```

In this sort program the TAC peak is assumed to lie between channel 400 and 600 in both TAC spectra. Also, the gate on the kinematic spectra corresponds to a gate between the Compton scattering angles, $\theta = 60° \rightarrow 120°$. Note that the gains of the detectors are matched before the full γ-peak energies and F values are calculated. If the gain-matching is performed carefully, then the the resolution of the summed spectra will only be marginally worse than for the individual detectors. Once gated spectra have been obtained, peak areas for transitions of interest may be extracted in the normal way.

4.4.2 Experimental polarization

In order to compare experimental data with the calculated degree of linear polarization $P(90)$, defined by equation (1.48), the experimental *asymmetry* Δ_{exp} for a transition is measured,

$$\Delta_{exp} = \frac{N_\gamma^c(90) - N_\gamma^c(0)}{N_\gamma^c(90) + N_\gamma^c(0)} \tag{4.34}$$

where $N_\gamma^c(0)$ and $N_\gamma^c(90)$ are the full energy peak areas for the axial ($\theta = 0$) and equatorial ($\theta = 90$) analysers. When different detectors are used for simultaneous measurement of $N_\gamma^c(0)$ and $N_\gamma^c(90)$, then equation (4.34) must be modified as follows

$$\Delta_{exp} = \frac{a(E_0)N_\gamma^c(90) - N_\gamma^c(0)}{a(E_0)N_\gamma^c(90) + N_\gamma^c(0)} \tag{4.35}$$

where $a(E_0)$ is the relative counting efficiency for the two analyser-scatterer pairs. In LTNO experiments, $a(E_0)$ is measured for a randomly oriented (i.e. warm) source under the same conditions (and for the same transitions) as the oriented (cold) source. For the warm source, $\Delta_{exp} = 0$, which from equation (4.35), leads to the relation

$$a(E_0) = \frac{N_\gamma^w(0)}{N_\gamma^w(90)} \tag{4.36}$$

Substituting for $a(E_0)$ into equation (4.35) now gives

$$\Delta_{exp} = \left(\frac{N_\gamma^w(0)}{N_\gamma^w(90)} - \frac{N_\gamma^c(0)}{N_\gamma^c(90)}\right) \Big/ \left(\frac{N_\gamma^w(0)}{N_\gamma^w(90)} + \frac{N_\gamma^c(0)}{N_\gamma^c(90)}\right) \tag{4.37}$$

A program PANAL has been written to evaluate polarization asymmetries using this equation. As input the program requires four peak area input files for axial and equatorial cold and warm spectra (analogous to ANAL2 in section 4.3.1).

To compare the polarization asymmetries Δ_{exp} with the theoretical expressions $P(90)$ and $P_{NO}(90)$, the *effective* polarization detection efficiency $Q(90)$ must first be introduced by

$$P_{exp}(90) = \frac{\Delta_{exp}}{Q(90)} \tag{4.38}$$

The efficiency of a polarimeter for point detectors placed to detect γ-rays Compton scattered through 90° can be shown to be [16]

$$Q_0(90) = \frac{\alpha + 1}{\alpha^2 + \alpha + 1} \tag{4.39}$$

where $\alpha = E_0/511$. For a real polarimeter the detectors cannot be assumed to be point like, but the polarization efficiency may be represented reasonably well by

$$Q(90) = q(E_0)Q(90) \tag{4.40a}$$

where

$$q(E_0) = AE_0 + B \tag{4.40b}$$

The constants A and B can be determined from a least-squares fit to the values $Q(90) = \Delta_{exp}/P(90)$, determined experimentally from transitions for which $P(90)$ may be calculated. Polarization efficiencies of $30 - 40\%$ (up to 1 MeV) have been achieved in on-line experiments at the NSF (see chapter 5.5.3).

4.5 Time dependent relaxation measurements

4.5.1 Equilibrium conditions

The experimental details of a new method, using a slow pulsing technique of source preparation, to observe time dependent relaxation are given in chapter 3.6.3. A source is implanted for a time $t_{on}(< \tau_{SLR})$ into a cooled iron foil, and the γ-ray anisotropy is observed as the nuclei cool to the lattice temperature. To build up statistics, this is performed in a repetitive cycle, with a waiting time t_{off} between the end of one implantation and the start of the next.

This waiting time is to allow nuclei from the previous implant to die away before implanting again, so that any relaxation effects for these *freshly* implanted nuclei are not attenuated by the presence of *fully relaxed* nuclei from the previous implant. If the half-life $t_{1/2}$ is long compared to the relaxation time τ_{SLR}, it is then necessary for $t_{off} \gg t_{on}$. However, a large value of t_{off} means that only a few cycles can be performed in a given time, and in practice, a balance must be struck so that t_{off} is long enough to maximize the observed relaxation effects, but also short enough to maximize the number of cycles, so that adequate counting statistics can be obtained.

The first step in the analysis of such an experiment is to investigate how the source strength will vary with time, to enable the effects of previous implants on the current one to be determined. Consider the situation illustrated in [Fig 4.2] where implantation of I_o atoms/s for a time t_{on} is performed periodically at intervals of $(t_{on} + t_{off})$. Let n^i_{on} and n^i_{off} be the numbers of nuclei at the start and end of the i^{th} implantation cycle. For the first implantation, $n^1_{on} = 0$, but after a few cycles an equilibrium will be established where n^i_{on} and n^i_{off} will approach their limiting values of n^∞_{on} and n^∞_{off} respectively (assuming that the implantation rate is the same for each implantation). These limiting values are shown in appendix $II.1$ to be

$$\begin{aligned} n^\infty_{off} &= \frac{1 - \mathrm{e}^{-t_{on}/\tau}}{1 - \mathrm{e}^{-(t_{on}+t_{off})/\tau}} \\ n^\infty_{on} &= n^\infty_{off}\, \mathrm{e}^{-t_{off}/\tau} \end{aligned} \tag{4.41}$$

where the normalization condition $I_o\tau = 1$ has been applied (see chapter 2.4.2).

Once equilibrium has been established, the source strength as a function of time can be written in terms of n^∞_{on} and n^∞_{off}, as

$$n(t) = \begin{cases} n^\infty_{on}\, \mathrm{e}^{-t/\tau} + (1 - \mathrm{e}^{-t/\tau}) & 0 \le t \le t_{on} \\ n^\infty_{off}\, \mathrm{e}^{-(t-t_{on})/\tau} & t_{on} \le t \le t_{on} + t_{off} \end{cases} \tag{4.42}$$

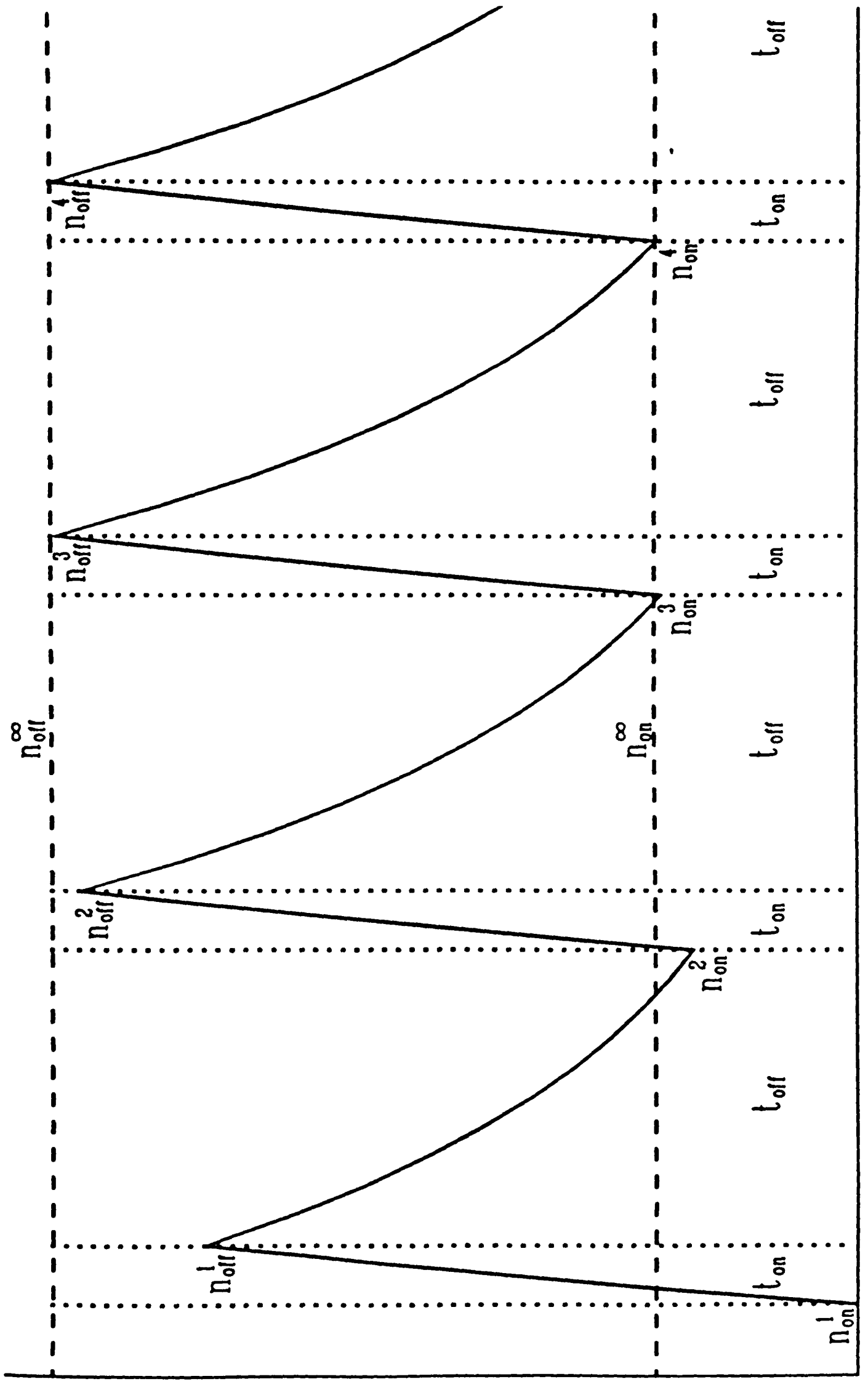

Figure 4.2. Time dependent source strength for a relaxation experiment, where implantation of I_o atoms/s for a time t_{on} is performed periodically at intervals of $(t_{on} + t_{off})$. The source strengths at the start and end of each successive implantation approach their equilibrium values of n^∞_{on} and n^∞_{off}.

where the implantation is defined to start at $t = 0$. The equilibrium source strength must be periodic in time, with $n(t) \equiv n(t + N(t_{on} + t_{off}))$. Thus, it is only necessary to consider times in the region $0 \leq t \leq t_{on} + t_{off}$.

In order to see how applicable these equilibrium conditions might be in practice, two additional factors must also be considered,

(i) how many cycles does it take to attain equilibrium, compared to the total number of cycles?

(ii) how do the sub-level populations behave?

To investigate these considerations, it is necessary to follow the time evolution of both the source strength and the sub-level populations, as they approach their equilibrium values. This is a straightforward calculation and a program EQPOP has been written for this purpose, details of which are given in appendix *II*.2. This time dependent behaviour is demonstrated in the following example, using the parameters,

$$\begin{aligned} C_k &= T_{int} = T_L \\ t_{on} &= \tau_{SLR} \ln 2 \\ \frac{t_{1/2}}{t_{on}} &= 10 \\ \frac{t_{off}}{t_{on}} &= 5, 20 \end{aligned} \tag{4.43}$$

The implantation time t_{on} is chosen to be of order the spin lattice relaxation time, which is taken as τ_{SLR} from equation (2.21). Two values for the wait time of $\frac{1}{2}t_{1/2}$ and $2t_{1/2}$ are chosen for comparison, where the half-life is taken to be an order of magnitude larger than the relaxation time. The resultant source strengths and $B_2/B_2(eq)$ values for these parameters are shown in [Fig 4.3] . In the lower plot, the dashed and dotted lines trace out the source strengths (relative to that for continuous implantation) at the start and end of subsequent implantations. In the upper plot, the dashed/dotted lines indicate

the orientation parameters at the end of implantation, with the dot-dashed line representing the orientation parameters at the start of implantation.

It is of interest to compare the results shown in [Fig 4.3] for the two values of t_{off} taken. For the long wait time, the source achieves equilibrium after only 3 cycles, whereas for the short wait time $\sim$ 10 such cycles are required. However, it should be noted that in a given time, $\sim 3\frac{1}{2}$ times as many cycles for $t_{off} = \frac{1}{2}t_{1/2}$ can be performed, so that in fact equilibrium for these two cases can be reached in similar times.

Consider now the relative source strengths in equilibrium at the end of an implantation, which is where the implanted nuclei will be observed to relax to the lattice temperature. It is seen that the source for the short wait time is $\sim 2\times$ stronger than for the long wait time. Hence, the total number of counts that could be observed for the short wait time (in a given time period) would be about $8\times$ that for the long wait time.

However, this increased number of counts is obtained at the expense of reduced sensitivity in observing relaxation effects, as can be seen from the upper plot in [Fig 4.3] . At the end of implantation for the short wait time, $B_2/B_2(eq)$ will rise from $\sim$ 0.74 to unity in a time of order τ_{SLR}. For the long wait time the situation is more healthy, with the observable variation in $B_2/B_2(eq)$ being more than twice as large.

To sum up, it is seen that the count rate may be determined with greater precision for the short wait time. This advantage, however, is virtually cancelled out because the corresponding variation in $B_2/B_2(eq)$ is smaller. However, another factor which may have an influence, is the possibility of a fluctuating implantation rate. For the short wait time, the larger value of $B_2/B_2(eq)$ at the end of an implant is simply due to the larger number of residual nuclei present from previous implants. Thus, any variation in the implantation rate for successive implants will have a more pronounced effect for the short wait

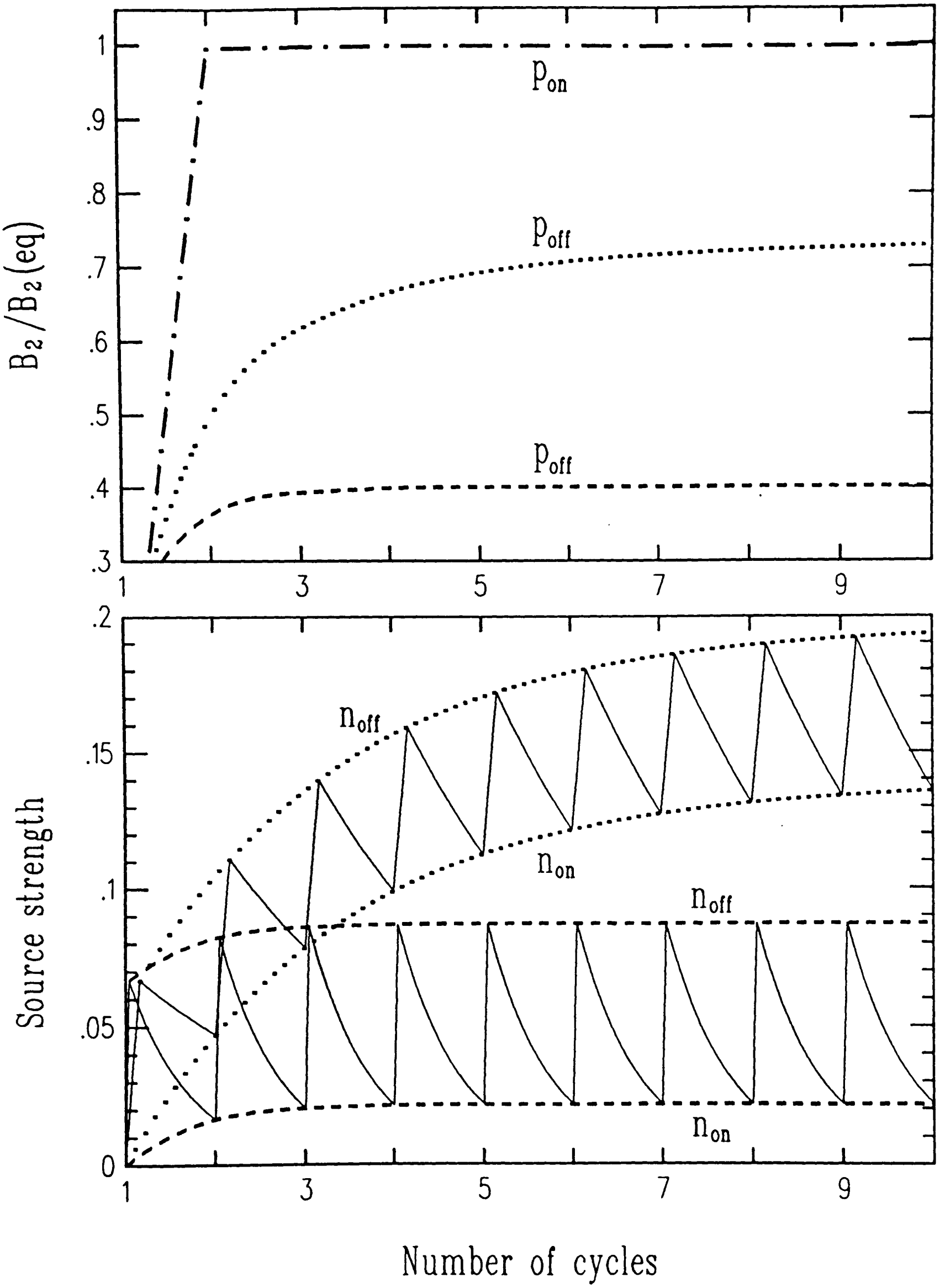

Figure 4.3. The approach to equilibrium of the source strengths and the sub-level populations in an example pulsed experiment. The dashed lines correspond to a waiting time $t_{off} = 2t_{1/2}$, and the dotted lines to $t_{off} = \frac{1}{2}t_{1/2}$. See text for details.

time. This makes the long wait time perhaps the more reliable of the two measurements.

It is possible to estimate how long an experiment would be needed in order to obtain reasonable counting statistics. If the period of the Time Frame Generator is set to be t_{TFG}, then each spectrum will acquire data for a time t_{TFG} per cycle (of duration $t_{on} + t_{off}$). The ratio of the count rate just after implantation to the count rate for continuous implantation is given by n_{off}^{∞}. Hence, if N_{TFG}^{i} and N_{cont} are the the numbers of counts obtainable in a given time (corresponding to many cycles), in a pulsed experiment (for the i^{th} routed spectrum), and in a continuous implantation experiment respectively, then the following relation may be written

$$\frac{N_{TFG}^{i}}{N_{cont}} \approx n_{off}^{\infty} \left(\frac{t_{TFG}}{t_{on} + t_{off}} \right) \tag{4.44}$$

Taking $t_{TFG} = \frac{1}{2} t_{on}$, for the particular examples quoted above, gives ratios of 0.016 and 0.002 for the short and long wait times respectively.

This example serves to show that it is not immediately obvious what combination of parameters is best suited to a particular situation, and some thought is required to *optimize* these parameters. This is particularly important, bearing in mind that it is very hard to achieve statistics comparable with a continuous implantation experiment.

4.5.2 Interpretation of the observed count rates

Now that the variation of source strength over an equilibrium implantation/wait cycle has been determined, it is possible to use this to extract experimental anisotropies from the observed time dependent count rates, and then to compare them with the predictions of relaxation theory.

Let the number of counts observed in a particular peak in a detector at angle θ be denoted by $N_\gamma^c(\theta, \Delta t_{12})$, for a counting period between times t_1 and t_2, where $\Delta t_{12} = t_2 - t_1$. Following the notation used in section 4.3.1 the observed anisotropy during this counting period, denoted by $W(\theta, \Delta t_{12})_{exp}$, can be written in a form analogous to equation (4.6)

$$W(\theta, \Delta t_{12})_{exp} = \frac{N_\gamma^c(\theta, \Delta t_{12})}{N_\gamma^w(\theta)} \times R_c^w(\theta, \Delta t_{12}) \qquad (4.45a)$$

where

$$R_c^w(\theta, \Delta t_{12}) = \frac{D_\tau^w}{D_\tau^c(\Delta t_{12})} \qquad (4.45b)$$

In this last equation, D_τ^w corresponds to the warm count source strength, corrected for dead time, and $D_\tau^c(\Delta t_{12})$ represents the integrated source strength over the counting period, which is given by $\int_{t_1}^{t_2} n(t)\ dt$ from equation $(II.9)$, neglecting any dead time correction as the counting rate is so low in a *pulsed* experiment.

This integrated source strength is straightforward, but somewhat messy, to calculate. A subroutine HLINT has been written to calculate $\int_{t_1}^{t_2} n(t)\ dt$ over an equilibrium cycle, which is described in more detail in appendix $II.1$. This subroutine enables the integrated source strength to be evaluated for *any* portion of the implantation/wait cycle.

The experimental anisotropy above may now be re-written in the form

$$W(\theta, \Delta t_{12})_{exp} = \left(\frac{N_\gamma^c(\theta, \Delta t_{12})}{D_\tau^c(\Delta t_{12})}\right) \Big/ \left(\frac{N_\gamma^w(\theta)}{D_\tau^w}\right) \qquad (4.46)$$

Hence, it is possible to get a direct indication of any relaxation effects by studying the ratio $N_\gamma^c(\theta, \Delta t_{12})/D_\tau^c(\Delta t_{12})$ for successive counting periods, as it approaches some equilibrium value, corresponding to complete relaxation.

However, to go one step further and to determine the anisotropies from equation (4.46), the normalization factor, $N_\gamma^w(\theta)/D_\tau^w$, must first be deduced. This may simply be done by evaluating the ratio $N_\gamma^c(\theta, \Delta t_{12})/D_\tau^c(\Delta t_{12})$ for *all*

the counting periods showing complete relaxation, and dividing by the thermal equilibrium anisotropy $W(\theta)$, which can easily be calculated (assuming that all the relevant parameters are known). Once this is done, it is possible to evaluate the anisotropies, $W(\theta, \Delta t_{12})_{exp}$ corresponding to the counting periods over which the nuclei are observed to be *relaxing*.

In order to compare the experimental anisotropies, given by equation (4.46), with theoretical values, it is necessary to be able to work out the *time averaged* anisotropy, $\overline{W(\theta, \Delta t_{12})}$, over the relevant counting period, which is given by

$$\overline{W(\theta, \Delta t_{12})} = \frac{\int_{t_1}^{t_2} W(\theta, t) n(t)\, dt}{\int_{t_1}^{t_2} n(t)\, dt} \tag{4.47a}$$

where the time dependent anisotropy $W(\theta, t)$ is defined to be

$$W(\theta, t) = 1 + f \sum_{\lambda=2,4} B_\lambda(p_m(t)) A_\lambda U_\lambda Q_\lambda P_\lambda(\cos\theta) \tag{4.47b}$$

The denominator in equation (4.47*a*) is the integrated source strength between times t_1 and t_2, which is equivalent to the term $D_\tau^c(\Delta t_{12})$ used above. Also, it can be seen that the time dependence of the anisotropy $W(\theta, t)$ is contained within the orientation coefficients, $B_\lambda(p_m(t))$, and equation (4.47) may be written as

$$\begin{aligned}\overline{W(\theta, \Delta t_{12})} &= \frac{\int_{t_1}^{t_2} \left(1 + f \sum_\lambda B_\lambda(p_m(t)) A_\lambda U_\lambda Q_\lambda P_\lambda(\cos\theta)\right) n(t)\, dt}{\int_{t_1}^{t_2} n(t)\, dt} \\ &= 1 + f \sum_{\lambda=2,4} \overline{B_\lambda}(\Delta t_{12}) A_\lambda U_\lambda Q_\lambda P_\lambda(\cos\theta)\end{aligned} \tag{4.48a}$$

where the *time averaged* orientation coefficients, $\overline{B_\lambda}(\Delta t_{12})$, are given by

$$\overline{B_\lambda}(\Delta t_{12}) = \frac{\int_{t_1}^{t_2} B_\lambda(p_m(t)) n(t)\, dt}{\int_{t_1}^{t_2} n(t)\, dt} \tag{4.48b}$$

The calculation of the $\overline{B_\lambda}(\Delta t_{12})$ terms from equation (4.48*b*) relies upon knowing both the source strength, and the sub-level populations as a function of time. A method for doing this (for an equilibrium cycle) is discussed in appendix *II*.3.

If the experimental number of counts for the i^{th} counting period is now suitably normalized, a quantity y_i may be defined as

$$\begin{aligned} y_i &= W(\theta, \Delta t^i_{12})_{exp} \times D^c_\tau(\Delta t^i_{12}) \\ &= N^c_\gamma(\theta, \Delta t^i_{12}) \Big/ \left(\frac{N^w_\gamma(\theta)}{D^w_\tau} \right) \end{aligned} \tag{4.49}$$

using equation (4.46).

This is now in a convenient form to be compared with the theoretical value, $y(\Delta t^i_{12})$, defined to be

$$y(\Delta t^i_{12}) = \overline{W(\theta, \Delta t^i_{12})} \times D^c_\tau(\Delta t^i_{12}) \tag{4.50}$$

where $\overline{W(\theta, \Delta t^i_{12})}$ is given by equation (4.48), and $D^c_\tau(\Delta t^i_{12})$ by equation $(II.9)$.

As described in chapter 2, the relaxation process is characterized the Korringa constant C_k, which is implicit in the calculation of $y(\Delta t^i_{12})$. In order to determine the value of C_k that best describes the experimental data, y_i, a least-squares fitting procedure may be performed to find the minimum χ^2, defined as

$$\chi^2 = \sum_{i=1}^{N} \frac{1}{\sigma_i^2} \left[y(\Delta t^i_{12}) - y_i \right]^2 \tag{4.51}$$

where there are N data points y_i, each with an experimental error σ_i. A program has been written to calculate equation (4.51), which is then *minimized* using the CERN library routine MINUIT.

References

[1] . S.S.L.Ooi, D.Phil. Thesis (University of Oxford,1986) unpublished.

[2] . P.R.Bevington, in Data reduction and error analysis for the physical sciences (McGraw-Hill,New York,1969)

[3] . O.U.Anders, Nucl. Instr. and Meth., **68**(1969)205.

[4] . H.H.Bolotin, M.G.Strauss, D.A.McClure,
Nucl. Instr. and Meth., **83**(1970)1.

[5] . M.Wiernik, Nucl. Instr. and Meth., **96**(1971)325.

[6] . D.C.Camp and A.L van Lehn,
Nucl. Instr. and Meth., **76**(1969)192.

[7] . K.S.Krane, Nucl. Instr. and Meth., **98**(1972)205.

[8] . R.D.Evans, in The atomic nucleus
(McGraw-Hill,New York,1955)687.

[9] . D.W.Murray, D.Phil. Thesis (University of Oxford,1980) unpublished.

[10] . E.Storm and H.I.Israel, Los Alamos Scientific Laboratory Report LA-3753(1967).

[11] . H.Marshak, in Low-Temperature Nuclear Orientation,
eds. N.J.Stone and H.Postma
(North Holland,Amsterdam,1987) Ch 16.

[12] . E.Klein, in Low-Temperature Nuclear Orientation,
eds. N.J.Stone and H.Postma
(North Holland,Amsterdam,1987) Ch 12.

[13] . F.James and M.Roos, Comp. Phys. Comm. **10**(1975)343.

[14] . D.W.O.Rogers, Nucl. Instr. and Meth., **127**(1975)253.

[15] . J.Kasagi, N.Kishida and H.Ohnuma,
Nucl. Instr. and Meth., **144**(1977)201.

P.A.Butler, P.E.Carr, L.L.Gadeken, A.N.James, P.J.Nolan,
J.F.Sharpey-Schafer, P.J.Twin and D.A.Viggars,
Nucl. Instr. and Meth., **108**(1973)497.

[16] . J.Rikovska, Hyp. Int. **26**(1985)963.

Chapter 5

The study of ^{118}I decay to ^{118}Te

5.1 Introduction

At DOLIS–COLD a systematic study of even-even Te isotopes has been made in the mass region 118–122, with a particular interest in the search for *intruder* states. These states arise from the excitation of a pair of particles across a closed shell gap, and have been observed in nuclei near both proton and neutron closed shells [1] .

A general feature of these *intruder* configurations is that they should lie low in energy when one type of nucleon is near a closed shell, and for the other type the number of *active* nucleons, and hence the neutron-proton interactions are maximized. As ^{118}Te has two protons outside the $Z = 50$ closed shell, and is in the middle of the neutron shell, it is a very suitable candidate in which to look for *intruder* states.

The work described in this thesis deals with the spectroscopic investigation of ^{118}Te, populated in the β-decay of its I parent. The decay chain for the Cs to Te nuclei produced at mass 118 in these studies is shown in [Fig 5.1] [2] .

Excited states in ^{118}Te were populated by the β^+/EC decay of ^{118}I^g (spin 2^- and $t_{1/2} = 13.7$ min), and ^{118}I^m (spin 7^- and $t_{1/2} = 8.5$ min) [3] . The presence of two isomers of similar half-life but widely differing spins, coupled

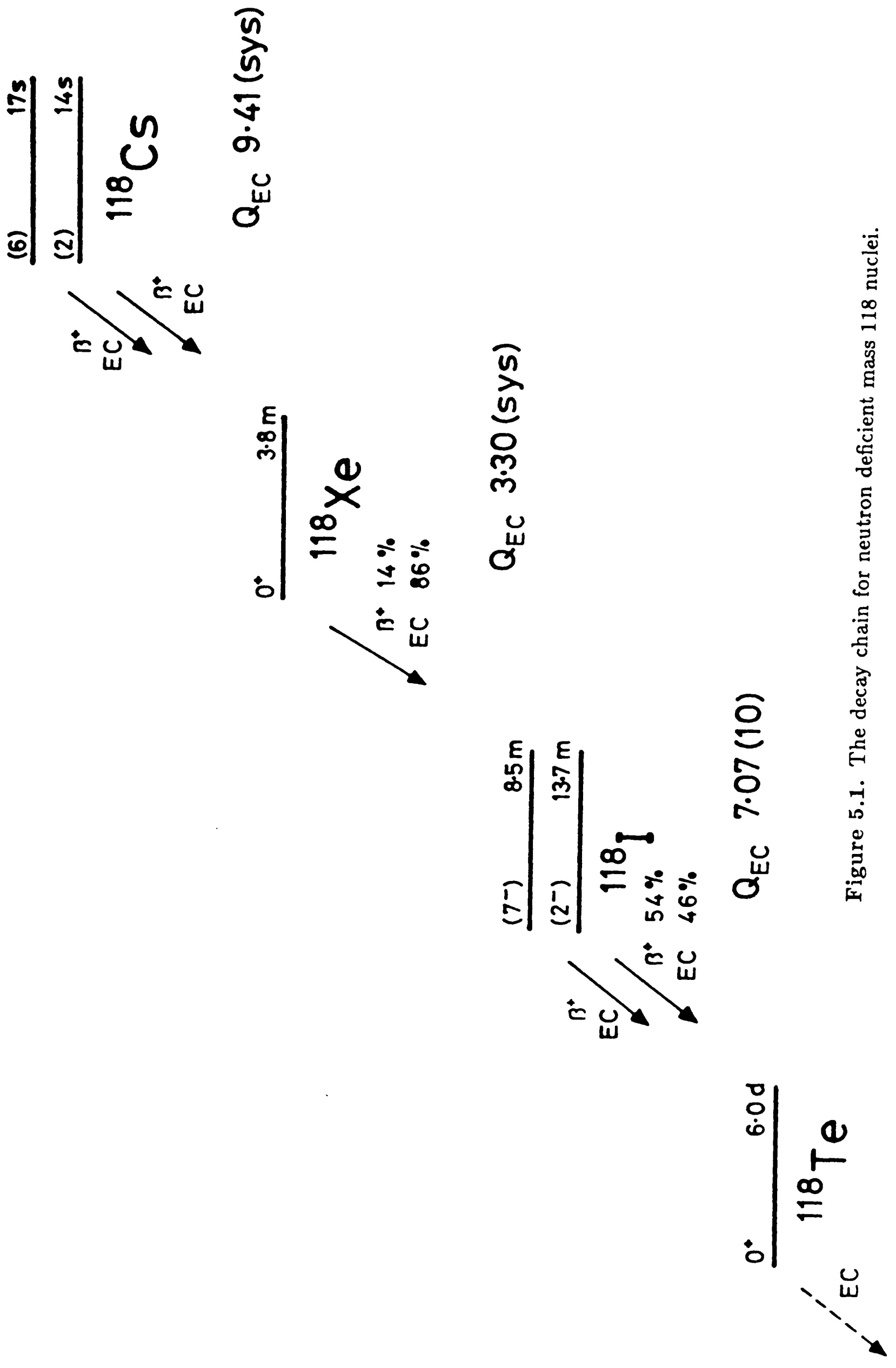

Figure 5.1. The decay chain for neutron deficient mass 118 nuclei.

with $\sim$ 7MeV of decay energy, results in a large number of states in the daughter ^{118}Te being populated, giving rise to very complex spectra. The following experimental techniques have been used to investigate the decay of ^{118}I to ^{118}Te,

(i) γ-γ coincidence (and correlation) measurements, either with or without half-life selection using the tape transport system in the focal plane of the isotope separator,

(ii) nuclear orientation and γ-ray linear polarization measurements, following implantation of $^{118}I^{g+m}$ into a cold, polarized iron foil,

(iii) electron conversion measurements, using a cooled Si(Li) detector and a mini-orange magnetic filter.

The combination of these three different, but complimentary techniques provides a very powerful tool for the spectroscopic study of nuclei far from stability. In this work, knowledge of the decay scheme of ^{118}Te, populated by ^{118}I decay has been considerably extended, and Table 5.1 gives a summary of the experiments that have been performed, using the techniques mentioned above (MBL refers to the Mini-Beam Line).

There are two types of LTNO measurement referred to in Table 5.1. The *moments* measurements were performed to obtain anisotropies for the stronger lines for magnetic moment determinations, whereas the *spectroscopy* experiments were aimed at providing spectroscopic information on weaker transitions (in conjunction with a Compton polarimeter).

The various experimental procedures and data analysis techniques used will be described in this chapter. A full discussion of the ^{118}Te level scheme will be presented in the next chapter, along with an interpretation of the low lying levels in terms of the IBM-2 model.

Date	Beam	γ-γ	LTNO	Electrons
Nov 83	^{32}S		(moments)$^{(i)}$	
Feb 84	^{32}S		(moments)$^{(ii)}$	
May 84	^{34}S	focal plane		
	^{34}S	MBL		
Dec 84	^{32}S		spectroscopy$^{(i)}$	MBL$^{(i)}$
Apr 85	^{34}S		moments$^{(iii)}$	
Apr 85	^{32}S		moments$^{(iv)}$	
Aug 85	^{32}S			MBL$^{(ii)}$
Jul 86	^{32}S		spectroscopy$^{(ii)}$	
	^{34}S			MBL+tape$^{(iii)}$
Jul 86	^{32}S			MBL$^{(iv)}$

Table 5.1 Experiments performed on the decay of $^{118}I^{g+m}$. Beam energies of $150-175$ MeV were used in conjunction with a ^{93}Nb target (of thickness 2-3 mg/cm^2), forming the entrance window of a FEBIAD ion source.

5.2 $\gamma-\gamma$ coincidence measurements

5.2.1 Experimental details

The levels and transitions in ^{118}Te, populated in the decay of $^{118}I^{g}$ and $^{118}I^{m}$, that have been established from previous work on ^{118}I decay[3] and in-beam γ-ray spectroscopy on ^{118}Te [4] [5] are shown in [Fig 5.2] . In order to supplement these level schemes, two separate $\gamma-\gamma$ coincidence experiments have been performed (see Table 5.1) on the decay of $^{118}I^{g+m}$.

The first was performed by the Sussex group, using the tape transport system in the focal plane of the isotope separator to move radioactive atoms from the *collection* point up to the *counting* position. The latter consisted

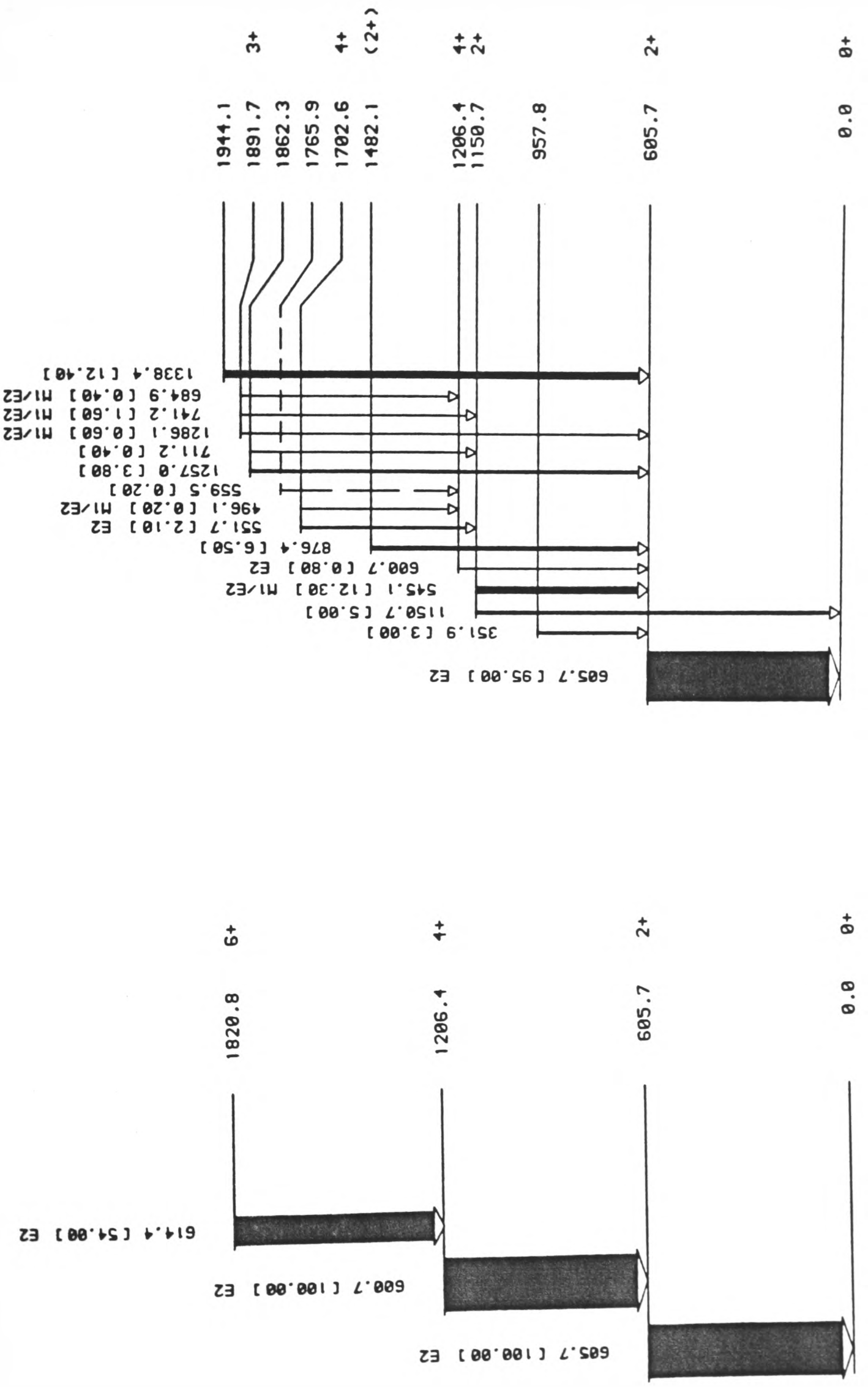

Figure 5.2. The previously known levels and transitions in ^{118}Te, populated in the decay of $^{118}I^{g}$ and $^{118}I^{m}$

of four Ge(Li) detectors placed symmetricaly in a horizontal plane around the source. The collection time for the tape system was set to be 16min, so that unwanted ^{118}Cs ($t_{1/2}$ = 17sec), and ^{118}Xe ($t_{1/2}$ = 3.8min) could be *filtered* out.

The second experiment, performed by the Oxford group, consisted of collecting a source in a thin-walled aluminium cap on the end of the mini-beam line, around which were placed four Ge(Li) detectors. In this case no half-life filtering was possible, and the relative intensities from these two experiments differ slightly because the half-life filtering effectively changes the ratio of $^{118}I^{m}$ to $^{118}I^{g}$.

In both experiments the detectors were set up to record $\gamma-\gamma$ coincidences, which were written event-by-event onto magnetic tape for subsequent analysis.

5.2.2 Decay scheme of $^{118}I^{g+m}$

Replay of the event-by-event data enabled coincidence spectra to be obtained by setting digital gates on peaks of interest. Spectra for each gate were *gain-matched* and added to improve statistics. Due to problems with steering the beam down the mini-beam line, the statistics obtained for that experiment were much poorer than for the focal plane experiment. However, the two sets of data did complement one another, particularly for high energy transitions seen in the mini-beam line experiment which were missed by the focal plane detectors (which were only set to detect γ-rays up to 2200keV).

Singles spectra were also taken and were used for energy and intensity measurements, except for the case of unresolved multiplets, where the coincidence spectra were used. A ^{152}Eu source was used to calibrate the focal plane detectors, and both ^{152}Eu and ^{56}Co calibration sources were used for the mini-beam line experiment.

From the coincidence relationships (mainly using the focal plane data), and from energy and intensity considerations, a level scheme for $^{118}I^{g+m}$ decay has

been deduced, and is shown in [Fig 5.3] . The majority of this very complicated analysis has been done by S.P.Collins [6] (of Sussex University), and the decay scheme presented in [Fig 5.3] provides a basic framework for the analysis and interpretation of the nuclear orientation and conversion electron data also obtained for this system.

In addition, $\gamma - \gamma$ angular correlation measurements were also performed for some of the stronger γ-rays , using the detectors at the focal plane. Where relevant, these results will be quoted later, with reference to the results deduced from the nuclear orientation and conversion electron measurements.

In this work many new γ-rays have been assigned to the decay of $^{118}I^{g+m}$, but no evidence has been found for the 104 keV γ-ray , proposed by Ladenbauer-Bellis and Bakhru [7] as the γ-transition associated with the decay of the metastable $^{118}I^{m}$ to the ground state $^{118}I^{g}$. The only unplaced γ-ray attributed to $^{118}I^{g+m}$ decay that is close in energy is at 112.6 keV. However, this transition is not highly converted (as would be expected for a $^{118}I^{m} \rightarrow {}^{118}I^{g}$ transition), and the fact that is is not seen in $\gamma-\gamma$ coincidence is probably just a consequence of the very low coincidence efficiency at this energy.

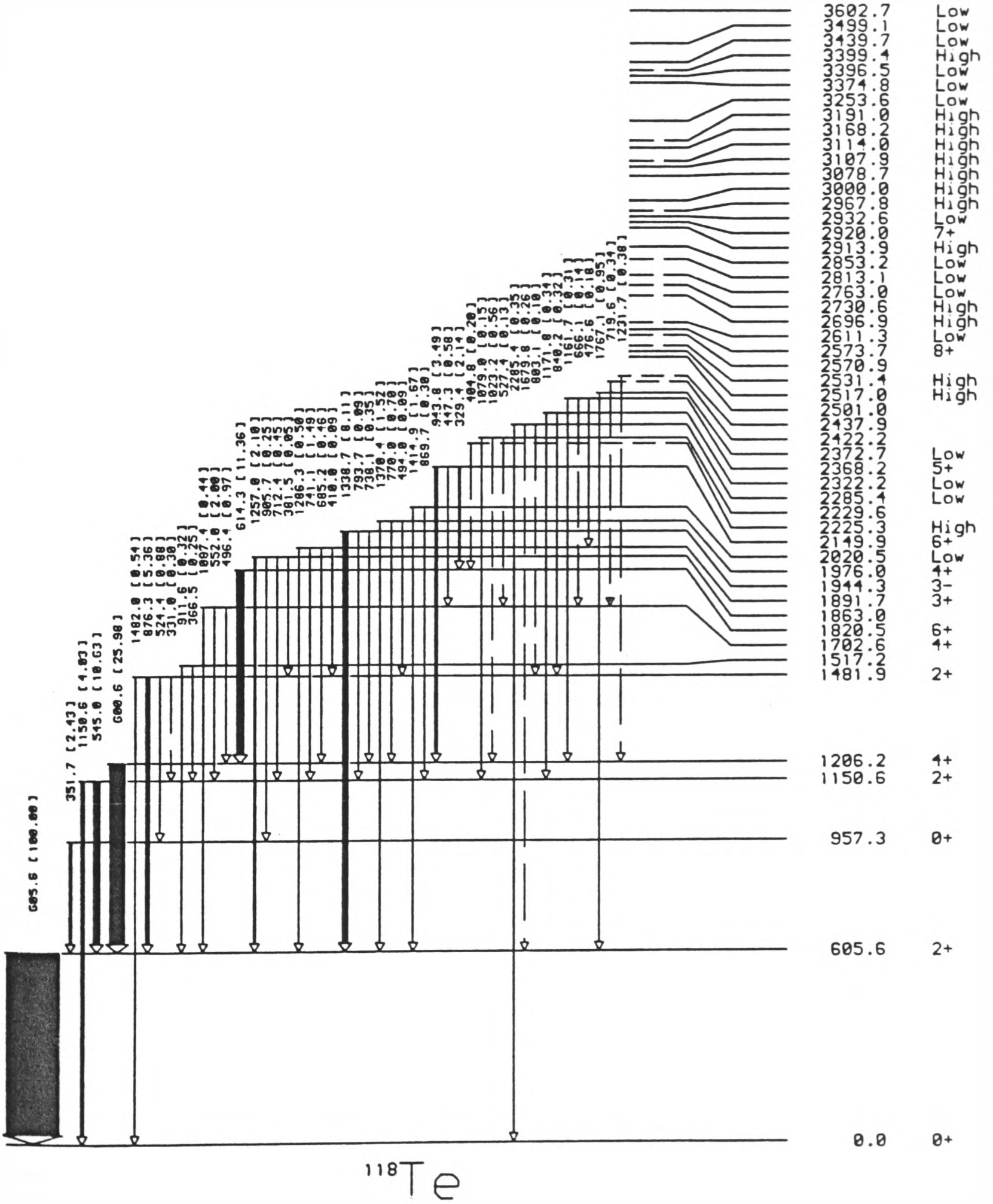

Figure 5.3. Levels and transitions in ^{118}Te, as determined from the decay of $^{118}I^{g+m}$

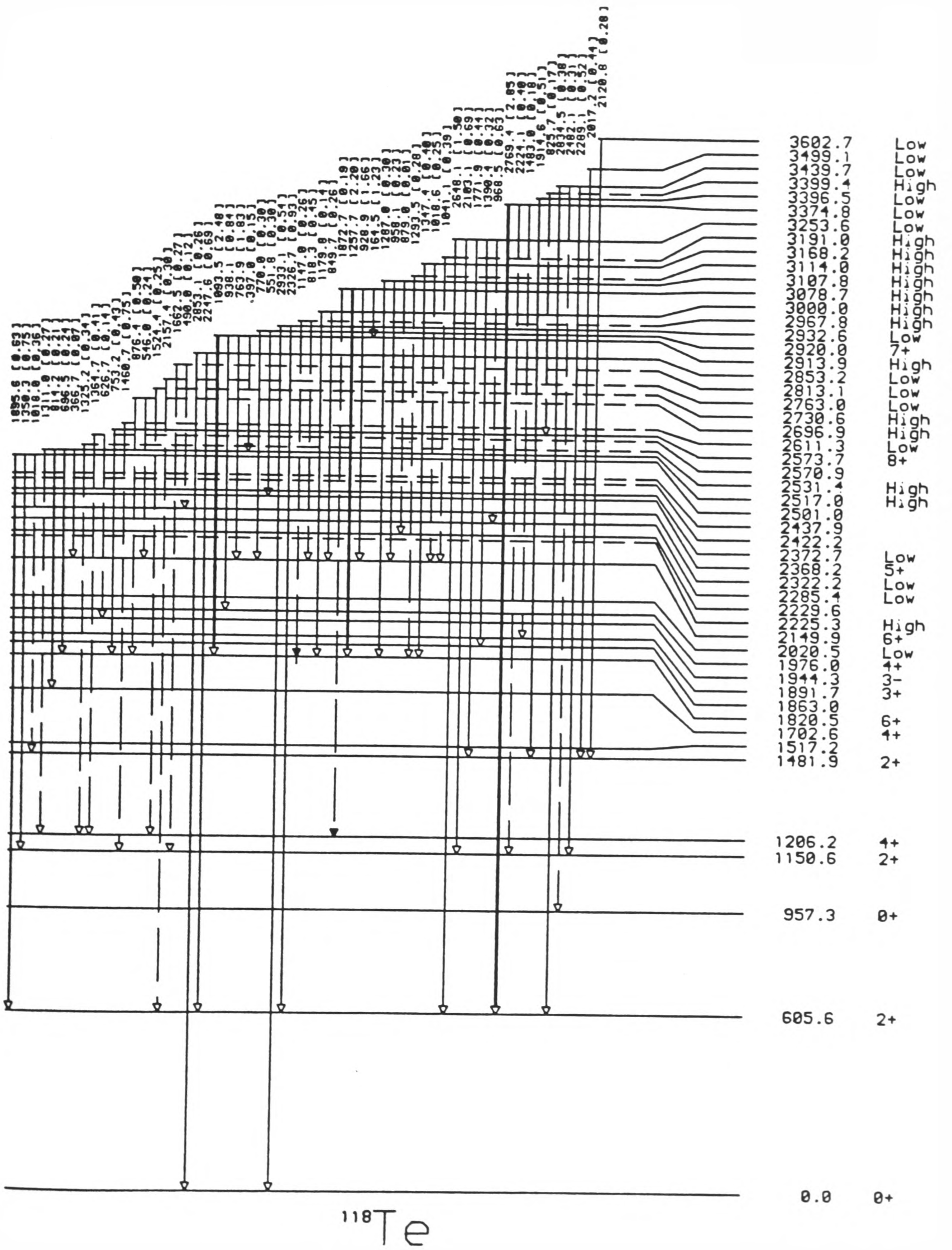

Figure 5.3. Levels and transitions in ^{118}Te, as determined from the decay of $^{118}I^{g+m}$

5.3 Separate Level Schemes from $^{118}I^{g}$ decay and $^{118}I^{m}$ decay

5.3.1 Mass 118 yields with ^{32}S and ^{34}S beams

The decay scheme given in [Fig 5.3] shows levels populated in the decay of $^{118}I^{g+m}$, produced with a ^{34}S beam. The relative intensities shown vary according to the relative proportion of high/low spin isomers present, which in turn depends upon the incident beam (^{32}S or ^{34}S), and also on how the measurement was made (i.e. with or without half-life filtering). The refrigerator data was taken using a ^{32}S beam, resulting in a different yield of high/low spin isomers, and hence giving a different set of γ-ray intensities. As a result, it is advantageous to *separate* out the components which come from the two isomers, and to produce *two* level schemes, which would be populated by the decay of $^{118}I^{g}$ and $^{118}I^{m}$ individually.

Experimentally, the ^{118}I decay spectra obtained using the ^{34}S beam, although being much weaker, were much *cleaner* than with the ^{32}S beam, due to the yield of ^{118}Cs and ^{118}Xe being greatly reduced. Careful comparison of the two types of spectra allows unplaced transitions to be assigned to ^{118}I decay, the criterion being that they must appear in both sets of data with comparable intensities. Another important feature is that the ratio of high/low spin isomers ($^{118}I^{m}/^{118}I^{g}$) is roughly a factor of two higher in the ^{34}S experiment, giving rise to a very clear signature for transitions originating from the high spin isomer. These points are illustrated in [Fig 5.4] , where spectra from experiments using ^{32}S and ^{34}S beams are plotted for comparison, from 600 to 1000keV.

Table 5.2 shows all the γ-rays that can be associated with ^{118}I decay, either from $\gamma - \gamma$ coincidence, or simply by comparison of their relative intensities in the two types of experiment. In [Fig 5.3] new levels are assigned as high and low spin mainly on the basis of the spins of levels they feed (or are fed by),

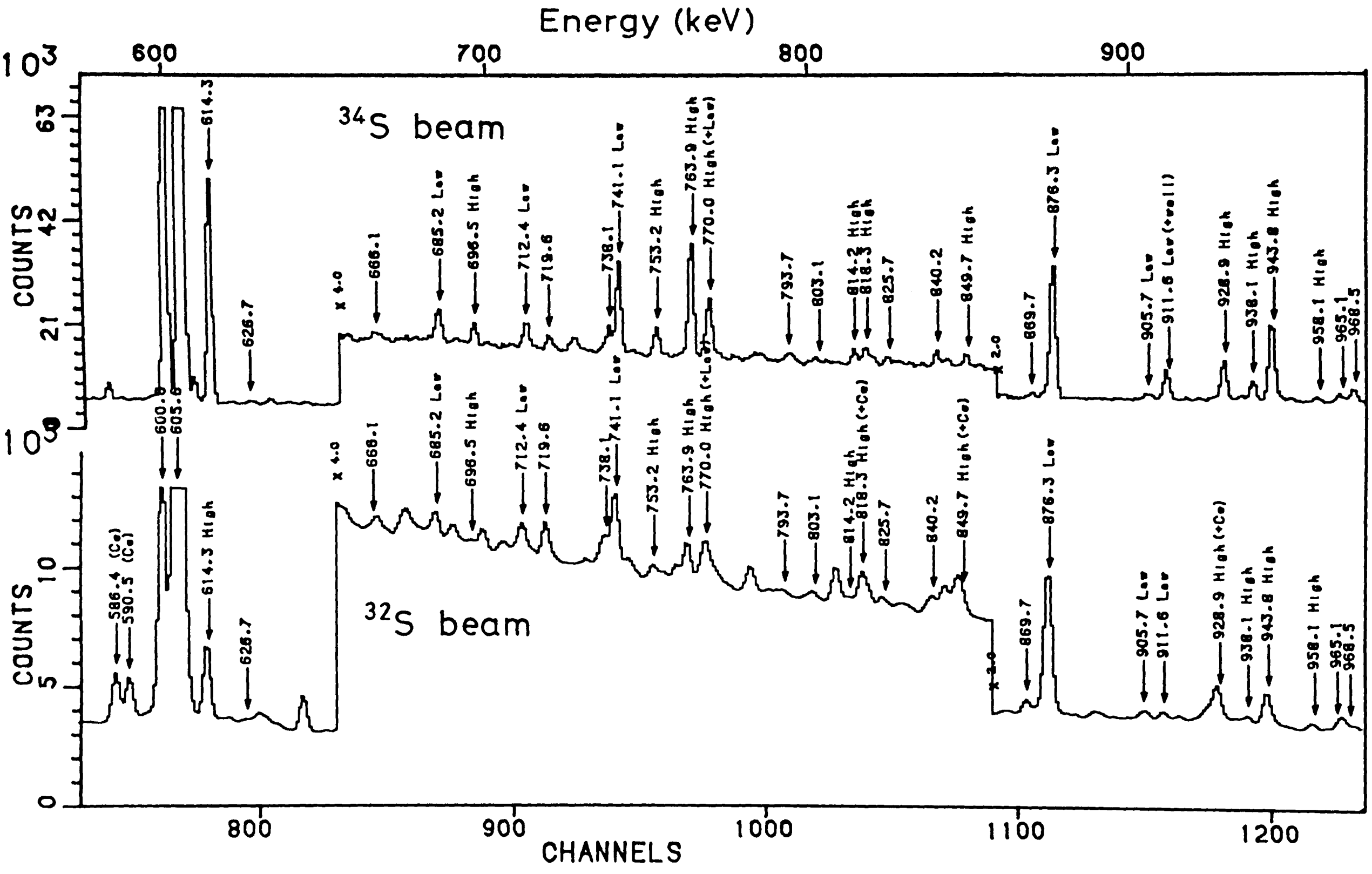

Figure 5.4. Comparison of mass 118 spectra, obtained with ^{32}S and ^{34}S beams

but also by comparison of the $^{34}S/^{32}S$ relative intensities of their associated γ-transitions.

5.3.2 The separation of high and low spin components

The basic assumption under which the separation of high and low spin components can made is that any level in ^{118}Te can be directly β-fed by only *one* of the two ^{118}I isomers (for purposes of this discussion β-decay includes electron capture decay as well). In this picture, $^{118}I^{g}$ ($J^{\pi} = 2^{-}$) is assumed to feed only levels of spins 0 to 4, and $^{118}I^{m}$ ($J^{\pi} = 7^{-}$) levels with spins 5 to 9. This requires transitions with $j_{\beta} = 0, 1, 2$, which can occur for allowed, first and second forbidden β-decays . The probability of a $j_{\beta} = 3$ transition (e.g. $7 \rightarrow 4$, or $2 \rightarrow 5$) competing successfully with these is regarded as unlikely, and forms the basis for the above assumption.

Adopting the convention used in chapter 1.2.4, let $\Im_{nm}$ be the intensity of a β or γ-transition between states of spins I_n and I_m. From the known γ-intensities (Table 5.2) and decay scheme ([Fig 5.3]), the direct β-feed to a level of spin I_i is simply derived from the γ-ray intensity balance (neglecting electron conversion) to be

$$\Im_{0i} = \sum_{m=i+1}^{N} \Im_{im} - \sum_{n=1}^{i-1} \Im_{ni} \qquad (5.1)$$

$$(from \rightarrow) \quad (\rightarrow to)$$

where N is the total number of levels and $i = 0$ corresponds to either the high or low spin isomer (no distinction being made between them at this stage). It is obviously unphysical for $\Im_{0i}$ to be negative, but in cases where there is very little direct feed, the two summation terms above may not cancel one another exactly, and a small negative $\Im_{0i}$ can result. In the few situations where this happens, $\Im_{0i}$ is taken to be zero.

E_γ	$I_\gamma(^{32}S)$	$I_\gamma(^{34}S)$	I_i	I_f	W(0) 15mK	W(0) 32mK	W(90) 15mK	W(90) 32mK	$P_\gamma^{exp}(90)$
112.6	(1.50)	(1.80)			22.2 (1.0)	11.1 (1.8)	−12.0 (1.0)	−4.3 (2.0)	
164.5	(0.56)	1.23	3078.7	2913.9	28.1 (4.0)	30.5 (6.9)	−14.0 (4.7)	−19.4 (9.2)	
329.4	(0.97)	2.14	2149.9	1820.5	−59.4 (2.3)	−40.0 (5.3)	29.0 (4.1)	23.3 (6.8)	
(331.0)	(0.35)	0.30	1481.9	1150.6					
351.7	(2.76)	2.43	957.3	605.6	1.7 (1.1)	0.3 (1.9)	−0.9 (1.4)	−0.9 (2.6)	
366.5	(0.30)	0.25	1517.2	1150.6	−9.0 (8.4)	−14.9 (12.5)	9.2 (11.1)	−1.9 (20.2)	
366.7	(0.03)	0.07	2517.0	2149.9					
381.5	(0.05)	0.05	1863.0	1481.9					
(397.0)	(0.07)	0.15	2913.9	2517.0	−3.4 (7.2)		12.5 (9.9)		
(404.8)	(0.09)	0.20	(2225.3)	1820.5	−18.1 (6.7)	−22.8 (16.3)	7.2 (8.5)	5.8 (16.0)	
410.0	(0.09)	0.09	1891.7	1481.9					
447.3	(0.26)	0.58	2149.9	1702.6	−48.2 (8.0)		18.6 (10.8)		
476.6	(0.08)	0.18	2368.2	1891.7					
(490.0)	(0.13)	0.12	(2813.1)	2322.2					
494.0	(0.08)	0.09	1976.0	1481.9					
496.4	(0.79)	0.97	1702.6	1206.2	−18.4 (1.5)	−14.8 (3.1)	8.5 (2.1)	4.3 (3.8)	
524.4	1.00	0.88	1481.9	957.3	−26.5 (1.3)	−19.8 (3.9)	8.6 (1.9)	3.4 (4.0)	
(527.4)	0.13	0.13	2229.6	1702.6					
545.0	(11.29)	10.63	1150.6	605.6	2.5 (0.4)	0.9 (0.7)	−2.0 (0.5)	−1.1 (0.9)	0.18 (0.18)
(546.0)	(0.11)	0.24	(2696.9)	2149.9					
551.8	(0.14)	0.30	2920.0	2368.2					
552.0	(1.67)	2.00	1702.6	1150.6	−35.7 (0.8)	−23.8 (1.7)	15.4 (1.3)	13.3 (2.3)	
(561.2)	0.45	0.38							
600.6	16.90	25.98	1206.2	605.6	−40.6 (0.3)	−28.8 (0.6)	15.9 (0.7)	11.3 (1.2)	
605.6	100.00	100.00	605.6	0.0	−24.9 (0.3)	−15.6 (0.5)	10.2 (0.4)	7.9 (0.8)	−0.43 (0.08)
614.3	5.05	11.36	1820.5	1206.2	−59.9 (0.3)	−44.0 (0.7)	20.5 (0.7)	18.6 (1.2)	
(626.7)	(0.16)	0.14	(2570.9)	1944.3					
(666.1)	0.06	0.14	2368.2	1702.6					

Table 5.2. Intensities and *separated* anisotropies, $W(0)$ and $W(90)$, for γ-rays seen in the decay of $^{118}I^{g+m}$.

E_γ	$I_\gamma(^{32}S)$	$I_\gamma(^{34}S)$	I_i	I_f	W(0) 15mK	W(0) 32mK	W(90) 15mK	W(90) 32mK	$P_\gamma^{exp}(90)$
685.2	0.46	0.46	1891.7	1206.2	3.4 (3.1)	0.5 (5.8)	−2.7 (4.1)	5.6 (8.0)	
696.5	0.11	0.24	2517.0	1820.5	−41.2 (12.8)		19.3 (17.8)		
712.4	0.61	0.45	1863.0	1150.6	−19.7 (3.7)	−16.5 (7.6)	12.2 (3.9)	5.9 (6.9)	
(719.6)	0.32	0.34	(2422.2)	1702.6	13.5 (9.2)	15.6 (16.6)	5.4 (9.7)	−2.1 (17.9)	
738.1	0.48	0.35	1944.3	1206.2	12.8 (3.7)	9.5 (6.6)	−9.8 (5.5)	−11.8 (7.1)	
741.1	1.62	1.49	1891.7	1150.6	−2.8 (1.2)	−1.8 (2.2)	3.7 (1.5)	2.1 (2.8)	
753.2	0.25	0.43	2573.7	1820.5	−59.8 (5.5)	−31.7 (13.1)	19.6 (11.0)	13.2 (19.4)	
763.9	0.81	1.83	2913.9	2149.9	−69.1 (1.5)	−51.3 (3.7)	37.3 (3.4)	28.6 (5.7)	
770.0	(0.14)	0.30	2920.0	2149.9					
770.0	(0.57)	0.70	1976.0	1206.2	6.3 (2.7)	−0.6 (5.0)	0.9 (3.1)	−2.5 (5.9)	
793.7	(0.11)	0.09	1944.3	1150.6					
(803.1)	(0.11)	0.10	2285.4	1481.9					
814.2	0.11	0.21	2517.0	1702.6	−58.0 (9.2)	−21.8 (22.0)	11.1 (16.9)	3.9 (30.5)	
(818.3)	0.47	0.45	(2967.8)	2149.9	−7.8 (2.8)	−4.0 (5.4)	2.1 (3.1)	−7.3 (5.8)	
(825.7)	0.17	0.17	(3399.4)	2573.7	−24.8 (7.6)	−10.3 (16.0)	12.1 (10.2)	6.1 (18.5)	
840.2	0.29	0.32	2322.2	1481.9	46.7 (8.5)	37.9 (13.9)	−14.8 (5.9)	2.1 (12.1)	
849.7	0.18	0.26	3000.0	2149.9	−25.2 (4.3)	−39.2 (8.6)	5.0 (6.9)	19.1 (13.2)	
869.7	0.47	0.30	2020.5	1150.6	0.9 (2.6)	1.7 (4.9)	0.8 (2.7)	1.6 (5.2)	
876.3	(6.57)	5.36	1481.9	605.6	18.1 (0.6)	11.1 (1.0)	−9.3 (0.5)	−4.6 (1.0)	0.08 (0.25)
(876.4)	(0.22)	0.50	(2696.9)	1820.5					
(879.0)	0.01	0.01	3107.8	2229.6					
905.7	0.37	0.25	1863.0	957.3	−25.3 (4.8)	−11.8 (10.1)	14.0 (8.8)	7.2 (15.7)	
911.6	0.35	0.32	1517.2	605.6	3.7 (4.9)	−14.6 (8.9)	2.8 (6.4)	7.0 (12.0)	
928.9	(0.75)	1.66	3078.7	2149.9	−39.9 (1.2)	−36.1 (2.6)	23.2 (2.0)	12.1 (3.4)	
938.1	0.33	0.84	2913.9	1976.0	−70.5 (3.2)	−60.1 (7.8)	20.4 (5.8)	17.5 (10.3)	
943.8	1.58	3.49	2149.9	1206.2	−53.6 (0.9)	−37.3 (2.1)	18.5 (1.5)	14.0 (2.7)	
958.1	0.07	0.23	3107.8	2149.9	36.9 (25.0)		−38.4 (43.6)		
(965.1)	0.21	0.37			7.5 (10.2)	42.2 (19.9)	−5.3 (7.2)	4.6 (14.0)	

Table 5.2. Intensities and *separated* anisotropies, $W(0)$ and $W(90)$, for γ-rays seen in the decay of $^{118}I^{g+m}$.

E_γ	$I_\gamma(^{32}S)$	$I_\gamma(^{34}S)$	I_i	I_f	W(0) 15mK	W(0) 32mK	W(90) 15mK	W(90) 32mK	$P_\gamma^{exp}(90)$
(968.5)	0.51	0.63	3253.6	2285.4	−7.0 (3.9)	−1.6 (7.7)	11.9 (6.5)	−14.9 (11.3)	
(1018.0)	(0.37)	0.36	2501.0	1481.9	−26.4 (3.6)	−16.4 (7.5)	8.2 (4.2)	9.9 (7.7)	
(1018.6)	(0.11)	0.25	3168.2	2149.9					
(1023.2)	1.06	0.56	2229.6	1206.2	−14.1 (2.1)	−9.7 (4.1)	7.1 (2.9)	−4.5 (5.2)	
(1041.1)	0.27	0.39	(3191.0)	2149.9	−32.1 (6.3)	−38.1 (13.3)	19.8 (10.9)	21.4 (17.8)	
(1055.5)	0.61	0.37			−0.1 (2.5)	−4.2 (4.7)	−5.0 (2.9)	−4.5 (5.5)	
1079.0	0.09	0.15	2229.6	1150.6	−38.9 (10.6)		31.0 (20.9)		
1093.5	1.33	2.48	2913.9	1820.5	−60.9 (1.1)	−50.7 (2.5)	30.4 (2.3)	19.4 (3.9)	
1097.4	0.33	0.44	1702.6	605.6	−36.7 (6.5)		13.3 (8.5)		
(1147.0)	0.39	0.26	(2967.8)	1820.5	−30.2 (3.8)	−31.2 (8.0)	13.7 (5.5)	11.1 (13.4)	
1150.6	4.31	4.03	1150.6	0.0	−19.3 (0.6)	−10.7 (1.1)	8.1 (0.8)	6.5 (1.5)	−0.71 (0.43)
1161.7	0.19	0.31	2368.2	1206.2	−13.9 (7.3)	−19.8 (14.2)	16.1 (10.5)	8.0 (18.6)	
1171.8	0.33	0.34	2322.2	1150.6	32.1 (6.4)	8.5 (13.1)	−21.9 (5.6)	−4.0 (11.7)	
1179.8	0.06	0.14	3000.0	1820.5					
(1231.7)	0.46	0.38	(2437.9)	1206.2	−29.2 (3.0)	−22.5 (6.2)	11.4 (4.6)	17.5 (8.6)	
1257.0	(2.06)	2.10	1863.0	605.6	−16.9 (0.7)	−14.8 (1.5)	10.8 (1.0)	10.1 (1.9)	
1257.7	(0.88)	2.20	3078.7	1820.5					
1286.3	(0.66)	0.50	1891.7	605.6	−5.2 (2.4)	−2.5 (4.7)	4.0 (3.0)	1.5 (5.7)	
1287.0	(0.14)	0.30	3107.8	1820.5					
(1293.5)	(0.13)	0.28	(3114.0)	1820.5					
(1311.0)	(0.12)	0.27	2517.0	1206.2					
(1325.2)	0.22	0.34	(2531.4)	1206.2	34.1 (8.9)	11.4 (14.5)	−22.3 (8.0)	−1.6 (17.1)	
1338.7	10.80	8.11	1944.3	605.6	23.5 (0.6)	14.2 (0.9)	−11.8 (0.5)	−7.1 (0.9)	−0.55 (0.29)
1347.4	(0.18)	0.40	3168.2	1820.5	−67.9 (3.8)	−50.8 (9.2)	24.6 (5.2)	28.2 (12.7)	
1350.3	0.96	0.75	2501.0	1150.6	−5.6 (1.8)	−0.5 (3.6)	7.0 (2.5)	4.1 (4.7)	
(1364.7)	0.61	0.41	(2570.9)	1206.2	−19.8 (3.4)	−13.4 (7.0)	13.9 (5.0)	9.9 (8.8)	
1370.4	1.30	1.52	1976.0	605.6	−41.3 (1.5)	−31.1 (3.3)	17.9 (2.3)	12.9 (4.0)	
1390.4	0.41	0.32	3253.6	1863.0	−23.1 (4.1)	7.8 (8.8)	3.3 (5.1)	12.0 (9.8)	

Table 5.2. Intensities and *separated* anisotropies, $W(0)$ and $W(90)$, for γ-rays seen in the decay of $^{118}I^{g+m}$.

E_γ	$I_\gamma(^{32}S)$	$I_\gamma(^{34}S)$	I_i	I_f	W(0) 15mK	W(0) 32mK	W(90) 15mK	W(90) 32mK	$P_\gamma^{exp}(90)$
1414.9	2.32	1.67	2020.5	605.6	−8.9 (1.1)	−5.0 (2.0)	4.7 (1.3)	2.5 (2.3)	
(1460.7)	(0.80)	0.75	(2611.3)	1150.6	−9.9 (2.1)	−6.5 (4.2)	−1.5 (2.7)	−9.8 (5.0)	
1482.0	(0.64)	0.54	1481.9	0.0	−15.8 (2.5)	−6.7 (5.1)	2.1 (3.3)	3.2 (6.2)	
(1483.0)	(0.21)	0.18	3374.8	1891.7					
(1524.4)	0.08	0.25	(2730.6)	1206.2	−11.0 (11.0)	−22.9 (19.3)	1.6 (14.1)	−18.5 (26.0)	
(1532.3)	0.40	0.24			9.3 (5.0)	−6.7 (9.0)	−7.1 (5.2)	4.3 (10.3)	
(1662.5)	0.33	0.27	(2813.1)	1150.6	−17.2 (4.9)	−6.1 (10.0)	7.3 (7.7)	12.9 (14.2)	
(1679.8)	(0.28)	0.26	2285.4	605.6	−0.5 (4.1)	7.1 (8.0)	−0.2 (5.1)	15.0 (10.0)	
1767.1	1.07	0.95	2372.7	605.6	−18.3 (1.6)	−14.4 (3.2)	9.9 (2.3)	5.1 (4.1)	
1771.9	0.57	0.44	3253.6	1481.9	−3.4 (4.1)	−11.0 (7.8)	−1.7 (5.6)	−7.2 (10.5)	
1849.3	0.63	0.41			−11.9 (7.2)	−8.2 (14.1)	15.9 (11.2)	−55.0 (19.5)	
(1872.7)	(0.09)	0.19	3078.7	1206.2	−23.1 (15.4)		−1.8 (19.1)		
1881.1	0.47	0.32			8.1 (4.5)	−10.5 (7.9)	4.9 (5.0)	14.0 (9.4)	
1885.1	0.24	0.22			15.4 (8.5)	2.3 (15.0)	2.5 (8.0)	12.7 (15.2)	
1895.6	0.87	0.63	2501.0	605.6	−14.3 (2.9)	−7.6 (5.9)	12.5 (3.4)	8.5 (6.2)	
1914.6	0.77	0.51	3396.5	1481.9	−8.1 (3.2)	−8.2 (6.2)	7.6 (3.7)	10.2 (6.9)	
2017.2	0.50	0.44	3499.1	1481.9	−21.8 (4.3)	−17.4 (8.8)	10.8 (4.6)	7.7 (8.3)	
(2039.5)	0.47	0.48			25.8 (5.6)	6.6 (9.8)	−11.8 (5.1)	−7.5 (10.1)	
2103.1	0.67	0.69	3253.6	1150.6	−12.8 (3.0)	−1.5 (6.0)	0.6 (3.3)	0.1 (6.8)	
2120.8	0.44	0.28	3602.7	1481.9	4.5 (5.3)	3.2 (9.9)	0.9 (5.4)	−7.6 (10.0)	
2145.4	0.19	0.17			10.8 (9.3)	−13.2 (16.4)	−18.9 (10.7)	−15.2 (21.4)	
(2157.4)	0.43	0.30	(2763.0)	605.6	19.4 (5.3)	16.1 (9.3)	−0.8 (6.4)	−0.6 (12.3)	
(2224.1)	0.43	0.40	3374.8	1150.6	−24.7 (4.4)	−16.0 (9.2)	9.8 (6.6)	0.4 (11.9)	
2247.6	0.92	0.69	2853.2	605.6	5.1 (2.6)	4.1 (4.7)	2.3 (2.9)	−3.0 (5.5)	
2273.0	0.29	0.36			−28.5 (5.3)	−17.6 (11.2)	13.8 (7.1)	18.0 (13.0)	
2277.7	0.28	0.21			−15.1 (11.1)	−13.4 (22.3)	1.2 (13.8)	4.6 (25.9)	
2285.4	0.40	0.35	2285.4	0.0	22.2 (8.9)	3.8 (15.3)	−23.0 (10.0)	6.0 (17.3)	
2289.1	0.55	0.52	3439.7	1150.6	−22.0 (3.2)	−15.6 (6.8)	7.1 (4.8)	12.4 (8.7)	

Table 5.2. Intensities and *separated* anisotropies, $W(0)$ and $W(90)$, for γ-rays seen in the decay of $^{118}I^{g+m}$.

E_γ	$I_\gamma(^{32}S)$	$I_\gamma(^{34}S)$	I_i	I_f	W(0) 15mK	W(0) 32mK	W(90) 15mK	W(90) 32mK	$P_\gamma^{exp}(90)$
2298.4	0.59	0.56			−25.9 (3.5)	−26.4 (7.2)	7.6 (4.9)	−9.8 (8.8)	
2326.7	1.02	0.93	2932.6	605.6	4.5 (2.3)	1.4 (4.3)	−3.4 (2.6)	−2.7 (4.9)	
2355.1	1.25	1.17			−10.3 (1.8)	−11.1 (3.6)	9.0 (2.3)	10.0 (4.3)	
2362.3	0.45	0.50			−20.4 (3.5)	−9.5 (7.3)	16.9 (5.4)	11.7 (9.6)	
2410.2	0.42	0.33			33.1 (8.3)	29.8 (13.9)	−21.9 (6.2)	2.5 (13.2)	
2432.1	0.28	0.27			17.5 (8.1)	26.2 (14.6)	−14.6 (6.6)	−12.7 (13.1)	
2448.1	0.36	0.54			20.6 (6.5)	−12.9 (10.8)	−7.8 (5.7)	3.5 (11.3)	
2458.2	0.88	0.88			−12.6 (2.3)	−5.8 (4.6)	8.6 (2.9)	3.9 (5.3)	
(2482.1)	0.30	0.31	3439.7	957.3	31.0 (10.1)	41.0 (17.5)	−16.6 (8.6)	11.1 (17.9)	
2490.8	1.37	1.31			24.3 (2.3)	18.7 (3.9)	−14.3 (2.1)	−9.9 (4.1)	
2639.8	0.22	0.24			17.0 (8.4)	2.8 (14.6)	−15.0 (7.4)	8.0 (15.2)	
2648.1	1.65	1.50	3253.6	605.6	−17.0 (1.3)	−13.1 (2.6)	8.7 (1.8)	5.3 (3.3)	
2679.2	0.64	0.51			−15.8 (3.1)	−13.0 (6.3)	2.6 (3.7)	15.1 (7.1)	
2769.4	3.34	2.85	3374.8	605.6	−19.5 (0.8)	−14.5 (1.6)	6.9 (1.1)	7.9 (2.0)	
2791.7	1.05	0.88			26.2 (2.5)	15.2 (4.2)	−12.5 (2.2)	−10.7 (4.4)	
2834.5	0.38	0.38	3439.7	605.6	−18.4 (4.0)	−11.0 (8.1)	17.2 (6.0)	5.5 (10.5)	
2853.1	0.32	0.26	2853.2	0.0	23.7 (6.3)	10.8 (10.8)	−14.1 (5.5)	−7.4 (11.0)	
2933.1	0.54	0.54	2932.6	0.0	33.2 (5.2)	11.3 (8.6)	−11.9 (5.8)	−20.1 (11.3)	

Table 5.2. Intensities and *separated* anisotropies, $W(0)$ and $W(90)$, for γ-rays seen in the decay of $^{118}I^{g+m}$. Transitions with no initial or final levels assigned are unplaced in the level scheme, whereas bracketed transitions are only tentatively associated with ^{118}I decay. Relative γ-ray intensities are also quoted for each transition, for both ^{32}S and ^{34}S experiments (those values shown in brackets are subject to possible systematic errors, and should be treated with caution.

Levels near the top of the decay scheme are, by necessity, mostly directly β-fed by one or other isomer. However, levels lower down may be populated not only by direct β-feeds, but also by γ-rays , which may have either high or low spin character (or a mixture of both). By starting at the top of the decay scheme and working down, it is possible to keep track of *all* the feeding, and hence to determine the fractional parental contribution of each isomer to each level.

Let $\Re_i^{h,l}$ denote the high and low spin contributions for a level of spin I_i, normalized such that $\Re_i^h + \Re_i^l = 1$. In order to distinguish the high/low character of β-feeds to a particular level, the following definitions can be made

$$\Re_0^h = \begin{cases} 1 & \text{high spin character} \\ 0 & \text{low spin character} \end{cases} \tag{5.2}$$

and

$$\Re_0^l = \begin{cases} 0 & \text{high spin character} \\ 1 & \text{low spin character} \end{cases} \tag{5.3}$$

The fractional parental contribution to a level (I_i) may now be written as an average of the parental *character* of all transitions feeding the level, weighted by the intensities of the transitions, as follows

$$\Re_i^{l,h} = \sum_{n=0}^{i-1} \Im_{ni} \Re_n^{l,h} \Big/ \sum_{n=0}^{i-1} \Im_{ni} \tag{5.4}$$

The values $\Im_{ni}$ are quoted in Table 5.2 as combined $(h + l)$ intensities, relative to the total $(h + l)$ intensity of the 605.6keV $(2_1^+ \rightarrow 0_1^+)$ transition, (which is given a relative intensity of 100). In order to separate out the h and l relative intensities for a particular transition $(I_n \rightarrow I_i)$, it is necessary to know the h/l spin proportions of *both* the 605.6keV level and the level (I_n) from which the γ-ray originates. Separated h and l intensities, $\Im_{ni}^{h,l}$, may be now be written as

$$\Im_{ni}^{h,l} = \frac{\Re_n^{h,l}}{\Re_{605.6}^{h,l}} \times \Im_{ni} \tag{5.5}$$

From [Fig 5.3] and Table 5.2 a complete set of β and γ-intensities from two different experiments (^{32}S and ^{34}S) may be used independently to separate out the high and low spin intensities, using equations (5.4) and (5.5). The program UACALC (see chapter 4.3.6) evaluates $\Re_n^{h,l}$ and $\Im_{ni}^{h,l}$, using the formalism described above, and the results of this procedure are shown in Tables 5.3,5.4 and 6.1,6.7. The good agreement between the two sets of data justifies the method used.

Tables 5.3 and 5.4 show the levels populated in the decay of $^{118}I^g$ and $^{118}I^m$ respectively, along with the relative β-feed intensity, deduced from equation (5.1), for the two experiments. The relative h/l contribution (in %) to each level is also given (for the ^{32}S experiment), along with corresponding values of U_λ^{min} and U_λ^{max}, which are relevant to the nuclear orientation analysis to be described later.

5.4 The magnetic moments of $^{118}I^g$ and $^{118}I^m$

5.4.1 Experimental Details

A total of four different experiments have been performed, as seen from Table 5.1. The magnetic moments of $^{118}I^g$ and $^{118}I^m$, deduced from the first two of these experiments (the first on-line experiments to be performed at DOLIS–COLD), served to demonstrate the phenomenon of *shape co-existence* in ^{118}I [8] . However, the experimental uncertainties were relatively large and two further experiments were performed to determine the moments more precisely, which were found necessary for the interpretation of the *spectroscopy* experiments. The results of the latter two *moment* experiments will be presented here.

Level	Spin	$I_\beta(^{32}S)$	$I_\beta(^{34}S)$	$\Re^l(^{32}S)$	U_2^{max}	U_2^{min}	U_4^{max}	U_4^{min}
3602.7	$(2,3)^+$	0.48	0.34	100.0	1.000	0.500	1.000	−0.667
3499.1	$(2,3^+)$	0.54	0.54	100.0	1.000	0.500	1.000	−0.667
3439.7	(1^+)	2.50	2.65	100.0	0.592	0.592	0.000	0.000
3396.5	$(2,3^+)$	0.84	0.62	100.0	1.000	0.500	1.000	−0.667
3374.8	2^+	4.33	4.33	100.0	1.000	0.500	1.000	−0.667
3253.6	$(2)^+$	4.15	4.34	100.0	1.000	0.500	1.000	−0.667
2932.6	1	1.70	1.72	100.0	0.592	0.592	0.000	0.000
2853.2	1	1.35	1.19	100.0	0.592	0.592	0.000	0.000
(2813.1)	$(2,3^+)$	0.50	0.48	100.0	1.000	0.500	1.000	−0.667
(2763.0)	$(3)^+$	0.47	0.37	100.0	1.000	0.500	1.000	−0.667
(2611.3)	$(0,2,3,4)$	0.87	0.91	100.0	1.000	0.500	1.000	−0.667
(2570.9)	$(3^+,4)$	0.84	0.67	100.0	0.749	0.749	0.285	0.285
2501.0	$(3)^+$	2.39	2.12	100.0	0.828	0.828	0.418	0.418
(2437.9)	$(3^+,4)$	0.50	0.46	100.0	0.749	0.749	0.285	0.285
(2422.2)	$(0,2,3,4)$	0.49	0.30	100.0	0.749	0.749	0.285	0.285
2372.7	$(2,3^+)$	1.16	1.16	100.0	1.000	0.500	1.000	−0.667
2322.2	$(2,3)^+$	0.53	0.66	100.0	0.895	0.350	0.883	−0.667
2285.4	1	0.30	0.10	100.0	0.592	−0.172	0.000	0.000
2229.6	$(3,4)^+$	1.38	1.01	99.2	0.828	0.828	0.418	0.418
2020.5	$(2,3)^+$	3.04	2.40	100.0	1.000	0.500	1.000	−0.667
1976.0	4^+	1.76	1.79	83.1	0.749	0.749	0.285	0.285
1944.3	3^-	12.22	10.25	100.0	0.826	0.822	0.415	0.411
1891.7	3^+	2.76	2.66	97.2	0.828	0.773	0.418	0.338
1863.0	2^+	2.92	3.08	100.0	0.934	0.405	0.926	−0.667
1702.6	4^+	1.94	2.56	84.6	0.728	0.672	0.258	0.201
1517.2	$(0)^+$	0.71	0.70	100.0	0.000	0.000	0.000	0.000
1481.9	2^+	5.78	5.36	99.8	0.817	0.254	0.766	−0.628
1206.2	4^+	5.59	7.24	55.2	0.711	0.624	0.242	0.150
1150.6	2^+	6.87	7.23	98.0	0.603	0.235	0.491	−0.459
957.3	0^+	0.00	0.00	99.9	0.000	0.000	0.000	0.000
605.6	2^+	37.76	39.47	91.9	0.561	0.281	0.463	−0.302
0.0	0^+	0.00	0.00	92.3	0.000	0.000	0.000	0.000

Table 5.3. Energy and spin assignments to levels observed in ^{118}Te following $^{118}I^g$ decay. Level energies that are in brackets denote uncertainty in the placement of that level. Relative β-feed intensities, deduced from equation (5.1), are also given. The parental *low* spin character of each level is given for the ^{32}S experiment (in %), along with values of U_λ^{min} and U_λ^{max}, evaluated using UACALC.

Level	Spin	$I_\beta(^{32}S)$	$I_\beta(^{34}S)$	$\Re^h(^{32}S)$	U_2^{max}	U_2^{min}	U_4^{max}	U_4^{min}
(3399.4)	$(7,8,9)^+$	2.10	0.95	100.0	1.000	0.946	1.000	0.821
(3191.0)	$(5,6,7)^+$	3.34	2.17	100.0	1.000	0.946	1.000	0.821
3168.2	$(6,8)^+$	3.58	3.61	100.0	0.969	0.969	0.897	0.897
(3114.0)	(5,6,7,8)	1.61	1.56	100.0	1.000	0.946	1.000	0.821
3107.8	$(5,6)^+$	2.72	3.00	100.0	0.929	0.929	0.772	0.772
3078.7	$(5,6)^+$	28.17	29.35	100.0	0.929	0.929	0.772	0.772
3000.0	$(7^-,8^+)$	2.96	2.22	100.0	1.000	0.946	1.000	0.821
(2967.8)	$(5,6,7)^+$	10.62	3.95	100.0	1.000	0.946	1.000	0.821
2920.0	7^+	3.46	3.34	100.0	1.000	0.946	1.000	0.821
2913.9	6^+	24.46	22.63	100.0	0.952	0.918	0.846	0.762
(2730.6)	(5^+)	0.99	1.39	100.0	0.929	0.929	0.772	0.772
(2696.9)	(5,6,7,8)	4.08	4.11	100.0	1.000	0.946	1.000	0.821
2573.7	8^+	0.99	1.45	100.0	0.976	0.881	0.922	0.646
(2531.4)	(5)	2.72	1.89	100.0	0.929	0.929	0.772	0.772
2517.0	$(5,6)^+$	3.71	3.56	100.0	0.925	0.891	0.763	0.679
2368.2	5^+	2.35	1.83	100.0	0.929	0.908	0.772	0.713
2229.6	$(3,4)^+$	0.00	0.00	0.8	0.789	0.789	0.419	0.419
(2225.3)	$(5,6,7)^+$	1.11	1.11	100.0	1.000	0.946	1.000	0.821
2149.9	6^+	0.00	2.95	100.0	0.919	0.795	0.750	0.423
1976.0	4^+	0.00	0.00	16.9	0.857	0.826	0.580	0.523
1891.7	3^+	0.00	0.00	2.8	0.789	0.771	0.419	0.388
1820.5	6^+	3.71	9.95	100.0	0.900	0.797	0.697	0.442
1702.6	4^+	0.00	0.00	15.4	0.844	0.682	0.552	0.211
1481.9	2^+	0.00	0.00	0.2	0.643	0.546	0.167	0.084
1206.2	4^+	0.00	0.00	44.8	0.808	0.710	0.475	0.291
1150.6	2^+	0.00	0.00	2.0	0.561	0.456	0.097	0.011
957.3	0^+	0.00	0.00	0.1	0.000	0.000	0.000	0.000
605.6	2^+	0.00	0.00	8.1	0.586	0.515	0.132	0.082
0.0	0^+	0.00	0.00	7.7	0.000	0.000	0.000	0.000

Table 5.4. Energy and spin assignments to levels observed in ^{118}Te following $^{118}I^m$ decay. Level energies that are in brackets denote uncertainty in the placement of that level. Relative β-feed intensities, deduced from equation (5.1), are also given. The parental *high* spin character of each level is given for the ^{32}S experiment (in %), along with values of U_λ^{min} and U_λ^{max}, evaluated using UACALC.

In both experiments, axial/equatorial γ-ray anisotropies, $\{W(0)/W(90) - 1\}\%$, were measured (as a function of temperature) using two independent pairs of detectors, with the quoted anisotropies being averaged between the two pairs. The solid angle correction factors, Q_λ, used in the analysis of these anisotropies, correspond to values obtained from the program QK (for the relevant detector). Temperature determination was performed using a standard ^{57}Co$\underline{Fe}$ thermometer.

For each temperature dependence, the least-squares fitting procedure used is based on the simple two-site model. The term $\mu^{l,h}B_{eff}$ is a parameter in fit, where $\mu^{l,h}$ refers to the moment of the low or high spin isomer (dependent on the parentage of the observed γ-ray). The hyperfine field for I$\underline{Fe}$ has been measured as +114.5T [9] , which combined with an applied field of +0.7T gives an effective field, B_{eff} = +115.2T, using equation (1.57).

5.4.2 The $^{118}I^g$ experiment

The latter two *moment* experiments listed in Table 5.1 used ^{34}S and ^{32}S beams respectively. The first of these resulted in a poor yield of the low spin isomer, with only the 605.6 keV transition providing good temperature dependent data. In the second experiment a stronger source strength enabled usable anisotropy data to be obtained for additional low spin transitions at energies of 1150.6 and 1338.7 keV. Taking the spin of $^{118}I^g$ as 2^- [3] , fits to the various temperature dependences obtained will now be discussed.

1338.7 *keV* : $3_1^- \rightarrow 2_1^+$

This transition is identified clearly as E1 in this work (see chapter 6.2.1 for details), and its anisotropy temperature dependence is shown in [Fig 5.5] . The results of a least-squares fit yield the following parameters (a * refers to a parameter which has been varied).

^{32}S	$\chi^2_\nu = 1.37$	$^*\mu^l = 1.94(16)$	$^*fU_2 = 0.653(33)$	$fU_4 = 0$

Taking a value of $U_2 = 0.822(1)$ for this transition from Table 5.3, gives a fraction in good sites, $f = 79(4)\%$.

1150.6 *keV* : $2_2^+ \rightarrow 0_1^+$

This is an E2 ground state transition, for which the small high spin component $(2-4\%)$ is neglected in this analysis (due to the large experimental errors). The fit to the temperature dependence shown in [Fig 5.5] gives the parameters,

^{32}S	$\chi^2_\nu = 0.41$	$^*\mu^l = 2.0(5)$	$^*fU_2 = 0.31(6)$	$fU_4 = 0.1$

In this fit the value of fU_4 is set at a value of 0.1 on the basis of the value $U_4 = 0.12(7)$, obtained from the spectroscopy experiments (see chapter 6.2.1). The errors quoted on the above parameters take into account an *uncertainty* in fU_4 of ± 0.1. Taking $U_2 = 0.355(20)$ from chapter 6.2.1, gives a fraction in good sites, $f = 87(18)\%$.

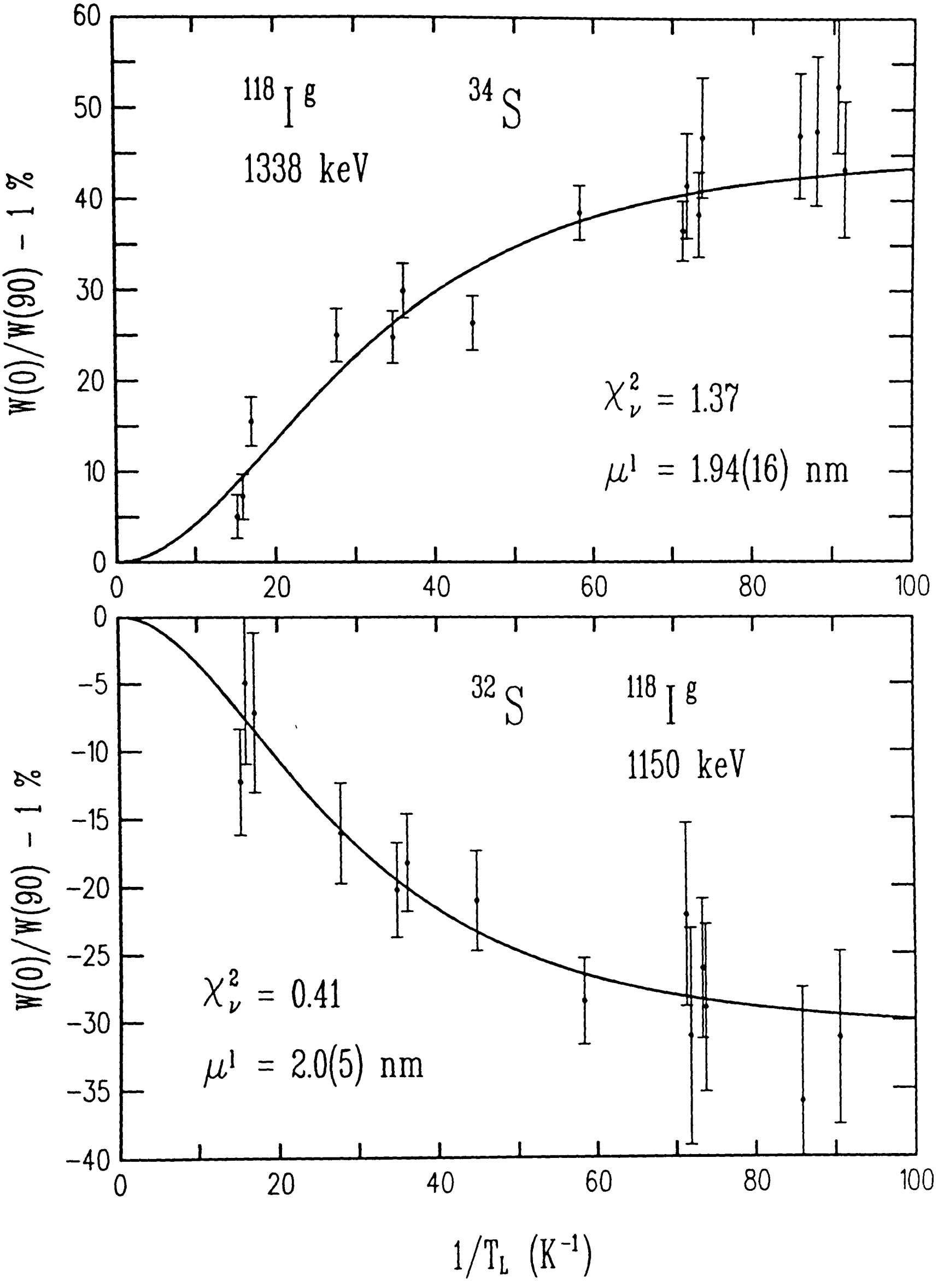

Figure 5.5. Anisotropies for the 1338.7 and 1150.6 keV transitions seen in the decay of $^{118}I^g$

605.6 *keV* : $2_1^+ \rightarrow 0_1^+$

This is the strongest transition observed in ^{118}I decay, being from the lowest 2^+ state to the ground state. However, it is not a *pure* low spin transition, and for the ^{34}S and ^{32}S experiments high spin components to this transition may be calculated to be 18% and 8% respectively. The main source of this high spin feeding comes from the 614.3 and 943.8 keV transitions, and their effects are simple to eliminate by *subtraction* of their combined peak areas from the peak area of the 605.6 keV transition, using equation (6.1).

The anisotropy data shown in [Fig 5.6] for the ^{34}S and ^{32}S experiments were calculated using the above mentioned *subtracted* peak areas. Least-squares fits yield the parameters,

^{34}S	$\chi^2_\nu = 0.68$	$^*\mu^l = 1.96(11)$	$^*fU_2 = 0.300(20)$	$fU_4 = 0.1$
^{32}S	$\chi^2_\nu = 1.74$	$^*\mu^l = 1.86(7)$	$^*fU_2 = 0.362(15)$	$fU_4 = 0.1$

In these fits the value of fU_4 is set at a value of 0.1 on the basis of the measured value of $U_4 = 0.135(36)$, obtained from the spectroscopy experiments. The errors quoted on the fitted parameters allow for an *uncertainty* of ± 0.05 in fU_4. Taking $U_2 = 0.419(12)$ from chapter 6.2.1, gives fractions in good sites of 72(5)% and 86(4)% for the ^{34}S and ^{32}S experiments respectively.

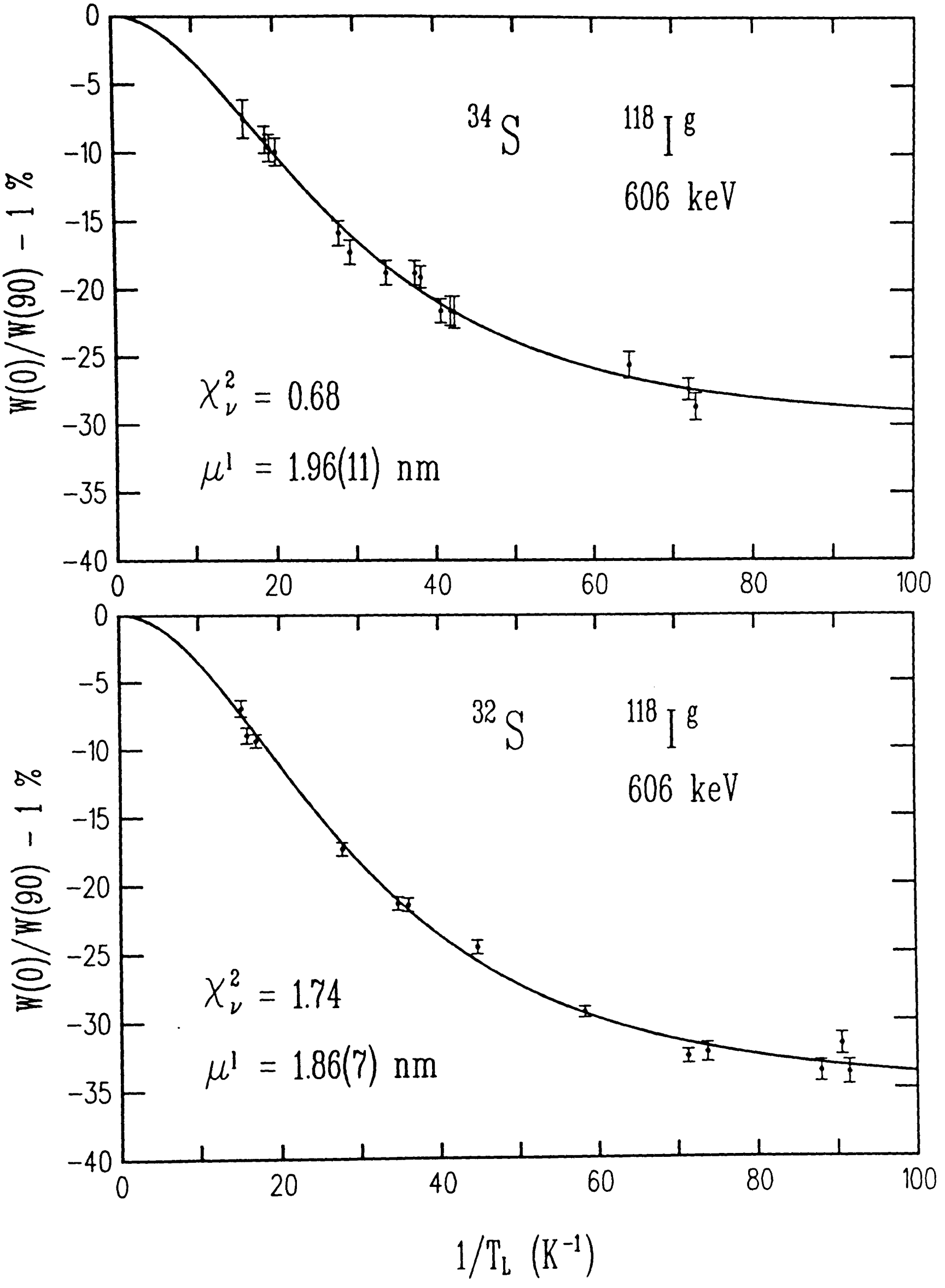

Figure 5.6. Anisotropy data for the 605.6 keV transition seen in the decay of $^{118}I^{g}$, for experiments using ^{34}S and ^{32}S beams.

5.4.3 The $^{118}I^m$ experiment

In both the ^{34}S and ^{32}S experiments reasonable yields of the high spin isomer were obtained, giving data of comparable statistical quality. Anisotropies were measured for the $6^+ \rightarrow 4^+$ high spin transitions at energies of 614.3 and 943.8 keV. Taking the spin of $^{118}I^m$ as 7^- [10] , the resulting fits to the observed temperature dependences will now be discussed.

<u>614.3 *keV* : $6_1^+ \rightarrow 4_1^+$</u>

This is the strongest transition observed in $^{118}I^m$ decay, and as it is also E2, it is easily the most suitable candidate for this type of measurement. The anisotropy temperature dependent data are shown in [Fig 5.7] for the ^{34}S and ^{32}S experiments. Least-squares fits to these data give the parameters,

^{34}S	$\chi^2_\nu = 0.80$	$f = 78(8)\%$	$^*\mu^h = 4.11(26)$
^{32}S	$\chi^2_\nu = 0.34$	$f = 90(9)\%$	$^*\mu^h = 4.54(30)$

where the values $U_2 = 0.85(5)$ and $U_4 = 0.57(13)$ have been taken from Table 5.4. The uncertainties in these calculated de-orientation coefficients have been taken into consideration in the errors quoted for the fitted parameters.

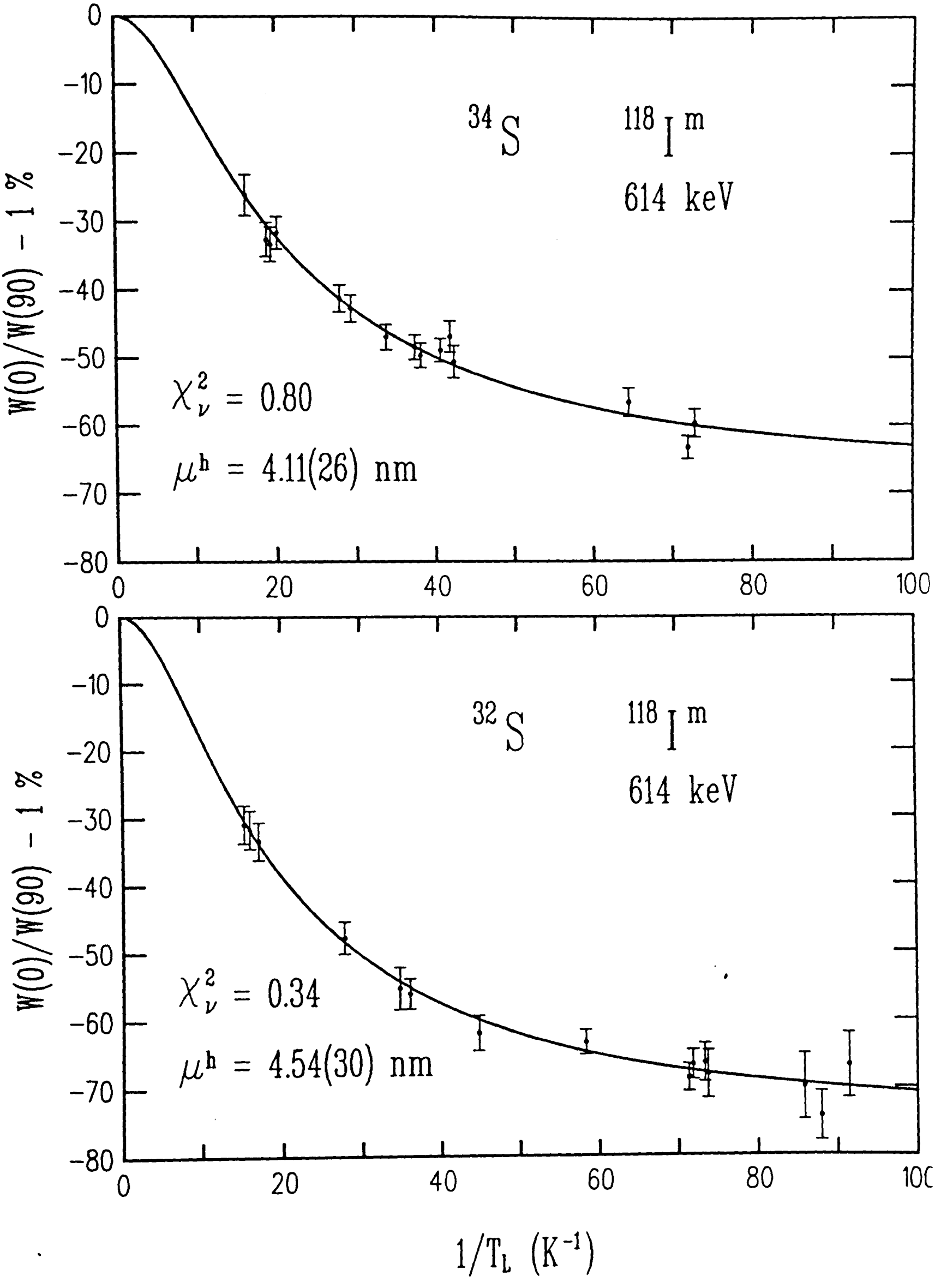

Figure 5.7. Anisotropy data for the 614.3 keV transition seen in the decay of $^{118}I^{g}$, for experiments using ^{34}S and ^{32}S beams.

$943.8\ keV\ :\ 6_2^+ \rightarrow 4_1^+$

This is the second strongest E2 transition observed in the decay of $^{118}I^m$. The anisotropy data are shown in [Fig 5.8] for the ^{34}S and ^{32}S experiments, and results of the corresponding least-squares fits give the parameters,

^{34}S	$\chi^2_\nu = 0.53$	$f = 72(10)\%$	$^*\mu^h = 4.3(9)$
^{32}S	$\chi^2_\nu = 0.72$	$f = 84(12)\%$	$^*\mu^h = 4.0(9)$

In these fits the values $U_2 = 0.86(6)$ and $U_4 = 0.59(16)$ have been taken from Table 5.4. The uncertainties in these calculated values have been taken into account in the quoted errors for the above parameters.

5.4.4 Discussion

As stated earlier, all the temperature dependence data for the various transitions observed in ^{118}I decay have been analysed in terms of the 2-site model (see chapter 1.2.6). The results of the fits performed in the previous subsections for the low and high spin transitions are now summarized in Table 5.2, in terms of the values of f and μ derived.

The values for the low and high spin magnetic moments of ^{118}I, listed in Table 5.5 are consistent for the different transitions considered in each case. Taking a weighted mean for each set of values gives the following results,

$$\langle \mu^l \rangle_{av} = 1.90(6)\text{nm}$$
$$\langle \mu^h \rangle_{av} = 4.28(19)\text{nm} \qquad (5.6)$$

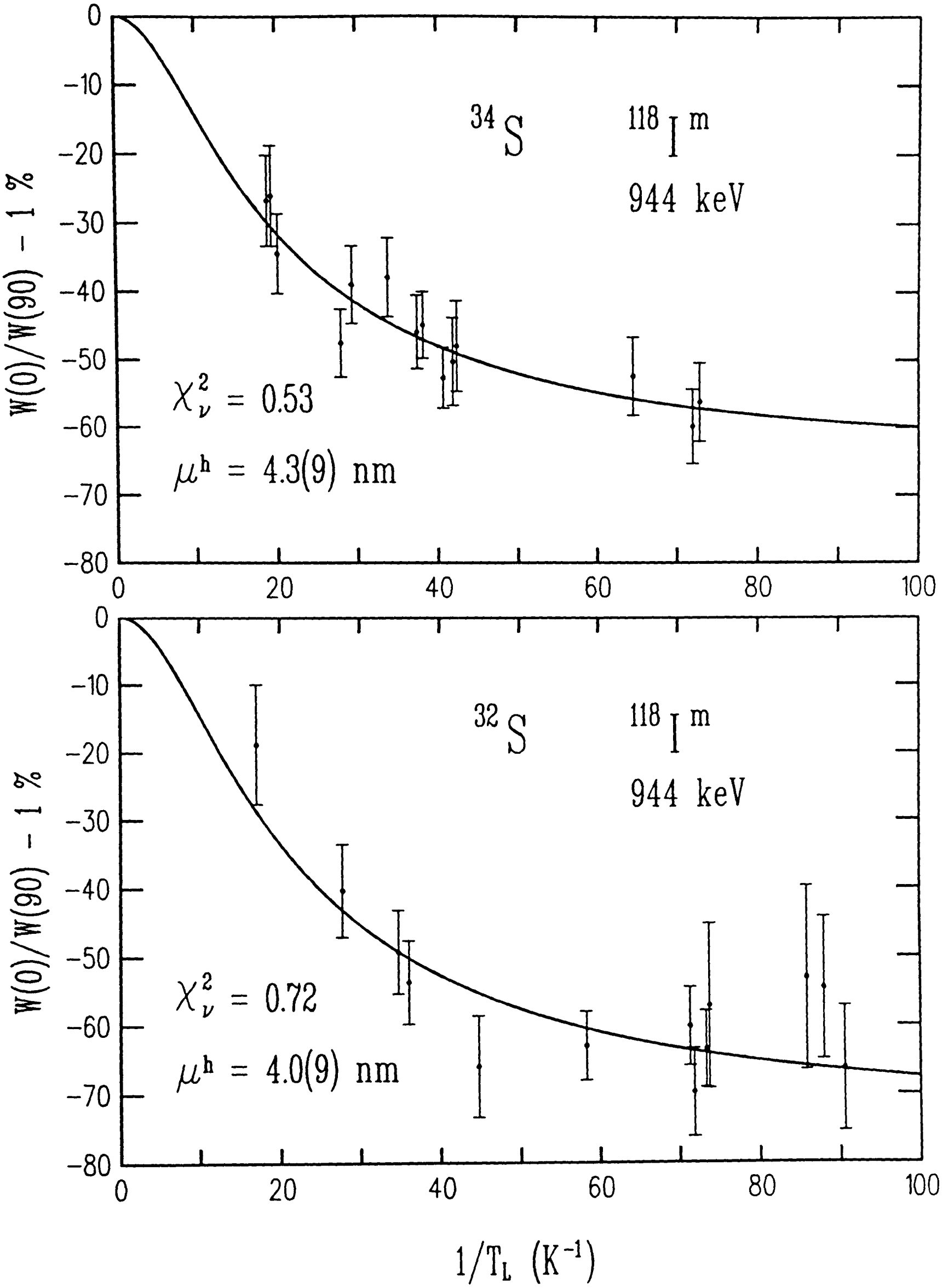

Figure 5.8. Anisotropy data for the 943.8 keV transition seen in the decay of $^{118}I^{g}$, for experiments using ^{34}S and ^{32}S beams.

Isotope	E_γ	$I_i \rightarrow I_f$	Deduced f	Fitted $\|\mu\|$
$^{118}I^g$ (2^-)	1338.7	$3_1^- \rightarrow 2_1^+$	79(4) %	1.94(16)nm
$B_{hf} = 114.5$T	1150.6	$2_2^+ \rightarrow 0_1^+$	87(18)%	2.0(5) nm
	605.6	$2_1^+ \rightarrow 0_1^+$	*72(5) %	*1.96(11)nm
			86(4) %	1.86(7) nm
$^{118}I^m$ (7^-)	614.3	$6_1^+ \rightarrow 4_1^+$	*78(8) %	*4.11(26)nm
$B_{hf} = 114.5$T			90(9) %	4.54(30)nm
	943.8	$6_2^+ \rightarrow 4_1^+$	*72(10)%	*4.3(9) nm
			84(12)%	4.0(9) nm

Table 5.5 Summary of temperature dependence data for ^{118}I. The values obtained in the two different experiments are distinguished by use of a * to denote those from the ^{34}S experiment.

These are slightly different from the earlier published values[10] and the reason for this is that the present results were obtained using the MINUIT package, which was not available when the data were first analysed. However, these slightly modified values do not alter the conclusions reached in these earlier publications[10] .

It is interesting to compare the fractions in good sites obtained in the above two experiments. Taking values from Table 5.5, the following results may be deduced, for the ^{34}S experiment,

$$\langle f \rangle_{av} = \begin{cases} 72(5)\% & \text{low spin } (^{34}\text{S}) \\ 76(6)\% & \text{high spin } (^{34}\text{S}) \end{cases} \tag{5.7}$$

and the ^{32}S experiment,

$$\langle f \rangle_{av} = \begin{cases} 83(3)\% & \text{low spin } (^{32}\text{S}) \\ 88(7)\% & \text{high spin } (^{32}\text{S}) \end{cases} \tag{5.8}$$

It can be seen that the low and high spin fractions are consistent for each separate experiment, but that f is $\sim$ 10% higher in the ^{32}S experiment. This

indicates that the surface quality of the implantation foil was somewhat better in this later experiment, but it is reassuring to note that the fitted moments are consistent between the two experiments.

Now that the magnetic moments have been determined it is possible to show that relaxation times are not a problem for these isotopes. From the tabulation of relaxation time measurements by Klein [11] , a value of $C_k T_{int}^2 = 2.35 \times 10^{-4}$ may be deduced for I*Fe*. Using this value along with the above B_{hf} and $\mu^{l,h}$, empirical relaxation times of 5s (low spin) and 6s (high spin) may be estimated (from equation (2.23)). These short relaxation times mean that in a continuous implantation experiment ^{118}I will show full thermal equilibrium effects.

5.5 LTNO spectroscopic measurements

5.5.1 Experimental details

As shown in Table 5.1, two experiments have been performed, and in both cases γ-ray anisotropies were measured using four Ge(Li) detectors (8cm from the sample) placed along (*axial*) and perpendicular (*equatorial*) to the orientation axis, as described in chapter 3.3.3. The first experiment consisted of running for 4 hours warm and 4 hours at a base temperature of only 26mK, due to problems with the refrigerator. An on-line temperature of 15mK was attained in the second experiment, in which 8 hours warm and 8 hours cold data were taken. In addition, 2 hours data were taken at an intermediate temperature of 32mK.

γ-ray intensities were deduced from a ^{152}Eu source, attached to a cold finger and loaded into the refrigerator afterwards, in as close a position to the

actual source position as possible. The LTNO data from these two experiments are, in general, in very good agreement. However, the second experiment produced much the better data, not only because of the longer running time (with detectors of generally better resolution), but also because of a stronger and steadier accelerator beam ($\sim$ 40pnA of ^{32}S). The data and results presented here are those from this second experiment. In [Fig 5.9] cold (15mK) axial and equatorial spectra are shown for comparison.

In addition to the standard nuclear orientation setup (used above and in the magnetic moment measurements described in the previous section), γ-ray linear polarizations were also measured using a three detector polarimeter (see chapter 3.6.2), with a vertical *scatterer* (of volume 60cm^3), and two horizontal *analysers* (of volume 150cm^3 each). The distance between the centre of the *scatterer* and the front front face of each *analyser* was $\sim$ 5cm.

Coincidence between pulses in the *scatterer* and the *analysers* were recorded in both experiments as summed coincidence spectra. In the latter experiment, coincidence data were also stored event-by-event on magnetic tape (giving a total of 5×10^6 events). This allowed both timing and kinematic gates to be used in the subsequent analysis.

5.5.2 Extraction of $W(0)$ and $W(90)$

In the section 5.4, the magnetic moments of $^{118}I^g$ and $^{118}I^m$ were deduced from the temperature dependence of axial/equatorial intensity ratios for well known transitions. However, in order to extract spectroscopic information for the weaker, less well known transitions, it is necessary to measure *separate* axial $\{W(0) - 1\}$ and equatorial $\{W(90) - 1\}$ anisotropies, which then allows the extraction of the $\lambda = 2$ and $\lambda = 4$ terms (see chapter 4.3.6).

The method of separating the axial and equatorial effects (described in chapter 4.3.1) relies upon a knowledge of the relative strength of the source

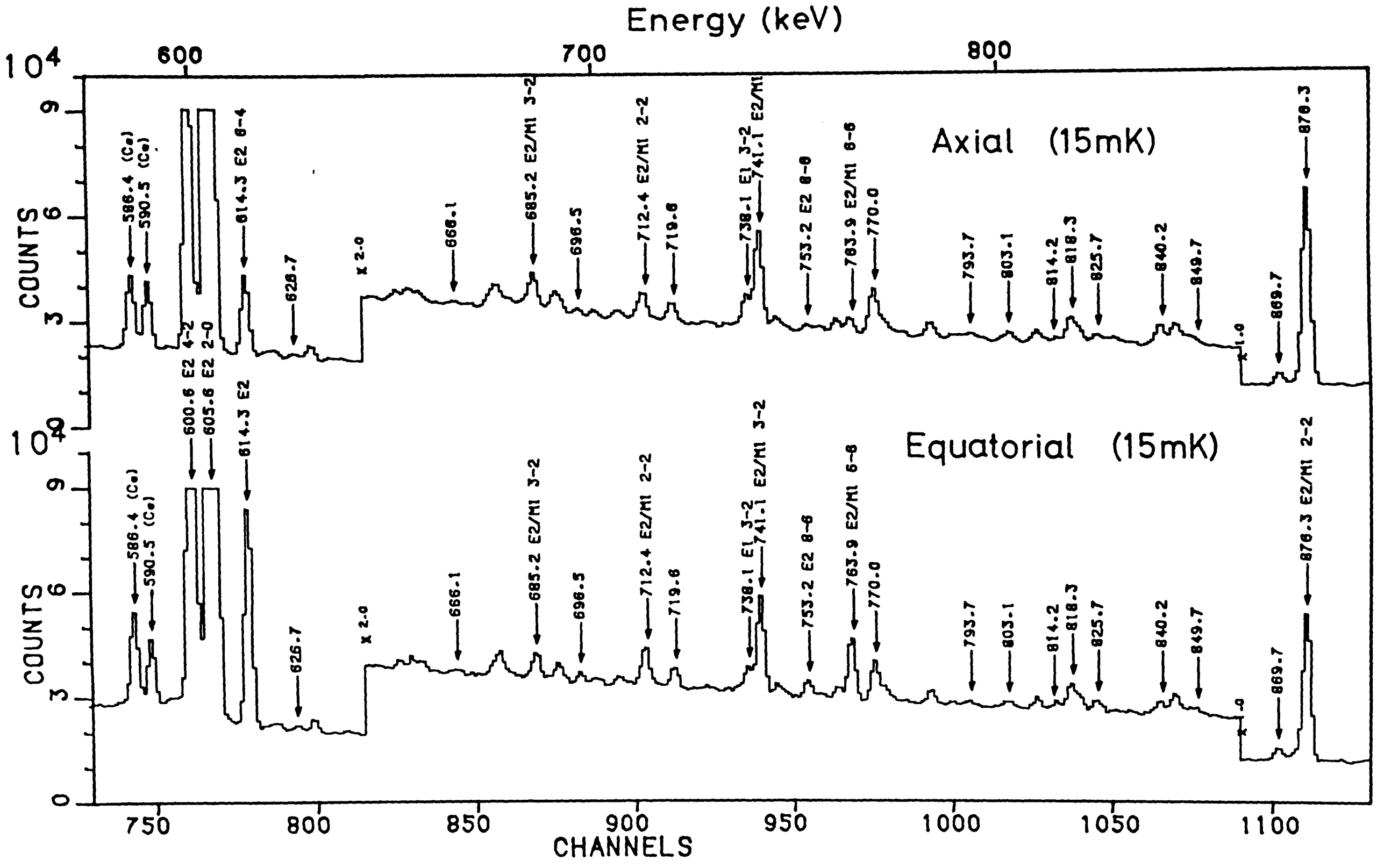

Figure 5.9. Comparison of axial and equatorial cold (15mK) spectra.

during the cold and warm implantations. This relative source strength may well vary for isotopes of different half-lives, due to their differing responses to fluctuating implantation rates. In the following analysis, normalization factors have been deduced using *known* transitions in the relevant isotopes (for which $W(0)$ and $W(90)$ can be predicted). Two such transitions were considered for $^{118}I^{g}$ and one for $^{118}I^{m}$, and the normalization parameters used are given in Table 5.6.

Isotope	$\|\mu\|$	E_γ **(keV)**	f	U_2	U_4
$^{118}I^{g}$	1.90(6) nm	351.7 $(0_2^+ \rightarrow 2_1^+)$		0.0	0.0
		1338.7 $(3_1^- \rightarrow 2_1^+)$	80(2)%	0.822(1)	
$^{118}I^{m}$	4.28(19)nm	614.3 $(6_1^+ \rightarrow 4_1^+)$	90(9)%	0.85(5)	0.57(13)

Table 5.6 Normalization parameters for *known* lines in $^{118}I^{g+m}$ decay.

The moments μ and de-orientation coefficients U_λ quoted are taken from the previous section. Using these parameters, the fractions in good sites f given in Table 5.6 were derived from the 1338.7 keV (low spin) and 614.3 keV (high spin) transitions, using their axial/equatorial anisotropies at the two different temperatures, T_L, given below,

$$1/T_L = \begin{cases} 68.5(1.0) & \text{base (15mK)} \\ 31.0(1.0) & \text{intermediate (32mk)} \end{cases}$$

as measured with a standard $^{57}Co\underline{Fe}$ nuclear orientation thermometer. The quoted errors on f reflect the uncertainties in the de-orientation coefficients. For the four detectors used, the solid angle correction factors were taken as $\overline{Q_2} = 0.96(1)$ and $\overline{Q_4} = 0.89(2)$, over the γ-ray energies considered.

E_γ	$W_{norm}(0)$	$R_c^w(0)$ AD1	$R_c^w(0)$ AD2	$W_{norm}(90)$	$R_c^w(90)$ AD3	$R_c^w(90)$ AD4
351.7	0.0	1.05(1)	1.05(2)	0.0	1.07(2)	1.09(2)
	0.0	6.4(1)	6.5(2)	0.0	6.6(2)	6.6(3)
1338.7	23.5(4)	1.060(5)	1.074(6)	−11.7(2)	1.070(5)	1.061(7)
	14.2(4)	6.44(5)	6.41(6)	−7.1(2)	6.46(6)	6.47(7)
614.3	−60(2)	1.05(6)	1.08(6)	21(1)	1.07(1)	1.07(1)
	−42(2)	6.6(3)	6.8(3)	17(1)	6.43(8)	6.32(9)

Table 5.7 Normalization ratios for the four individual detectors (AD1–4). The upper and lower figures for each transition correspond to implantation at 15mK and 32mK respectively.

Using the above parameters for the three normalization lines , the program WTHETA was then used to calculate normalization ratios, using equation (4.9), for each detector individually. The values obtained are shown in Table 5.7.

The very good agreement between these ratios for the 351.7 and 1338.7 keV transitions, over the four detectors, serves as a consistency check for this method of analysis. Moreover, the agreement with the 614.3 keV ratios is also very good, implying that the warm and cold implantation rates were very stable (which was not the case during the Dec 84 experiment). Thus, the 1338.7 keV transition was chosen to normalize *both* high and low spin transitions, as it gives the more precise normalization ratios. Using this normalization line, separate anisotropies were calculated for each detector, and then the results averaged over each pair of axial and equatorial detectors. These anisotropies are listed in Table 5.2.

From a knowledge of $W(0)$ and $W(90)$, the parameters $fB_\lambda Q_\lambda U_\lambda A_\lambda$ were then extracted for $\lambda = 2, 4$, using the program K24, which solves two simultaneous linear equations for the two required parameters (see chapter 4.3.6).

The parameters f, B_λ, $\overline{Q_\lambda}$ (where $\overline{Q_\lambda}$ are solid angle correction factors, averaged over the detectors used and the γ-ray energies considered) are the same for each transition, and depend only on their high/low spin character. Values of the products $fB_\lambda\overline{Q_\lambda}$ are given in Table 5.8, for the base and intermediate temperature measurements.

Isotope	T_L (mK)	$fB_2\overline{Q_2}$	$fB_4\overline{Q_4}$
$^{118}I^g$	15	0.828(16)	0.134(11)
	32	0.500(29)	0.034(26)
$^{118}I^m$	15	1.451(81)	0.900(53)
	32	1.101(65)	0.380(32)

Table 5.8 Orientation parameters for $^{118}I^{g+m}$.

Using the appropriate values of $fB_\lambda\overline{Q_\lambda}$, the products $U_\lambda A_\lambda$ for many high and low transitions have been calculated, average values being quoted for the measurements at the two different temperatures. These results are given in Tables 6.1 (low spin) and 6.7 (high spin), and are discussed in more detail in the next chapter.

5.5.3 Linear Polarization Data

In the second of the two spectroscopy experiments, polarization data were taken and stored event-by-event, which after subsequent sorting, considerably improved the quality of the final polarization spectra, compared with those obtained in the first experiment. The event-by-event sorting allowed the spectra to be carefully gain-matched before summing (thus optimizing the resolution of the resulting polarization spectra), and also allowed timing and kinematic gates

to be set (see chapter 4.4 for details of the general procedure). The TAC and and kinematic spectra, with the gates used, are shown in [Fig 5.10] for one *arm* of the polarimeter (the other arm being very similar).

TAC spectra for both scatterer-analyser pairs showed very good timing resolution ($\sim$ 12ns) and two gates were tried (wide and narrow), which are shown in [Fig 5.10] . Due to large errors in the measured polarization asymmetry, it was not possible to distinguish between these two gates. The kinematic spectrum clearly shows regions of inverse, normal and multiple scattering processes, and the gate shown selects primarily the normal processes. In fact, the kinematic spectrum shown is gated using the wide TAC gate, and this was found to considerably reduce the multiple scattering region of the spectrum.

Having obtained the sorted polarization spectra, polarization asymmetries, Δ_{exp} (as defined in chapter 4.4.2), were then evaluated for the stronger transitions. [Fig 5.11] shows an efficiency calibration curve for three-detector polarimeter [12], very similar to the one used in this experiment. The data points shown are polarization efficiencies deduced for transitions of known multipolarity observed with the present polarimeter (for ^{118}Te and ^{120}Te [13]).

This efficiency curve has been used to convert the measured polarization asymmetries to the polarization values quoted in Table 5.2. An example of a polarization plot is shown in [Fig 5.11] for the 1338.7 keV normalization line. The sign of the experimental asymmetry gives an unambiguous solution for the mixing ratio ($\delta(M2/E1) = 0$ in this case). Comparison of the experimental asymmetry with the theoretical polarization, given by the intersection of P_{cal} and P_{cal}^{NO} (see chapter 1.3) at $\delta = 0$, gives the polarization efficiency.

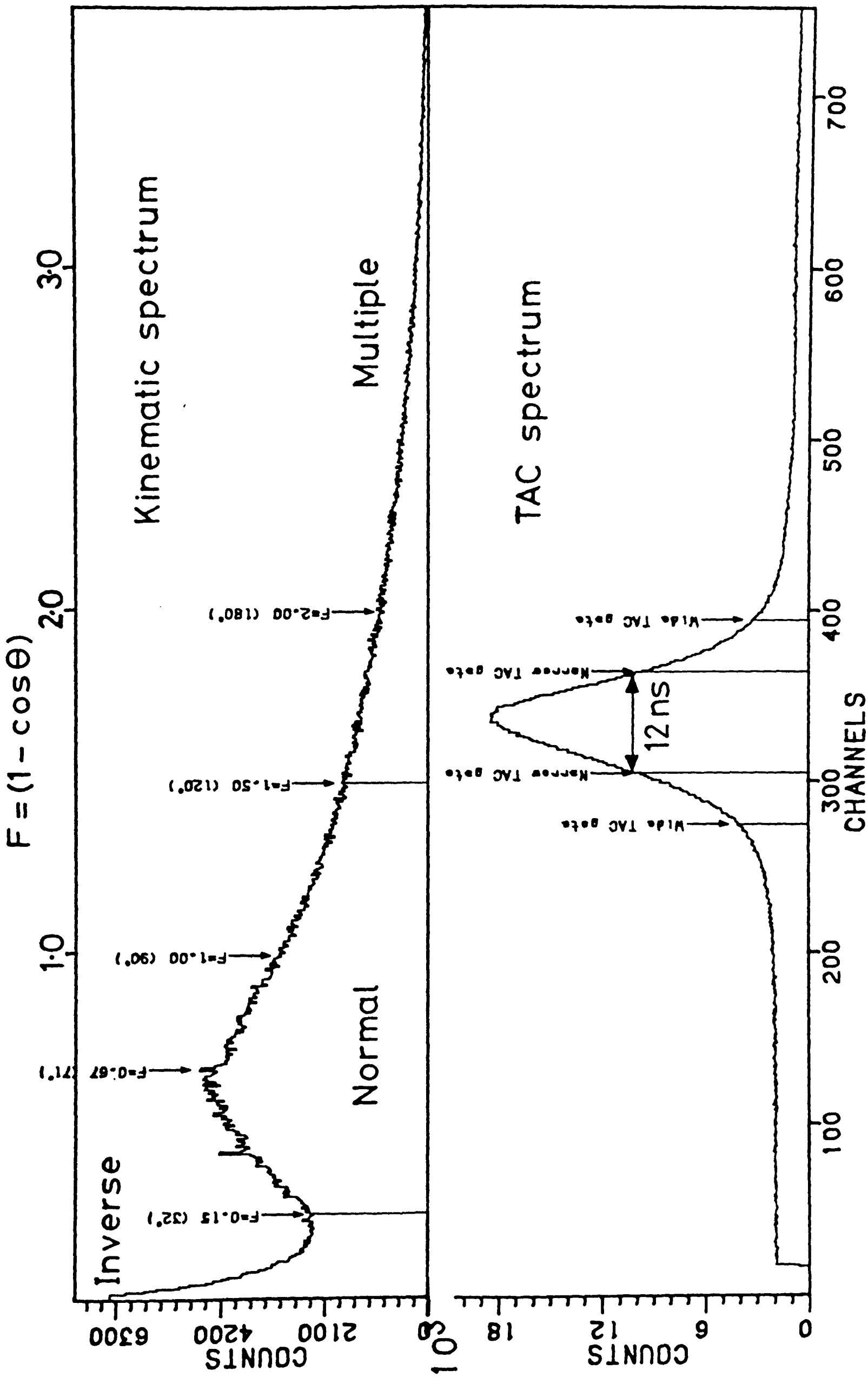

Figure 5.10. TAC and kinematic spectra showing the gates used to obtain *summed* polarization spectra, for one *arm* of the polarimeter.

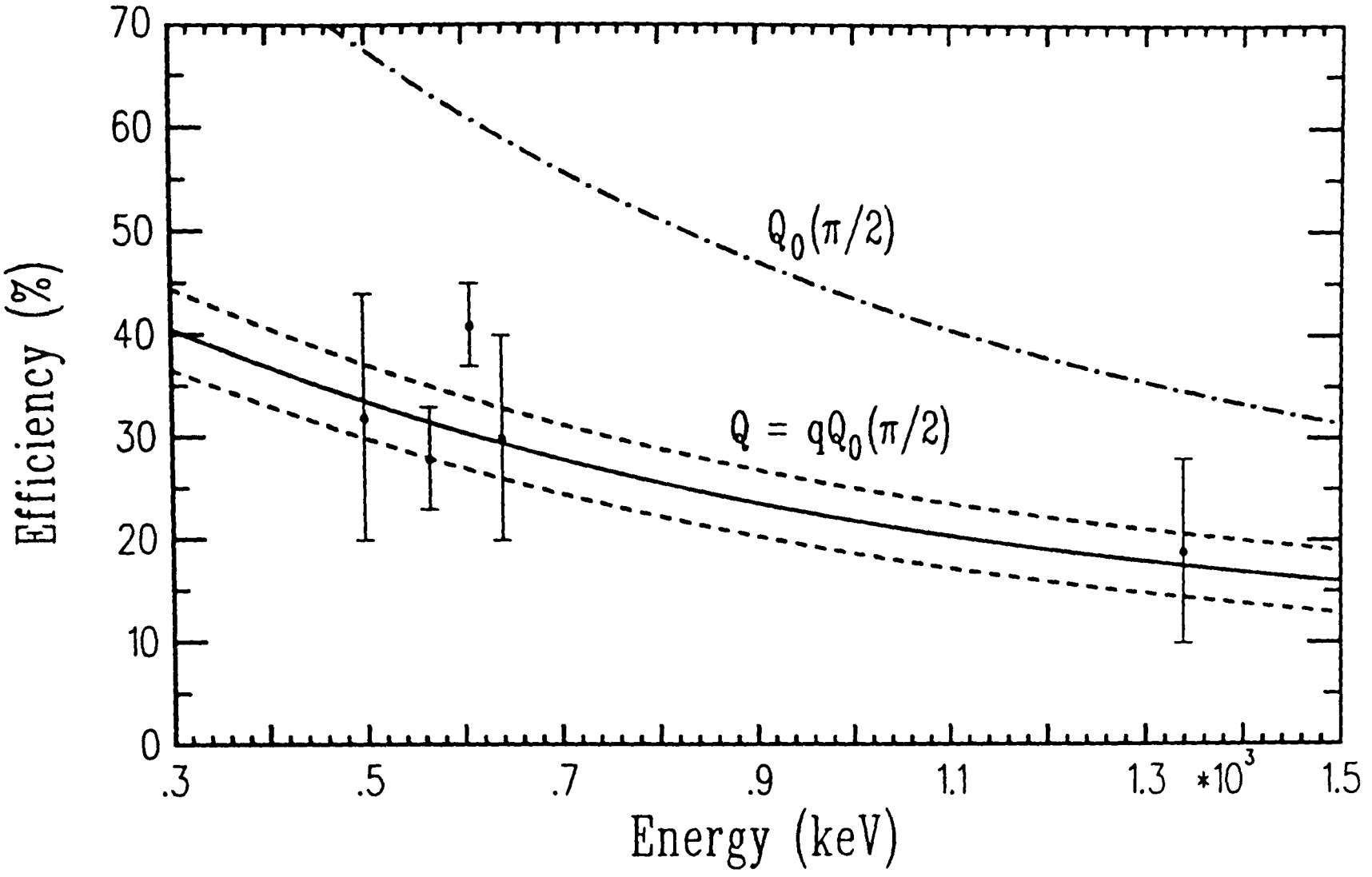

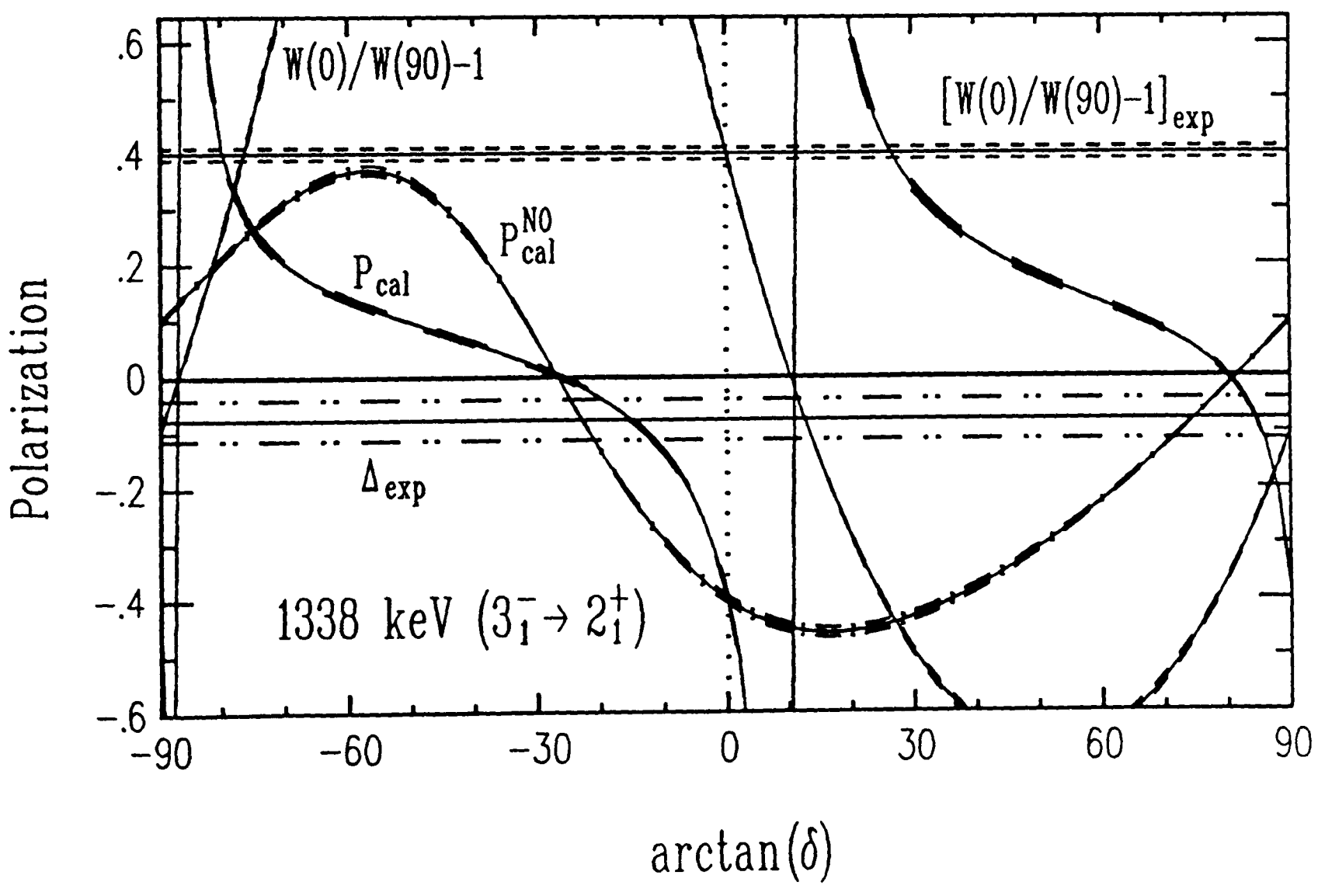

Figure 5.11. Efficiency calibration curve for a typical 3D-polarimeter, with the data points corresponding to polarization efficiencies for known transitions in ^{118}Te and ^{120}Te, along with a polarization plot for the 1338.7 keV E1 transition in ^{118}Te.

5.6 Electron Conversion Measurements

5.6.1 Experimental details

In all, four experiments have been performed on the conversion electron spectroscopy of ^{118}Te, using the mini-orange electron spectrometer and a Ge(Li) detector, set up at the mini-beam line (MBL). The first experiment suffered from problems of contamination of the mass 118 spectra from adjacent masses, and in the second experiment data of poor statistical quality were obtained. However, much improved data were taken in the third and fourth experiments, in which the Si(Li) detector was cooled more efficiently, and gave good energy resolution ($\sim$ 3keV FWHM).

The third experiment was performed using a ^{34}S incident beam, and a tape transport system to filter out the Cs and Xe activities. This resulted in very clean ^{118}I decay spectra, but the total count rate was low and information on weaker lines was poor.

The fourth experiment (performed a few weeks later) made use of a ^{32}S beam, giving a higher yield of mass 118 products, which were studied without use of the tape transport system. This gave data of much better statistical quality ($\sim$ 15$\times$ the total number of counts), but with the added complication of contamination of the spectra due to the presence of ^{118}Cs and ^{118}Xe. The electron spectrum along with the corresponding γ-ray spectrum for the fourth experiment are plotted in [Fig 5.12] .

The Si(Li) detector was energy calibrated using a *thin* ^{207}Bi conversion electron source, and the Ge(Li) detector with a ^{152}Eu source. Efficiency calibration of the system was achieved using transitions in mass 118 decay of known multipole character.

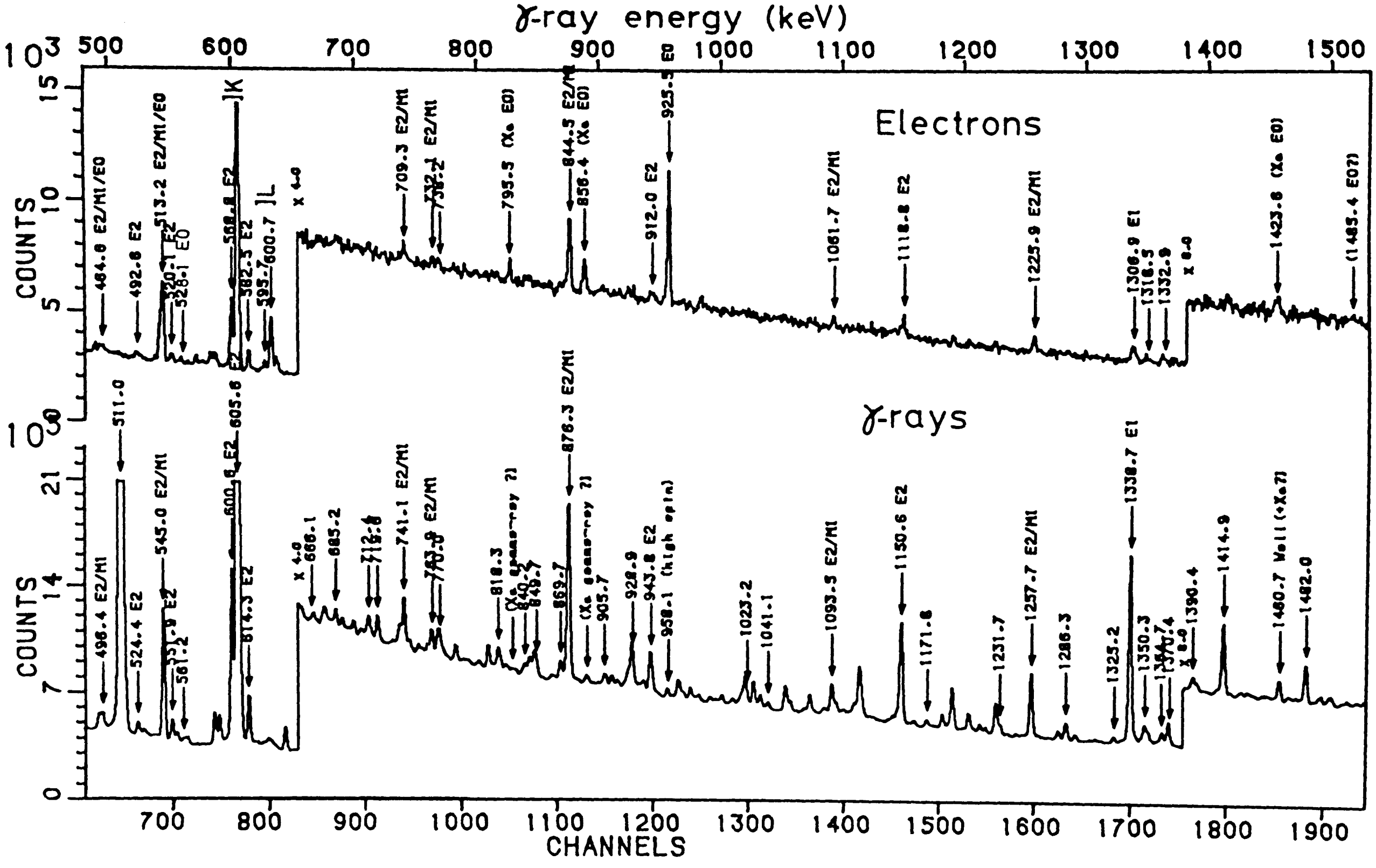

Figure 5.12. Electron and γ-ray spectra obtained in the decay of ^{118}Cs,Xe,I.

5.6.2 Measured conversion coefficients

Conversion coefficients, α_K, were evaluated for the stronger lines using the following internal calibration lines,

^{118}Xe	:	337.4, 472.4 and 586.5 keV
^{118}I	:	149.5 keV
^{118}Te	:	351.7, 600.6, 605.6, 614.3, 943.8, 1150.6 and 1338.7 keV

and the values obtained are listed in Tables 6.1 and 6.7. Comparison of these with theoretical values [14] are shown in [Fig 5.13] . It is clear that the errors are too large to be able to deduce mixing ratios for E2/M1 transitions, but the data is good enough to distinguish between transitions of E1 ($\Delta\pi = -$), and E2/M1 ($\Delta\pi = +$) character.

What is of more interest, however, are E0 transitions which are clearly seen in [Fig 5.12]. An unambiguous signature for an E0 transition linking two 0^+ states is the presence of an electron transition, for which there is no corresponding γ-ray . This is the case for the 925.5 keV transition in [Fig 5.12], which firmly establishes the level at 957.3 keV as 0^+. Two other strong E0 transitions are seen (at 795.5 and 856.4 keV), which have previously been observed in the decay of ^{118}Cs [15]. In a recent experiment performed at DOLIS–COLD on the decay of ^{118}Cs, these results have been confirmed, with also the E0 transition at 1423.6 keV being assigned to this decay.

E0 transitions can also occur when the initial and final spins have equal, but non-zero spin values. Such transitions compete with the usual M1 and E2 radiative decays, and comparison of the E0 and E2 strengths is sensitive to model predictions. A parameter that measures the intensity of the E0 branch relative to the E2 branch may be written in terms of the K-shell electron transition probabilities as [16]

$$X(E0:E2) = 2.54 \times 10^9 A^{4/3} \alpha_K(E2) \frac{E_\gamma^5}{\Omega_K(Z)} \frac{I_e(E0; I_i \rightarrow I_f)}{I_e(E2; I_i \rightarrow I_{f'})} \qquad (5.9)$$

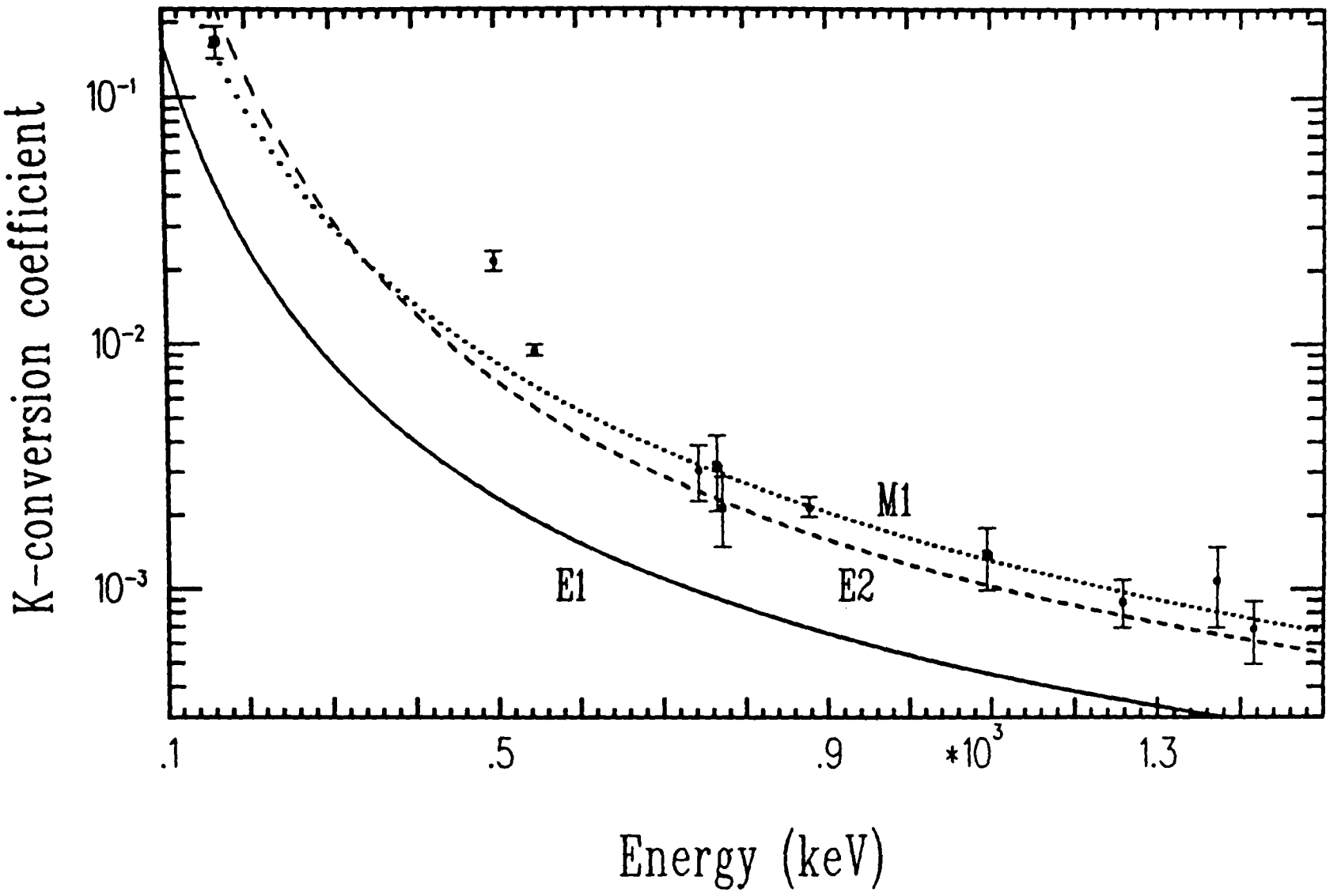

Figure 5.13. Experimental α_K for transitions in ^{118}Te plotted for comparison with the theoretical curves for E1, E2 and M1 transitions.

where $\Omega_K(Z)$ is an electronic factor tabulated by Bell *et al* [17], and $I_f = I_{f'}$ when $I_i = I_f \neq 0$, but $I_{f'} = 2^+$ when $I_i = I_f = 0$. With this definition, X values may be used in all cases involving E0 transitions, and a number of X-factors for ^{118}Te have been calculated, and are given in Table 5.9.

Referring to Table 5.9, the level at 1517.2 keV is taken as 0_3^+, as this spin assignment is the most probable for this level. The values quoted involving the $0_3^+ \rightarrow 0_1^+$ electron transition are upper limits only. There is no well defined peak corresponding to this transition, and the limits were obtained from the maximum possible peak area a transition at this energy could have.

$I_i \to I_f$	$E_i - E_f$	$I_i \to I_{f'}$	$E_i - E_{f'}$	$X(E0:E2)$
$0_2^+ \to 0_1^+$	351.7	$0_2^+ \to 2_1^+$	957.3	0.0093(8)
$0_3^+ \to 0_2^+$	559.9	$0_3^+ \to 2_1^+$	911.6	1.6(5)
$0_3^+ \to 0_1^+$	1517.2	$0_3^+ \to 2_1^+$	911.6	<0.33
$0_3^+ \to 0_2^+$	559.9	$0_3^+ \to 2_2^+$	366.6	0.017(4)
$0_3^+ \to 0_1^+$	1517.2	$0_3^+ \to 2_2^+$	366.6	<0.004

Table 5.9 Experimental $X(E0:E2)$ values for transitions in ^{118}Te.

References

[1] . K.Heyde, P. van Isacker, M.Waroquier, J.L.Wood and R.A.Meyer, Phys. Reports, **102**(1983)291.

[2] . C.M.Lederer and V.S.Shirley, in the Table of Isotopes (7^{th} Ed.) (Wiley,New York,1978).

[3] . G.H.Carlson, W.L.Talbert and S.Raman, Nuclear Data Sheets **17**(1976)1.

T.Tamura, K.Miyano and S.Ohya, Nuclear Data Sheets **51**(1987)329.

[4] . J.J. van Ruyven, W.H.A.Hesselink, J.Akkerman, P. van Nes and H.Verheul, Nucl. Phys. **A380**(1982)125.

[5] . P.Chowdhury, W.F.Fiel Jr. and D.B. Fossan, Phys. Rev. **C25**(1982)813.

[6] . S.P.Collins, private communication (1985).

[7] . I.M.Ladenbauer-Bellis and H.Bakhru, Phys. Rev. **175**(1968)1507.

[8] . T.L.Shaw, V.R.Green, N.J.Stone, J.Rikovska, P.M.Walker, S.Collins, S.A.Hamada, W.D.Hamilton and I.S.Grant, Phys. Lett. **153B**(1985)221.

[9] . D.Visser, L.Niesen, H.Postma and H. de Waard, Phys. Rev. Lett. **41**(1978)882.

[10] . T.L.Shaw, V.R.Green, N.J.Stone, P.M.Walker, W.D.Hamilton, S.Collins, I.S.Grant and J.Rikovska, Hyp. Int. **22**(1985)539.

V.R.Green, N.J.Stone, T.L.Shaw, J.Rikovska, K.S.Krane, P.M.Walker and I.S.Grant, Phys. Lett. **173B**(1986)115.

[11] . E.Klein, in Low-Temperature Nuclear Orientation,
eds. N.J.Stone and H.Postma
(North Holland,Amsterdam,1987) Ch 12.

[12] . J.Rikovska, N.J.Stone and V.R.Green,
Nucl. Instr. and Meth. **241**(1985)461.

[13] . V.R.Green, private communication (1986).

[14] . F.Rõsel, H.M.Fries, K.Alder and H.C.Pauli,
Atomic and Nuclear Data Tables **21**(1978)91.

[15] . J.Genevey-Rivier, A.Charvet, G.Marguier, C.Richard-Serre,
J.D'Auria, A.Huck, G.Klotz, A.Knipper, G.Walter
and the ISOLDE Collaboration, Nucl. Phys. **A283**(1977)45.

[16] . K.Alder and R.M.Steffen, in The Electromagnetic Interaction in
Nuclear Spectroscopy, ed. W.D.Hamilton
(North Holland,Amsterdam,1975)39.

[17] . D.A.Bell, C.E.Aveledo, M.G.Davidson and J.P.Davidson,
Can. J. Phys. **48**(1970)242.

Chapter 6

Level Structure of ^{118}Te

6.1 Introduction

In the previous chapter a full discussion of the experimental techniques and associated methods of data analysis were presented, on the study of the decay of $^{118}I^{g+m} \rightarrow {}^{118}Te$. Comparison of [Fig 5.2] and [Fig 5.3] shows that the $\gamma - \gamma$ coincidence measurements, outlined in chapter 5.2, have established many new levels and transitions in ^{118}Te. A method of separation of this very complex decay scheme into *high* and *low* spin components was described in chapter 5.3, and the first two parts on this chapter are devoted to a detailed discussion of the levels and transitions that have been assigned to the decay of $^{118}I^{g}$ and $^{118}I^{m}$ respectively.

In the final part of the chapter, the low lying levels in ^{118}Te are discussed in terms of IBM-2 calculations that include particle-hole *intruder* excitations, which *mix* with the normal low energy collective excitations. Experimental values obtained for ^{118}Te in this work are compared with the results of these calculations [1] .

6.2 Levels and transitions in ^{118}Te from $^{118}I^{g}$ decay

The level scheme of ^{118}Te populated in the decay of the low spin ^{118}I isomer is shown in [Fig 6.1] . The γ-ray intensities (relative to the 605.6 keV transition) are the *separated* intensities taken from Table 6.1 and averaged over the ^{32}S and ^{34}S experiments. Experimental anisotropies and polarizations are given in Table 5.2, and Tables 5.3 and 6.1 summarize the parameters deduced for individual levels (spins and parities) and transitions ($U_\lambda A_\lambda$ and mixing ratios) respectively. The information summarized in these tables will now be discussed in more detail.

6.2.1 Low spin levels below 2MeV

0.0 *keV* : 0_1^+

Assuming no direct feed, then the population from the low spin isomer is 92.3% in the ^{32}S experiment, to be compared with 82.8% in the ^{34}S experiment. On this basis the high/low spin proportions in each experiment are of order 8% and 21% respectively.

605.6 *keV* : 2_1^+

The 605.6 keV transition to the ground state contains an 8.1% high spin component, the major *pure* high spin feeds being the 614.3 and 943.8 keV transitions (making up 6.6%). They are both essentially stretched E2 transitions, and have the same $U_\lambda A_\lambda$ coefficients as the high spin component in the 605.6 keV transition, which they feed. As a consequence, this high spin component may be removed simply by subtracting the 614.3 and 943.8 keV peak areas (corrected for detector efficiency) from the 605.6 keV peak areas. Assuming the

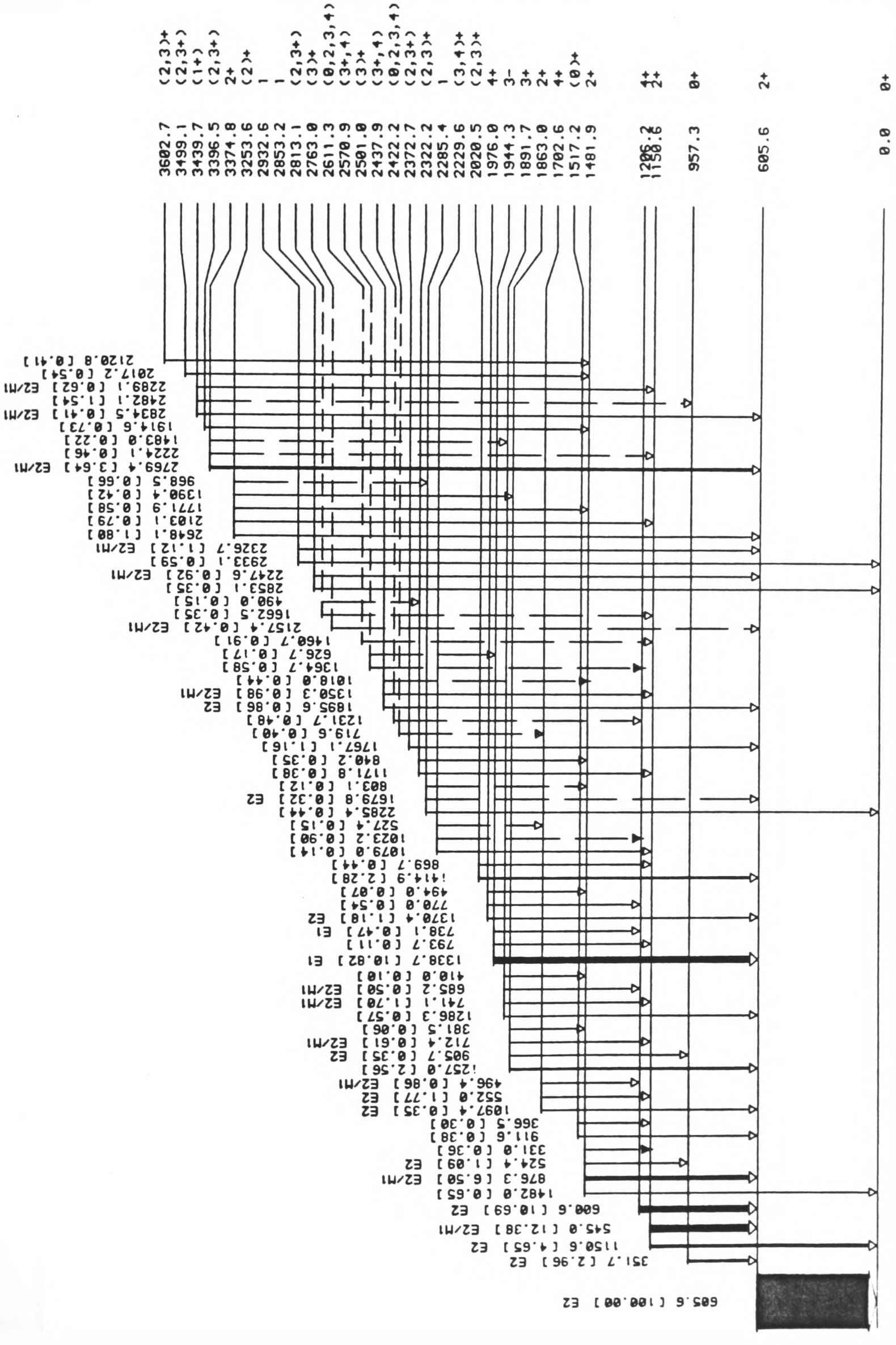

Figure 6.1. ^{118}Te levels populated in the decay of ^{118}I$_g$.

E_γ	$I_\gamma(^{32}S)$	$I_\gamma(^{34}S)$	U_2A_2	U_4A_4	$\lambda = 2$ term	$\lambda = 4$ term	$\alpha_k \times 10^3$	Comment
(331.0)	(0.38)	0.36						
351.7	(3.00)	2.96	0.022 (0.019)	−0.009 (0.127)				
366.5	(0.33)	0.30	−0.164 (0.151)	0.337 (1.100)				$I_i = 0^+$
381.5	(0.05)	0.06						Doublet
410.0	(0.10)	0.10						
(490.0)	(0.14)	0.15						
494.0	(0.07)	0.07						
496.4	(0.73)	0.86	*	*	$A_2 = -0.268$ (0.037)	$A_4 = -0.142$ (0.317)	22(2)	δ,X(E0:E2)
524.4	1.11	1.07	−0.256 (0.027)	−0.395 (0.174)	$U_2 = 0.428$ (0.046)	$U_4 = 0.370$ (0.163)		E2
(527.4)	0.14	0.16						
545.0	(12.04)	12.38	0.040 (0.007)	−0.067 (0.046)	$A_2 = 0.113$ (0.021)	$A_4 = -0.536$ (0.479)	9.5(5)	δ,X(E0:E2)
552.0	(1.54)	1.77	*	*	$A_2 = -0.452$ (0.028)	$A_4 = -0.163$ (0.200)		E2(see text)
600.6	10.15	11.23	*	*	$A_2 = -0.453$ (0.023)	$A_4 = -0.311$ (0.051)		E2(see text)
605.6	100.00	100.00	−0.250 (0.007)	−0.144 (0.038)	$U_2 = 0.419$ (0.012)	$U_4 = 0.135$ (0.036)		E2(see text)
(626.7)	(0.17)	0.17						
685.2	0.49	0.52	0.055 (0.059)	−0.085 (0.373)	$A_2 = 0.068$ (0.073)	$A_4 = -0.226$ (0.995)		(δ)
712.4	0.66	0.55	−0.271 (0.054)	0.183 (0.364)	$A_2 = -0.509$ (0.214)	$A_4 = -1.614$ (3.882)		(δ)
(719.6)	0.49	0.30						(Cs)
738.1	0.52	0.43	0.202 (0.078)	−0.290 (0.494)	$A_2 = 0.245$ (0.096)	$A_4 = 0.705$ (1.203)		$I_i = 3^-$
741.1	1.71	1.69	−0.065 (0.021)	0.186 (0.138)	$A_2 = -0.082$ (0.026)	$A_4 = 0.495$ (0.372)	3.1(8)	δ
770.0	(0.52)	0.54					2.2(7)	Doublet
793.7	(0.12)	0.11						
(803.1)	0.12	0.12						
840.2	0.32	0.39	0.431 (0.089)	0.775 (0.619)				E2/M1
869.7	0.51	0.37	−0.008 (0.038)	0.118 (0.253)				E2/M1
876.3	(7.14)	6.50	0.220 (0.008)	−0.018 (0.050)	$A_2 = 0.514$ (0.058)	$A_4 = -0.047$ (0.136)	2.2(2)	δ,X(E0:E2)
905.7	0.40	0.30	−0.318 (0.118)	0.121 (0.162)	$U_2 = 0.533$ (0.197)	$U_4 = -0.113$ (0.152)		$I_i = 2^+$
911.6	0.38	0.39	0.009 (0.087)	0.386 (0.579)				$I_i = (0)^+$

Table 6.1. Properties of γ-rays in ^{118}Te seen in the decay of $^{118}I^g$.

E_γ	$I_\gamma(^{32}S)$	$I_\gamma(^{34}S)$	U_2A_2	U_4A_4	$\lambda = 2$ term	$\lambda = 4$ term	$\alpha_k \times 10^3$	Comment
(968.5)	0.55	0.77	−0.145 (0.087)	0.653 (0.578)				
(1018.0)	(0.40)	0.44						
(1023.2)	1.14	0.67	−0.152 (0.039)	−0.018 (0.261)				E2/M1
1079.0	0.10	0.18	−0.629 (0.294)	0.983 (1.837)				E2/M1
1097.4	0.30	0.39	*	*	$A_2 = -0.471$ (0.156)	$A_4 = -0.728$ (1.324)		E2
1150.6	4.60	4.69	−0.212 (0.012)	−0.133 (0.075)	$U_2 = 0.355$ (0.020)	$U_4 = 0.124$ (0.070)		E2
1171.8	0.36	0.41	0.445 (0.081)	−0.490 (0.546)				E2/M1
(1231.7)	0.50	0.46	−0.335 (0.063)	−0.240 (0.410)				(Cs)
1257.0	(2.24)	2.56					0.9(2)	Doublet
1286.3	(0.70)	0.57						Doublet
1338.7	11.75	9.89	0.285 (0.009)	−0.004 (0.049)	$A_2 = 0.346$ (0.011)	$A_4 = -0.011$ (0.120)		$I_i = 3^-$
1350.3	1.04	0.91	−0.123 (0.034)	0.370 (0.227)	$A_2 = -0.148$ (0.041)	$A_4 = 0.885$ (0.543)		$I_i = (3^+),\delta$
(1364.7)	0.66	0.50	−0.299 (0.068)	0.354 (0.370)			2.7(7)	(Cs)
1370.4	1.18	1.18	*	*	$A_2 = -0.533$ (0.040)	$A_4 = -0.271$ (0.239)	1.1(4)	E2(see text)
1390.4	0.45	0.39	−0.171 (0.070)	−0.641 (0.470)				$I_i = (2)^+$
1414.9	2.52	2.04	−0.110 (0.018)	0.021 (0.119)			0.7(2)	E2/M1
(1460.7)	(0.87)	0.91						(^{40}Ca)
1482.0	(0.70)	0.65						Doublet
(1483.0)	(0.23)	0.22						doublet
(1662.5)	0.36	0.33	−0.205 (0.104)	−0.061 (0.682)				
(1679.8)	(0.30)	0.32	−0.024 (0.070)	0.000 (0.466)	$A_2 = -0.066$ (0.193)	$A_4 = 0.000$ (0.000)		(δ)
1767.1	1.16	1.16	−0.232 (0.032)	0.051 (0.205)				
1771.9	0.62	0.54	0.012 (0.076)	−0.331 (0.506)				E2/M1
1895.6	0.95	0.77	−0.248 (0.047)	0.471 (0.314)	$A_2 = -0.299$ (0.057)	$A_4 = 1.128$ (0.752)		$I_i = (3^+),\delta$
1914.6	0.84	0.62	−0.162 (0.051)	0.325 (0.342)				
2017.2	0.54	0.54	−0.268 (0.064)	−0.014 (0.428)				
2103.1	0.73	0.84	−0.070 (0.046)	−0.489 (0.309)				$I_i = (2)^+$
2120.8	0.48	0.34	0.029 (0.076)	0.232 (0.508)				E2/M1

Table 6.1. Properties of γ-rays in ^{118}Te seen in the decay of $^{118}I^g$.

E_γ	$I_\gamma(^{32}S)$	$I_\gamma(^{34}S)$	U_2A_2	U_4A_4	$\lambda = 2$ term	$\lambda = 4$ term	$\alpha_k \times 10^3$	Comment
(2157.4)	0.47	0.37	0.115 (0.088)	0.783 (0.589)				$I_i = (3^+),\delta$
(2224.1)	0.47	0.46	−0.252 (0.089)	−0.253 (0.588)				
2247.6	1.00	0.84	0.005 (0.040)	0.400 (0.270)	$A_2 =$ 0.011 (0.091)	$A_4 =$ 0.000 (0.000)		(δ)
2285.4	0.44	0.43	0.260 (0.120)	−0.831 (0.912)	$U_2 =$ 0.368 (0.170)	$U_4 =$ 0.000 (0.000)		$I_i = 1$
2289.1	0.60	0.63	−0.232 (0.065)	−0.302 (0.428)	$A_2 =$ −0.448 (0.198)	$A_4 =$ 0.000 (0.000)		(δ)
2326.7	1.11	1.13	0.071 (0.036)	−0.107 (0.240)	$A_2 =$ 0.140 (0.078)	$A_4 =$ 0.000 (0.000)		(δ)
(2482.1)	1.49	1.60	0.366 (0.125)	−0.025 (0.846)	$U_2 =$ 0.517 (0.176)	$U_4 =$ 0.000 (0.000)		$(I_i = 1)$
2648.1	1.80	1.80	−0.211 (0.025)	0.010 (0.162)				E2/M1
2769.4	3.63	3.65	−0.206 (0.015)	−0.234 (0.101)				$I_i = 2^+,\delta$
2834.5	0.41	0.41	−0.321 (0.081)	0.667 (0.536)	$A_2 =$ −0.620 (0.263)	$A_4 =$ 0.000 (0.000)		δ
2853.1	0.35	0.35	0.313 (0.079)	−0.193 (0.268)	$U_2 =$ 0.442 (0.112)	$U_4 =$ 0.000 (0.000)		$I_i = 1$
2933.1	0.59	0.59	0.356 (0.081)	0.350 (0.539)	$U_2 =$ 0.503 (0.114)	$U_4 =$ 0.000 (0.000)		$I_i = 1$

Table 6.1. Properties of γ-rays in ^{118}Te seen in the decay of $^{118}I^g$. Relative γ-ray intensities are quoted for each transition, as deduced from both ^{32}S and ^{34}S experiments (those values shown in brackets are subject to possible systematic errors, and should be treated with caution). Bracketed transitions are only tentatively associated with $^{118}I^g$ decay. The values of $U_\lambda A_\lambda$ quoted are derived from the axial and equatorial anisotropies given in Table 5.2 (a * denotes transitions which are *mixed* high and low spin - see text). Where possible, separate U_λ or A_λ terms are deduced. Conversion coefficients are also quoted for the stronger transitions.

detector efficiencies do not change significantly between 605.6 and 614.3 keV, the *subtracted* peak area may be written as

$$N^{sub}_{605.6} = N^{tot}_{605.6} - N_{614.3} - \left(\frac{\epsilon_{614.3}}{\epsilon_{943.8}}\right) N_{943.8} \qquad (6.1a)$$

where

$$\frac{\epsilon_{614.3}}{\epsilon_{943.8}} = \frac{N^{warm}_{614.3}}{N^{warm}_{943.8}} \frac{I_{943.8}}{I_{614.3}} \qquad (6.1b)$$

and N refers to peak areas, ϵ to detector efficiencies, and I to relative γ-ray intensities.

The anisotropies quoted in Table 5.2 are *unsubtracted* (as well as the quoted polarization), which may be compared with the *subtracted* anisotropies, which are

$$W(0) - 1 = \begin{cases} -22.5(0.3) & 15\text{mK} \\ -13.6(0.5) & 32\text{mk} \end{cases}$$

$$W(90) - 1 = \begin{cases} 9.5(0.4) & 15\text{mK} \\ 7.2(0.8) & 32\text{mk} \end{cases} \qquad (6.2)$$

With the high spin taken out, the effects are slightly reduced, leading to values of $U_2 = 0.419(12)$ and $U_4 = 0.135(36)$. These lie well within the limits of U^{max}_λ and U^{min}_λ quoted in Table 5.3, where the range is so large due to the cumulative effect of uncertainties in the many transitions which feed into this level.

957.3 *keV* : 0^+_2

In this work, this level has been unambiguously assigned to be 0^+, due to the strong E0 transition to the ground state, with no corresponding γ-ray . Supportive evidence for this assignment comes from both the nuclear orientation and angular correlation data. From the nuclear orientation data, the 351.7 keV transition (to the 2^+_1) gives $U_2A_2 = 0.022(19)$ and $U_4A_4 = -0.009(127)$, which are consistent with a $0^+ \rightarrow 2^+$ transition. The angular correlation asymmetry ratio $\{W(0)/W(90) - 1\}$ for this transition shows a large value of 0.51(4) [2] , characteristic of a $0^+ \rightarrow 2^+ \rightarrow 0^+$ sequence, for which the theoretical value is 0.54, allowing for finite detector solid angle.

1150.6 *keV* : 2_2^+

The ground state E2 transition is used as a normalization line, from which the de-orientation parameters $U_2 = 0.355(20)$ and $U_4 = 0.124(70)$ are deduced. As can be seen from Table 5.3, these values are much more precise than those calculated using UACALC, and are used to extract $A_2 = -0.113(21)$ and $A_4 = -0.54(48)$ for the 545.0 keV ($2_2^+ \rightarrow 2_1^+$) transition. The small high spin feed (2%) to the level is neglected in this analysis, which is justified by comparison with the 1891.7 keV level (described below), where a 2.8% high spin admixture is shown to have very little effect.

In addition, linear polarization was observed for this γ-ray , and [Fig 6.2] shows a plot of $\{W(0)/W(90) - 1\}$, P_{cal} and P_{cal}^{NO} using the parameters

$$\begin{aligned} A_{22} &\equiv f B_2 U_2 A_2 \overline{Q_2} = \quad 0.0336(60) \\ A_{44} &\equiv f B_4 U_4 A_4 \overline{Q_4} = -0.0086(62) \\ M_2 &\equiv f B_2 U_2 \overline{Q_2} \quad = \quad 0.294(18) \\ M_4 &\equiv f B_4 U_4 \overline{Q_4} \quad = -0.017(10) \end{aligned} \tag{6.3}$$

The positive value of polarization P_{exp} picks out the solution $\arctan(\delta) = 88.5(1.0)$, giving the E2/M1 mixing ratio, $\delta = 38(^{+77}_{-15})$, which is in agreement with the E2 assignment of van Ruyven *et al* [3] (hereafter referred to as van Ruyven). In addition, the angular correlation data for this transition give two possible solutions of $0.34 < \delta < 0.47$ and $\delta > 13$ *or* $\delta < -26$, the latter being in agreement with the orientation data.

However, there is a complication in the form of a high spin transition at 545.7 keV which contaminates the 545.0 keV line at the 1% level (the A_λ coefficients quoted in Table 6.1 neglect this contamination). By calculating the maximum possible effect this could have on $W(0)$ and $W(90)$ using equation (4.14), a mean value of $U_2 A_2 = 0.036(23)$ can be obtained, giving a modified

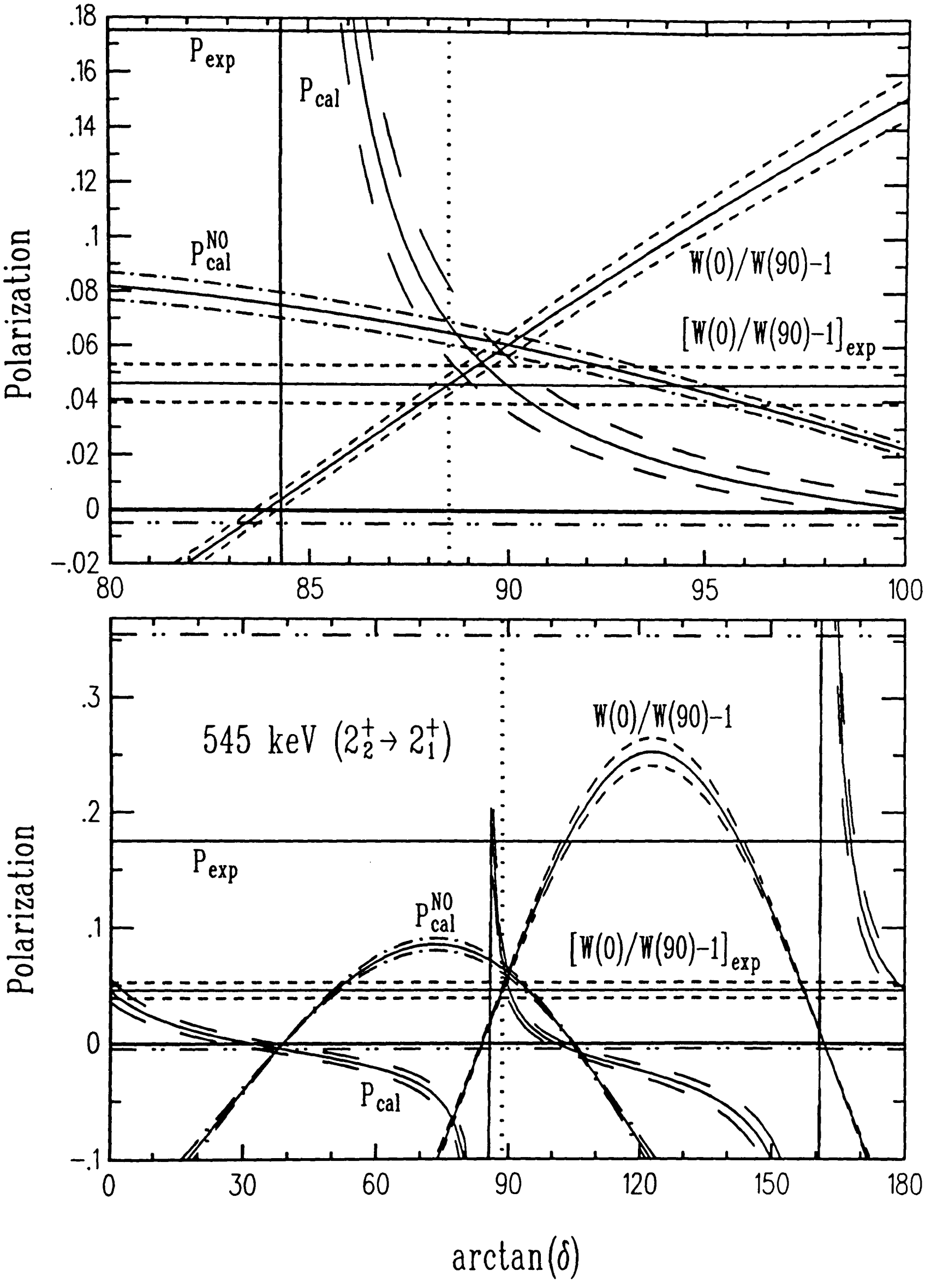

Figure 6.2. Experimental and theoretical anisotropies and polarizations plotted as a function of arctan(δ) for the 545.0 keV ($2^+_2 \rightarrow 2^+_1$) transition.

$A_2 = 0.10(7)$. Taking into account the maximal effects of this contamination yields a mixing ratio of $\delta > 12$ *or* $\delta < -29$. This shows that even a very small contamination line (which may show large effects) can affect the results obtained for the main transition significantly.

1206.2 *keV* : 4_1^+

This level is calculated to be 55.2% fed by the low spin isomer, assuming no direct feed from the high spin isomer. From the anisotropies quoted in Table 5.2 for the 600.6 keV transition, separate $\lambda = 2, 4$ terms may be calculated, which are *averaged* over the high and low spin components (the errors quoted on these values are statistical only and do not take into account possible systematic errors in peak area determination, due to the proximity of the 605.6 keV transition). Using equation 4.14 the contribution of the high and low spin components may be calculated, and values of A_λ thus determined. Taking the high/low spin ratio, $\alpha = 0.812$, and the parameters $U_2^l = 0.668(43)$, $U_4^l = 0.196(46)$ and $U_2^h = 0.759(49)$, $U_4^h = 0.383(92)$ from Tables 5.3 and 5.4 respectively, *averaged* values for $fB_\lambda Q_\lambda U_\lambda$ are obtained, and are shown in Table 6.2.

Isotope	$\mathbf{T_L}$ **(mK)**	$\langle \mathbf{fB_2Q_2U_2} \rangle_{av}$	$\langle \mathbf{fB_4Q_4U_4} \rangle_{av}$
$^{118}I^{g+m}$	15	0.784(46)	0.169(11)
	32	0.556(37)	0.069(6)

Table 6.2 Averaged orientation parameters for the 1206.2 keV level.

Using these values, along with the separated $\lambda = 2, 4$ terms gives $A_2 = -0.453(23)$ and $A_4 = -0.311(51)$, which are consistent with the values of $A_2 = -0.4477$ and $A_4 = -0.3044$ expected for a $4^+ \rightarrow 2^+$ transition.

1481.7 *keV* : 2_3^+

The tentative assignment of Chowdhury [4] is confirmed for this level from the observation of negative $U_\lambda A_\lambda$ coefficients for the 524.4 keV transition to the 0_2^+ level, consistent with an E2 transition. The 1481.9 keV transition to the ground state is contaminated, and no useful data could be extracted from the measured anisotropies.

Following the procedure adopted above for the 1150.6 keV level, the 524.4 keV transition is used to extract $U_2 = 0.428(46)$ and $U_4 = 0.370(163)$ for this level (again ignoring the negligible high spin feeding). Hence, the values $A_2 = 0.514(58)$ and $A_4 = -0.05(14)$ have been deduced for the 876.3 keV $(2_3^+ \rightarrow 2_1^+)$ transition. A plot of $\{W(0)/W(90) - 1\}$, P_{cal} and P_{cal}^{NO} is shown in [Fig 6.3] , for the parameters

$$\begin{aligned} A_{22} \equiv f B_2 U_2 A_2 \overline{Q_2} &= \quad 0.184(6) \\ A_{44} \equiv f B_4 U_4 A_4 \overline{Q_4} &= -0.003(7) \\ M_2 \equiv f B_2 U_2 \overline{Q_2} &= \quad 0.352(39) \\ M_4 \equiv f B_4 U_4 \overline{Q_4} &= -0.050(22) \end{aligned} \tag{6.4}$$

In this case, the two solutions merge into one at a value of $\arctan(\delta) = -57(11)$, giving $\delta = -1.5(^{+5}_{-9})$. However, as with the 545.0 keV γ-ray , the 876.3 keV transition is also contaminated with a high spin component, at the 3% level. Taking the possible effects of this into account in a similar way to before leads to $0.32 < A_2 < 0.69$, giving a possible range of mixing ratios of $-0.7 > \delta > -5.8$. In this case, a 3% high spin admixture introduces a large degree of uncertainty to the deduced mixing ratio. From the angular correlation data (neglecting contamination), the solutions $-0.18 > \delta > -0.51$ or $-0.87 > \delta > -1.6$ are obtained, the latter of which may be compared with the *uncontaminated* value of $-1.5(^{+5}_{-9})$ obtained above (this suggests that the high spin comtamination does not have a pronounced effect).

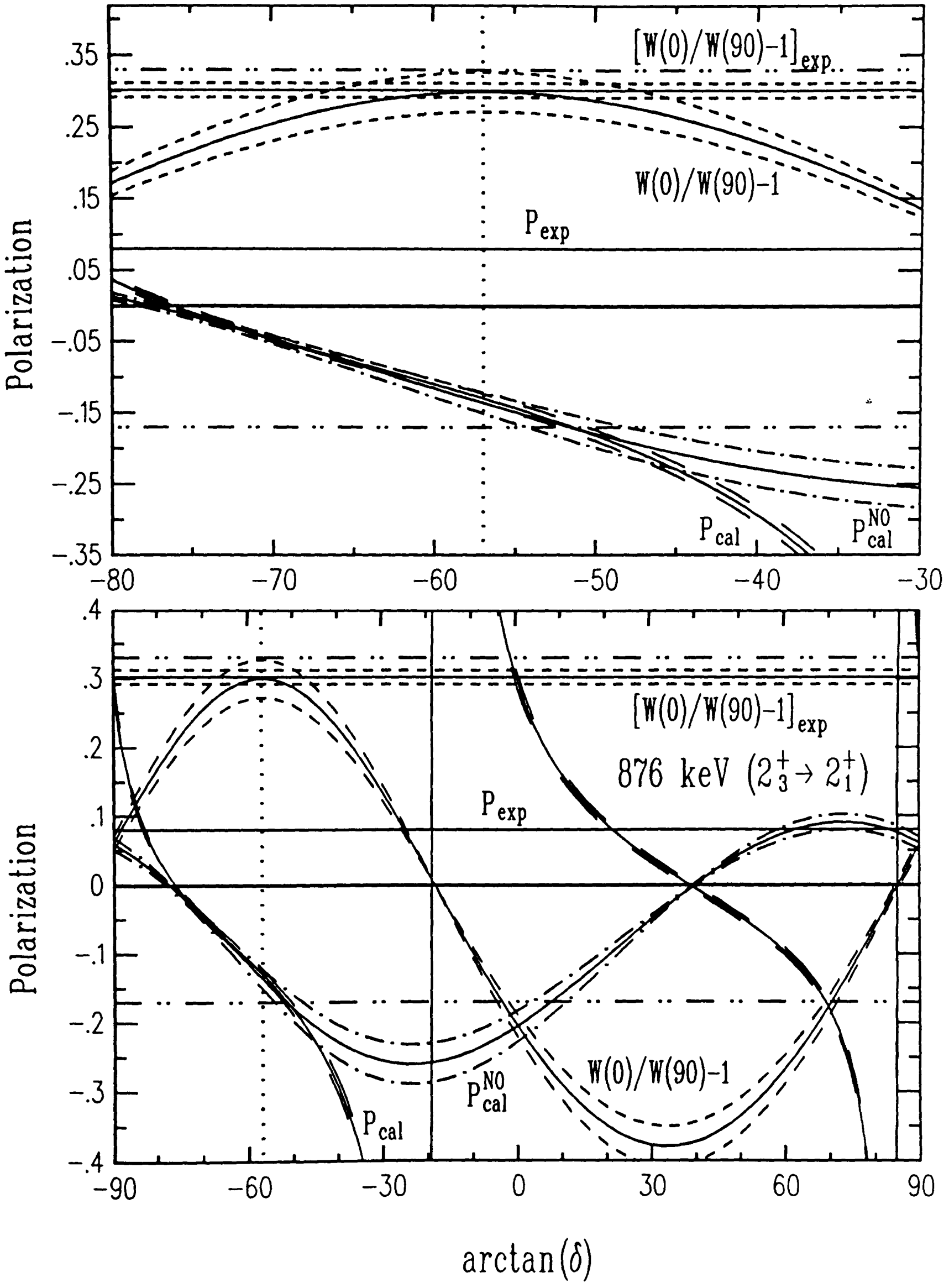

Figure 6.3. Experimental and theoretical anisotropies and polarizations plotted as a function of arctan(δ) for the 876.3 kev ($2_3^+ \rightarrow 2_1^+$) transition.

1517.2 *keV* : $(0_3)^+$

Two γ-rays are observed to depopulate this newly placed level, at 366.5 (to the 2_2^+) and 911.6 keV (to the 2_1^+). There are two γ-rays placed at this former energy, with the component from this level dominant. Neglecting this contamination gives $U_2A_2 = -0.16(15)$ (trying to subtract out the contaminant would essentially make the quoted error much larger). Of more interest is the 911.6 keV transition which gives values $U_2A_2 = 0.009(87)$ and $U_4A_4 = 0.39(58)$, consistent with a $0^+ \rightarrow 2^+$ transition. On this basis, and the absence of a ground state γ-transition, this level is assigned $(0)^+$.

1702.6 *keV* : 4_2^+

As with the 1206.2 keV level, this level is also fed by both high and low spin isomers, with the ratio $\alpha(h/l) = 0.183$, assuming no direct feed from the high spin isomer. Using the parameters $U_2^l = 0.700(28)$, $U_4^l = 0.230(28)$ and $U_2^h = 0.763(81)$, $U_4^h = 0.382(170)$, averaged high/low spin values for $fB_\lambda Q_\lambda U_\lambda$ may be calculated as

Isotope	T_L (mK)	$\langle fB_2Q_2U_2\rangle_{av}$	$\langle fB_4Q_4U_4\rangle_{av}$
$^{118}I^{g+m}$	15	0.656(30)	0.079(20)
	32	0.426(26)	0.029(7)

Table 6.3 Averaged orientation parameters for the 1702.6 keV level.

From the base temperature anisotropies for the 1097.4 kev line, and using equation 4.14 with the above values, leads to $A_2 = -0.47(16)$, consistent with the predicted $A_2 = -0.4477$ for a $4^+ \rightarrow 2^+$ transition.

The transition at 552.0 keV is also an E2 ($4^+ \rightarrow 2^+$) transition, but with the complication of a high spin contamination line at 551.8 keV ($7^+ \rightarrow 5^+$).

The effects of this may be *subtracted* out of the observed anisotropies quoted in Table 5.2. Taking $\alpha(h/l) = 0.084$, with $U_2A_2 = -0.380(11)$ and $U_4A_4 = -0.171(17)$, revised low spin anisotropies may be written (using equation 4.14) as

$$W(0) - 1 = \begin{cases} -30.4(0.9) & 15\text{mK} \\ -20.1(1.7) & 32\text{mk} \end{cases}$$

$$W(90) - 1 = \begin{cases} 13.8(1.3) & 15\text{mK} \\ 11.9(2.3) & 32\text{mk} \end{cases} \qquad (6.5)$$

Separating the $\lambda = 2,4$ components from these anisotropies, and using the *averaged* $fB_\lambda Q_\lambda U_\lambda$ quoted above, yields $A_2 = -0.452(28)$ and $A_4 = -0.16(20)$.

The A_λ values obtained for the 1097.4 and 552.0 keV transitions are consistent with them being $4^+ \rightarrow 2^+$ transitions, thus giving strong support for this method of analysis. The same high/low averaged parameters are also used for the 496.8 keV transition ($4_2^+ \rightarrow 4_1^+$), giving $A_2 = -0.268(37)$ and $A_4 = -0.14(32)$. These yield solutions for the E2/M1 mixing ratio of $\delta = 1.48(^{+14}_{-13})$ or $\delta = -0.22(^{+4}_{-3})$. The angular correlation data give solutions of $\delta < -10$ or $\delta > 0.85$, supporting the solution $\delta = 1.48(^{+14}_{-13})$. This is also consistent with the mixing ratio of $\delta = 1.0(^{+3}_{-2})$ measured by van Ruyven.

1863.0 *keV* : 2_4^+

This level can unambiguously be assigned 2^+ on the basis of the negative U_2A_2 value for the 905.7 keV transition to the 0_2^+ level (a transition from spins $1 \rightarrow 0$ would show $U_2A_2 > 0$). Taking this transition as E2, the values $U_2 = 0.53(20)$ and $U_4 = -0.11(15)$ may be deduced for the level. Two other transitions are observed to depopulate this level, at energies 712.4 and 1257.0 keV, both going to 2^+ states. The latter of these is heavily contaminated with a high spin transition (at 1257.7 keV), and because of the large uncertainty this introduces, all that can be deduced is that $A_2 \leq 0$ for the low spin component of this doubled line. However, for the 712.4 keV transition a value of

$A_2 = -0.51(21)$ may be determined, for which there are two possible solutions for the mixing ratio, δ(E2/M1) of $1.8(^{+1.2}_{-0.7})$ or $0.08(^{+24}_{-18})$.

1891.7 *keV* : 3^+_1

This level is fed by both high and low spin isomers, with the ratio $\alpha(h/l) = 0.029$. Using the parameters $U^l_2 = 0.800(28)$, $U^l_4 = 0.378(40)$ and $U^h_2 = 0.780(9)$, $U^h_4 = 0.404(16)$, averaged high/low spin values for $fB_\lambda Q_\lambda U_\lambda$ may be calculated as

Isotope	T_L (mK)	$\langle fB_2Q_2U_2\rangle_{av}$	$\langle fB_4Q_4U_4\rangle_{av}$
$^{118}I^{g+m}$	15	0.675(26)	0.060(5)
	32	0.413(27)	0.017(10)

Table 6.4 Averaged orientation parameters for the 1891.7 keV level.

Three transitions are seen to originate from this level, with energies of 685.2, 741.1 and 1286.3 keV. The last of these is a doublet with a non-negligible high spin component, and as a result, no useful information can be deduced about this transition to compare with the E2/M1 mixing ratio, $\delta = -1.7(^{+2}_{-1})$ of van Ruyven (this mixing ratio is used in the next section to look at this high spin component from the 3108.7 keV level).

For the 685.2 keV transition $A_2 = 0.048(69)$ from which possible mixing ratios of $\delta = -11(^{+3}_{-8})$ or $0.16(^{+3}_{-4})$ may be deduced. For the 741.1 keV transition $A_2 = -0.080(25)$ and $A_4 = 0.41(31)$. From the value of A_2, possible mixing ratios are $\delta = -44(^{+16}_{-60})$ [$A_4 = 0.67$] and $0.22(^{+2}_{-1})$ [$A_4 = 0.03$]. The former of these two solutions is slightly preferred from the measured value of A_4. This is just about consistent with the value of $-9.5(^{+4}_{-19})$ obtained by van Ruyven, although for $\delta = -9.5$, the sign of A_2 would opposite to that observed here.

The values of $U_\lambda A_\lambda$ and A_λ quoted in Table 6.1 are calculated neglecting any high spin contamination, and by comparing with the values in the text, it can be seen that the contamination has little effect in this level.

1944.3 *keV* : 3_1^-

This level can be positively assigned 3^- in this work. It decays by a 738.1 keV transition to the 4_1^+ level and a 1338.7 keV transition to the 2_1^+ level. For both these transitions, the measured values of $A_2 > 0$ indicate the presence of $L = 1$ component. In addition, from the angular correlation data the observed mixing ratio for the 1338.7 keV transition ($-0.06 < \delta < -0.01$) shows a negligible quadrupole component. Thus, spins 2 or 4 can be ruled out for this level, leaving spin 3 as as the only possibility.

From the electron conversion data, the 1338.7 keV transition is clearly identified as E1, which establishes the 3^- assignment. The strong direct feed to this level suggests an *allowed* β-decay from the 2^- parent, also supporting the negative parity assignment. This level appears to be the analogue of the 2083 keV level in ^{120}Te, for which negative parity has previously been established [5] [6]

The 1338.7 keV γ-ray is especially important as it used in chapter 5.5.2 as a normalization line, from which the fraction in good sites $f = 80(2)\%$ is deduced for the low spin parent. There are two main factors which make this line particularly suitable for normalization. Firstly, the absence of any quadrupole term, and secondly, the spin of 3^- allows calculation of the U_2 term (assuming direct *allowed* β-feeding). These factors, along with the strength of the line are responsible for the good precision on the normalization ratios quoted in Table 5.6.

For the 738.1 keV transition a value $A_2 = 0.24(10)$ is obtained, to be compared with a value of $A_2 = 0.144$ for a $3^- \rightarrow 4^+$ E1 transition (the error quoted does not include possible systematic errors occuring in peak area determination, due to the adjacent peak at 741.1 keV).

1976.0 *keV* : 4_3^+

This level is assigned 4^+ on the basis that it is fed by a 938.1 keV transition from the 2913.9 keV 6^+ level, and it feeds the 605.6 keV 2^+ level via a 1370.4 keV transition, both of which are assumed to be stretched E2. The level also has feeds from both high and low spin isomers, with the ratio $\alpha(h/l) = 0.203$. Using the parameters $U_2^l = 0.749$, $U_4^l = 0.285$ and $U_2^h = 0.841(15)$, $U_4^h = 0.552(29)$, averaged high/low spin values for $fB_\lambda Q_\lambda U_\lambda$ may be calculated as

Isotope	T_L (mK)	$\langle fB_2Q_2U_2\rangle_{av}$	$\langle fB_4Q_4U_4\rangle_{av}$
$^{118}I^{g+m}$	15	0.715(16)	0.116(7)
	32	0.468(21)	0.043(7)

Table 6.5 Averaged orientation parameters for the 1976.0 keV level.

Using these parameters for the 1370.4 keV transition, the values $A_2 = -0.533(40)$ and $A_4 = -0.27(24)$ are obtained, to be compared with the values of $A_2 = -0.4477$ and $A_4 = -0.3044$ expected for a $4^+ \rightarrow 2^+$. The agreement for the A_2 term is not very good, perhaps indicating that there are additional high spin feeds which have not been identified.

The other transition from this level is at an energy of 770.0 keV. However, it is a doublet with a large high spin component. Van Ruyven has measured the mixing ratio ($\delta = 0.00(^{+0.03}_{-0.18})$) for this high spin transition ($7^+ \rightarrow 6^+$). However, this value is not precise enough to be able to subtract out this transition, as the A_2 term is not well defined ($0.2 < A_2 < 0.6$), and no useful information can be obtained from the 770.0 keV γ-ray , except that the conversion coefficient for the doublet is consistent with the components being mixed E2/M1.

6.2.2 Proposed spin 1 levels

$2285.4^{(a)}, 2853.2^{(b)}, 2932.6^{(c)}$ *keV* : 1

A common feature of these levels is that they all have ground state transitions, as well as transitions to the 2_1^+ level, at γ-ray energies of $1679.8^{(a)}$, $2247.6^{(b)}$ and $2326.7^{(c)}$ keV. They are all assigned as spin 1 on the basis of the positive U_2A_2 values for their respective ground state transitions. This is a clear signature as a $2 \rightarrow 0$ E2 transition would be expected to show a negative U_2A_2 value. The values $U_2^{(a)} = 0.37(17)$, $U_2^{(b)} = 0.44(11)$ and $U_2^{(c)} = 0.50(11)$ may thus be deduced, to be compared with $U_2 = 0.59$ for a spin $1 \rightarrow 2$ β-decay (with $j_\beta = 1$).

It is now possible to determine A_2 values, and hence possible mixing ratios for the transitions to the 2_1^+ level, mentioned above,

$$A_2(1679.8^{(a)}) = -0.07(0.19) : \delta = -2.1(^{+1.1}_{-2.2}) \text{ or } 0.15(^{+21}_{-38})$$
$$A_2(2247.6^{(b)}) = 0.011(91) : \delta = -2.7(^{+0.7}_{-1.1}) \text{ or } -0.06(^{+9}_{-11})$$
$$A_2(2326.7^{(c)}) = 0.140(78) : \delta = -4.5(^{+1.3}_{-2.7}) \text{ or } 0.07(^{+8}_{-8})$$

Each of the above mixing ratios is consistent with the relevant transition being either pure E1, or mixed E2/M1. Hence, the parity of these levels cannot be deduced.

3439.7 *keV* : (1^+)

Unlike the levels discussed above, no ground state transition was observed for this level. However, a transition seen at 2482.1 keV is of the correct energy for a transition to the 0_2^+ level, and is tentatively taken as such. This transition shows a positive U_2A_2 value, consistent with a spin 1 assignment, which leads to a value $U_2 = 0.52(18)$.

In addition, transitions are observed from this level to the 2_2^+ (at 2289.1 keV) and 2_1^+ (at 2834.5 keV) levels, for which the values of $A_2 = -0.62(26)$ and $A_2 = -0.45(20)$ respectively may be derived. For these parameters, allowed

ranges of mixing ratio are given by $0.5 < \delta(2289.1) < 1.1$ and $0.6 < \delta(2834.5) < 0.9$. Neither transition is consistent with being E1 ($1^- \rightarrow 2^+ : A_2 = 0.0707$), and both must be taken as mixed E2/M1, hence the positive parity assignment.

6.2.3 Low spin levels above 2MeV

Ground state transitions are not observed from any of the levels discussed in this subsection, and on this basis, the levels are assumed unlikely to be spin 1. However, there are many transitions from these levels to lower lying 2^+ states, and hence it is useful to compare the properties of the $U_\lambda A_\lambda$ coefficients for a transition $I_i \rightarrow 2^+$. By assuming direct feeding to the levels I_i (with $j_\beta = 1$ for $I_i = 1, 3$, $j_\beta = 0, 1$ for $I_i = 2$, and $j_\beta = 2$ for $I_i = 4$), the possible values or ranges of $U_\lambda A_\lambda$ are shown in Table 6.6 for the types of transition indicated

I_i	Transition	U_2A_2	U_4A_4
1^+	E2/M1	$0.418 > \ldots > -0.167$	0.0
1^-	E1	0.042	0.0
2^+	E2/M1	$0.525 > \ldots > -0.816$	$0.204 > \ldots > -0.305$
2^-	E1	$-0.209 > \ldots > -0.418$	0.0
3^+	E2/M1	$0.902 > \ldots > -0.717$	$0.287 > \ldots > 0.0$
3^-	E1	0.287	0.0
4^+	E2	-0.335	-0.087

Table 6.6 $U_\lambda A_\lambda$ parameters for possible $I_i \rightarrow 2^+$ transitions.

3374.8 *keV* : 2^+

This level is identified as 2^+ by the negative $U_4A_4 = -0.23(10)$ for the 2769.4 keV transition to the 2^+ level. This value also suggests a large quadrupole component, the magnititude of which may be estimated as follows. As $A_4^{min} = -0.305$ for a $2^+ \rightarrow 2^+$ transition, the above value of U_4A_4 implies that $U_4 > 0.4$, which in turn implies that $1.0 > U_2 > 0.8$ (assuming direct β-feeding with $j_\beta = 0, 1$ terms dominant). Taking a value of $U_2 \simeq 0.9(1)$ yields $A_2 \simeq -0.23(3)$ for this transition, which in turn leads to an E2/M1 mixing ratio, $\delta \simeq 3.6(3)$.

This transition is also the most intense above 1500keV, and as a consequence single and double escape peaks are observed in the γ-spectrum (at energies 2257.5 and 1747.1 keV). These peaks appear in coincidence with the 605.6 keV transition, and have roughly similar anisotropies as the 2769.4 keV transition, as would be expected. Weaker escape peaks can also be seen for the 2490.8, 2648.1 and 2791.7 keV γ-rays .

3253.6 *keV* : $(2)^+$

There are four transitions from this level (at energies 1390.4, 1771.9, 2103.1, and 2648.1 keV) which go to various 2^+ states. The U_2A_2 values for these transitions are not consistent with them being E1, ruling out a negative parity assignment for the level. Also, the U_4A_4 values for the 1390.4 and 2103.1 keV transitions are $-0.64(47)$ and $-0.49(31)$ respectively, which suggest spin 2 for this level, with large E2 components for both these transitions. Possible mixing ratios have not been estimated because of the large uncertainty in U_λ for this spin assignment.

The 968.5 keV transition (tentatively placed between this level and the 2285.4 keV level) shows a value $U_4A_4 = 0.65(57)$, the sign of which is consistent with that for a $2^+ \rightarrow 1^+$ mixed E2/M1 transition.

$2020.5^{(a)}, 2322.2^{(b)}, 3602.7^{(c)}$ *keV* : $(2,3)^+$

The transitions from these levels all go to 2^+ states, and the measured U_2A_2 values are consistent with mixed E2/M1 transitions from initial states with spins of either 2 or 3 (the $1414.9^{(a)}$ keV transition is confirmed as E2/M1 from the conversion electron data). This leads to the positive parity assignment, but as the U_4A_4 values are within errors of zero, it is impossible to distinguish between spins 2^+ and 3^+. For the $2120.8^{(c)}$ keV transition, $U_2A_2 = 0.029(76)$, which is also consistent with a spin 0^+ assignment for the $3602.7^{(c)}$ keV level.

$2372.7^{(a)}, 2813.1^{(b)}, 3396.5^{(c)}, 3499.1^{(d)}$ *keV* : $(2,3^+)$

The transitions at $1767.1^{(a)}$, $1662.5^{(b)}$, $1914.6^{(c)}$ and $2017.2^{(d)}$, keV, all of which go to 2^+ states, have U_2A_2 values between -0.16 and -0.27, which are consistent with spin assignments of either $2^\pm$ or 3^+. As in the previous case the U_4A_4 terms cannot distinguish between these possibilities.

$2501.0^{(a)}, 2763.0^{(b)}$ *keV* : $(3)^+$

These two levels have transitions to 2^+ states only, at γ-ray energies of $1018.0^{(a)}$, $1350.3^{(a)}$, $1895.6^{(a)}$ and $2157.4^{(b)}$ keV. For the latter 3 transitions, their U_2A_2 values are inconsistent with them being E1, establishing positive parity for these levels. In addition, the U_4A_4 values for these transitions are all positive, suggesting spin 3 initial levels. Although spin 2 cannot be ruled out, it is considered less likely, and the levels are assigned as $(3)^+$.

Based on this assignment, the following mixing ratios may be deduced,

$$\delta(1350.3^{(a)}) = 76(^{\geq 28}_{<-115})$$
$$\delta(1895.6^{(a)}) = 10(^{+6}_{-3})$$
$$\delta(2157.4^{(b)}) = -8.1(^{+2.2}_{-4.7})$$

All of these solutions give large positive values for A_4.

2229.6 *keV* : $(3,4)^+$

This level has transitions at 527.4 and 1023.2 keV to 4^+ states, and at 1079.0 keV to a 2^+ state. Also, it is fed from the 3108.7 keV level which is assigned as spin (5,6), thus limiting the possible spins to be 3 or 4. From the measured U_2A_2 values, E1 transitions may be ruled out, resulting in the spin assignment $(3,4)^+$ for this level.

2437.9$^{(a)}$, 2570.9$^{(b)}$ *keV* : $(3^+,4)$

Transitions at 1231.7$^{(a)}$ and 1364.7$^{(b)}$ both show large negative values for U_2A_2, which eliminates spins 2 and 3^-, and results in a $(3^+,4)$ spin assignment for these levels. There is a possibility of an E0 component to the 1364.7$^{(b)}$ keV transition which would favour spin 4 for the 2570.9$^{(b)}$ keV level.

There is some evidence that both of these transitions may be contaminated [7] due to the presence of ^{118}Cs. If this is actually so, then the deductions made above for these levels will not be valid.

2422.2$^{(a)}$, 2611.3$^{(b)}$ *keV* : $(2,3,4)^{(a)}$, $(0,2,3,4)^{(b)}$

The anisotropies for the 719.6$^{(a)}$ (to a 4^+) and 1460.7$^{(b)}$ (to a 2^+) keV transitions are unreliable due to contamination from ^{118}Cs and ^{40}K (a strong background line) respectively. The spin assignments given covers the likely range of possible spins for these levels.

6.3 Levels and transitions in ^{118}Te from $^{118}I^m$ decay

The level scheme of ^{118}Te populated in the decay of the high spin ^{118}I isomer is shown in [Fig 6.4] . The γ-ray intensities (relative to the 605.6 keV transition) are the *separated* intensities taken from Table 6.7 and averaged over the ^{32}S and ^{34}S experiments. Experimental anisotropies and polarizations are given in Table 5.2, and Tables 5.4 and 6.7 summarize the parameters deduced for individual levels (spins and parities) and transitions ($(U_\lambda A_\lambda$ and mixing ratios) respectively.

The levels at energies 0.0, 605.6, 957.3, 1150.6, 1206.2, 1481.9, 1702.6, 1891.7, 1976.0 and 2229.6 keV are populated in the decay of both isomers. In the ^{32}S experiment the low spin feed to each of these levels is dominant, and they are all discussed in the previous section. Thus, in this section, levels fed purely by the high spin isomer are discussed.

6.3.1 The first two 6^+ levels

1820.5 *keV* : 6_1^+

This level decays strongly to the 4_1^+ level via a transition at 614.3 keV. In chapter 5.5.2, this was used to obtain a fraction in good sites, $f = 90(9)\%$ from its axial/equatorial anisotropies, using $U_2 = 0.85(5)$ and $U_4 = 0.57(13)$ from Table 5.4. As the *high* spin normalization ratio this gave was the same (to within errors) as the *low* spin ratio from the 1338.7 keV transition, the latter ratio was used for both *high* and *low* spin transitions.

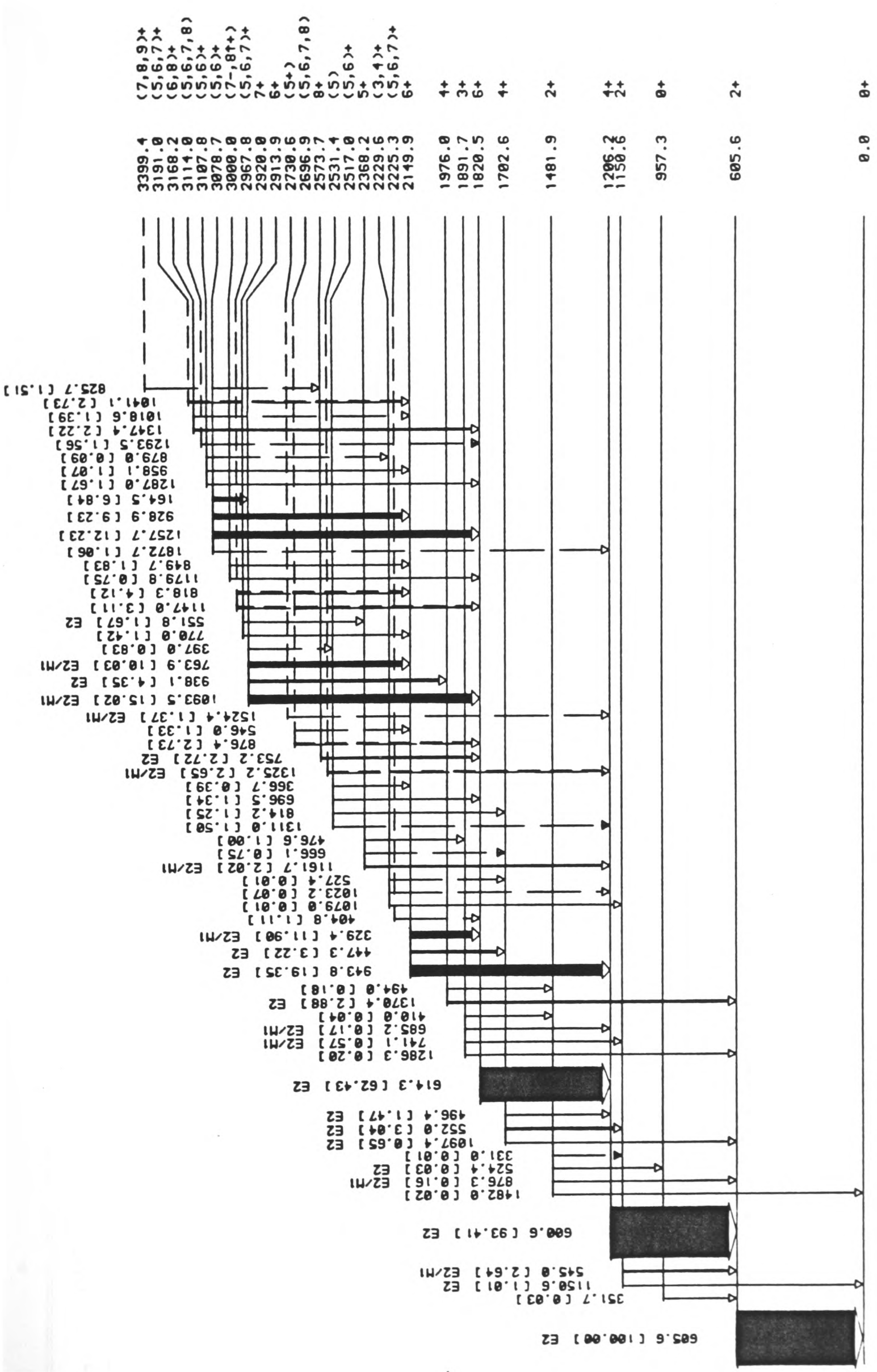

Figure 6.4. ^{118}Te levels populated in the decay of ^{118}I^{m}.

E_γ	$I_\gamma(^{32}S)$	$I_\gamma(^{34}S)$	U_2A_2	U_4A_4	$\lambda = 2$ term	$\lambda = 4$ term	$\alpha_k \times 10^3$	Comment
164.5	(6.84)	6.84	0.211 (0.037)	−0.005 (0.063)			169(25)	E2/M1
329.4	(11.85)	11.90	−0.421 (0.036)	−0.003 (0.052)	$A_2 = -0.538$ (0.059)	$A_4 = -0.005$ (0.107)		δ
(331.0)	0.01	0.01						see low spin
351.7	0.02	0.03						see low spin
366.7	(0.37)	0.39						doublet
(397.0)	(0.86)	0.83	−0.108 (0.081)	0.137 (0.134)				
(404.8)	(1.10)	1.11	−0.115 (0.065)	−0.030 (0.113)				
410.0	0.03	0.04						see low spin
447.3	(3.18)	3.22	−0.289 (0.090)	−0.070 (0.146)	$U_2 =$ 0.717 (0.223)	$U_4 =$ 0.320 (0.700)		E2
476.6	(0.98)	1.00						
494.0	(0.17)	0.18						
496.4	(1.49)	1.47	*	*	$A_2 = -0.268$ (0.037)	$A_4 = -0.142$ (0.317)		see low spin
524.4	0.02	0.03						see low spin
(527.4)	0.01	0.01						
545.0	(2.70)	2.64						see low spin
(546.0)	(1.34)	1.33						
551.8	(1.71)	1.67						see low spin
552.0	(3.15)	3.04	*	*	$A_2 = -0.452$ (0.028)	$A_4 = -0.163$ (0.200)		see low spin
600.6	93.59	93.23	*	*	$A_2 = -0.453$ (0.023)	$A_4 = -0.311$ (0.051)		see low spin
605.6	100.00	100.00						see low spin
614.3	61.70	63.16	−0.348 (0.015)	−0.119 (0.011)	$U_2 =$ 0.864 (0.038)	$U_4 =$ 0.568 (0.053)		E2
(666.1)	0.73	0.78						
685.2	0.16	0.18						see low spin
696.5	1.34	1.33	−0.274 (0.146)	−0.017 (0.240)				
741.1	0.56	0.59						see low spin
753.2	3.05	2.39	−0.320 (0.083)	−0.128 (0.140)	$U_2 =$ 0.839 (0.217)	$U_4 =$ 0.741 (0.813)		E2
763.9	9.90	10.17	−0.498 (0.034)	0.038 (0.043)	$A_2 = -0.532$ (0.075)	$A_4 =$ 0.040 (0.050)	3.2(11)	δ
770.0	(1.71)	1.67						doublet

Table 6.7. Properties of γ-rays in ^{118}Te seen in the decay of $^{118}I^m$.

E_γ	$I_\gamma(^{32}S)$	$I_\gamma(^{34}S)$	U_2A_2	U_4A_4	$\lambda = 2$ term	$\lambda = 4$ term	$\alpha_k \times 10^3$	Comment
770.0	(1.18)	1.42						Doublet
814.2	1.34	1.17	−0.239 (0.126)	−0.227 (0.217)				
(818.3)	5.74	2.50	−0.025 (0.024)	−0.035 (0.042)				
(825.7)	2.08	0.95	−0.159 (0.078)	−0.002 (0.135)				
849.7	2.20	1.45	−0.146 (0.052)	−0.093 (0.090)				
876.3	0.15	0.16						see low spin
(876.4)	2.69	2.78						
(879.0)	0.12	0.06						
928.9	(9.16)	9.23	−0.292 (0.020)	0.029 (0.026)				
938.1	4.03	4.67	−0.377 (0.047)	−0.197 (0.094)	$U_2 =$ 0.935 (0.115)	$U_4 =$ 0.942 (0.453)		$I_i = 6^+$
943.8	19.30	19.40	−0.302 (0.018)	−0.104 (0.020)	$U_2 =$ 0.748 (0.043)	$U_4 =$ 0.496 (0.097)		E2
958.1	0.86	1.28	0.412 (0.352)	−0.253 (0.576)				
(1018.6)	(1.34)	1.39						
(1023.2)	0.10	0.04						
(1041.1)	3.30	2.17	−0.272 (0.081)	0.049 (0.140)				
1079.0	0.01	0.01						
1093.5	16.25	13.79	−0.414 (0.025)	−0.009 (0.029)	$A_2 = -0.442$ (0.061)	$A_4 = -0.010$ (0.031)	1.4(4)	δ
1097.4	0.62	0.67	*	*	$A_2 = -0.471$ (0.156)	$A_4 = -0.728$ (1.324)		see low spin
(1147.0)	4.77	1.45	−0.201 (0.044)	−0.021 (0.073)				
1150.6	1.03	1.00						see low spin
1161.7	2.32	1.72	−0.167 (0.064)	0.107 (0.137)	$A_2 = -0.182$ (0.070)	$A_4 =$ 0.144 (0.185)		(δ)
1179.8	0.73	0.78						
1257.7	(10.75)	12.23						doublet
1286.3	(0.23)	0.20						doublet
1287.0	(1.71)	1.67	−0.343 (0.032)	−0.005 (0.050)				Doublet
(1293.5)	(1.59)	1.56						
(1311.0)	(1.47)	1.50						
(1325.2)	3.42	1.89	0.250 (0.065)	−0.059 (0.114)	$A_2 =$ 0.269 (0.071)	$A_4 = -0.076$ (0.148)		δ

Table 6.7. Properties of γ-rays in ^{118}Te seen in the decay of $^{118}I^m$.

E_γ	$I_\gamma(^{32}S)$	$I_\gamma(^{34}S)$	U_2A_2	U_4A_4	$\lambda = 2$ term	$\lambda = 4$ term	$\alpha_k \times 10^3$	Comment
1347.4	(2.20)	2.22	−0.404 (0.045)	−0.113 (0.070)				
1370.4	2.69	3.07	*	*	$A_2 = -0.533$ (0.040)	$A_4 = -0.271$ (0.239)		see low spin
1482.0	0.01	0.02						see low spin
(1524.4)	1.34	1.39	−0.024 (0.107)	−0.092 (0.426)	$A_2 = -0.025$ (0.115)	$A_4 = -0.119$ (0.552)		δ
(1872.7)	(1.10)	1.06	−0.054 (0.157)	−0.169 (0.262)				

Table 6.7. Properties of γ-rays in ^{118}Te seen in the decay of $^{118}I^m$. Relative γ-ray intensities are quoted for each transition, as deduced from both ^{32}S and ^{34}S experiments (those values shown in brackets are subject to possible systematic errors, and should be treated with caution). Bracketed transitions are only tentatively associated with $^{118}I^m$ decay. The values of $U_\lambda A_\lambda$ quoted are derived from the axial and equatorial anisotropies given in Table 5.2 (a * denotes transitions which are *mixed* high and low spin - see text). Where possible, separate U_λ or A_λ terms are deduced. Conversion coefficients are also quoted for the stronger transitions.

2149.9 *keV* : 6_2^+

There are two transitions at 447.3 and 943.8 keV which go to 4^+ levels, and taking them to be E2($6^+ \rightarrow 4^+$), the averaged de-orientation coefficients $U_2 = 0.75(4)$ and $U_4 = 0.49(10)$ are obtained. These are slightly low compared to the ranges predicted by UACALC in Table 5.4, and significantly lower than the values for the 1820.5 keV level obtained above (this is evident just by comparing the anisotropies of the 614.3 and 943.8 keV transitions).

Using the above U_λ values for the 329.4 keV transition ($6^+ \rightarrow 6^+$), the values $A_2 = -0.54(6)$ and $A_4 = -0.01(11)$ are deduced. This value of A_2 spans the minimum possible value, $A_2^{min}(6^+ \rightarrow 6^+) = -0.51$, and from this a mixing ratio of $\delta \simeq 0.3(3)$ may be estimated. The lower limit of this is close to the more precise measurement, $\delta = 0.01(5)$, of van Ruyven.

6.3.2 High spin levels above 2 MeV

There are many transitions from these high spin levels to the lower lying first and second 6^+ states, and hence it is useful to compare the properties of the $U_\lambda A_\lambda$ coefficients for a transition $I_i \rightarrow 6^+$. By assuming direct feeding to the levels I_i (with $j_\beta = 1$ for $I_i = 5, 7$, $j_\beta = 0, 1$ for $I_i = 7$, and $j_\beta = 2$ for $I_i = 8$), the possible values or ranges of $U_\lambda A_\lambda$ are shown in Table 6.8 for the types of transition indicated

I_i	Transition	U_2A_2	U_4A_4
5^+	E2/M1	$0.927 > \ldots > -0.521$	$0.173 > \ldots > 0.0$
5^-	E1	0.158	0.0
6^+	E2/M1	$0.349 > \ldots > -0.494$	$0.0 > \ldots > -0.514$
6^-	E1	-0.430	0.0
7^+	E2/M1	$1.085 > \ldots > -0.763$	$0.515 > \ldots > 0.0$
7^-	E1	$0.273 > \ldots > 0.259$	0.0
8^+	E2	-0.372	-0.159

Table 6.8 $U_\lambda A_\lambda$ parameters for possible $I_i \rightarrow 6^+$ transitions.

2368.2 *keV* : 5^+

This level spin assignment is from the work of van Ruyven, and there are transitions at 476.6, 666.1 and 1161.7 keV. The first of these is swamped by a strong line in the decay of $^{118}Cs^m$, and the second is too weak to measure useful anisotropies. For the third transition, taking de-orientation coefficients from Table 5.4, values of $A_2 = -0.182(70)$ and $A_4 = 0.14(9)$ are obtained. From this A_2 value, possible mixing ratios $\delta = 10(^{+6}_{-3})$ [$A_4 = 0.56$] or $\delta = 0.26(^{+5}_{-4})$ [$A_4 = 0.04$] may be deduced, the latter of which is slightly preferred due to the small A_4 value. This may be compared with $\delta = 7.2(^{+0.5}_{-1.2})$ by van Ruyven.

2531.4$^{(a)}$, 2730.6$^{(b)}$ *keV* : $(5)^{(a)}, (5^+)^{(b)}$

These levels are tentatively assigned to the high spin decay scheme because of comparison of ^{32}S and ^{34}S intensities for the 1325.2$^{(a)}$ and 1524.4$^{(b)}$ keV transitions, both to the 4_1^+ state. For these transitions, the U_2A_2 values are not consistent with the large negative value expected for a $6^+ \rightarrow 4^+$ transition, leaving the spin 5 alternative.

On this basis, and using Table 5.4, the values $A_2^{(a)} = 0.269(71)$, $A_4^{(a)} = -0.08(15)$ and $A_2^{(b)} = -0.03(12)$, $A_4^{(b)} = -0.12(55)$ are obtained. From the A_2

values the possible mixing ratios are deduced to be $\delta(1325.2)^{(a)} = 0.01(^{+4}_{-3})$ or $-6.9(^{+1.4}_{-2.5}$ and $\delta(1524.4)^{(b)} = 0.17(^{+7}_{-6})$ or $73(^{>+13}_{<-21})$. In both cases, the small A_4 terms favour the solution with a small quadrupole contribution. Unlike the $1524.4^{(b)}$ transition, the $1325.2^{(a)}$ transition could be either E1 or E2/M1, hence the parity of the 2531.4 keV level cannot be determined.

$\underline{2517.0^{(a)}, 3078.7^{(b)}, 3107.8^{(c)}\ keV\ :\ (5,6)^+}$

The transitions at energies $696.5^{(a)}$ and $814.2^{(a)}$ keV, to 6^+ and 4^+ states respectively, both show negative values of U_2A_2, which are inconsistent with the 5^- assignment of van Ruyven for the $2517.0^{(a)}$ keV level, for which positive U_2A_2 values would be expected. It is not possible to distinguish spins 5 and 6, but the U_2A_2 values clearly indicate even parity for this level.

For the $3078.7^{(b)}$ keV level, the positive parity assignment is deduced from the α_k conversion coefficient for the $164.5^{(b)}$ keV transition. The $U_\lambda A_\lambda$ values for the transitions at $928.9^{(b)}$ and $1872.7^{(b)}$ keV (to 6^+ and 4^+ levels respectively) hint at a spin 5 assignment. However, both these transitions have in them some contamination due to transitions in the decay of $^{118}Cs^{g+m}$, making them unreliable[7].

For the $3107.8^{(c)}$ keV level, spin 7 is ruled out on the basis of the $879.0^{(c)}$ keV transition to the $(3,4)^+$ level at 2229.6 keV. The transition at $1287.0^{(c)}$ is the weaker component of a doublet, the other component at 1286.3 being the $3_1^+ \rightarrow 2_1^+$ transition, for which van Ruyven has measured a mixing ratio of $-1.7(^{+2}_{-1})$. Knowing this, it is possible to try and *subtract* out the low spin component. Taking $\alpha(h/l) = 0.21$, with $U_2A_2 = 0.67(5)$ and $U_4A_4 = -0.18(2)$, revised high spin anisotropies may be estimated (using equation 4.14) as

$$W(0) - 1 = \begin{cases} -53.0(4.3) & 15\text{mK} \\ -30.7(5.4) & 32\text{mk} \end{cases}$$

$$W(90) - 1 = \begin{cases} 26.1(3.5) & 15\text{mK} \\ 15.1(5.9) & 32\text{mk} \end{cases} \qquad (6.6)$$

Separation of the $\lambda = 2,4$ components from these anisotropies gives $U_2A_2 = -0.34(3)$ and $U_4A_4 = -0.01(5)$ for the $1287.0^{(c)}$ high spin component. Positive parity for the 3108.7 keV level is based on this negative value of U_2A_2.

2913.9 *keV* : 6^+

This level is assigned 6^+ on the basis of the negative $U_4A_4 = -0.20(9)$ for the 938.1 keV transition to the 4_3^+ level at 1976.0 keV. Taking this transition to be E2, then de-orientation coefficients $U_2 = 0.94(12)$, $U_4 = 0.94(45)$ may be deduced for the level.

There are also two strong transitions from this level to the first two excited 6^+ states, at energies 763.9 and 1093.5 keV. Electron conversion coefficients for these transitions show clearly them to be E2/M1, consistent with the positive parity assignment to the level. Both transitions have large negative U_2A_2 terms and small U_4A_4 terms, and taking the above U_λ values, then $A_2(763.9) = -0.532(75)$, $A_4(763.9) = 0.040(50)$ and $A_2(1093.5) = -0.442(61)$, $A_4(1093.5) = 0.010(31)$.

As in the case of the 329.4 keV transition ($6_2^+ \rightarrow 6_1^+$), the A_2 value for the 763.9 keV transition spans the minimum possible value for a $6^+ \rightarrow 6^+$ transition. From the values of A_2 and A_4, a mixing ratio for this transition can be estimated to lie in the range $0.3 > \delta > 0.0$.

For the 1093.5 keV transition there are two possible solutions for the mixing ratio (from A_2), which are $\delta = 0.63(^{+17}_{-24})$ [$A_4 = -0.15$] or $\delta = 0.00(^{+20}_{-11})$ [$A_4 = 0.00$]. In this case, the small value of A_4 clearly picks out the latter solution.

$2225.3^{(a)}, 2967.8^{(b)}, 3191.0^{(c)}$ *keV* : $(5,6,7)^+$

Three transitions depopulate these levels at energies $404.8^{(a)}$, $818.3^{(b)}$ and $1041.1^{(c)}$ keV, all of which go to either the first or second 6^+ state. The U_2A_2 values for them rule out a negative parity assignment for the initial level, and also are not consistent with being $8^+ \rightarrow 6^+$ E2 transitions. The spin assignment reflects the fact that the U_4A_4 terms are not precise enough to be more selective.

$2696.9^{(a)}, 3114.0^{(b)}$ *keV* : $(5,6,7,8)$

These levels are assigned as high spin on the basis that their transitions, at energies $546.0^{(a)}$, $876.4^{(a)}$ and $1293.5^{(b)}$ keV, all go to 6^+ states. No anisotropy data were available for the first two transitions because they were swamped by strong low spin transitions at very similar energies, and the third transition was too weak for meaningful anisotropies to be quoted.

3168.2 *keV* : $(6,8)^+$

This level has transitions at 1018.6 and 1347.4 keV, both to 6^+ states. The 1018.6 keV transition is the weaker component of a doublet, where the other component is from the low spin 2501.0 $(3)^+$ level. As the properties of both these components are uncertain it is not possible to interpret the combined anisotropies. However, for the 1347.4 keV transition, the negative $U_4A_4 = -0.11(7)$ can be used to eliminate spins 5 and 7, resulting in the assignment $(6,8)^+$.

2920.0 *keV* : 7^+

This level is also observed in the work of van Ruyven where a spin 7^+ assignment is made. There are two transitions from this level at 551.8 and 770.0 keV, both of which are members of doublets, where the major component is a low spin transition. For the 552 keV doublet, the high spin component (assumed $E2^{[2]}$) was successfully subtracted out in the analysis of the 1702.6 4_2^+ level. However, for the 1976.0 4_3^+ level, neither high nor low spin components of the 770 keV doublet are well enough known to make analysis possible.

3000.0 *keV* : $(7^-, 8^+)$

In the work of van Ruyven two levels of spin 8^+ and 7^- are placed at energies of 2999.6 and 2999.8 keV respectively. The 8^+ level has an E2 849.3 keV γ-ray ($I_\gamma = 9.7$) to the 6_2^+ level, and the 7^- level decays to the 6_2^+ and 6_1^+ levels by E1 transitions of energy 849.6 ($I_\gamma = 1.1$) and 1178.9 ($I_\gamma = 7.1$) keV. In this work, transitions at energies 849.7 and 1178.9 keV were observed, and the relative intensities would suggest both these levels to be populated. From the measured $U_2A_2 = -0.15(5)$ for the proposed doublet at 849 keV, it is possible to estimate the relative proportions of the two components. Taking $U_2A_2(8^+) = -0.37$ and $U_2A_2(7^-) = 0.26$, the intensity of the 8^+ component is about 1.8(5) times that of the 7^- component, which would make the two transitions from the 7^- comparable in intensity (in contradiction to van Ruyven).

In this work, the coincidence data does not show any clear evidence for these very closely spaced levels at 3 MeV, and the data can be interpreted in terms of just a single level at 3000.0 keV, decaying by 849.7 and 1178.9 keV γ-rays . In this the case, the spin assignment of this level would be $(5, 6, 7)^+$.

Unfortunately, it is not possible to distinguish between the existence of one or two discrete levels at 3 MeV in this data.

2573.7 *keV* : 8^+

This level decays to the 6_1^+ level by a transition at 753.2 keV. The measured anisotropies for this transition, being comparable with those of the 614.3 keV transition ($6^+ \rightarrow 4^+$), are consistent with it being stretched E2, with a spin 8^+ assignment for the level[2]. Taking $A_2 = -0.38$ for an $8^+ \rightarrow 6^+$ transition, a value $U_2 = 0.84(22)$ may be deduced for this level, which is consistent with the values estimated in Table 5.4.

3399.4 *keV* : $(7,8,9)^+$

This level decays via an 825.7 keV transition to the 8_1^+ level, and is assigned 9^- by van Ruyven. However, the measured $U_2A_2 = -0.16(8)$ is not consistent with the expected value of -0.43 for such an assignment. In fact, the transition looks to be E2/M1 rather than E1, and leads to the above assignment.

6.4 The Interacting Boson Model

6.4.1 General outline

The structure of nuclei near to closed shells is largely understood on the basis of the shell model [8] , which emphasizes independent particle motion. However, on moving away from closed shells, such calculations rapidly become impractical, due to the enormous number of basis states that are required in the full shell model space. Instead, the structure of these nuclei can be related to the occurrence of *collective* phenomena, which have been discussed extensively in terms of *geometrical* models [9] . Such models describe collective features in

terms of a few collective parameters, which are connected with the concept of nuclear *shape* and its deformations.

The Interacting Boson Model (IBM) is an alternative *algebraic* approach to describe collective states in nuclei. In its simplest form (IBM-1), it is assumed that the low lying states in nuclei away from closed shells can be formed from a system consisting of N bosons, which can have angular momentum $L = 0$ (s-bosons), or $L = 2$ (d-bosons). The total number (N) of such bosons is determined by the number of nucleon or hole pairs outside the nearest closed shells, no distinction being made between protons and neutrons. In this respect, IBM-1 is similar to the collective model[9], which describes the observed spectra in terms of *shape*-variables, without any reference to nucleon degrees of freedom. Such a geometric interpretation of the IBM has been given by Dieperink [10] .

In order to connect the collective (boson) degrees of freedom with the microscopic (nucleon) degrees of freedom the IBM-2 model was introduced [11] . In this model the assumption is that the important particle configurations in even-even nuclei are those in which *identical* particles are paired together in states with total angular momentum $L = 0$ and $L = 2$. Proton (neutron) bosons with angular momentum $L = 0$ are denoted by $s_{\pi(\nu)}$, and those with $L = 2$ by $d_{\pi(\nu)}$. The numbers of proton (N_π) and neutron bosons (N_ν) are counted from the nearest closed shells.

Thus, the IBM offers a bridge between the shell model[8], in which nuclei are described in terms of individual nucleons, and the rotational and vibrational models of collective motion[9], which largely ignore the motion of individual nucleons. The IBM has been extensively described in various review articles covering both theoretical [12] [13] [14] and experimental aspects [15] , and in particular, a full and very readable introduction to the subject is given by Scholten in his Ph.D. thesis [16] . The main features of the IBM-2 model, relevant to the present discussion will now be given.

6.4.2 The IBM-2 Hamiltonian

The principal assumption in this model is that the low lying collective states in even-even nuclei (away from closed shells) can be described in terms of *interacting* proton and neutron bosons, with angular momenta $L = 0$ and $L = 2$. Shell model calculations of the effective interaction between pairs of identical nucleons in the same shell model orbit [17] show that the interaction is most strongly attractive when the pair are in an $L = 0$ (S) state. This is the well known pairing interaction which, for example, is responsible for the 0^+ ground states observed in even-even nuclei, and which limits the number of valence nucleons active in low lying states. The interaction remains attractive for a pair in an $L = 2$ (D) state, while the states with spins $L \geq 4$ become repulsive. Consequently, the nucleons tend to form pairs with relative angular momentum of $L = 0$ or $L = 2$.

For a given shell there are several orbits and hence several possible 0^+ or 2^+ pairs. The *s*- and *d*-bosons may be identified with the *lowest-lying* pairs with spins 0 and 2, respectively, which are in some sense collective states[16] . Thus, the bosons are interpreted as *collective* pairs of protons (π) or neutrons (ν) coupled to angular momentum $L = 0$ (*s*-boson) or $L = 2$ (*d*-boson), and although the *full* shell model space has been truncated to a much smaller model space, it should still be capable of describing the low lying collective states of the nucleus. The details of the transformation or *mapping* of both states and matrix elements from the shell model subspace of the lowest lying 0^+ and 2^+ states to the boson model space are technically complex, and this is discussed, for instance, by Otsuka, Arima, Iachello and Talmi[11] [18] .

In the above discussion, only pairs of *identical* nucleons have been considered. The reason that proton-neutron pairs are excluded is that in medium to heavy nuclei the valence protons and valence neutrons occupy different major shells, with the result that the formation of proton-neutron pairs becomes very

improbable (for lighter nuclei, however, such pairs do need to be taken into account).

The boson IBM-2 Hamiltonian, therefore, reflects the interactions between the valence protons and neutrons. The Hamiltonian is written in terms of boson creation and annihilation operators and has the form,

$$H_{IBM-2} = \epsilon_\pi n_{d_\pi} + \epsilon_\nu n_{d_\nu} + \kappa\, Q_\pi^{(2)} \cdot Q_\nu^{(2)} + V_{\pi\pi} + V_{\nu\nu} + M_{\pi\nu} \tag{6.7}$$

where the operators are defined by,

(i) $\epsilon_{\pi(\nu)}$ is the energy required to create a proton (neutron) d-boson from a proton (neutron) s-boson. The proton (neutron) d-boson number operator is $n_{d_\rho} = d_\rho^\dagger \tilde{d}_\rho$, with $\rho = \pi(\nu)$, where $\tilde{d}_{\rho\mu} = (-1)^\mu d_{\rho-\mu}$ creates a boson hole with angular momentum $(L, M) = (2, \mu)$.

(ii) $Q^{(2)}_{\pi(\nu)}$ is the proton (neutron) quadrupole operator and has the form

$$Q_\rho^{(2)} = (s_\rho^\dagger \tilde{d}_\rho + d_\rho^\dagger s_\rho)^{(2)} + \chi_\rho (d_\rho^\dagger \tilde{d}_\rho)^{(2)} \tag{6.8}$$

where χ_ρ is the ratio of the d_ρ-boson conserving component to the d_ρ-boson non-conserving component. The superscript $^{(2)}$ denotes that the boson operators are coupled to angular momentum $L = 2$, and $\rho = \pi(\nu)$ corresponds to proton (neutron) bosons.

(iii) κ is the strength of the quadrupole interaction between proton and neutron bosons.

(iii) $V_{\rho\rho}$, which has parameters C_0^ρ, C_2^ρ and C_4^ρ, is the *residual* interaction between like bosons and takes the form,

$$V_{\rho\rho} = \frac{1}{2} \sum_{L=0,2,4} C_L^\rho \sqrt{2L+1}\, \left[(d_\rho^\dagger d_\rho^\dagger)^{(L)} (\tilde{d}_\rho \tilde{d}_\rho)^{(L)} \right]^{(0)} \tag{6.9}$$

(iv) and $M_{\pi\nu}$, which has parameters ξ_1, ξ_2 and ξ_3, acts between proton and neutron bosons and has the form,

$$M_{\pi\nu} = \xi_2 (d_\pi^\dagger s_\nu^\dagger - s_\pi^\dagger d_\nu^\dagger)^{(2)} \cdot (\tilde{d}_\pi s_\nu - s_\pi \tilde{d}_\nu)^{(2)} + \sum_{L=1,3} 2\xi_L (d_\pi^\dagger d_\nu^\dagger)^{(L)} \cdot (\tilde{d}_\pi \tilde{d}_\nu)^{(L)} \tag{6.10}$$

The main part of the interaction between like bosons is incorporated into the boson energies ϵ_π and ϵ_ν from (i), which originate from the strong pairing interaction between identical nucleons (giving rise to a difference in the *s*- and *d*-boson energies).

Furthermore, multipole expansions of the neutron-proton interaction, as determined for example from the level structure of ^{208}Bi [19] show that the strongest multipole component in the interaction is the quadrupole term (apart from the monopole interaction, which contributes to the binding energies but has little affect on the spectrum of excited states). Therefore, the quadrupole interaction (ii) is included in the Hamiltonian, as this is expected take into account the most important properties of the neutron-proton interaction (which plays a dominant role in the spectra of even-even nuclei, as Casten [20] for instance, discusses).

The *d*-boson energies and the neutron-proton quadrupole interaction are the principal terms in the Hamiltonian, and in most calculations it is assumed that while ϵ_ρ and κ_ρ vary with both N_π and N_ν, ξ_π and ξ_ν depend only on N_π and N_ν respectively.

Although the major part of the interaction between like nucleons is included in the *d*-boson energies, additional terms are taken into account by $V_{\pi\pi}$ and $V_{\nu\nu}$ in (iii). These interactions are expected to be important only when either the protons or neutrons are near a closed shell, so that the normally dominant neutron-proton quadrupole interaction is suppressed by the lack of valence neutrons or protons.

Finally, the Majorana term, $M_{\pi\nu}$, is added to the Hamiltonian. This term affects only the position of those states which are not fully symmetric with respect to exchange of the proton and neutron degrees of freedom, relative to those which are fully symmetric, and is used to adjust the relative positions of the two sets of states. It is usually found that the low lying states are fully symmetric, so $M_{\pi\nu}$ is used to push the *mixed* symmetry states up in energy.

The fully symmetric states correspond to those calculated in IBM-1, while the mixed symmetry states are unique to IBM-2.

The energy levels and corresponding wavefunctions of the IBM-2 Hamiltonian, described above, may be calculated using the code NPBOS (written by Otsuka).

6.4.3 Electromagnetic transition rates

In addition to energy levels, it is also possible to calculate other nuclear properties within the framework of IBM-2. Among these are electromagnetic transition rates, and of particular interest for the present studies are the comparison of observed E2, M1 and E0 *relative* transition rates with theoretical predictions.

The E2 transition operator can be written as[13]

$$T(E2) = e_\pi Q_\pi^{(2)} + e_\nu Q_\nu^{(2)} \tag{6.11}$$

where e_π and e_ν are the proton and neutron boson effective charges respectively (in units of $e\text{fm}^2$), and the operators $Q_\rho^{(2)}$ are given by equation (6.8). Although, the quadrupole operators in the Hamiltonian may in principle be different from those in the above transition operator, they are usually taken to be the same. The boson effective charges e_π and e_ν are assumed to depend only on N_π and N_ν respectively.

The M1 transition operator may be written in the form [21]

$$T(M1) = \sqrt{\frac{3}{16\pi}}\,(g_\pi - g_\nu)\left[L_\pi^{(1)} - L_\nu^{(1)}\right] \tag{6.12a}$$

where

$$L_\rho^{(1)} = \sqrt{10}\,\left[d_\rho^\dagger \tilde{d}_\rho\right]^{(1)} \tag{6.12b}$$

and g_π, g_ν are boson g-factors, in units of $\mu_N = e\hbar/2mc$, for protons and neutrons respectively (values of $g_\pi = 1$ and $g_\nu = 0$ are commonly taken). An important feature is that while all M1 transitions are forbidden in IBM-1 (using lowest order operators), this is not the case in IBM-2, when $g_\pi \neq g_\nu$.

The corresponding reduced transition rates are given by

$$B(E2, I_i \rightarrow I_f) = \frac{|\langle I_f \| T(E2) \| I_i \rangle|^2}{2I_i + 1} \tag{6.13}$$

and

$$B(M1, I_i \rightarrow I_f) = \frac{|\langle I_f \| T(M1) \| I_i \rangle|^2}{2I_i + 1} \tag{6.14}$$

and the $E2/M1$ multipole mixing ratio can be written,

$$\delta(E2/M1) = 0.00832 \times E_\gamma\,[\mathrm{MeV}] \times \frac{\langle I_f \| T(E2) \| I_i \rangle\,[\mathrm{efm}^2]}{\langle I_f \| T(M1) \| I_i \rangle\,[\mu_N]} \tag{6.15}$$

using the Steffen phase convention [22] .

Finally, the E0 transition operator may be written as [23] [24]

$$T(E0) = \gamma_{\pi\pi} N_\pi + \gamma_{\pi\nu} N_\nu + \beta_{\pi\pi} d_\pi^\dagger \tilde{d}_\pi + \beta_{\pi\nu} d_\nu^\dagger \tilde{d}_\nu \tag{6.16}$$

where $\gamma_{\pi\pi}$ and $\gamma_{\pi\nu}$ are the proton monopole polarizabilities due to the proton and neutron bosons, while $\beta_{\pi\pi}$ and $\beta_{\pi\nu}$ describe the effects of the proton and neutron deformation on the proton distribution (i.e. the proton quadrupole polarizability). Information on these parameters may most easily be obtained from studies of nuclear charge radii [25] .

The corresponding E0 transition matrix element between states $|i\rangle$ and $|f\rangle$ is given by,

$$\begin{aligned} \rho_{if}(E0) &= \frac{Z}{R_0^2} \langle f | r_\pi^2 | i \rangle \\ &= \frac{Z}{R_0^2} \left[\beta_{\pi\pi} \langle f | d_\pi^\dagger \tilde{d}_\pi | i \rangle + \beta_{\pi\nu} \langle f | d_\nu^\dagger \tilde{d}_\nu | i \rangle \right] \end{aligned} \tag{6.17}$$

where R_0 is the nuclear radius.

Electromagnetic transition rates may be calculated using the code NPBEM, written by Otsuka, which makes use of the wavefunctions of the IBM-2 Hamiltonian that are calculated by the code NPBOS.

6.4.4 Configuration mixing

A characteristic feature of many semi-magic (or nearly semi-magic) nuclei is the occurrence of low lying *intruder* states. These states typically involve configurations in which a few particles are excited across a major shell gap. In heavy nuclei, where such states have only recently been identified and studied [26], the valence neutrons occupy the orbits of the next major shell relative to the protons. Excitation of protons into the same major shell as the valence neutrons can lead to a significant increase in the neutron-proton interaction energy [27], giving rise to a low lying intruder configuration (one reason for this is simply that the neutron-proton interaction energy scales roughly as $N_p \times N_n$, whereas the pairing interaction scales roughly as $N_p + N_n$).

As a consequence of the increased neutron-proton interaction the *intruder* configuration is also more deformed than the normal configuration. Generally speaking, the normal configuration has a *vibrational* character, while the intruder, being more deformed, is more *rotational* in character. Thus, two quite different structures may *co-exist* in the same energy region, and in general, there will also be some *mixing* between these two structures.

In order to provide a quantitative description of this kind of configuration mixing, Duval and Barrett [28] have introduced an extension of the IBM-2 model. The normal configuration is described in a basis with N_π proton and N_ν neutron bosons, which interact via the usual IBM-2 Hamiltonian given by equation (6.7). The intruder configuration is assumed to involve a two-proton excitation, and is again described in the IBM-2 formalism, but now with $N_\pi + 2$

proton and N_ν neutron bosons (for simplicity no distinction is made between bosons which are in different major shells). The two configurations are now coupled by the interaction

$$H_{mix} = \alpha(s_\pi^\dagger s_\pi^\dagger + s_\pi s_\pi)^{(0)} + \beta(d_\pi^\dagger d_\pi^\dagger + \tilde{d}_\pi \tilde{d}_\pi)^{(0)} \tag{6.18}$$

which creates a proton boson above the relevant shell gap, and a boson hole below it. The terms α and β are adjustable parameters to describe the strength of the interaction between the two configurations.

Mixing calculations of this type are usually performed in two steps,

(i) the Hamiltonian H_{IBM-2} is diagonalized for each configuration separately, using the appropriate parameters in each case (i.e. *vibration*-like or *rotation*-like).

(ii) the combined Hamiltonian $(H_{IBM-2} + H_{mix})$ is then diagonalized in a basis provided by the lowest eigenstates of the N_π and $N_\pi + 2$ configurations. In this step an energy Δ is added to the eigenvalues of the intruder configuration, which represents the *extra* energy needed to excite this configuration. The code NPMIX (written by Heyde *et al*) is used to perform the *mixing* of the normal and intruder wavefunctions, provided by NPBOS.

The results of such mixing calculations will be presented in the next section with reference to even-even Te isotopes, concentrating in particular on ^{118}Te.

6.5 Interpretation of the low lying levels in ^{118}Te

6.5.1 Introduction

In the vicinity of the $Z = 50$ proton shell closure, intruder configurations, although strongly mixed with the normal ones, have been identified in even-even Pd ($Z = 46$) [29], Cd ($Z = 48$) [30] [31], Sn ($Z = 50$) [32] and Xe ($Z = 54$) [33]. In odd-A nuclei, the presence of *rotation-like* particle-hole excitations across the $Z = 50$ shell gap have also been identified [34] in Ag ($Z = 47$), In ($Z = 49$), Sb ($Z = 51$), I ($Z = 53$) and Cs ($Z = 55$). Hence the question arises, do intruder states also exist in even-even Te ($Z = 52$) nuclei?

There are several distinctive properties associated with intruder states,

(i) considerable deformation due to the neutron-proton interaction between the *increased* number of valence particles outside the closed shell, as compared with the normal configuration,

(ii) a rotational band built upon the intruder 0^+,

(iii) increased excitation cross-sections in specific few nucleon transfer reactions, as compared with cross-sections to the ground state.

As mentioned in chapter 5.1, the study of ^{118}Te forms part of a broader systematic study of even-even Te nuclei in this mass region, which has been undertaken using the Daresbury on-line isotope separator. One of the most important aspects of this work has been the recent experimental identification [35] of *intruder* states and their theoretical description in terms of the *mixed* IBM-2 formalism, outlined in the previous section.

As compared with the structures observed in the even-even Cd and Sn isotopes, the low lying levels in Te have a very different pattern, suggesting a stronger *mixing* between the two *co-existing* configurations. Some results of

these IBM-2 *mixed* calculations[1] will now be presented, for comparison with experimental data obtained in this work for ^{118}Te.

6.5.2 The normal and intruder configurations

The basic philosophy behind the calculations was to choose the intruder ($N_\pi = 3$) parameters to reproduce the behaviour of the low lying excitations together with electromagnetic transition probabilities, in a system where the normal configuration ($N_\pi = 1$) was considered to be transitional between the SU(5) and O(6) symmetries. As a whole, the parameters of the IBM-2 Hamiltonian used for the normal configuration were basically in line with previously published values in the region around $Z \sim 50$ (e.g. see Sambataro [36]).

The main source of ambiguity in mixing calculations is the choice of parameters for the intruder configuration. In particular, the strength of the neutron-proton interaction (via the $Q_\pi^{(2)} \cdot Q_\nu^{(2)}$ term) should be larger for the intruder configuration than for the normal configuration, in order to bring it low in energy. As a result, The parameters for the $N_\pi = 3$ configuration were chosen so that the energy spectra resembled those observed in Ru(6 proton holes) [37] and Ba(6 protons) [38], which clearly display rotational properties.

In ^{118}Te the best fit to the experimental data was achieved for the following values of the mixing parameters,

$$\Delta = 5.20 \quad \text{MeV}$$

$$\alpha = 0.22 \quad \text{MeV}$$

$$\beta = 0.11 \quad \text{MeV}$$

The value of Δ is in agreement with the following estimate in terms of two-proton separation energies [39]

$$\Delta = S_{2p}(Z,N) - \Big\{ S_{2p}(Z+2,N) + \big[S_{2p}(Z+2,N) - S_{2p}(Z+4,N) \big] \Big\} \qquad (6.19)$$

which gives a value $\Delta \approx 5$ MeV in the $Z = 50$ region. The value of the mixing parameter α is relatively large when compared with previous calculations (e.g. values of $\alpha = \beta = 0.08$ MeV were used for Cd isotopes[31]).

Recent microscopic calculations of mixing parameters [40] predict values of α roughly a factor of 2 larger than β, but with both being considerably larger in maginitude than is observed experimentally. These results are, however, sensitive to the method of calculation, and the *apparent* dependence of α and β on the detailed structure of a particular nucleus does not at present allow any systematic trends for these parameters to be deduced.

6.5.3 Energy spectra

To give an illustration of general trends as a function of neutron number, the experimental 0^+ and 2^+ energy levels are compared with the results of *mixed* IBM-2 calculations in [Fig 6.5] and [Fig 6.6] respectively. In both these figures, levels drawn with *thickened* lines indicate admixtures of the *lowest* intruder state (of that particular spin). The size of this admixture is also quoted as a percentage.

In both figures the intruder *strength* can be seen to be at a minimum in energy at mid-shell (i.e. for ^{118}Te), and to rise rapidly as the number of valence neutrons decreases, on moving away from mid-shell. This is particularly pronounced for the first two excited 0^+ states, which both have sizable intruder components. In contrast, the 2_1^+ states in [Fig 6.6]are almost pure normal configuration and their energies show very little neutron number dependence, as would be expected.

In [Fig 6.7] the first two calculated excited 0^+ states are shown (along with the relative intruder admixtures). Also the position of the *unmixed* 0^+ intruder state (denoted by $0_{3\pi}^+$) is shown. The 0^+ intruder strength, taken as a weighted *average* between the two 0_{cal}^+ levels, is indicated by a * for each nucleus.

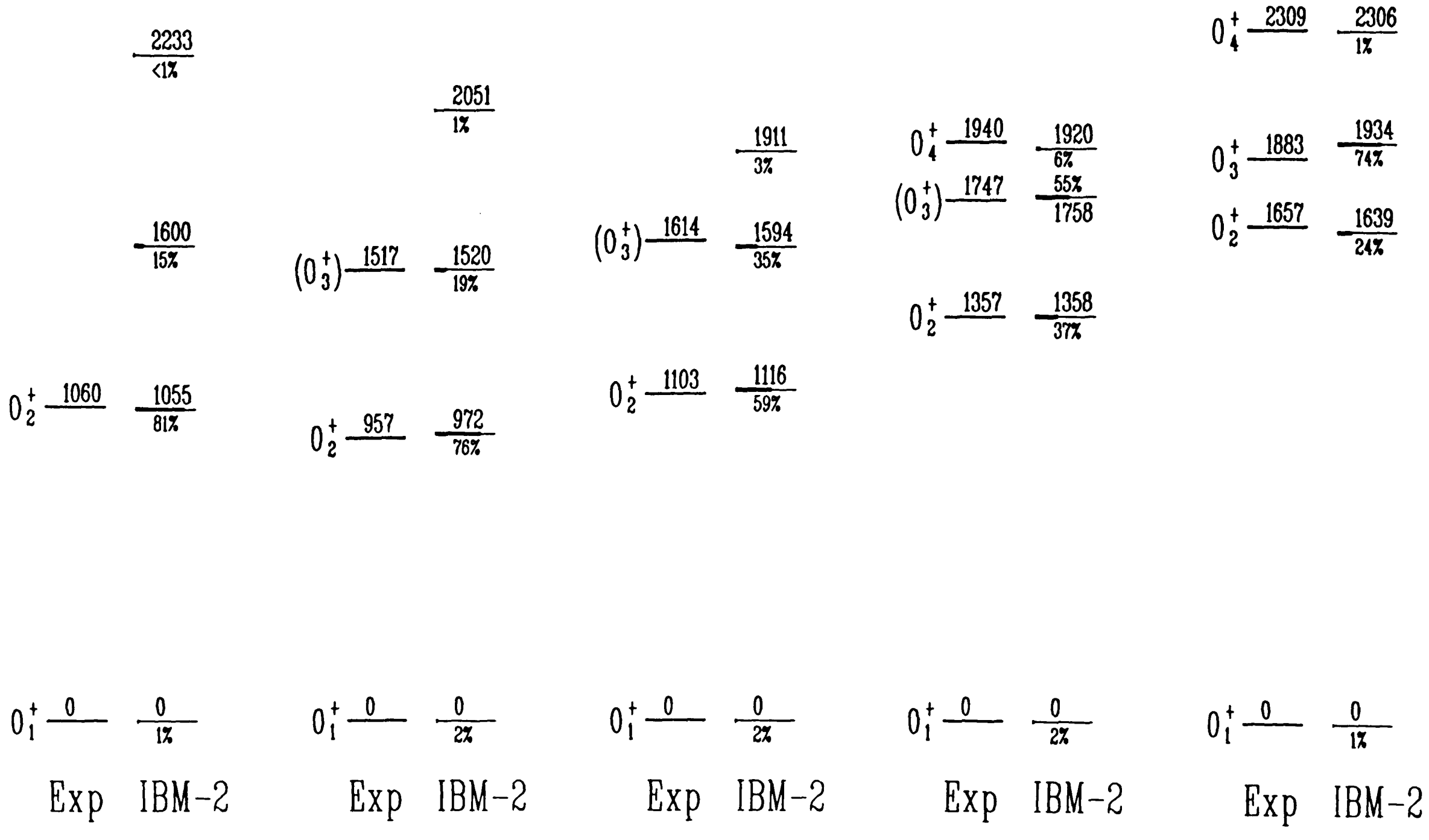

Figure 6.5. Comparison of experimental and calculated (IBM-2) 0^+ levels for $^{116-122}$Te.

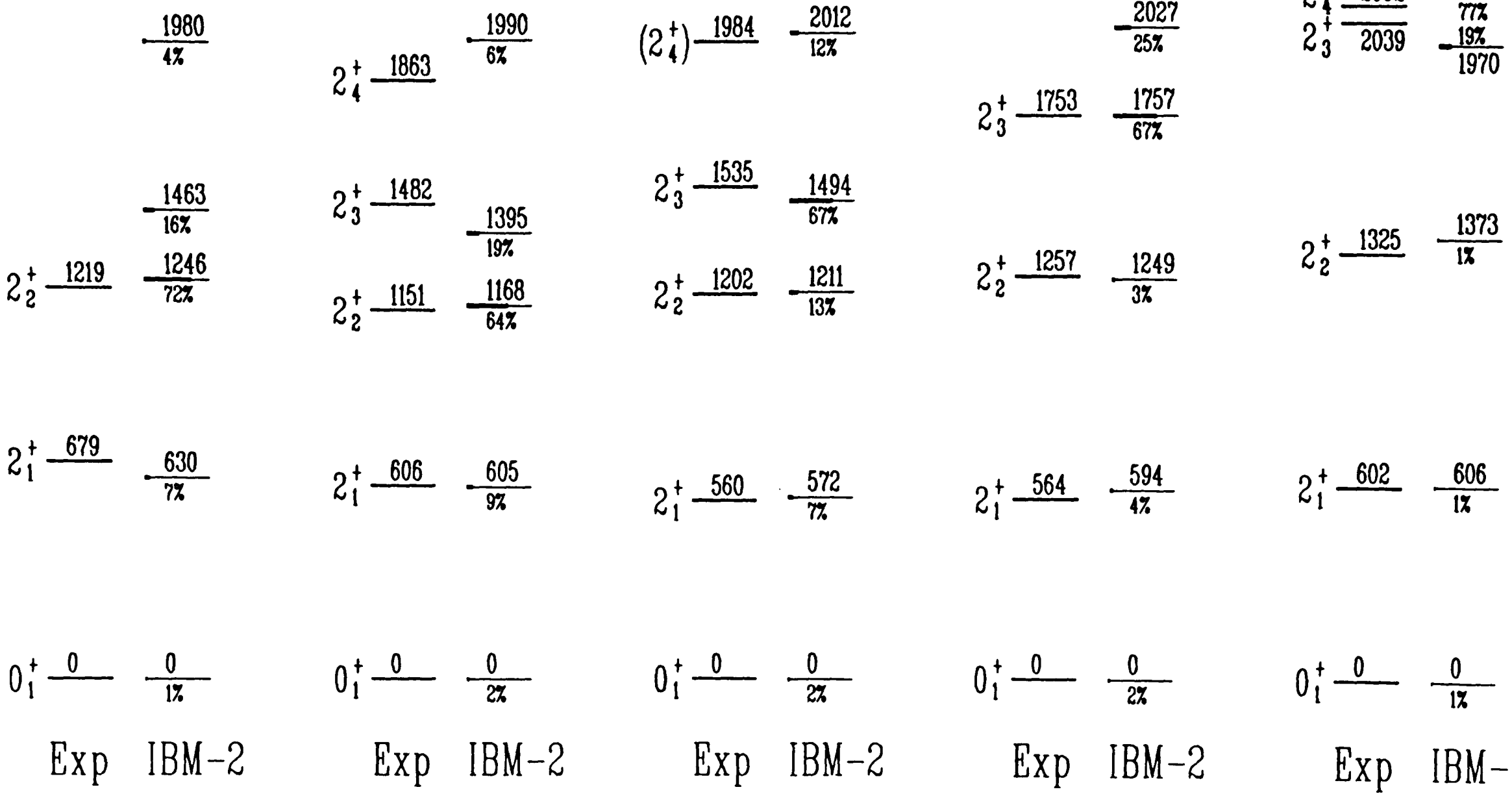

Figure 6.6. Comparison of experimental and calculated (IBM-2) 2^+ levels for $^{116-122}$Te.

For comparison, the experimental $9/2^+$ energy levels for the corresponding odd-A I nuclei are also plotted. These levels have been clearly identified with the [404]9/2 intruder orbital [41] [42] [43], and it is interesting to note the strong similarity between the intruder configuration excitation energies for these two systems, as a function of neutron number.

However, the Te intruder configuration (a two-proton excitation) lies at an energy roughly twice that of the I intruder configuration (which is a one-proton excitation). Such a *scaling* property has recently been discussed by Heyde *et al* [44].

The calculated energy levels for ^{118}Te are shown in [Fig 6.8] for energies up to $\sim$ 2.5 MeV. They are ordered into groups according to increasing number of *d*-bosons, which provides an opportunity to study possible collective band structures in this nucleus. For comparison, the *better* known experimental levels are also plotted in [Fig 6.8] , and the agreement is seen to be good, particularly for the 0^+ and 2^+ states.

In [Fig 6.8] it can be seen that there is strong mixing between the normal and intruder configurations. This is perhaps one of the reasons why rotational bands built on intruder states in Te nuclei have not been observed experimentally (due to the *strong* mixing of these bands giving rise to different structures).

6.5.4 Electromagnetic properties

In order to estimate E2 and M1 transition strengths in these *mixed* calculations, it is first of all necessary to modify the operators introduced in section 6.4.3, to take into account contributions from both the normal and intruder configurations.

Consequently, the E2 operator may be written in the form

$$T(E2) = e_1(e_{\pi 1}Q_\pi^{(2)} + e_{\nu 1}Q_\nu^{(2)}) + e_3(e_{\pi 3}Q_\pi^{(2)} + e_{\nu 3}Q_\nu^{(2)}) \qquad (6.20)$$

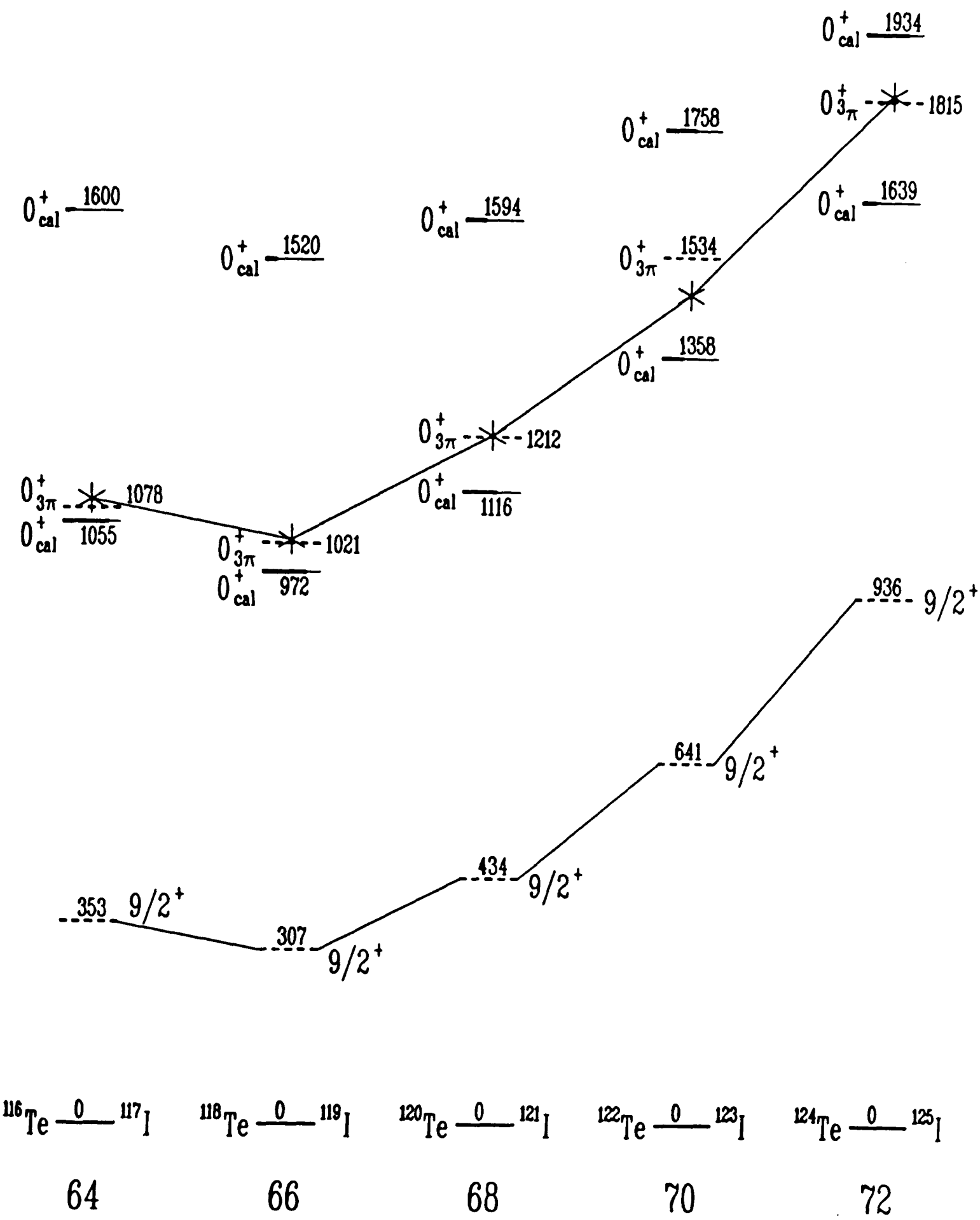

Figure 6.7. Comparison of the calculated (IBM-2) 0^+ intruder *strength* in Te isotopes, with the $9/2^+$ intruder states observed in odd-A I nuclei, as a function of neutron number (64 – 72).

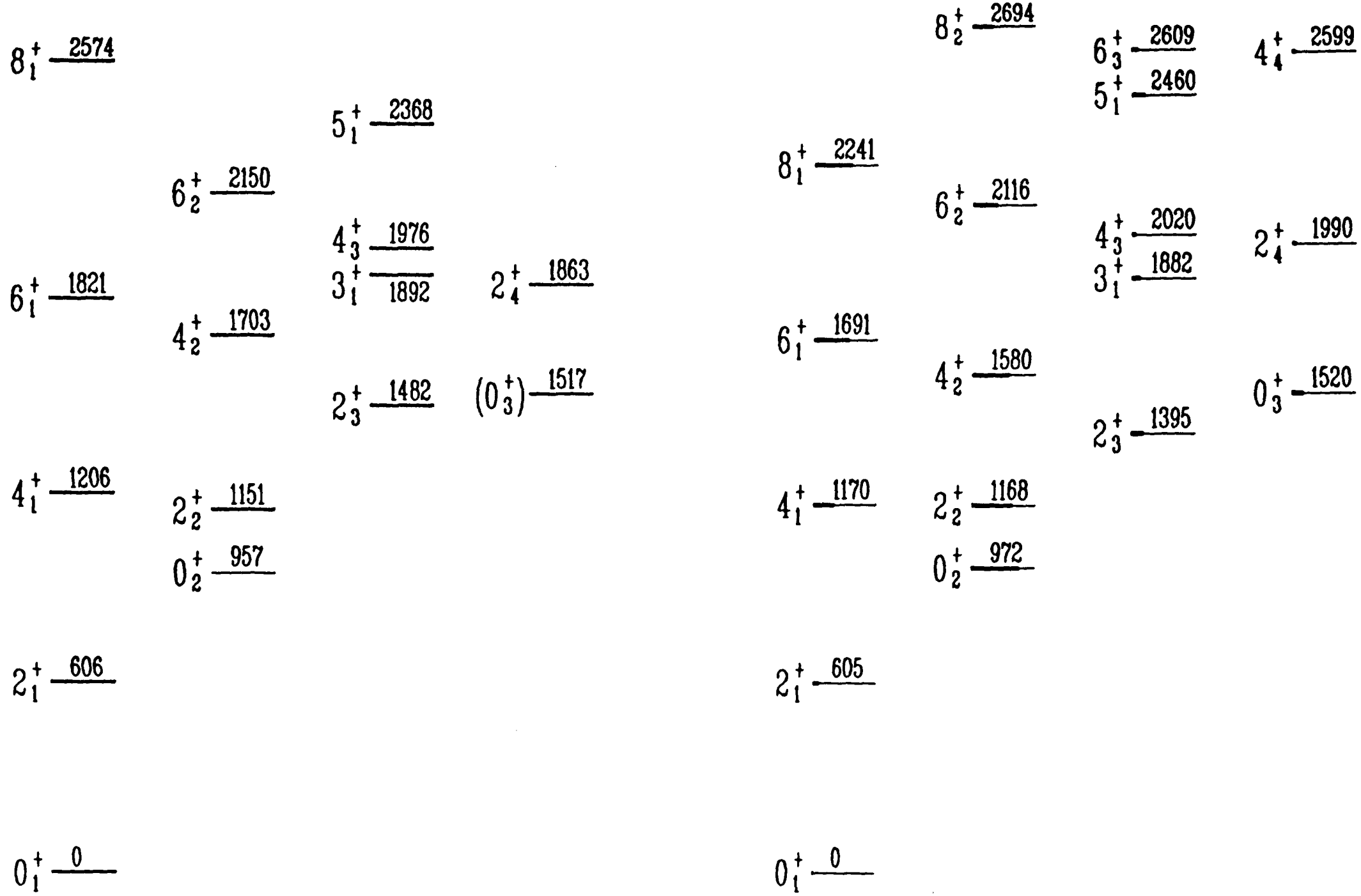

Figure 6.8. The better known experimental energy levels for ^{118}Te below 2.5 MeV, as compared with IBM-2 *mixed* calculations. The strength of an intruder admixture to a level is indicated by *heavy* line.

where the terms $Q_\rho^{(2)}$ are defined in equation (6.8), and the subscripts $_1$ and $_3$ refer to the normal and intruder configuration respectively. For simplicity, the effective boson charges for the two configurations $e_{\rho 1,3}$ were taken to be the same. In the present calculations the ratio $e_3/e_1 = 1.2$ was taken, and comparison of theoretical B(E2) branching ratios with the corresponding experimental values is given in Table 6.9.

$(I_i \rightarrow I_f)/(I_i \rightarrow I_{f'})$	Theory (IBM-2)	Experiment
$(2_2^+ \rightarrow 2_1^+)/(2_2^+ \rightarrow 0_1^+)$	103	115(10)
$(2_3^+ \rightarrow 2_2^+)/(2_3^+ \rightarrow 2_1^+)$	2.8	7(2)
$(3_1^+ \rightarrow 2_2^+)/(3_1^+ \rightarrow 2_1^+)$	17	48(9)
$(3_1^+ \rightarrow 2_2^+)/(3_1^+ \rightarrow 4_1^+)$	1.0	0.75(7)
$(4_2^+ \rightarrow 2_2^+)/(4_2^+ \rightarrow 2_1^+)$	120	140 (20)
$(4_2^+ \rightarrow 2_2^+)/(4_2^+ \rightarrow 4_1^+)$	4.0	1.2(2)
$(0_3^+ \rightarrow 2_2^+)/(0_3^+ \rightarrow 2_1^+)$	10.3	65(20)

Table 6.9 Theoretical B(E2) branching ratios compared with experimental values in ^{118}Te. Any possible M1 contribution to these transitions has been neglected in the ratios quoted.

In a similar way to above, the M1 transition operator for the mixed configurations can be approximated as

$$T(M1) = \sqrt{\frac{3}{4\pi}}\,(g_\pi - g_\nu)\left[L_{\pi 1}^{(1)} + L_{\pi 3}^{(1)}\right] \tag{6.21}$$

The effective proton and neutron g-factors were taken as 0.7 and 0.15 respectively, for both configurations. Also, the contributions from the two configurations were assumed to be equal (due lack of information on the various parameters). E2/M1 mixing ratios were calculated using the mixed wavefunctions, and the results are presented in Table 6.10, along with the experimental values for comparison.

The results of the B(E2) branching ratio and mixing ratio calculations are in generally in good agreement with the experimental data, which combined

E_γ (exp)	$I_i \rightarrow I_f$	Theory (IBM-2)	Experiment
545.0	$2_2^+ \rightarrow 2_1^+$	-13.1	$\delta > 12$ or $\delta < -29$
876.3	$2_3^+ \rightarrow 2_1^+$	-5.1	$-0.7 > \delta > -5.8$
712.4	$2_4^+ \rightarrow 2_2^+$	$+3.1$	$\delta = 1.8(^{+1.2}_{-0.7})$ or $0.08(^{+24}_{-18})$
1286.3	$3_1^+ \rightarrow 2_1^+$	-5.5	$-1.7(^{+2}_{-1})$[3]
741.1	$3_1^+ \rightarrow 2_2^+$	-7.6	$\delta = -44(^{+16}_{-60})$
685.2	$3_1^+ \rightarrow 4_1^+$	-5.1	$\delta = -11(^{+3}_{-8})$ or $0.16(^{+3}_{-4})$
496.4	$4_2^+ \rightarrow 4_1^+$	-2.1	$\delta = 1.48(^{+14}_{-13})$
329.4	$6_2^+ \rightarrow 6_1^+$	-1.1	$\delta \simeq 0.3(3)$

Table 6.10 Theoretical E2/M1 mixing ratios compared with experimental values in ^{118}Te.

with the very good fit to the observed energy levels, supports the validity of this method of interpretation.

It is also possible to to calculate E0 transition probabilities. If the E0 transition operator is approximated by neglecting neutron polarizability effects on the charge distribution, then

$$T(E0) = \gamma_{\pi\pi} N_\pi + \beta_{\pi\pi} d_\pi^\dagger \tilde{d}_\pi \tag{6.22}$$

and following the approach of Heyde *et al*[30] the following E0 transition matrix element can be defined,

$$\rho_{if}(E0) = A_{if} + \frac{Z}{R_0^2}\beta_{\pi\pi 1}\langle f|d_{\pi 1}^\dagger \tilde{d}_{\pi 1}|i\rangle + \frac{Z'}{R_0'^2}\beta_{\pi\pi 3}\langle f|d_{\pi 3}^\dagger \tilde{d}_{\pi 3}|i\rangle \tag{6.23a}$$

where

$$A_{if} = \langle f|\gamma_{\pi\pi 1} N_{\pi 1} + \gamma_{\pi\pi 3} N_{\pi 3}|i\rangle \tag{6.23b}$$

The parameters used in the evaluation of equation (6.23) were $A_{if} = 0.12\text{fm}^2$, $\beta_{\pi\pi 1} = 0.2\text{fm}^2$ and $\beta_{\pi\pi 3} = 0.25\text{fm}^2$[38]. In order to make a comparison with the experimental data quoted in Table 5.9, the following ratio may be formed,

$$X(E0:E2) = 2.074 \times 10^{-4} A^{4/3} \frac{\rho^2(E0: I_i \rightarrow I_f)}{B(E2: I_i \rightarrow I_{f'})} \tag{6.24}$$

where the notation is consistent with that of equation (5.9). Calculated X-factors are compared with experimental values in Table 6.11,

$(I_i \rightarrow I_f)/(I_i \rightarrow I_{f'})$	Theory (IBM-2)	Experiment
$(0_2^+ \rightarrow 0_1^+)/(0_2^+ \rightarrow 2_1^+)$	0.015	0.0093(8)
$(0_3^+ \rightarrow 0_2^+)/(0_3^+ \rightarrow 2_1^+)$	0.44	1.6(5)
$(0_3^+ \rightarrow 0_1^+)/(0_3^+ \rightarrow 2_1^+)$	0.028	<0.33
$(0_3^+ \rightarrow 0_2^+)/(0_3^+ \rightarrow 2_2^+)$	0.058	0.017(4)
$(0_3^+ \rightarrow 0_1^+)/(0_3^+ \rightarrow 2_2^+)$	0.0037	<0.004

Table 6.11 Comparison of theoretical and experimental $X(E0 : E2)$ values for transitions in ^{118}Te.

References

[1] . J.Rikovska, private communication (1987).

[2] . S.P.Collins, private communication (1985).

[3] . J.J. van Ruyven, W.H.A.Hesselink, J.Akkerman, P. van Nes and H.Verheul, Nucl. Phys. **A380**(1982)125.

[4] . P.Chowdhury, W.F.Fiel Jr. and D.B. Fossan, Phys. Rev. **C25**(1982)813.

[5] . C.M.Lederer and V.S.Shirley, in the Table of Isotopes (7^{th} Ed.) (Wiley,New York,1978).

[6] . M.Matoba, M.Hyakutake, K.Yagi, Y.Aoki and C.Rangachargulu, **A261**(1976)223.

[7] . W.B.Walters, private communication (1987).

[8] . A. de Shalit and I.Talmi, in Nuclear Shell Theory (Academic,New York,1963).

[9] . A.Bohr and B.R.Mottelson, in Nuclear Structure (Benjamin,New York,1975) vol 2.

[10] . A.E.L.Dieperink, Prog. Part. Nucl. Phys. 9(1983)121.

[11] . A.Arima, T.Otsuka, F.Iachello and I.Talmi, Phys. Lett. **66B**(1977)205.

T.Otsuka, A.Arima, F.Iachello and I.Talmi, Phys. Lett. **76B**(1978)139.

[12] . D.Wilkinson (ed.), Collective bands in nuclei, Prog. Nucl. Phys. 9(1982).

[13] . A.Arima and F.Iachello, Adv. Nucl. Phys.,
eds. J.W.Negele and E.Vogt, **13**(1984)139.

[14] . J.P.Elliot, Rep. Prog. Phys. **48**(1985)171.

[15] . J.L.Wood, Nucl. Phys. **A396**(1983)245c.

[16] . O.Scholten, Ph.D. Thesis (University of Groningen,1981).

[17] . J.P.Schiffer and W.W.True, Rev. Mod. Phys. **48**(1976)191.

[18] . T.Otsuka, A.Arima and F.Iachello, Nucl. Phys. **A309**(1987)1.

[19] . M.Moinester, J.P.Schiffer and W.P.Alford,
Phys. Rev. **179**(1969)984.

[20] . R.F.Casten, Nucl. Phys. **A443**(1985)1.

[21] . M.Sambataro, O.Scholten, A.E.L.Dieperink and G.Piccittio,
Nucl. Phys. **A423**(1984)333.

[22] . K.Alder and R.M.Steffen, in The Electromagnetic Interaction in
Nuclear Spectroscopy, ed. W.D.Hamilton
(North Holland,Amsterdam,1975).

[23] . R.Bijker, A.E.L.Dieperink and O.Scholten,
Nucl. Phys. **A344**(1980)207.

[24] . F.Iachello, Hyp. Int. **15**(1983)11.

F.Iachello, Nucl. Phys. **A358**(1981)89c.

[25] . C.E.Alonso, J.M.Arias and F.Iachello,
Phys. Lett. **164B**(1985)241.

[26] . K.Heyde, P. van Isacker, M.Waroquier, J.L.Wood and R.A.Meyer,
Phys. Reports, **102**(1983)No. 5,6.

[27] . P.Federman and S.Pittel, Phys. Rev. **C20**(1979)820.

[28] . P.D.Duval and B.R.Barrett, Phys. Lett. **100B**(1980)223.
P.D.Duval and B.R.Barrett, Nucl. Phys. **A376**(1982)213.

[29] . R.A.Meyer and L.Peker, Z. Phys. **A283**(1977)379.

[30] . K.Heyde, P. van Isacker, M.Waroquier, G.Wenes and M.Sambataro, Phys. Rev **C25**(1982)3160.

[31] . A.Mheemeed, K.Schreckenbach, G.Barreau, H.R.Faust, H.G.Börner, R.Brissot, P.Hungerford, H.H.Schmidt, H.J.Scheerer, T. von Egidy, K.Heyde, J.L.Wood, P. van Isacker, M.Waroquier, G.Wenes and M.L.Stelts, Nucl. Phys. **A412**(1984)113.

[32] . G.Wenes, P. van Isacker, M.Waroquier, K.Heyde, and J. van Maldeghem, Phys. Rev **C23**(1981)2291.

[33] . W.B.Walters, J.Rikovska, N.J.Stone, P.M.Walker and T.L.Shaw, to be published.

[34] . K.Heyde, P. van Isacker, M.Waroquier, J.L.Wood and R.A.Meyer, Phys. Reports, **102**(1983)291.

[35] . P.M.Walker, C.J.Ashworth, I.S.Grant, V.R.Green, J.Rikovska, T.L.Shaw and N.J.Stone, J. Phys. G. **13**(1987)L195.

[36] . M.Sambataro, Nucl. Phys. **A380**(1982)365.

[37] . P. van Isacker and G.Puddu, Nucl. Phys. **A348**(1980)125.

[38] . G.Puddu, O.Scholten and T.Otsuka, Nucl. Phys. **A348**(1980)109.

[39] . K.Heyde, P. van Isacker, R.F.Casten and J.L.Wood, Phys. Lett. **153B**(1985)303.

[40] . P. Van Isacker, S.Pittel, A.Frank and P.D.Duval, Nucl. Phys. **A451**(1986)202.

[41] . P. van Isacker, M.Waroquier, H.Vincx and K.Heyde, Nucl. Phys. **A292**(1977)125.

[42] . M.Gai, D.M.Gordon, R.E.Shroy, D.B.Fossan and A.K.Gaigalas, Phys. Rev. C**26**(1982)1101.

[43] . R.E.Shroy, D.M.Gordon, M.Gai, D.B.Fossan and A.K.Gaigalas, Phys. Rev. C**26**(1982)1089.

[44] . K.Heyde, J.Jolie, J.Moreau,J.Ryckenbusch, M.Waroquier, P van Duppen,
M.Huyse and J.L.Wood, Nucl. Phys. **A466**(1987)189.

Chapter 7

Nuclear Orientation and Relaxation of Cs Isotopes

7.1 Introduction

This chapter describes on-line nuclear orientation measurements made on neutron deficient Cs isotopes, covering masses 122 down to 118. The question of relaxation of these isotopes in an iron host is one of importance, much more so than for neighbouring Xe and I isotopes, for the following reasons,

(i) the hyperfine field is a factor of 3–4 times smaller, and as mentioned in chapter 2.3.3 for the low temperature limit, $\tau_{SLR} \propto 1/T_{int}^3 \propto 1/B_{hf}^3$. Thus, relaxation times for Cs will, in general, be an order of magnitude larger than for Xe and I isotopes.

(ii) the half-lives are relatively short, with the result that they can become comparable with the relaxation times.

Table 7.1 shows the Cs isotopes which have been observed, along with half-lives and estimated relaxation times. Estimates for $^{118}Cs^m$ have been derived assuming a spin of 7 and a moment of $\sim$ 5nm (more will be said concerning this later). Relaxation of Cs*Fe* has not previously been studied, so equation (2.25) has been used to estimate C_k, taking the hyperfine field as +27.6T [1]. Relaxation times have been estimated (in the low temperature limit), from τ_{emp} given in equation (2.23). These estimates strongly suggest that the majority of the

Isotope	Spin	Moment	Half-life	τ_{emp}	τ_{SLR}
$^{118}Cs^{g}$	2	4.29	14s	18s	2.5s
$^{118}Cs^{m}$	(7)	~ 5	17s	$\sim 160s$	$\sim 7s$
$^{119}Cs^{g}$	$9/2^{+}$	5.46	36s	50s	2.2s
$^{119}Cs^{m}$	$3/2^{+}$	0.838	28s	590s	36s
$^{120}Cs^{g}$	2^{-}	3.87	64s	25s	1.0s
$^{121}Cs^{g}$	$3/2^{+}$	0.770	136s	690s	43s
$^{121}Cs^{m}$	$9/2^{+}$	5.41	121s	52s	2.2s
$^{122}Cs^{g}$	1	-0.133	21s	$10^{4}s$	640s
$^{122}Cs^{m}$	8	4.77	252s	250s	11s

Table 7.1 Half-lives and estimated relaxation times for observed Cs isotopes.

above nuclei will not reach full thermal equilibrium before decay. Upon further investigation of these isotopes, to which this chapter is devoted, it turns out the relaxation times are in fact much faster than originally thought, and *revised* estimates τ_{SLR} are also shown.

The first part of the chapter describes experiments on $^{121}Cs^{m}$, $^{120}Cs^{g}$ and $^{119}Cs^{g}$ from which the hyperfine field of Cs*Fe* has been deduced to be (+)40.8(7) T, assuming a simple two field site model. This value is substantially higher than the high field site of 27.6 T previously reported[1]. Further investigation into this difference is currently in progress.

The second part of the chapter deals with time dependent relaxation measurements made on $^{121}Cs^{m}$ using a new technique, giving a Korringa constant, C_k, of 0.059(16)sK for this system (assuming $B_{hf} = 40.8$T). Combining these two results, the chapter concludes with a measurement of the magnetic moment of $^{118}Cs^{m}$ to be 5.4(1.1)nm. In this measurement, relaxation, although fast, cannot be ignored.

The main results and conclusions from this work, in which Cs nuclei have been oriented for the first time at low temperature, have recently been published [2] .

7.2 The hyperfine field of Cs*Fe*

7.2.1 Relaxation considerations

The spins and magnetic moments of a whole series of Cs isotopes from ^{145}Cs down to ^{118}Cs^{g} have been measured using the combined techniques of atomic-beam magnetic resonance [3] [4] and laser spectroscopy [5]. From observation of the orientation of these isotopes as a function of temperature, it is possible to determine the Cs*Fe* hyperfine field. The most suitable nuclei for this are ones for which the half-life is long enough to ensure complete relaxation before decay. From Table 7.1, such nuclei are seen to be ^{122}Cs^{m}, ^{121}Cs^{m}, ^{120}Cs^{g} and ^{119}Cs^{g}, for which the half-life is of order twenty times the *revised* relaxation time. Presupposing the results to be described later, reduction factors, defined by equation (2.39), have been calculated for each of these isotopes as a function of T_{int}/T_L, and are plotted in [Fig 7.1] . Values of the parameter $\tau T_{int}/C_k$ are given for each isotope, and the temperature ranges over which measurements were taken are also indicated.

It is clear from [Fig 7.1] that the reduction factors are close to unity. In addition, their variation over the relevant temperature ranges is small compared to the experimental errors involved. The experimental results, obtained for each of these isotopes, will be presented.

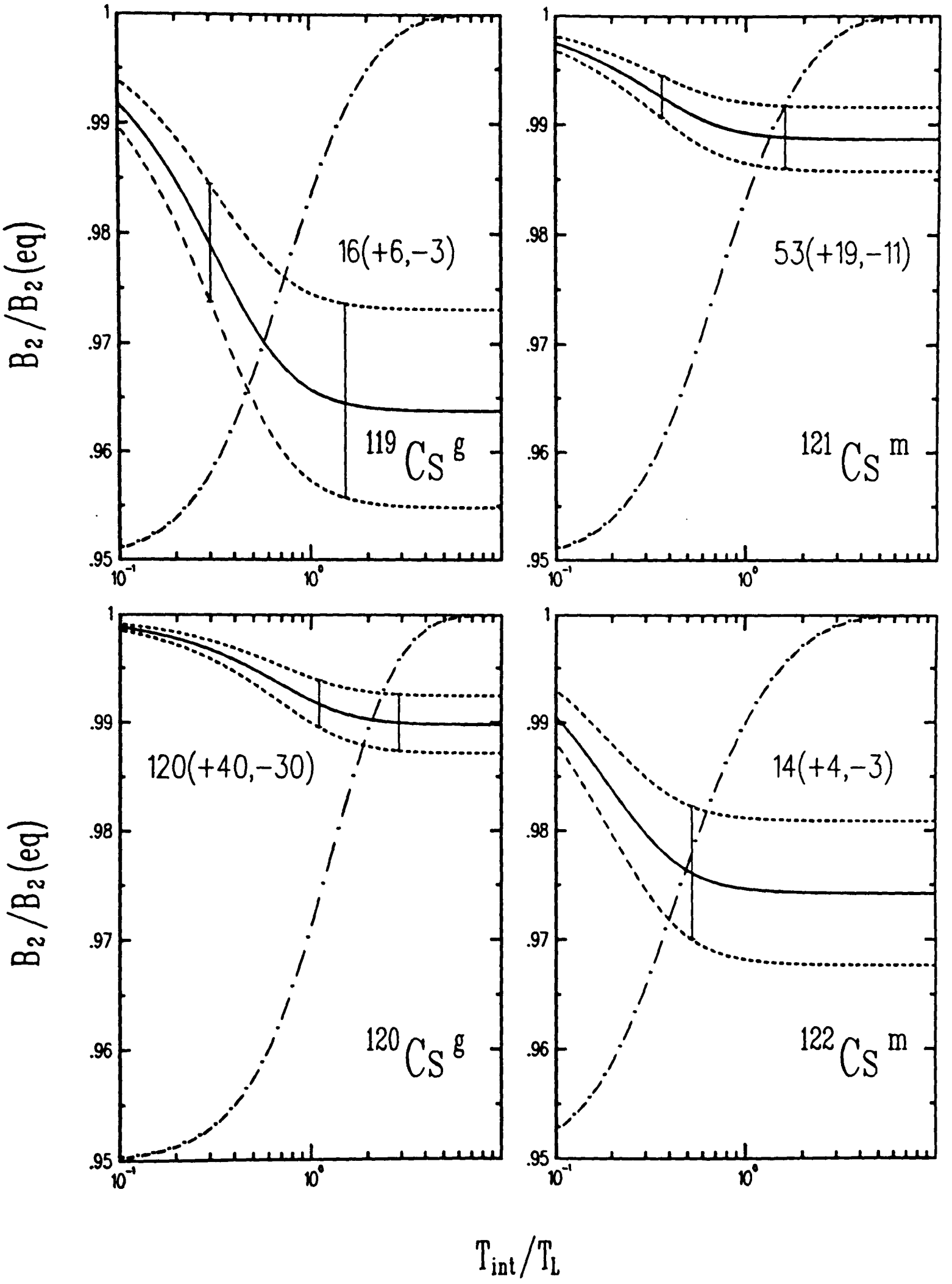

Figure 7.1. $B_2/B_2(eq)$ for $^{122}Cs^m$, $^{121}Cs^m$, $^{120}Cs^g$ and $^{119}Cs^g$ as a function of T_{int}/T_L. Values of the parameter $\tau T_{int}/C_k$ are given for each isotope. The vertical bars indicate the temperature range over which measurements were taken. The dot-dashed line represents the temperature variation of $B_2(eq)$ (the full thermal equilibrium value), normalized to its saturation value.

7.2.2 Experimental Details

These measurements have all been performed using the DOLIS–COLD facility at Daresbury, details of which are may be found in chapter 3. The Cs isotopes in this mass region were produced using a FEBIAD ion source with a ^{93}Nb entrance window (of thickness 2-3 mg/cm^2), and incident beams of ^{32,34}S ions in the energy range 150–175 MeV. Table 7.2 gives a summary of the experiments that have been performed (including for completeness the ^{118}Cs^m experiment and the ^{121}Cs^m *relaxation* experiment, which will be described later).

Isotope	Date	Beam	Experiment
^{118}Cs^m	Jul 85	^{32}S	*Temperature dependence*
^{119}Cs^g	Jul 85	^{32}S	*Temperature dependence*
^{120}Cs^g	Feb 84	^{34}S	*Two temperature points*
	Apr 85	^{34}S	*Temperature dependence*
^{121}Cs^m	Jul 85	^{32}S	*Temperature dependence*
	Mar 86	^{32}S	*Relaxation measurement*
^{122}Cs^m	Jul 86	^{34}S	*One temperature point*

Table 7.2 Summary of experiments performed on Cs isotopes.

In all these experiments, temperature determination was performed using a standard ^{57}Co*Fe* thermometer. Also axial/equatorial γ-ray anisotropies, $\{W(0)/W(90)-1\}\%$, were always measured (as a function of temperature) using two independent pairs of detectors, with the quoted anisotropies being averaged between the two pairs. In the analysis of these anisotropies, the solid angle correction factors, Q_λ, used correspond to values obtained from the program QK, for the relevant detector.

For each temperature dependence, the least-squares fitting procedure used is based on the simple two-site model. The term μB_{eff} is a parameter in the fit, from which the effective field B_{eff} may be deduced, taking the measured moments from Table 7.2. The sign of the hyperfine field is taken as positive[1], giving, from equation (1.57), the hyperfine field to be

$$B_{hf} = B_{eff} - B_{app} \tag{7.1}$$

In all these experiments the applied field, $B_{app} = +0.7T$. A common feature for all the transitions analysed below is that the fitted B_{hf} (expressed in Tesla) is higher than the 27.6T, expected from the work of S.R.Reintsema[1]. The comparison between fits with B_{hf} as a *fitted* parameter and as a *fixed* parameter (of 27.6T) is illustrated in the text (and figures) to follow. All transitions for which reasonable temperature dependence data (i.e. where the errors were small compared to the size of the effects) were obtained have been analysed, and the results are detailed below.

7.2.3 The $^{121}Cs^{m}$ experiment

^{121}Cs has two isomers, of similar half-lives, but with very different spins. The low spin isomer $^{121}Cs^{g}$ (spin $3/2^{+}$) has a low magnetic moment, and the high spin isomer $^{121}Cs^{g}$ (spin $9/2^{+}$) a high moment. This has a large influence on the relaxation times listed in Table 7.1, where $^{121}Cs^{m}$ is expected to relax much faster than $^{121}Cs^{g}$. In this experiment, all the useful data were taken on the decay of $^{121}Cs^{m}$, which is essentially fully relaxed for equilibrium on-line implantation as shown in [Fig 7.1] . This is not the case for $^{121}Cs^{g}$ where the low moment and slow relaxation result in a small degree of orientation (e.g. at 10mK $B_2 \sim 0.2$). The few transitions observed in $^{121}Cs^{g}$ decay indeed showed no anisotropy, to within the errors of the measurement.

The decay of $^{121}Cs^{g+m}$ has been observed by Sofia *et al* [6] (hereafter referred to as Sofia). Their measurements show that the decays of the two isomers populate different sets of levels in the daughter ^{121}Xe. The levels and transitions in ^{121}Xe from the decay of $^{121}Cs^{m}$, are shown in [Fig 7.2] . This decay scheme is taken from the work of Marguier *et al* [7] (hereafter referred to as Marguier), where the spin assignment of the 459.7 keV level has been changed from $(9/2^+)$ to $7/2^+$ (see later). There are several important discrepancies between this level scheme and that of Sofia, which will be investigated below.

Temperature dependences of the γ-ray anisotropy have been measured for five transitions in the decay of $^{121}Cs^{m}$, each of which will now be discussed in more detail.

196.0 *keV* : $7/2^- \rightarrow 5/2^+$

This transition is assigned as E1 by both Marguier and Sofia, but they disagree about whether the 38.4 keV transition feeds it or is fed by it. The discrepancy between their two decay schemes is illustrated in [Fig 7.3]

Sofia measure the K-conversion coefficient, $\alpha_K = 11(1)$ (E2 : 10.4 and M1 : 11.5) for the 38.4 keV transition. As this is such a low energy the transition is highly converted, and the *total* conversion coefficient is very large, and also very sensitive to the E2/M1 mixing ratio of the transition (due mainly to the L-conversion conversion coefficients). For an M1 transition, $\alpha_T = 13$ giving $\Im_{38.4} < \Im_{196.0}$ (and hence the sequence 38.4 $\rightarrow$ 196.0). However, for an E2 transition, $\alpha_T = 62$ giving $\Im_{38.4} > \Im_{196.0}$ (and thus the sequence 196.0 $\rightarrow$ 38.4). The placement of Sofia relies upon the determination of the mixing ratio from the α_K coefficient, which they admit is not precise enough to be certain about the correct order of the 38.4 and 196.0 keV transitions.

The 196.0 keV transition has also been observed by in-beam studies on ^{121}Xe by Chowdhury *et al* [8] (hereafter referred to as Chowdhury), where

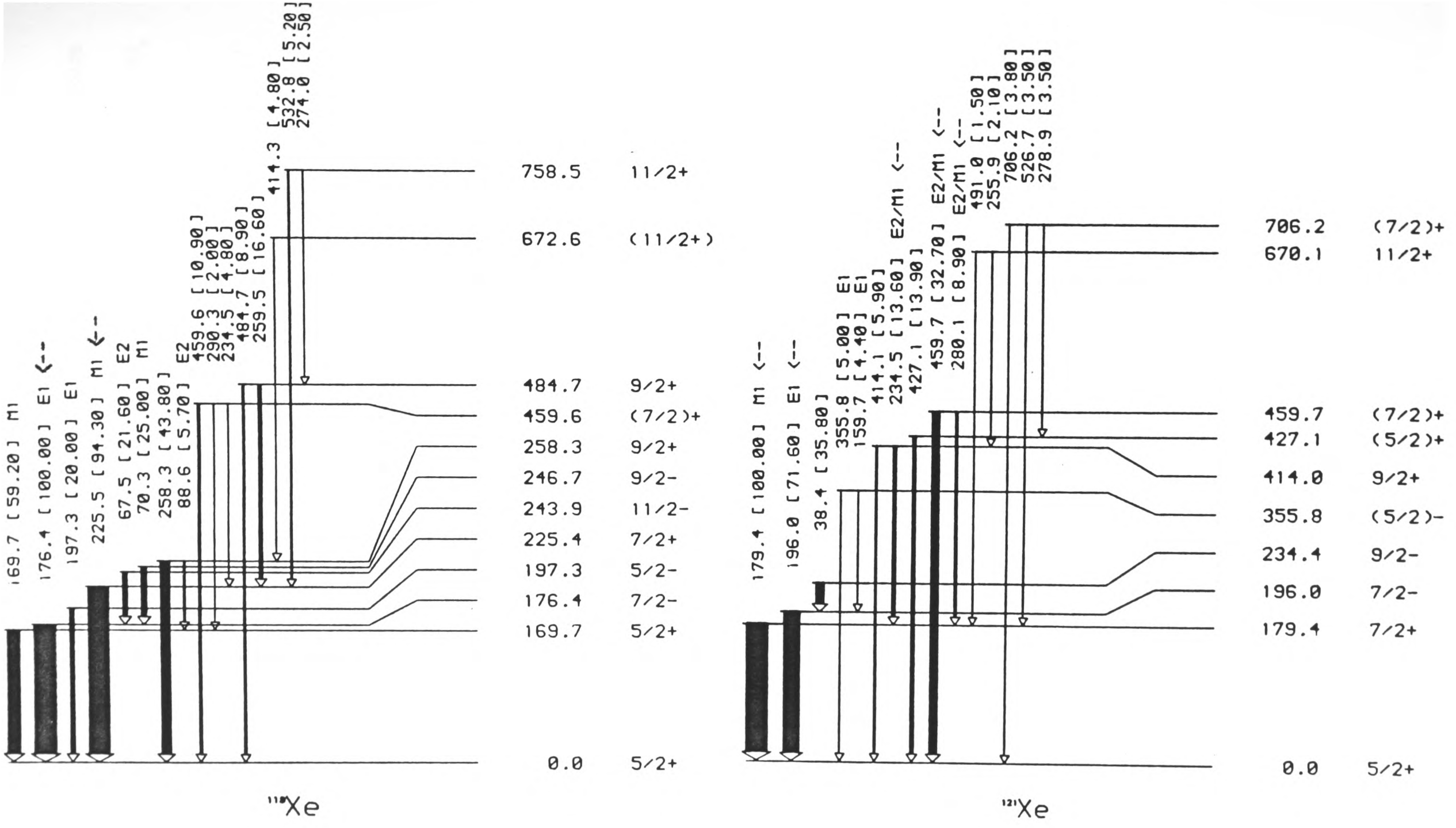

Figure 7.2. Level schemes of ^{119}Xe and ^{121}Xe, populated in the decay of ^{119}Cs^{g} and ^{121}Cs^{m}. Transitions for which a temperature dependence has been measured are indicated with an *arrow* $--$>.

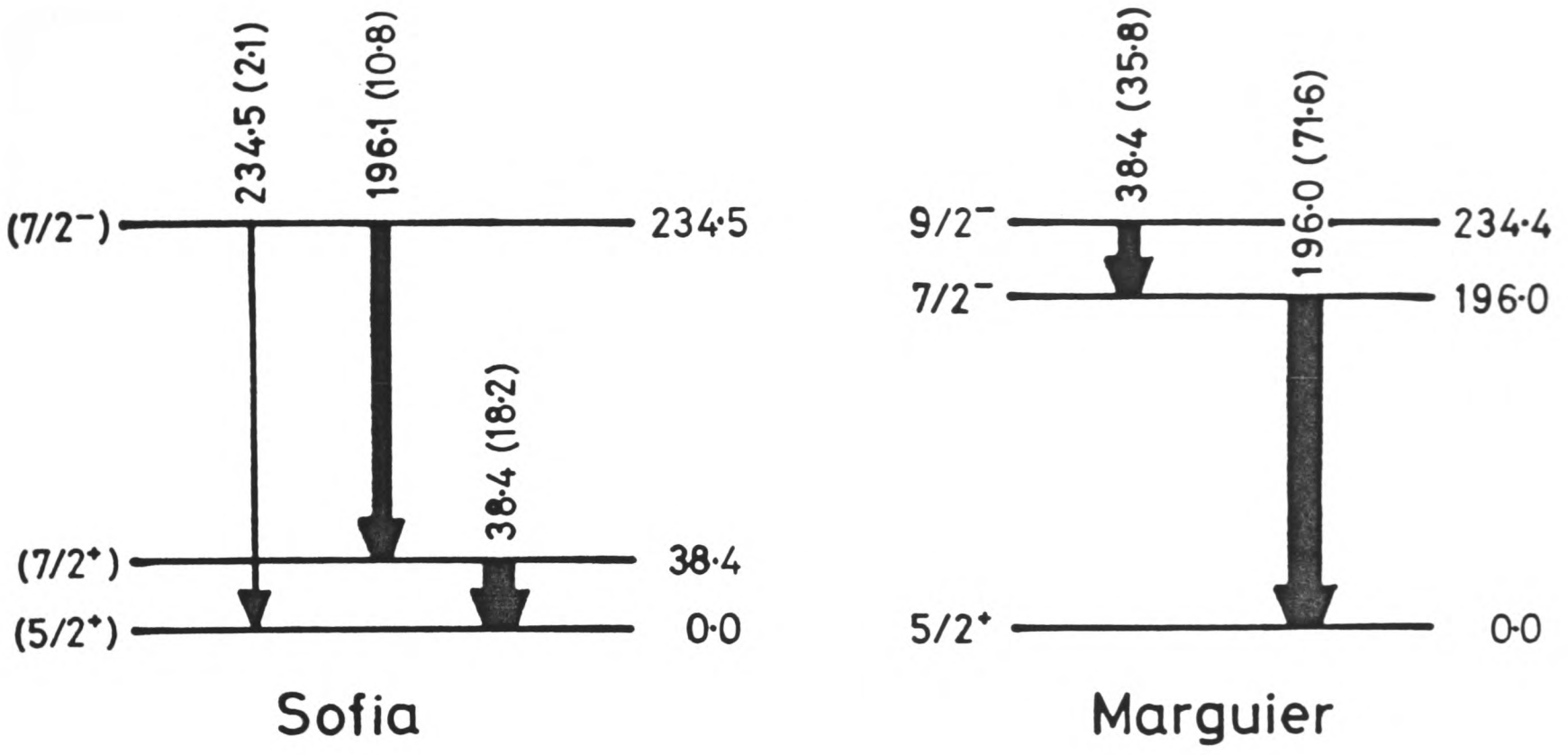

Figure 7.3. Two possible low-lying level structures assigned to ^{121}Xe.

it is placed as an E1 transition to the ground state, in agreement with Marguier. In addition, its angular distribution has also been measured giving values $\alpha_2 A_2^{max} = -0.20(1)$ and $\alpha_4 A_4^{max} = 0.02(1)$ (these coefficients have been tabulated by der Mateosian and Sunyar [9] and by Yamagazi [10]). These values can be used to distinguish between the two level schemes shown in [Fig 7.3] as follows.

Marguier	:	$7/2^- \rightarrow 7/2^+$	:	$A_2^{max} = -0.357$
Sofia	:	$7/2^- \rightarrow 5/2^+$	:	$A_2^{max} = 0.476$

The measured value of $\alpha_2 A_2^{max}$ clearly picks out the assignment of Marguier, giving the attenuation coefficient, $\alpha_2 = 0.56(3)$. Assuming a Gaussian distribution of sub-level populations [11] , a value of $\sigma/J = 0.47(2)$ may thus be deduced[9,10] for the initial level. The anisotropy data for this transition is shown in [Fig 7.4] , and the fitted curve yields the parameters (a * refers to a

parameter which has been varied).

$\chi^2_\nu = 0.97$	$^*B_{hf} = 36.1(2.4)$	$^*fU_2A_2 = 0.108(4)$	$fU_4A_4 = 0$
$\chi^2_\nu = 2.23$	$B_{hf} = 27.6$	$^*fU_2A_2 = 0.126(3)$	$fU_4A_4 = 0$

The E1 character of the transition has been used in the fit by setting $fU_4A_4 = 0$. Assuming the decay scheme shown in [Fig 7.2] and using the program UACALC, the de-orientation coefficient $U_2 = 0.82(9)$ has been estimated. Combining this with the measured value of fU_2A_2 gives a fraction in good sites of $f = 40(5)\%$. This is a little low compared to values obtained for other transitions, but it should be noted that the estimated value of U_2 is very sensitive to the *total* intensity of the 38.4 keV transition, for which *both* the γ-ray intensity and the mixing ratio must be precisely known (as seen above). For example, if the 38.4 keV transition is taken as E2 and also as the dominant feed to the level, a value of $U_2 \sim 0.57$ results, giving a value of $f \sim 58(2)\%$.

234.5 *keV* : $9/2^+ \rightarrow 7/2^+$

This is placed as a $9/2^+ \rightarrow 7/2^+$ transition by Marguier, feeding the 179.4 keV level. This placement is also supported by Sofia and Chowdhury. However, Sofia also place a stronger transition at the same energy between the 234.5 keV level and the ground state, which they assign as $7/2^- \rightarrow 5/2^+$. The 234.5 keV level is assigned $9/2^-$ by Marguier, and hence no transition to the ground state (spin $5/2^+$) is seen.

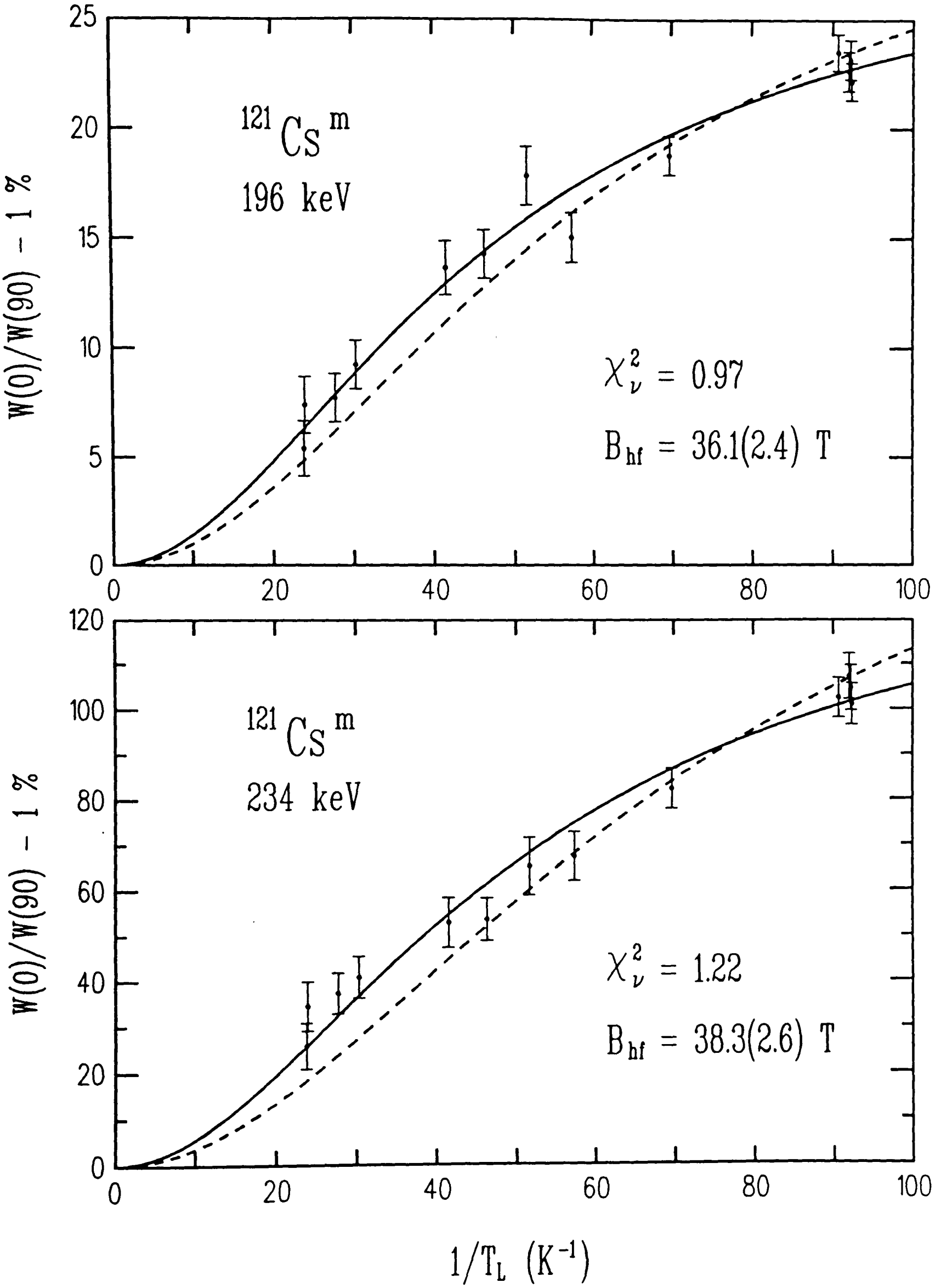

Figure 7.4. Anisotropies for the 196.0 and 234.5 keV transitions seen in $^{121}Cs^{m}$ decay. The full lines correspond to fits to the field, and the dashed lines assume a field of 27.6T.

The fitted temperature dependence for this transition is shown in [Fig 7.4] , and the following parameters were deduced.

$\chi^2_\nu = 1.22$ $\quad {}^*B_{hf} = 38.3(2.6)$ $\quad {}^*fU_2A_2 = 0.381(14)$ $\quad {}^*fU_4A_4 = 0.01(-)$

$\chi^2_\nu = 3.18$ $\quad B_{hf} = 27.6$ $\quad {}^*fU_2A_2 = 0.456(6)$ $\quad {}^*fU_4A_4 = 0.01(-)$

The only assumption made in this fit is a constraint that $A_4 \geq 0$, which is valid for either possible placement of the 234.5 keV transition.

In order deduce any more about this transition, it is necessary to look at the angular distribution (from Chowdhury) for the $9/2^+ \rightarrow 7/2^+$ transition, which shows $\alpha_2 A_2^{max} = -0.44(2)$ and $\alpha_4 A_4^{max} = 0.05(3)$. Assuming the same alignment as for the 196.0 keV level gives attenuation coefficients, $\alpha_2 = 0.54(3)$ and $\alpha_4 = 0.16(3)$. Thus, the values $A_2^{max} = -0.81(6)$ and $A_4^{max} = -0.3(2)$ may be deduced. The angular distribution coefficients, $A_\lambda^{max}(I_i \rightarrow I_f)$, are related to the those used in nuclear orientation, $A_\lambda(I_i \rightarrow I_f)$, by the relation[9]

$$A_\lambda^{max}(I_i \rightarrow I_f) = B_\lambda(I_i) A_\lambda(I_i \rightarrow I_f) \tag{7.2}$$

where $B_\lambda(I_i)$ is an *orientation* parameter for complete alignment of the initial state. In this case the orientation parameters are found to be $B_2 = -1.10$ and $B_4 = 1.06$, resulting in values $A_2 = 0.74(5)$ and $A_4 = -0.3(2)$, which can now be used to interpret the nuclear orientation data.

Assuming the decay scheme of Sofia, the measured fU_2A_2 value would be made up of two components. One would be the $7/2^- \rightarrow 5/2^+$ transition ($A_2 = 0.33$) with intensity $\Im_\gamma = 2.1$, and the other would be the $9/2^+ \rightarrow 7/2^+$ ($A_2 = 0.74$ from above) with intensity $\Im_\gamma = 0.6$. Taking $U_2 \leq 1$, an average over these two components, weighted by their intensities, gives $\langle U_2A_2 \rangle_{av} \leq 0.42$. This places a *lower* limit on the fraction in good sites of 91%.

On the other hand, assuming the placement of Marguier and Chowdhury and taking $A_2 = 0.74(5)$ from above, and estimating $U_2 = 0.93(6)$ from UACALC, the fraction in good sites is found to be $f = 56(6)\%$. This value is consistent with values of f deduced from other transitions, whereas the lower limit of 91% above seems too high. Hence, the decay scheme of Marguier is adopted in this case.

In addition, combining the A_2 value deduced from Chowdhury and $A_4 \sim 0$ from the temperature dependence, gives $\delta = -0.26(^{+4}_{-5})$ for this transition.

<u>179.4 *keV* : $7/2^+ \rightarrow 5/2^+$</u>

This is placed as a $7/2^+ \rightarrow 5/2^+$ ground state transition by both Sofia and Marguier. The anisotropy temperature dependence for this transition is shown in [Fig 7.5] , and the results of the least-squares fit are given below

---

$\chi^2_\nu =$ 6.49 $\quad {}^*B_{hf} = 40.7(1.0) \quad {}^*fU_2A_2 = 0.301(6) \quad {}^*fU_4A_4 = 0.01(-)$

$\chi^2_\nu = 43.71 \quad B_{hf} = 27.6 \quad {}^*fU_2A_2 = 0.372(3) \quad {}^*fU_4A_4 = 0.01(-)$

As $A_4 \geq 0$ for a $7/2^+ \rightarrow 5/2^+$ transition, the fit was constrained to keep fU_4A_4 positive, resulting in a very small value. From the level scheme of Marguier a value $U_2 = 0.870(28)$ was obtained (using UACALC). Using this and the maximum possible value of $A_2 = 1.09$ for such a transition, a lower limit of 32% may be set on the fraction in good sites.

A better estimate of f may be made by using the angular distribution value, $\alpha_2 A_2^{max} = -0.31(2)$, from Chowdhury. Assuming the same alignment as in the case of the 196.0 keV transition (i.e $\alpha_2 = 0.56(3)$), then $A_2^{max} = -0.55(5)$. The alignment parameter, $B_2 = -1.09$, thus $A_2 = 0.51(4)$, which, taking U_2 and

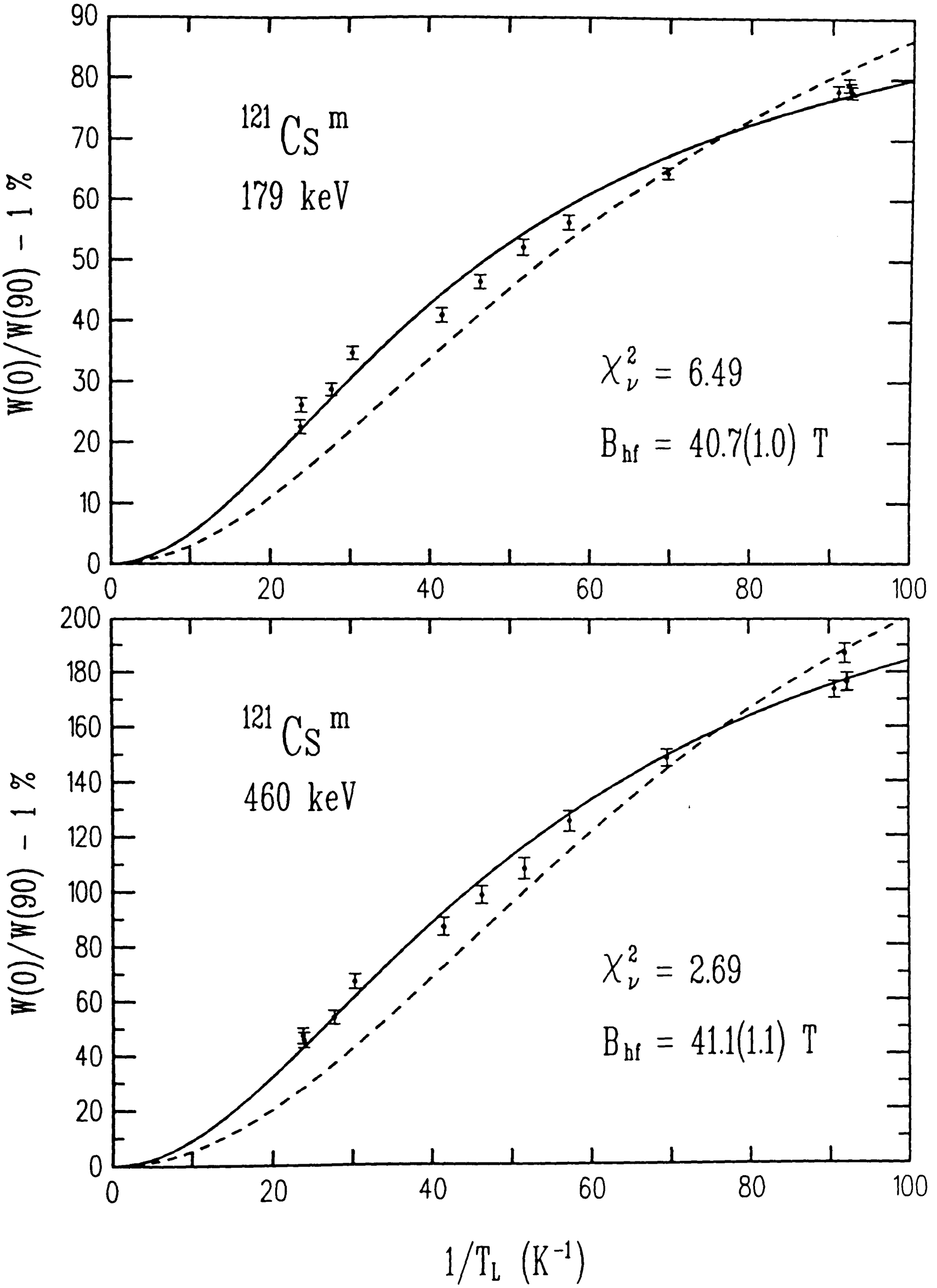

Figure 7.5. Anisotropies for the 179.4 and 459.7 keV transitions seen in $^{121}Cs^{m}$ decay. The full lines correspond to fits to the field, and the dashed lines assume a field of 27.6T.

fU_2A_2 from above, may be used to give a better estimate of the fraction in good sites, $f = 68(8)\%$.

The value deduced for A_2 gives possible mixing ratios, $\delta = -3.1(^{+2}_{-3})$ $[A_4 = 0.58(1)]$ or $\delta = -0.10(2)$ $[A_4 = 0.006(3)]$, the latter of which is preferred from the fitted fU_4A_4 value.

459.7 *keV* : $7/2^+ \rightarrow 5/2^+$

This again is a ground state transition from a level tentatively assigned $(9/2^+)$ by Marguier and $(7/2,9/2)^+$ by Sofia. The anisotropy data, shown in [Fig 7.5] , clearly identifies spin $7/2^+$ for the initial level, as a $9/2^+ \rightarrow 5/2^+$ E2 transition would show effects of the opposite sign. A least-squares fit to this data gives

$\chi^2_\nu = 2.69$	$^*B_{hf} = 41.1(1.1)$	$^*fU_2A_2 = 0.546(7)$	$^*fU_4A_4 = 0.01(-)$
$\chi^2_\nu = 28.42$	$B_{hf} = 27.6$	$^*fU_2A_2 = 0.675(3)$	$^*fU_4A_4 = 0.48(-)$

The fits were performed with the constraint $0 \leq fU_4A_4 \leq 0.48$, which are its limiting values (taking $f \sim 100\%$). Assuming a de-orientation coefficient $U_2 = 0.925$ and the maximum possible value $A_2 = 1.09$ for a $9/2^+ \rightarrow 7/2^+$ transition, gives a lower limit on the fraction in good sites of 54%.

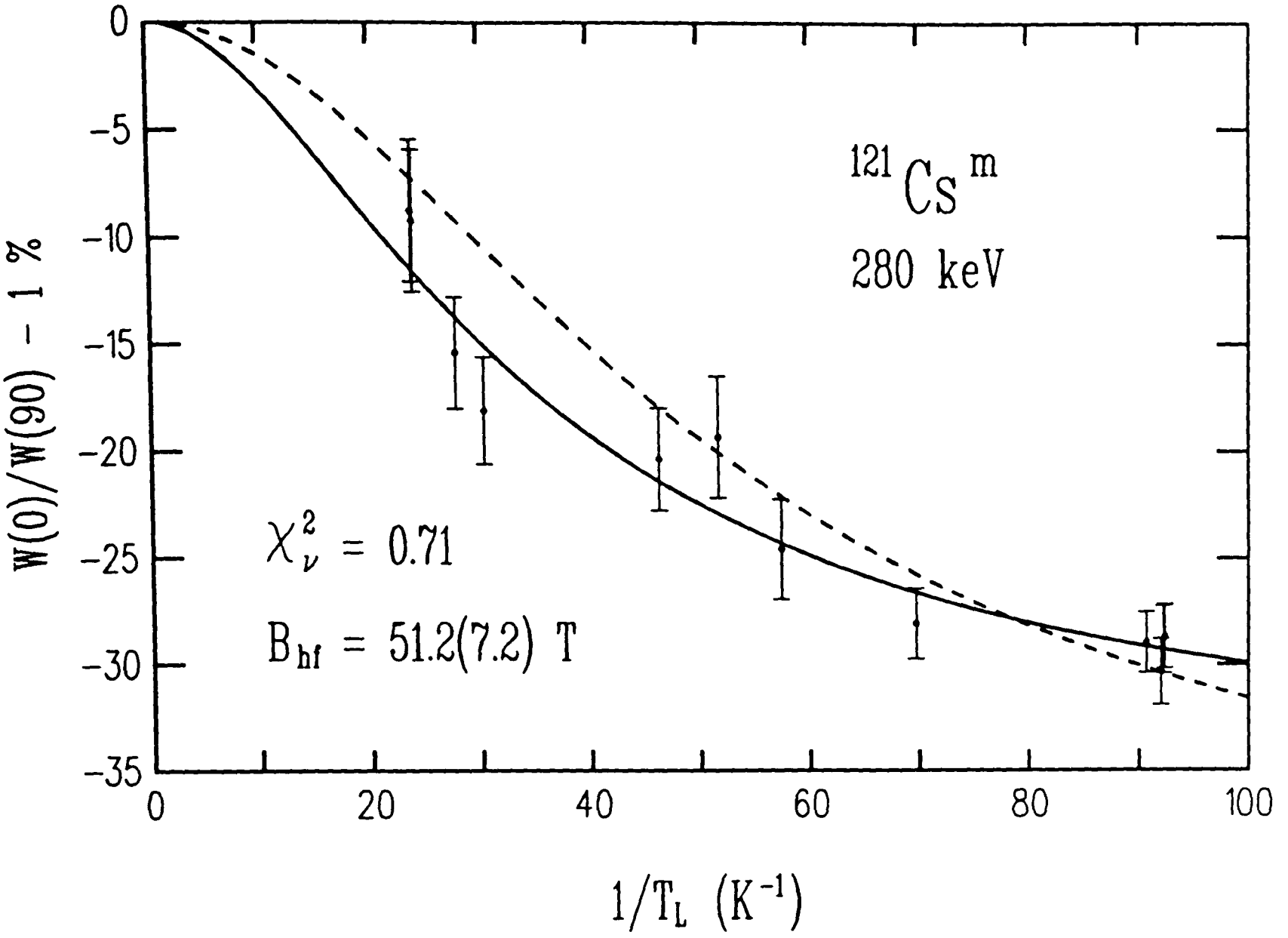

Figure 7.6. Anisotropy for the 280.1 keV transition seen in $^{121}Cs^{m}$ decay. The full line corresponds to a fit to the field, and the dashed line assumes a field of 27.6T.

280.1 *keV* : $7/2^+ \rightarrow 7/2^+$

This is a transition from the 459.7 keV level, confirmed as $7/2^+$ above, to the 179.4 keV level, also of spin $7/2^+$. The anisotropy temperature dependence is shown in [Fig 7.6] , and the results of the fit are given below as

---

$\chi^2_\nu = 0.71$ $^*B_{hf} = 51.2(7.2)$ $^*fU_2A_2 = -0.129(9)$ $^*fU_4A_4 = -0.08(6)$

$\chi^2_\nu = 2.27$ $B_{hf} = 27.6$ $^*fU_2A_2 = -0.196(5)$ $^*fU_4A_4 = -0.01(-)$

In this case, the variable fU_4A_4 was constrained to be negative as $A_4 \leq 0$. It is not possible to reliably extract a fraction in good sites for this transition. However, if a fraction in good sites $f = 59(3)\%$ is taken (see section 7.2.7), and values $U_2 = 0.925$ and $U_4 = 0.75$ (from UACALC), then the values $A_2 = -0.24(2)$ and $A_4 = -0.18(14)$ may be deduced. This value of A_2 gives possible solutions for the E2/M1 mixing ratio of $\delta = 1.77(^{+9}_{-8})$ [$A_4 = -0.36$] or $\delta = -0.23(2)$ [$A_4 = -0.02$]. The A_4 term is not sufficiently precise to distinguish between these two solutions.

7.2.4 The $^{119}Cs^{g}$ experiment

^{119}Cs also has two isomers, of similar half-lives, but with spins $3/2^+$ and $9/2^+$, as has ^{121}Cs. However, in contrast to ^{121}Cs, the high spin isomer is now the ground state, $^{119}Cs^{g}$ (with a large moment), and the low spin isomer, $^{119}Cs^{m}$ (with a small moment), has become the metastable state. By analogy with $^{121}Cs^{g}$, the isomer $^{119}Cs^{m}$ would not be expected to show any appreciable orientation, but it was not possible to check this, as no transitions from the decay of $^{119}Cs^{m}$ were seen. However, γ-rays were seen in the decay of $^{119}Cs^{g}$, and useful anisotropy data were obtained for two of these. A level scheme showing the levels and transitions populated in $^{119}Cs^{g}$ decay is given in [Fig 7.2], along with that for $^{121}Cs^{m}$ decay for comparison, both of which are taken from the work of Marguier. The low-lying level structure and transitions are consistent with the in-beam measurements of Chowdhury.

176.4 *keV* : $7/2^- \rightarrow 5/2^+$

The anisotropy temperature dependence for this transition is shown in [Fig 7.7] . It is placed as an E1 ground state transition, allowing fU_4A_4 to be set to zero in the least-squares fit, the results of which are given below

$\chi^2_\nu = 0.54$	$^*B_{hf} = 41.8(6.6)$	$^*fU_2A_2 = 0.088(18)$	$fU_4A_4 = 0$
$\chi^2_\nu = 1.37$	$B_{hf} = 27.6$	$^*fU_2A_2 = 0.118(9)$	$fU_4A_4 = 0$

Taking the decay scheme presented in [Fig 7.2], the de-orientation coefficient $U_2 = 0.89(2)$ has been calculated using the program UACALC. From this and taking $A_2 = 0.327$ for a $7/2^- \rightarrow 5/2^+$ transition results in a value for the fraction in good sites, $f = 30(6)\%$. Comparing this with values obtained from other transitions, this value is noticably low.

To investigate this further, it is possible to look at the angular distribution data of Chowdhury, where the value $\alpha_2 A_2^{max} = -0.27(1)$ is quoted for this transition. Taking $B_2 = -1.091$ for a spin 7/2 level gives $A_2^{max} = B_2A_2 = -0.357$, which in turn, yields $\alpha_2 = 0.76(3)$. This corresponds to a value $\sigma/J = 0.35(2)$, assuming a Gaussian distibution of the sub-level populations. This data is entirely consistent with the $7/2^- \rightarrow 5/2^+$ placement of the 176.4 keV transition, and is similar to the angular distribution data for the 196.0 keV transition in ^{121}Xe, which is the analogue of the 176.4 keV transition.

The fraction in good sites obtained from the 196.0 keV γ-ray in ^{121}Xe also seemed low, but in that case it was noted that the estimated U_2 value was very sensitive to the precise γ-ray intensity and multipolarity of the 38.4 keV transition, which directly feeds it. By analogy, in ^{119}Xe, there are two strong low energy feeds to the 176.4 keV level at energies 67.5 and 70.3 keV, which

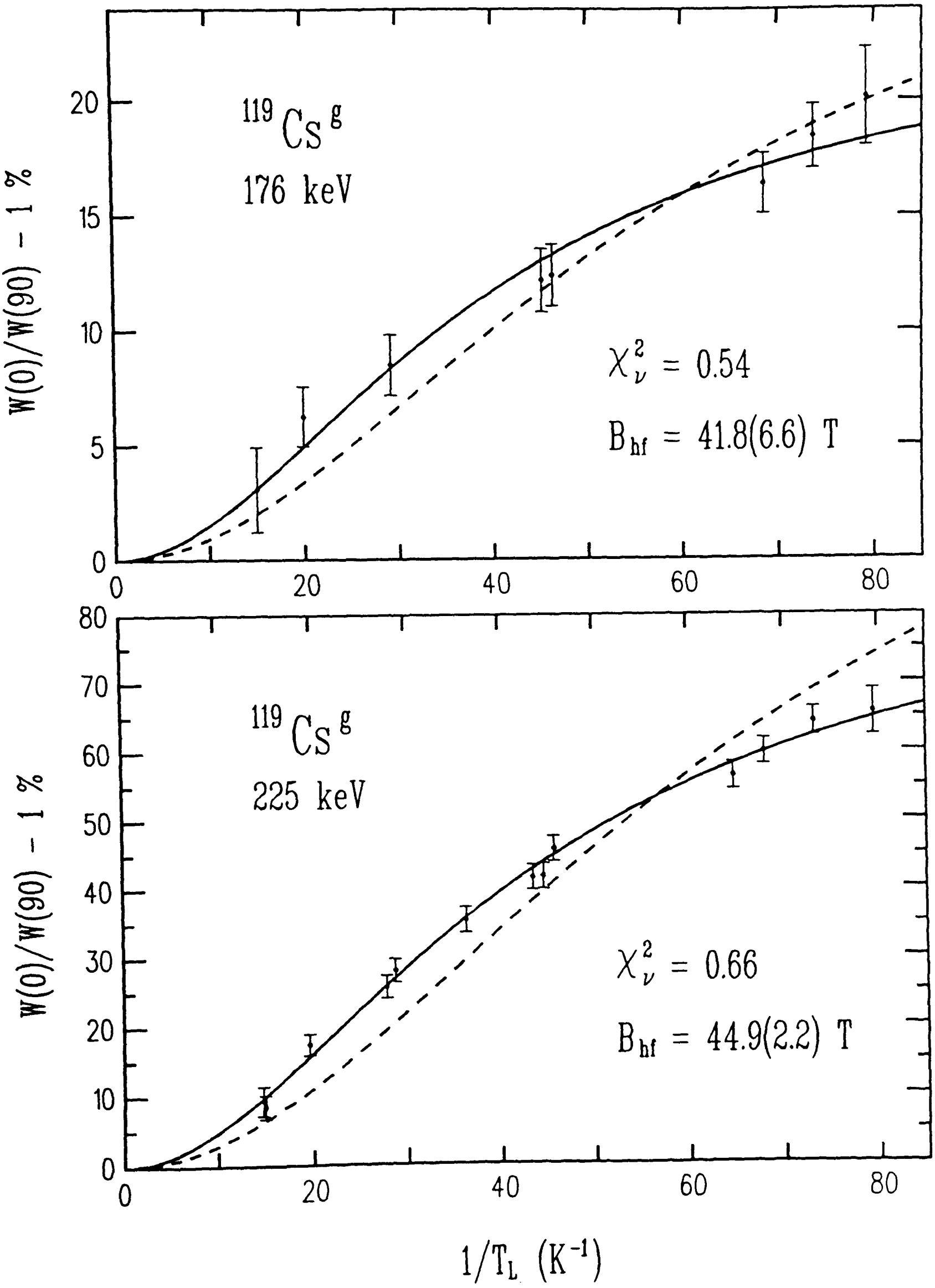

Figure 7.7. Anisotropies for the 176.4 and 225.5 keV transitions seen in $^{121}Cs^{m}$ decay. The full lines correspond to fits to the field, and the dashed lines assume a field of 27.6T.

are assigned M1 and E2 respectively. The *total* conversion coefficients for these transitions are large, and are also strongly dependent on the multipolarity of the transition (E2 : ~ 5.2 and M1 : ~ 1.9). Hence, the *total* intensities for these transitions depends upon precise measurements of *both* their γ-ray intensities and multipolarities. Any possible error in these measurements could significantly affect the the calculated value of U_2, and hence the fraction in good sites. For example, if the 70.3 keV transition were E2, then this could bring down the value of $U_2 \sim 0.6$, and hence give a value of $f \sim 45(9)\%$.

$\underline{225.5\ keV\ :\ 7/2^+ \rightarrow 5/2^+}$

This is placed as an M1 ground state transition, and the temperature dependence of its anisotropy is shown in [Fig 7.7] . The parameters obtained from a least-squares fit to this data are

$\chi^2_\nu = 0.66$	$^*B_{hf} = 44.9(2.2)$	$^*fU_2A_2 = 0.243(10)$	$^*fU_4A_4 = 0.27(19)$
$\chi^2_\nu = 0.61$	$^*B_{hf} = 42.3(1.9)$	$^*fU_2A_2 = 0.271(8)$	$fU_4A_4 = 0$
$\chi^2_\nu = 9.47$	$B_{hf} = 27.6$	$^*fU_2A_2 = 0.372(3)$	$^*fU_4A_4 = 0.01(-)$

The term fU_4A_4 is varied in two of the above fits with the constraint that it must be positive (as $A_4 \geq 0$ for a $7/2^+ \rightarrow 5/2^+$ transition). It is seen that the *best* fit is obtained for a non-zero value of fU_4A_4, which is in disagreement with the M1 assignment of Marguier.

A fit in which fU_4A_4 is set to zero yields a slightly lower value for B_{hf}, but with a slightly higher value of $\chi^2 = 7.33$, compared to $\chi^2 = 7.28$ when fU_4A_4 is varied too (the chi-squared values quoted above are reduced chi-squared values, defined as $\chi^2_\nu = \chi^2/\nu$, where ν is the number of free parameters in the fit). The

fit corresponding to the non-zero value of fU_4A_4 is adopted, but it is clear that there is not a great deal of difference between this and the fit where $fU_4A_4 = 0$.

To estimate a fraction in good sites, the angular distribution data of Chowdhury may again be used. For this transition, a value $\alpha_2 A_2^{max} = -0.43(3)$ has been measured, and assuming the same alignment as seen for the 176.4 keV transition ($\alpha_2 = 0.76(3)$), this gives a value $A_2^{max} = -0.57(5)$. Taking the alignment parameter, $B_2 = -1.09$, results in $A_2 = 0.52(5)$. Using UACALC for the decay scheme in [Fig 7.2], the de-orientation coefficient, $U_2 = 0.87(4)$ has been calculated. From this and the angular distribution data, a fraction in good sites, $f = 54(6)\%$ may be deduced.

From the above value of A_2, possible mixing ratios for this transition are found to be $\delta = -0.11(^{+3}_{-2})[A_4 = 0.007(3)]$ or $\delta = -3.1(3)$ $[A_4 = 0.58(2)]$. The non-zero value of fU_4A_4 suggests the latter of these two solutions, which, taking $U_2 = 0.63(8)$ from UACALC, leads to an estimate of $f \sim 70\%$.

The value of A_2 is almost the same as that deduced for the analogue transition at 179.4 keV in ^{121}Xe. However, this was was found to be consistent with a small mixing ratio of $\delta = -0.10(2)$ on the basis of its fitted fU_4A_4 term.

7.2.5 The $^{120}Cs^g$ experiment

Previous decay studies [12] have revealed the presence of an isomeric state in ^{120}Cs, of half-life 57(6) seconds, to be compared with a half-life of 64(3) seconds for the ground state. The spin ($I = 2$) and magnetic moment of $^{120}Cs^g$ have been measured by laser spectroscopy[5], but no such data is available for $^{120}Cs^m$. However, the $^{120}Cs^m$ is assigned high spin[12] on account of the feed to the 8^+ member of the ground state band in ^{120}Xe.

In this experiment, transitions originating from both the high ($^{120}Cs^m$) and low spin ($^{120}Cs^g$) isomers were seen, and a very simplified decay scheme is

given in [Fig 7.8] showing only the transitions most relevant to the following discussion. In the case of ^{119,121}Cs, the decay of the high and low spin isomers populated a completely different set of excited states, and each could thus treated separately. However, this is not the case for ^{120}Cs, where the two transitions for which anisotropy data were taken, are fed by both high and low spin isomers (to different extents). A full analysis of such a system is very complex, as in the case of $^{118}I^{g+m} \rightarrow {}^{118}$Te. Not enough information is available here in order to do this, and, as a consequence, the high spin decay has not been taken into account in the analysis below.

<u>322.4 *keV* : $2^+ \rightarrow 0^+$</u>

This is the most intense γ-ray seen in the decay of ^{120}Cs, and its anisotropy temperature dependence is shown in [Fig 7.9] . The high spin component is estimated as $< 10\%$ and by comparison the 605.6 keV transition in ^{118}I decay, this is not expected to affect the fits below significantly

---

$\chi^2_\nu = 1.55$	$^*B_{hf} = 38.2(2.6)$	$^*fU_2A_2 = -0.094(5)$	$fU_4A_4 = 0.14(9)$
$\chi^2_\nu = 1.88$	$B_{hf} = 27.6$	$^*fU_2A_2 = -0.132(3)$	$fU_4A_4 = 0.60(-)$
$\chi^2_\nu = 4.55$	$B_{hf} = 27.6$	$^*fU_2A_2 = -0.107(2)$	$fU_4A_4 = 0$

Two of the fits shown are with the field set at 27.6T. In the first, fU_4A_4 is varied with the constraint of a maximium possible value of $\sim$ 0.6 (taking $f \sim 100\%$), and in the second, fU_4A_4 is set to zero.

In a complex decay scheme such as this, it is usually not possible to estimate U_2 or U_4 for low-lying levels without large uncertainties, due to the cumulative

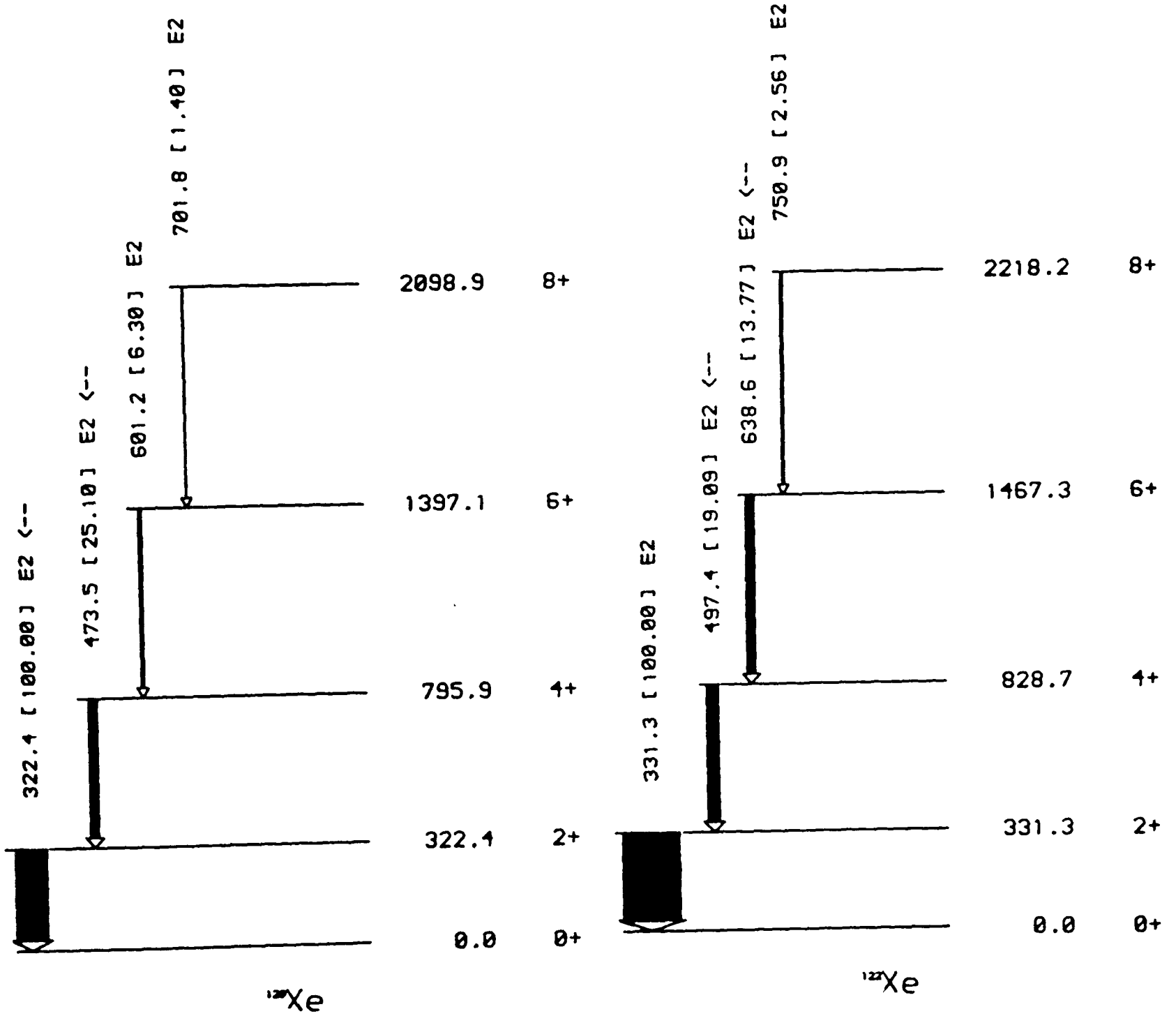

Figure 7.8. Simplified level schemes of ^{120}Xe and ^{122}Xe, populated in the decay of ^{120}Cs^{g+m} and ^{122}Cs^{g+m}. Transitions for data are presented are indicated with an *arrow* $-->$.

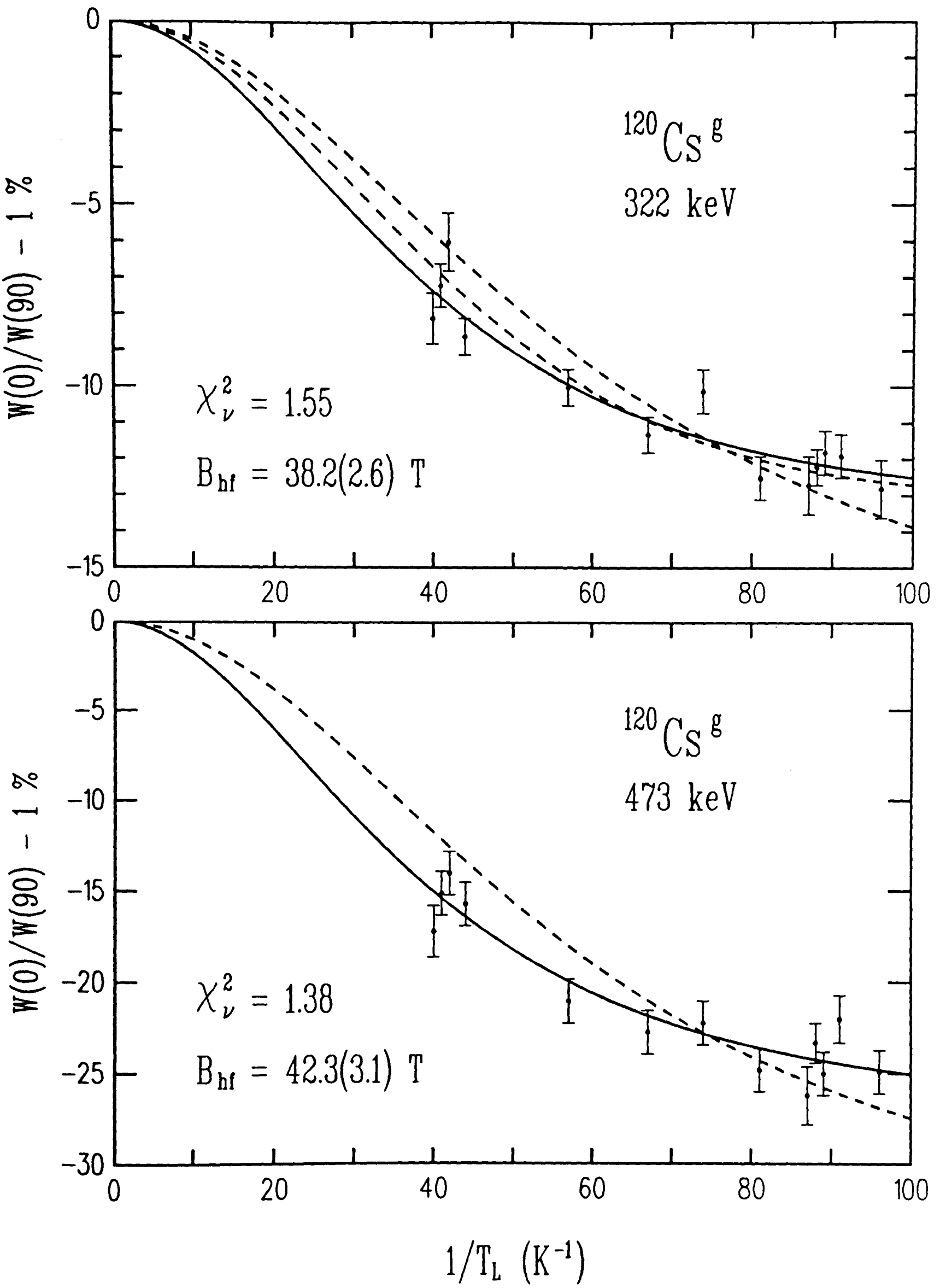

Figure 7.9. Anisotropies for the 322.4 and 473.5 keV transitions seen in $^{120}Cs^{g(+m)}$ decay. The full lines correspond to fits to the field, and the dashed lines assume a field of 27.6T.

effect of uncertainty in spin and multipolarity assignments of levels and transitions above (see chapter 6). Considering the effect of these feeding transitions on the 322.4 keV 2_1^+ level, each one will tend to give rise to a U_2 value of the same sign but a different magnitude, whereas each U_4 term will generally be of *both* varying sign and magnitude. The net effect thus expected is that U_4 will average out to some small value close to zero (as is seen for the 605.6 keV 2_1^+ level in ^{118}Te in the previous chapter).

Comparing the two fits for the 27.6T field, the better *fit* can only be obtained with a rather unlikely value of fU_4A_4 (the value close to zero being more realistic), whereas if the field B_{hf} is also fitted, a best fit can be obtained which has a physically reasonable value of fU_4A_4. This illustrates a general point when fitting for the fU_4A_4 term, in that it is very important to allow it to vary only within physically reasonable limits, otherwise the fit may be misleading.

<u>473.5 *keV* : $4^+ \rightarrow 2^+$</u>

The temperature dependence for this transition is shown in [Fig 7.9] , and the fits correspond to the parameters

---

$\chi^2_\nu = 1.38$ $\quad {}^*B_{hf} = 42.3(3.1)$ $\quad {}^*fU_2A_2 = -0.171(13)$ $\quad fU_4A_4 = -0.01(-)$

$\chi^2_\nu = 4.78$ $\quad B_{hf} = 27.6$ $\quad {}^*fU_2A_2 = -0.222(7)$ $\quad fU_4A_4 = -0.01(-)$

The constraint $fU_4A_4 < 0$ was imposed on the basis of a major direct feed from the low spin isomer. The amount of high feeding to the 797.9 keV level via the $6^+ \rightarrow 4^+$ transition at 601.2 keV cannot be extracted from this data because it is swamped by a strong γ-ray from ^{120}I^g decay at almost the same energy. However, from $\gamma - \gamma$ coincidence measurements, an estimate of $\sim 25\%$ has been made for the high spin component [13] . The possible effects of this have not

been taken into account in the fits above, which should be treated with some caution, even though B_{hf} is consistent with other fits.

7.2.6 The $^{122}Cs^{m}$ experiment

The existence of two isomers of ^{122}Cs has been established, and their spins and moments determined[5] . The low spin isomer $^{122}Cs^{g}$ (spin 1) has a very small moment, which, by comparison with $^{119}Cs^{m}$ and $^{121}Cs^{m}$, would not be expected to reach any measurable degree of orientation before decay. The high spin isomer $^{122}Cs^{m}$ (spin 8) has a large moment, and hence a fast relaxation rate, which ensures that full thermal equilibrium effects should be observed. A simplified decay scheme showing just those transitions to be discussed is shown in [Fig 7.8].

In this experiment, a temperature dependence was not feasible because of problems in peak area determination for a weak ^{57}Co thermometer γ-ray at 136 keV sitting on top of a very large Compton scattered background (due to a strong source). The base temperature during implantation could only be determined to $1/T_L = 55(10)$.

$E\gamma$	$I_i \rightarrow I_f$	W(0)/W(90)−1
331.3	$2^+ \rightarrow 0^+$	−4.5(1.5)%
497.4	$4^+ \rightarrow 2^+$	−26.9(2.6)%
638.6	$6^+ \rightarrow 4^+$	−29.1(1.7)%
750.9	$8^+ \rightarrow 6^+$	−31.5(1.0)%

Table 7.3 Anisotropies for transitions seen in the decay of $^{122}Cs^{g+m}$.

In spite of there being only one temperature point, a fraction in good sites can be estimated from the observed anisotropies, the most relevant of which are given in Table 7.3. These are all stretched E2 transitions, and as such, would all show the same anisotropy, if the only feed were via the 8^+ state. As can be seen from the table, this is reasonably well borne out for all except the 331.3 keV transition, which is the only one to have direct feeding from the low spin isomer. As the low spin isomer is not expected to orient, the low spin feed to this transition heavily attenuates the effect due to the high spin feed.

The decay scheme of $^{122}Cs^{g+m}$ is complex, but it is possible to estimate $U_2 = 0.98(2)$ and $U_4 = 0.93(7)$ for the 8^+ level, which is entirely β-fed. The additional feeding to the 6^+ and 4^+ levels is reflected in the slightly reduced effects observed for the 638.5 and 497.4 keV transitions. Taking $B_{hf} = 40.8$T (from the next sub-section), and the appropriate Q_λ values, the values $B_2U_2A_2Q_2 = -0.359(51)$ and $B_4U_4A_4Q_4 = -0.035(14)$ may be deduced. By defining $X_\lambda \equiv B_\lambda A_\lambda U_\lambda Q_\lambda$, the axial/equatorial ratio W_{eq}^{ax} may be written as

$$W_{eq}^{ax} + 1 = W(0)/W(90) = \frac{1 + f(X_2 + X_4)}{1 + f(-\frac{1}{2}X_2 + \frac{3}{8}X_4)} \tag{7.3}$$

and solving this equation for f gives

$$f = \frac{W_{eq}^{ax}}{(X_2 + X_4) - (W_{eq}^{ax} + 1)(-\frac{1}{2}X_2 + \frac{3}{8}X_4)} \tag{7.4}$$

This is easily evaluated using the above parameters to give a fraction in good sites, $f = 62(7)\%$.

Isotope	E_γ	$I_i \rightarrow I_f$	Deduced f	Fitted B_{hf}
$^{119}Cs^g(9/2^+)$	176.4	$7/2^- \rightarrow 5/2^+$	30(6)%	41.8(6.6)T
$\|\mu\| = 5.46(3)$	225.5	$7/2^+ \rightarrow 5/2^+$	54(6)%	44.9(2.2)T
$^{120}Cs^g(2^+)$	322.4	$2^+ \rightarrow 0^+$		38.2(2.6)T
$\|\mu\| = 3.88(2)$	473.5	$4^+ \rightarrow 2^+$		42.3(3.1)T
$^{121}Cs^m(9/2^+)$	196.0	$7/2^- \rightarrow 5/2^+$	40(5)%	36.1(2.4)T
$\|\mu\| = 5.41(3)$	179.4	$7/2^+ \rightarrow 5/2^+$	68(8)%	40.7(1.0)T
	234.5	$9/2^+ \rightarrow 5/2^+$	56(6)%	38.3(2.6)T
	280.1	$7/2^+ \rightarrow 7/2^+$		51.2(7.2)T
	459.7	$7/2^+ \rightarrow 5/2^+$	$> 54\%$	41.1(1.1)T
$^{122}Cs^m(8)$	750.9	$8^+ \rightarrow 6^+$	62(7)%	
$\|\mu\| = 3.88(2)$				

Table 7.4 Summary of temperature dependence data for Cs isotopes.

7.2.7 Discussion

All the temperature dependence data for the various transitions of the Cs isotopes studied have been analysed in terms of the 2-site model, where a fraction f of the nuclei are assumed to occupy substitutional sites and see a unique hyperfine field B_{hf}. Nuclei not in substitutional sites are assumed to experience no hyperfine interaction (see chapter 1.2.6). The results of the various experiments performed are given in Table 7.4.

The fitted values for B_{hf} for the three Cs isotopes in Table 7.4 are in good agreement with one another, and taking a weighted mean results in a value of

$$\langle B_{hf} \rangle_{av} = 40.8(0.7)\mathrm{T} \tag{7.5}$$

The sign of the hyperfine field is taken as positive from the previous measurement by Reintsema[1] . Assuming similar experimental conditions in the different experiments, a weighted average for the fraction in good sites may be made

(excluding the values from the 179.4 and 196.0 keV transitions). A mean value of

$$\langle f \rangle_{av} = 59(3)\% \tag{7.6}$$

is thus obtained for on-line Cs experiments (assuming the above hyperfine field).

This fitted value of the hyperfine field is significantly *higher* than the high field site of +27.6(4)T observed in Mössbauer measurements[1] . In their studies, they in fact saw three field sites at 27.6T, 13.5T and 5.0T, but it is not possible to fit the nuclear orientation data with any of these field sites, not even if a combination of different fractions of nuclei in each field site is tried. In the preceeding analysis, curves of best fit are plotted corresponding to the 27.6T field site. These all underpredict the data at low $1/T_L$ and overpredict at high $1/T_L$, clearly illustrating the need for a field site *higher* than 27.6T.

Why there is a difference between these two types of measurement is not at present understood, but it perhaps indicates that there is a significant difference between *warm* and *cold* implantation of Cs into an Fe lattice. The basic nuclear orientation technique is not very sensitive to the details of the field site distribution, and the 40.8(0.7)T deduced above may correspond to a *unique* high field site, or may be an *averaged* hyperfine field for the system. From a pragmatic point of view, however, the value of 40.8T for a single field site is adopted and used in the remainder of the chapter, and will be shown to yield sensible results.

7.3 Time dependent relaxation of $^{121}Cs^{m}$

7.3.1 Choice of experiment

In order to make a *full* analysis of the temperature dependence data for the range of Cs nuclei described in this chapter, it has been necessary to know how fast they relax to the lattice temperature. As can be seen from Table 7.1, the *estimated* relaxation time of $^{118}Cs^{m}$ is $\sim$ 120s, even assuming a high magnetic moment of $\sim$ 5nm, and, with a half-life of only 17s, this isomeric state would thus not be expected to orient. However, orientation data has been observed for $^{118}Cs^{m}$ (see next section), indicating that the true relaxation time must be significantly faster than the initial estimate. The purpose of this section is to describe an experiment in which the time dependent relaxation of Cs*Fe* has been measured.

The basic idea behind the experimental technique used to do this, is simply to implant a short burst of *hot* Cs ions into a cooled Fe foil, for a time $t_{on} < \tau_{SLR}$. The Cs nuclei are then observed to relax to the lattice temperature as a function of time, by measurement of the γ-ray anisotropy. In order to build up sufficient statistics, this needs to be repeated many times, with a waiting time $t_{off} > t_{1/2}$, between each implant to allow the source from the previous implant to die away.

To obtain good statistics in a given time certain other requirements must be fulfilled,

(i) as high a duty factor (which is just the ratio of the implantation time to the time between implants) as possible, that is consistent with the above restraints,

(ii) a high implantation rate.

In addition to obtaining good statistics, it is also important to bear in mind that the *sensitivity* of the measurement is enhanced for γ-rays which show large thermal equilibrium effects at the implantation temperature.

Based on these considerations, the two best candidates for such a measurement are $^{119}Cs^{g}$ and $^{121}Cs^{m}$. From comparison of their half-lives, the duty factor for $^{119}Cs^{g}$ is some 3$\times$ better than for $^{121}Cs^{m}$, but this is compensated for by the greater production rate of $^{121}Cs^{m}$. Also, there are two strong transitions for $^{121}Cs^{m}$ (at 179.4 and 459.7 keV) which show *larger* effects than the most suitable transition in $^{119}Cs^{g}$ (at 225.5 keV). It was thus decided to perform the experiment with $^{121}Cs^{m}$, for which the low duty factor is out-weighed by the large yield and large effects.

7.3.2 Experimental details

The experimental setup as regards source production, detector placement and thermometry was the same as for the experiments described in section 7.2.2. In addition, extra electronics were needed to enable a series of implant/wait cycles to be performed repetitively. The time dependent count rate was monitored by use of a Time Frame Generator to periodically *route* spectra (for each of the four detectors) into different portions of the relevant ADC memory. Each of the 2^N $(N = 1, \ldots, 8)$ routed spectra or *time frames* (for each detector) corresponds to a fixed acquisition time t_{TFG}, but they are separated in time according to the relation

$$t_n = t_1 + (n-1)t_{TFG} \tag{7.7}$$

where t_n is the start time for the n^{th} *time frame* $(n = 1, \ldots, 2^N)$, and $t = 0$ corresponds to the start of implantation for that cycle. Data from successive

t_{on}	n_{on}^{∞}	**Routed spectra**	t_{off}	n_{off}^{∞}	**Cycles**
10s	0.025	8 × 10s	200s	0.080	~ 11
10s		8 × 10s	200s		~ 22
4s	0.008	16 × 2s	228s	0.031	~ 21
4s		16 × 2s	228s		~ 27

Table 7.5 Summary of relaxation experiments for $^{121}Cs^{m}$.

cycles were added together for the appropriate *time frames*. Details of the full experimental setup used to achieve this are given in chapter 3.6.3.

A summary of the various experimental runs performed is given in Table 7.5, where t_{on} is the implantation time and t_{off} the time between implants. The column for *routed* spectra is in the format of *number of frames* × *the aquisition time per frame*, t_{TFG}. For the first pair of runs, the counting was started at the end of the implantation period, and at the start of the implantation period for the second pair of runs. For each run, the approximate number of implant/wait cycles performed is also shown. Values of n_{on}^{∞} and n_{off}^{∞} are also quoted for the different combinations of t_{on} and t_{off} tried. These are the *equilibrium* source strengths at the start of the implantation and wait periods respectively (relative to the source strength for continuous implantation), and are discussed more fully in chapter 4.5.1, and Appendix *II*.1.

The implantation time t_{on} refers to the time set on the Ortec 719 Timer. This was used to control the implantation by operating a gate valve, which could move a Faraday cup in and out of the beam. However, some delay was observed in the operation of the gate valve, which was significant when compared to the supposed implantation time t_{on}. As a result, a short series of experiments was performed in order to determine what effect this had on the *true* implantation time.

For simplicity, it was assumed that the operation of the gate valve could be described in terms of *response* times, t_r^{in} and t_r^{out} (i.e. the time taken to respond to an input signal) and by *travel* times, t_t^{in} and t_t^{out} (i.e. the time taken for the Faraday cup to travel completely *in* or *out*). A schematic diagram of the measurements performed is given in [Fig 7.10] .

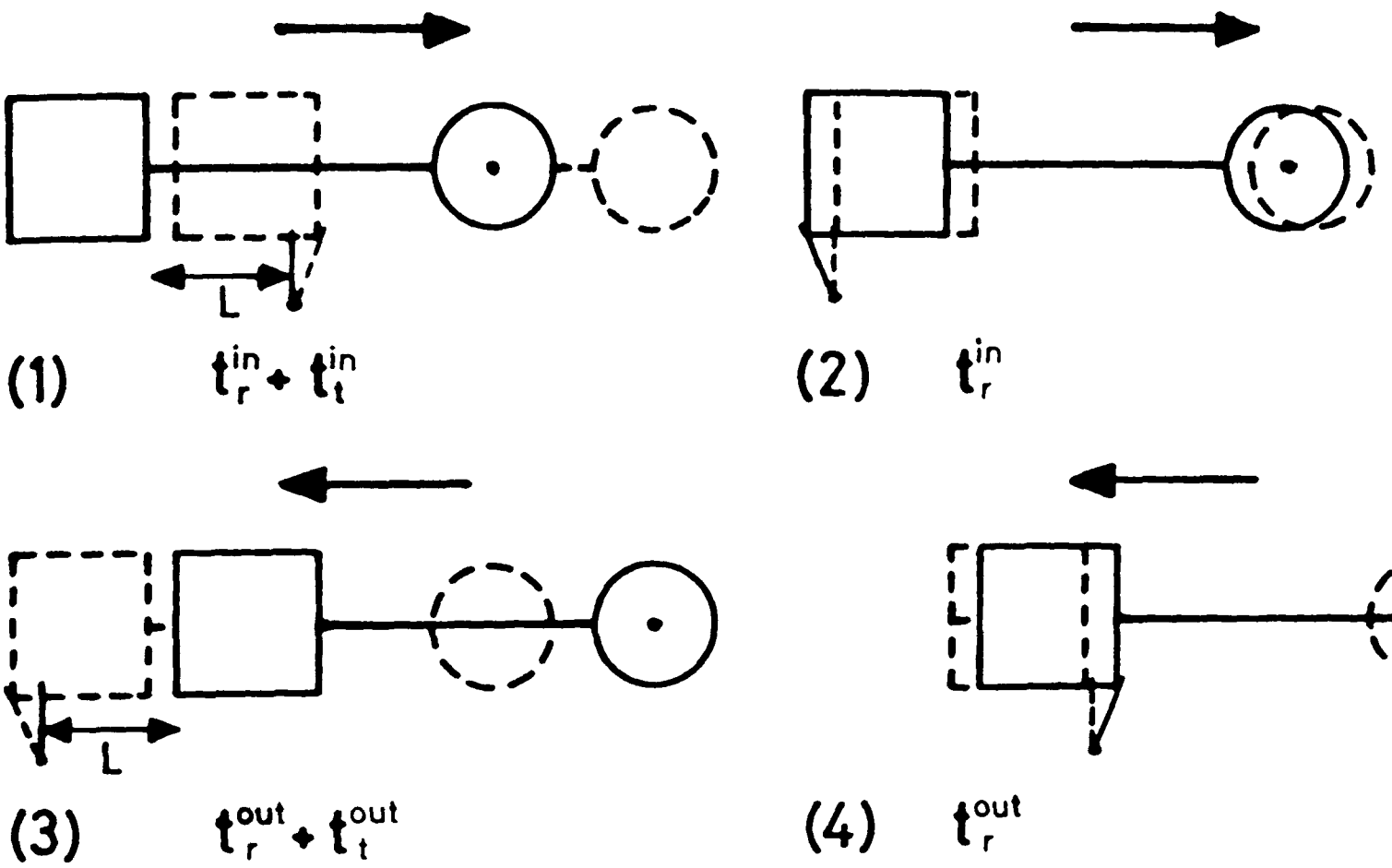

Figure 7.10. Measurements made to determine delays associated with the operation of the gate valve. The arrows show the direction of travel of the Faraday cup.

For each of the cases illustrated, the delay times were measured by synchronizing the signal to open/close the gate valve with the start of a counter (counting pulses from a stable pulse generator). The counter was stopped when the gate valve triggered a microswitch, positioned as shown in [Fig 7.10] for the four cases. Each measurement was repeated 20 times and an average count taken. These numbers were then converted to times through dividing by the

average count rate (of $\sim$ 500 count/s), which was deduced from a series of fixed 40s counting periods.

The results obtained for the gate valve travelling *in* were

$$\begin{aligned} t_r^{in} &= 0.46s \\ t_r^{in} + t_t^{in} = 0.70s \quad &\Longrightarrow \quad t_t^{in} = 0.24s \end{aligned} \tag{7.8}$$

and those for the gate valve travelling *out*

$$\begin{aligned} t_r^{out} &= 0.94s \\ t_r^{out} + t_t^{out} = 1.31s \quad &\Longrightarrow \quad t_t^{out} = 0.37s \end{aligned} \tag{7.9}$$

Taking L to be the length of travel and r the radius of the Faraday cup, then implantation will start when the cup has travelled *out* a distance r. Assuming a constant speed of motion, this takes a time t_d^{out}, where

$$t_d^{out} = t_r^{out} + \left(\frac{r}{L}\right) t_t^{out} \tag{7.10}$$

Similarly, the time delay before the end of implantation will be given by

$$t_d^{in} = t_r^{in} + \left(1 - \frac{r}{L}\right) t_t^{in} = t_r^{in} + t_t^{in} - \left(\frac{r}{L}\right) t_t^{in} \tag{7.11}$$

The *true* implantation time t_{imp} may now be written as

$$\begin{aligned} t_{imp} &= t_{on} + t_d^{in} - t_d^{out} \\ &= t_{on} + t_r^{in} + t_t^{in} - t_r^{out} - \frac{r}{L}\left(t_t^{in} + t_t^{out}\right) \end{aligned} \tag{7.12}$$

Now, the dimensions $L = 5.4$cm and $r = 1.0$cm were measured, and the following times may be deduced

$$\begin{aligned} t_d &= 1.0s \\ t_{imp} &= t_{on} - 0.35s \end{aligned} \tag{7.13}$$

The times t_{on} and t_{off}, along with the values of t_d and t_{imp} deduced above, are all necessary in order to interpret the data obtained in this experiment. How this was done will next be described.

7.3.3 Data analysis

The method of analysis for this type of experiment is described in chapter 4.5, and will now be applied to this experiment. For the two different kinds of implantation/wait cycles shown in Table 7.5, the equilibrium values n_{on} and n_{off} quoted, are reached within 3–4 cycles. This is less than the number of cycles performed in each of the runs, and in the following analysis, the data acquired are taken to correspond to a set of equilibrium cycles.

In order to improve statistics, corresponding spectra were added (after gain-shifting) for the two axial detectors, and also for the two equatorial detectors. Reasonable statistics were obtained only for the 179.4 and 459.7 keV transitions, and relaxation effects were then looked for, using these γ-rays , in the subsequent counting periods by,

(i) evaluating the anisotropies $\{W(0)/W(90)-1\}\%$, for which the time dependent source strength cancels out,

(ii) evaluating the ratios $N_\gamma^c(\theta, \Delta t_{12}^i)/D_\tau^c(\Delta t_{12}^i)$, defined by equation (4.46), for *separate* axial and equatorial counts. Care was taken that the integrated source strength, $D_\tau^c(\Delta t_{12}^i)$, calculated using the subroutine HLINT, should take into account the gate valve delay, which both alters the implantation time, and also shifts the start of implantation, relative to the start of the counting periods.

For the first set of runs, with 10s implantation and counting times, no signs of any relaxation effects were observed for either (i) or (ii) above, indicating that the relaxation time must be significantly faster than 10s. However, for

the second set of runs, with a $4s$ implantation time and $2s$ counting periods, a small effect was observed for the *normalized* axial count rate from (ii), but no such effects were seen for the corresponding equatorial count rate nor for the axial/equatorial anisotropies from (i). The reason for this lies in the statistical quality of data obtained. If N^i_{TFG} is the number of counts obtainable during the i^{th} counting period (over many cycles), and N_{cont} is the number of counts expected for continuous implantation, in the same total time, then from equation (4.44),

$$\frac{N^i_{TFG}}{N_{cont}} \approx n^{\infty}_{off} \left(\frac{t_{TFG}}{t_{on}+t_{off}}\right)$$
$$\approx 0.008 \left(\frac{2}{4+228}\right) = 7 \times 10^{-5} \qquad (7.14)$$

Although the continuous implantation source strength was very healthy (i.e. hundreds of counts/second in the peaks of interest), equation (7.14) gives an indication of why it proved so difficult to obtain good enough statistics to see *any* relaxation effects. There are two reasons why effects were seen for the axial, but not for the equatorial count rates,

(i) both the transitions observed have large *positive* U_2A_2 values, and the thermal equilibrium count rates in the axial direction are $\sim (3-4)\times$ higher than in the equatorial direction,

(ii) the axial anisotropy is *twice* the magnitude of the equatorial anisotropy, and is thus more sensitive.

Due to these factors, it is not too surprising that the *small* relaxation effect seen in the axial counts, is lost in the poorer statistics and reduced sensitivity of the equatorial counts.

From the rather *qualitative* analysis outlined so far, all that can be stated is that the relaxation time is of order a few seconds. To be be more quantitative, it is first necessary to determine the thermal equilibrium effects in the second of the two sets of runs performed, for which relaxation effects were observed. By looking

at the variation of $N_\gamma^c(0, \Delta t_{12}^i)/D_\tau^c(\Delta t_{12}^i)$, over the different counting periods, it was deduced that for $i = 5, \ldots, 16$ the source was fully relaxed. These spectra were then added, and axial/equatorial anisotropies were then extracted, which are shown in Table 7.6.

E_γ	W(0)/W(90)−1	W(0)−1	$(fU_2A_2)_{deduced}$	$(fU_2A_2)_{fitted}$
179.4	103(7) %	51(3)%	0.343(24)	0.301(6)
459.7	247(22)%	90(9)%	0.606(60)	0.546(7)

Table 7.6 Parameters deduced for the 179.4 and 459.7 keV transitions.

By adding the spectra for *all* the counting periods, the base temperature during the run was determined to be $1/T_L = 135(5)$, from the axial/equatorial anisotropy of the 136.5 keV transition for the ^{57}Co/Fe thermometer. This necessarily assumes that there is negligible beam heating during the implantations, which is a reasonable assumption to make. From this temperature, and taking the Cs*Fe* field to be 40.8(0.7)T from section 7.2.7, the thermal equilibrium orientation coefficient $B_2 = 1.55(2)$ can be deduced for $^{121}Cs^m$, for this run.

For both the 179.4 and 459.7 keV transitions, negligible $\lambda = 4$ terms were seen in the temperature dependence data, and thus equation (7.4) may be simplified to give, either

$$fU_2A_2 = \frac{2W_{eq}^{ax}}{B_2Q_2(3 + W_{eq}^{ax})} \qquad (7.15a)$$

or

$$W(0) - 1 = \frac{2W_{eq}^{ax}}{(3 + W_{eq}^{ax})} \qquad (7.15b)$$

where

$$W_{eq}^{ax} = W(0)/W(90) - 1 \qquad (7.15c)$$

Taking $Q_2 = 0.96(1)$, the values fU_2A_2 have been calculated using equation (7.15*a*) and the results are tabulated in Table 7.6, along with values of $W(0) - 1$,

also deduced. The *deduced* values of fU_2A_2 are compared with the *fitted* values obtained in section 7.2, from the temperature dependence data. It is clear that the *new* values are $\sim 10\%$ higher, corresponding to an increase in the fraction in good sites (which is assumed to be due to improved surface preparation).

If now the value of $N_\gamma^c(0, \Delta t_{12}^i)/D_\tau^c(\Delta t_{12}^i)$ is evaluated for those spectra which are fully relaxed, then the value of $N_\gamma^w(\theta)/D_\tau^w$ may be determined from equation (4.46). The *normalized* number of counts for the i^{th} counting period, y_{exp}^i, defined in chapter 4.5.2, as,

$$y_{exp}^i = N_\gamma^c(\theta, \Delta t_{12}^i) \Big/ \left(\frac{N_\gamma^w(\theta)}{D_\tau^w} \right) \tag{7.16}$$

can now be evaluated.

Using the parameters given in Table 7.6, it is also possible to evaluate the function y_{fit}^i, defined in chapter 4.5.2, to be

$$y_{fit}^i = \overline{W(\theta, \Delta t_{12}^i)} \times D_\tau^c(\Delta t_{12}^i) \tag{7.17}$$

The only *unknown* parameter in this equation is the Korringa constant C_k, which governs how fast the sub-level populations relax to their thermal equilibrium values. As mentioned in chapter 4.5.2, this may be found by a standard non-linear least-squares fitting procedure.

$\mathbf{E}_\gamma$	χ_ν^2	fU_2A_2	Fitted $\mathbf{C}_k$
179.4	1.11	0.343(24)	0.064(26)
459.7	1.54	0.606(60)	0.057(20)

Table 7.7 Results of fits to the time dependent data for $^{121}Cs^m$.

Fits to the time dependent count rate data, acquired for both the 179.4 and 459.7 keV γ-rays , have been performed, and the results are given in Table 7.7. The data, along with the corresponding fits, are shown in [Fig 7.11] . Note that the time $t = 0$ corresponds to the start of implantation, and the implantation time is $3.65s$, from equation (7.13). The first counting period starts at a time $t = -t_d = -1.0s$, and the count rates are shown at times corresponding to midway through the counting periods. Fits were also tried with slightly differing values of $t_d = 0.9, 1.1s$, but this only changed the fitted values by a small amount, compared to the associated errors.

7.3.4 Discussion

The results of the two fits performed in the previous section are consistent with one another, and taking a weighted mean gives

$$C_k = 0.059(16) \text{ sK} \tag{7.18a}$$

In order to get a feel for this value, it is helpful to write it in the form

$$T_{int}^2 C_k = 2.0(5) \times 10^{-5} \text{ sK}^3 \tag{7.18b}$$

where the value $T_{int} = 18.3\text{mK}$ has been assumed. This may now be compared with the empirical estimate of 1.4×10^{-4}, from equation (2.25), for this parameter. It is seen that the measured value is considerably smaller than the empirical estimate, corresponding to much faster relaxation rates than might at first be expected.

Before proceeding, it is worth mentioning a couple of points about the time dependent count rates analysed in the last section,

(i) in both sets of data, the experimental point for the *first* counting period is below the fitted line. This may be a consequence of fluctuations in beam

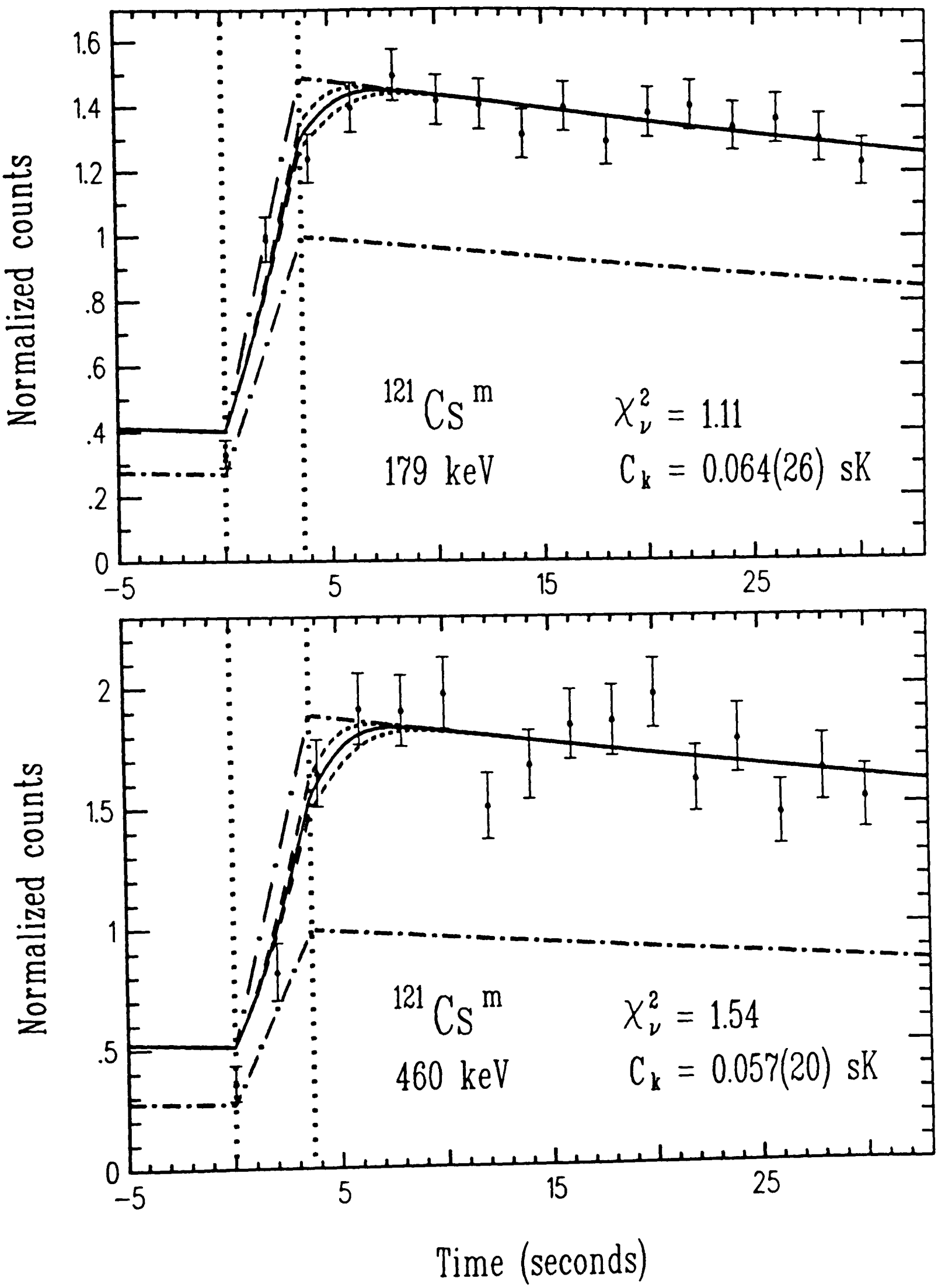

Figure 7.11. Results of fits to the time dependent count rate data for $^{121}Cs^{m}$, normalized such that $n_{off} = 1$. The vertical dashed lines indicate the implantation period, and the data points are positioned at times corresponding to half-way through their respective counting periods. The upper and lower dot-dashed lines represent the expected counts for the cases of *complete* relaxation and *no* relaxation (i.e. the source strength)

intensity, reducing $\langle n_{on} \rangle_{exp}$ compared with the value expected for an equilibrium set of cycles.

(ii) if the beam were to cause some momentary heating, this would lower the thermal equilibrium effect, and could possibly mimic a relaxation effect (however, no such effects were *apparent* for the longer 10s implantation time).

The effect of either (i) or (ii) would tend to require a faster relaxation time, than is obtained with the fitting procedure in the previous section. The fitted value of C_k is quoted with a large error, and this is assumed to encompass possible uncertainties associated with (i) or (ii), which would tend to make the quoted value an *upper* estimate.

As discussed in chapter 2.3.3, the product $\gamma_n^2 C_k$ may be taken as constant for a range of different isotopes, in the same host. Hence, it is possible to define a reduced rate constant, r, to be

$$r = (\gamma_n^2 C_k)^{-1} \tag{7.19a}$$

It is convenient to introduce the dimensionless quantity r', such that

$$r = r' \times 10^{-15}\ \mathrm{T^2 s K^{-1}} \tag{7.19b}$$

From equation (7.18), the reduced rate constant r' for $^{121}\mathrm{Cs}^{m}\underline{Fe}$ turns out to be

$$r' = 5.1(1.4) \tag{7.20}$$

To the extent to which hyperfine anomalies can be neglected, this reduced rate constant is now independent of nuclear parameters, and as such may be used to determine relaxation rates for the other Cs isotopes for which orientation data has been obtained. This is how the *revised* relaxation times, quoted in Table 7.1, were calculated.

It is also possible to compare the reduced rate constants, measured for a range of nuclei in this mass region, for which theoretical calculations have also been made. Kanamori *et al* [14] have carried out *ab initio* calculations of both hyperfine fields and relaxation rates. These calculations have been applied to impurities (Ag to Ba) in an Fe host by Yoshida *et al* [15] and Akai *et al* [16], and the results for the calculated hyperfine fields and reduced rate constants are shown in [Fig 7.12] , along with the corresponding experimental values for comparison.

Considering the fact that there are no adjustable parameters in these calculations, the agreement between experiment and theory is extremely good, with the systematic variations of the parameters being particularly well reproduced. In [Fig 7.12] the values of B_{hf} and r' obtained for Cs in this work are plotted, and both are seen to be consistent when compared with other measured values and the theoretical trends. The hyperfine field and reduced rate constant determined in this work for Cs*Fe* are now both used in the analysis of the $^{118}Cs^{m}$ orientation data.

7.4 The magnetic moment of $^{118}Cs^{m}$

7.4.1 Experimental details

The experimental setup and procedure used to measure the anisotropies $\{W(0)/W(90) - 1\}\%$ as a function of temperature are described earlier in section 7.2.2. The data for ^{118}Cs were acquired at the same time as temperature dependence data for $^{118}I^{g+m}$ (see chapter 5.4), using a ^{32}S beam on a ^{93}Nb target. The yield of the isomer $^{118}Cs^{m}$ was comparable to that of $^{118}I^{m}$, and good

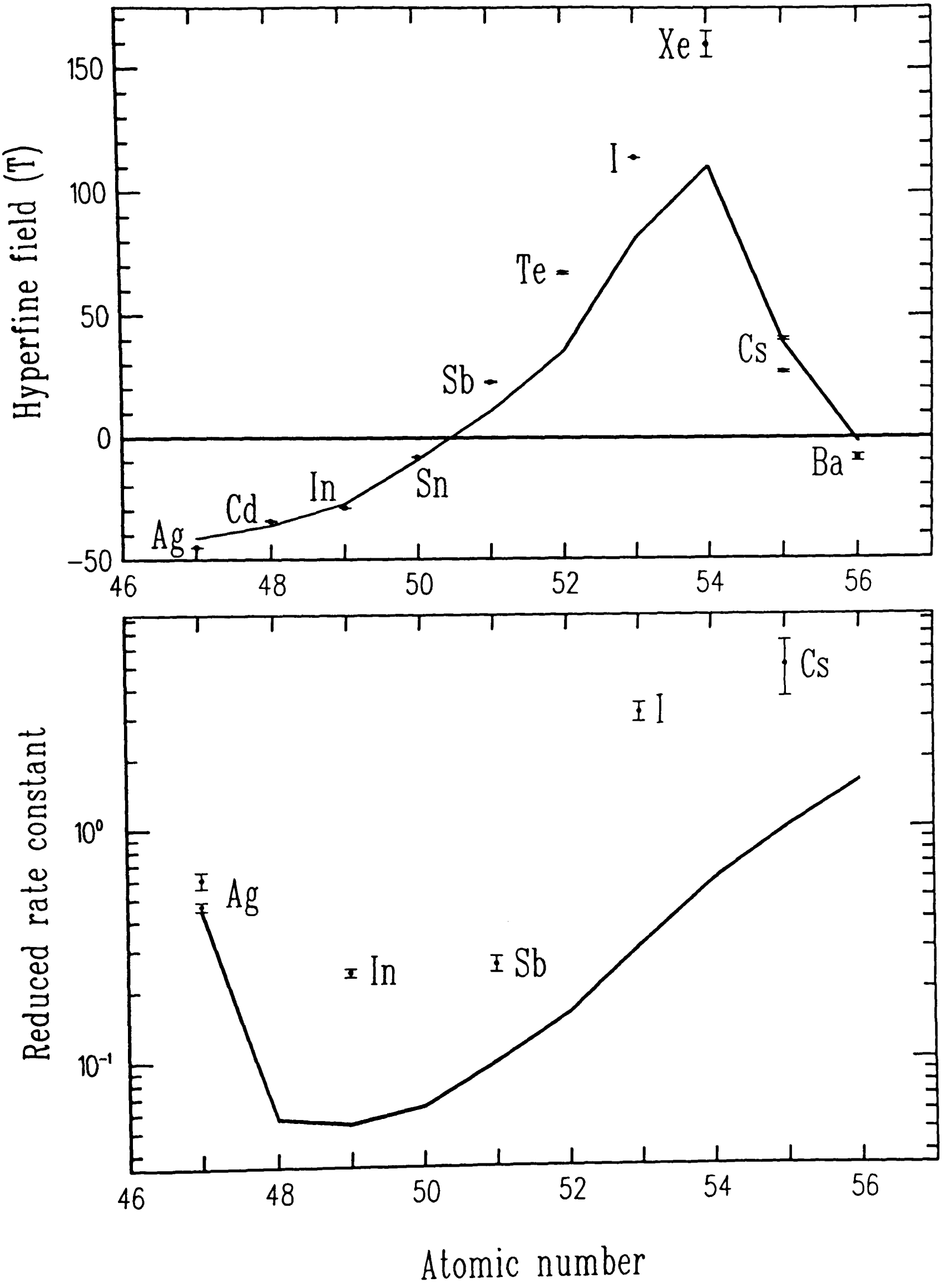

Figure 7.12. Experimental hyperfine fields and reduced rate constants for impurities Ag to Ba in an Fe host. The solid lines show the results of *ab initio* theoretical calculations for these quantities.

enough statistics were obtained to enable the previously unmeasured magnetic moment of this Cs isotope to be determined.

7.4.2 Data analysis and results

In common with other Cs isotopes in this mass region, ^{118}Cs has two isomers of similar half-life. The spin ($I = 2$) and magnetic moment ($\mu = 4.29$) of the low spin isomer ^{118}Cs^{g} have been determined by laser spectroscopy[5] . However, similar measurements have not been performed for ^{118}Cs^{m}, established from previous decay studies[12] as high spin ($I \geq 6$, due to a feed to the 8_1^+ state), with a half-life of 17(3) seconds. The main transitions populated in the decay of ^{118}Cs^{m} are illustrated in [Fig 7.13] .

The $8^+ \rightarrow 6^+$ transition at 676.3 keV was observed, but was too weak for useful data to be extracted from it. The $4^+ \rightarrow 2^+$ transition at 472.5 keV was also not used, because of contamination due to a γ-ray from ^{118}I decay, and also the possibility of a low spin component from ^{118}Cs^{g} being present (of unknown strength). The 337.1 keV ground state transition is predominantly fed from the low spin isomer, leaving the $6^+ \rightarrow 4^+$ transition at 586.2 keV as the only suitable candidate from which the ^{118}Cs^{m} magnetic moment can be determined.

In order to extract the magnetic moment from the anisotropy temperature dependence, observed for the 586.2 keV γ-ray , a non-standard least-squares fitting procedure was adopted in which the effect of relaxation was taken into account by constraining the product $T_{int}^2 C_k = C$, where C is held constant during the fit. The orientation coefficients B_λ are calculated assuming the system has reached *secular* equilibrium between implantation and decay (see chapter 2.4.3).

Fits have been performed for the fraction in good sites f, using the 2-site model, and the magnetic moment μ, where the hyperfine field has been taken

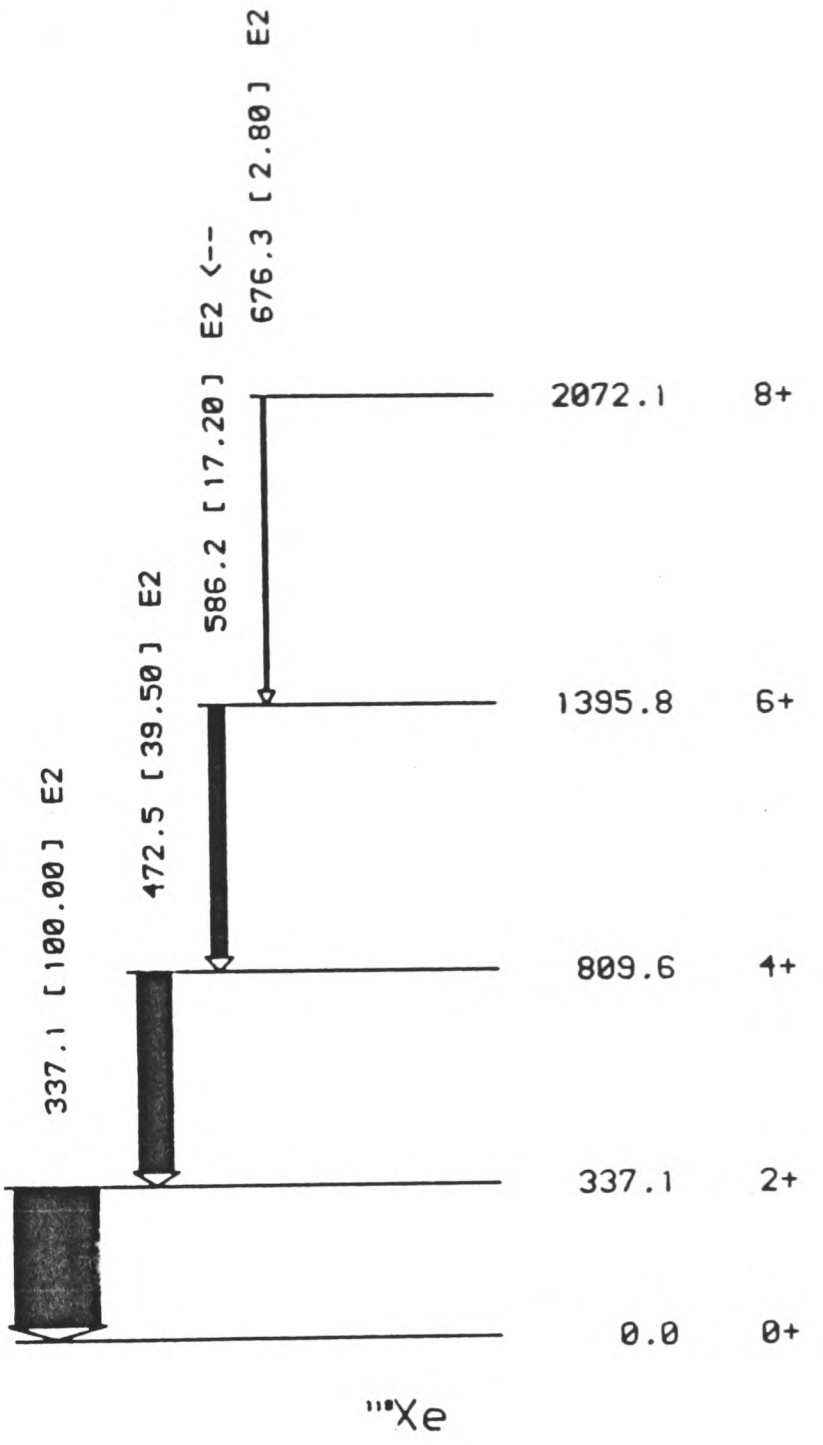

Figure 7.13. Levels in ^{118}Xe populated in the decay of ^{118}Cs^{m}. Transitions for which data are presented are indicated with an *arrow* $--$>.

as $B_{hf} = 40.8(0.7)$T, from section 7.2.7. As the spin of ^{118}Cs^{m} has not been measured, fits for spins 6,7 and 8 were tried, and for each fit the de-orientation coefficients were calculated on the assumption of a direct feed to the initial 6^+ level. The results of these fits are given in Table 7.8 where a value of 2.0×10^{-5} has been taken for the product $T^2_{int}C_k$. The fits marked with a * indicate fits performed assuming *instantaneous* relaxation, which are given for comparison.

Uncertainty in the value of $T^2_{int}C_k$, measured in the last section, leads to

Spin	U_2	U_4	χ^2_ν	f	μ
6	0.964	0.881	0.60	35(8)	5.4(1.0)
			*0.59	30(3)	5.6(0.9)
7	0.969	0.897	0.60	37(9)	5.4(1.0)
			*0.59	29(3)	5.6(0.9)
8	0.946	0.827	0.60	40(10)	5.4(1.0)
			*0.59	30(3)	5.8(1.0)

Table 7.8 Results of fits to the temperature dependence data for $^{118}Cs^m$.

the following results

$I = 6$	$f = 35(9)$ %	$\mu = 5.4(1.1)nm$
$I = 7$	$f = 37(10)\%$	$\mu = 5.4(1.1)nm$
$I = 8$	$f = 40(10)\%$	$\mu = 5.4(1.2)nm$

The anisotropy temperature dependence data and fits for the 586.2 keV transition are shown in [Fig 7.14] . The dashed lines correspond to effects calculated using the above parameters, but assuming *instantaneous* relaxation.

It can be seen that the *fitted* moment of 5.4(1.1)nm is insensitive to the value of the oriented spin assumed. Also, Table 7.8 and [Fig 7.14] indicate that the relaxation is very fast ($\tau_{SLR} \sim \frac{1}{3}t_{1/2}$), and the moment deduced changes slightly if the relaxation is assumed to be instantaneous. However, it is worth pointing out that this is largely due to the *large* value of the magnetic moment. As mentioned in chapter 2.3.3, the relaxation time $\tau_{SLR} \propto 1/\mu^3$, in the low temperature limit. Thus, if the moment had a smaller value of $\sim$ 2.5nm, then $\tau_{SLR} \sim 3t_{1/2}$, and the observed anisotropies would be considerably reduced, compared to the expected thermal equilibrium values.

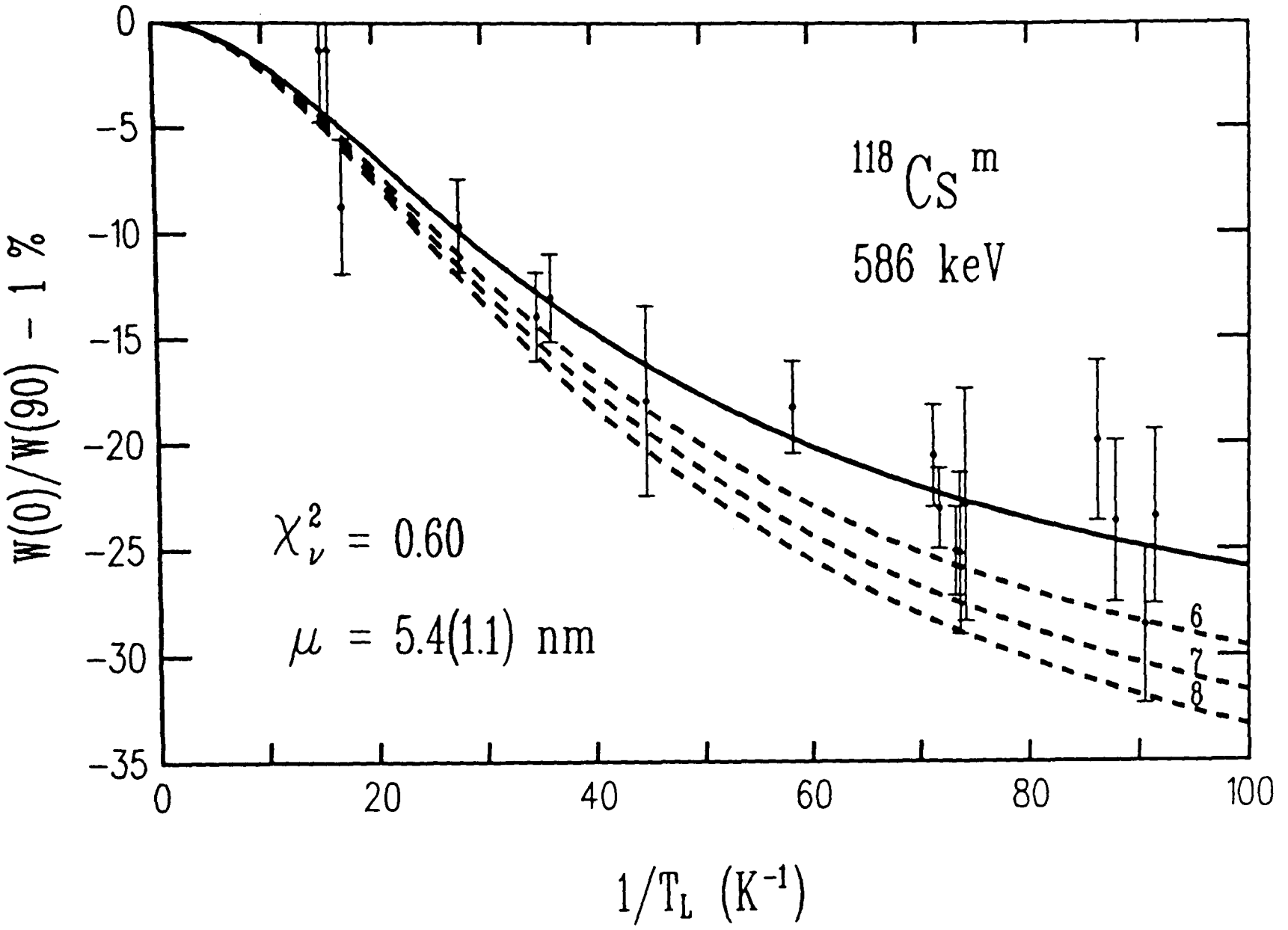

Figure 7.14. Anisotropy data and fits for the 586.2 keV transition seen in $^{118}Cs^{m}$ decay.

The fraction in good sites is seen to change slightly with spin, and seems slightly low, compared with other Cs orientation experiments. However, the errors are *large*, which is mainly a consequence of the *increased* correlation between f and μ. As $\mu^2 C_k$ is constant, a change in μ will alter the B_λ coefficients (mainly because the relaxation rate will change), and this directly affects f.

7.4.3 Discussion

In the first part of the chapter, the Cs*Fe* hyperfine field was determined using various Cs isotopes for which the spins and moments had previously been measured by Ekström *et al*[3,4] and Thibaut *et al*[5] . In these studies, hyperfine structure measurements in the mass range 118-145 have been performed, and in particular, the experimental data on spins and magnetic moments show a trend of increasing deformation as the mass number decreases towards mass 118.

As an example, the ground state spins of ^{123}Cs, ^{121}Cs and ^{119}Cs are known to be $1/2^+$, $3/2^+$ and $9/2^+$ respectively, with suggested Nilsson model assignments[4] of [420]1/2, [422]3/2 and [404]9/2. Single particle energy levels have been calculated as a function of quadrupole deformation ϵ_2 in the Nilsson model, using the shell parameters,

$$\text{Odd-proton orbitals} \quad : \quad \kappa_p = 0.0674 \text{ and } \mu_p = 0.569$$

$$\text{Odd-neutron orbitals} \quad : \quad \kappa_n = 0.0638 \text{ and } \mu_n = 0.478$$

and the results are plotted in [Fig 7.15] . These values of κ and μ were obtained (for mass 118) by linear extrapolation in A from *known* shell parameters (i.e. deduced from fits to energy levels) in the rare-earth ($A = 165$) and actinide ($A = 242$) regions [17]. By considering the orbitals occupied by the 55^{th} proton as a function of deformation (for $\epsilon_2 > 0.2$) in [Fig 7.15] , it is seen that the above ground state spin assignments can be interpreted in terms of increasing in quadrupole deformation, in going from ^{123}Cs to ^{119}Cs.

To go into a little more detail, high spin states have been studied in the odd-mass nuclei $^{119-125}$Cs by in-beam γ-ray spectroscopy [18] . One of the main features of this work was the observation of $\Delta J = 1$ rotational bands built on $9/2^+$ states, where the band spacings, as well as the bandhead energies, decrease with neutron number in going from ^{125}Cs to ^{119}Cs. The $9/2^+$ bandhead drops low enough in ^{119}Cs to become the ground state.

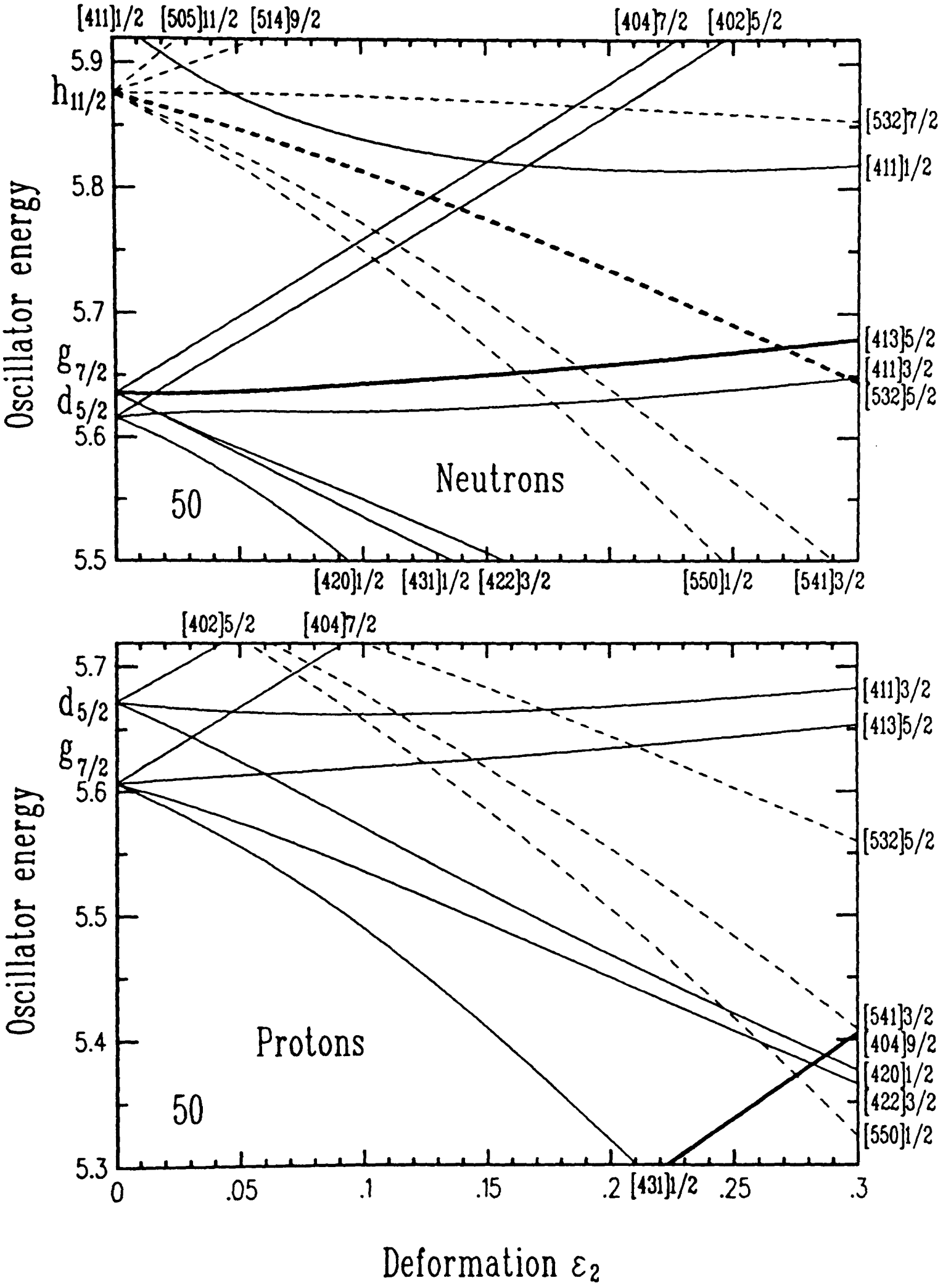

Figure 7.15. Nilsson diagrams for odd-proton and odd-neutron levels at mass 118, using *extrapolated* shell parameters. Full lines represent levels with positive parity, and dashed lines negative parity. The odd-proton level [404]9/2, and the odd-neutron levels [413]5/2 and [532]5/2, relevant to the discussion are emphasized by thick lines.

These bandheads have been interpreted in terms of the excitation of a $g_{9/2}$ proton across the $Z = 50$ closed shell. From [Fig 7.15] , it can be seen that the [404]9/2 proton orbital rises steeply at large prolate deformations. Hence, a *hole* state formed by excitation of a proton from this orbital would decrease in energy, with increasing deformation. The measured magnetic moments of the $9/2^+$ bandheads in ^{119}Cs and ^{121}Cs are large (5.46 and 5.42 nm respectively)[5] , which are consistent with this interpretation, as will now be shown.

In the Nilsson model, the magnetic moment operator for a deformed odd-A nucleus may be written as [19] ,

$$\boldsymbol{\mu}^{op} = g_R \mathbf{R} + g_\Omega \mathbf{J} \tag{7.21}$$

where $\mathbf{R}$ is the rotational angular momentum of the core, and $\mathbf{J}$ is the single particle angular momentum, given by

$$\mathbf{J} = \mathbf{l} + \mathbf{s} \tag{7.22}$$

which has a projection Ω on the nuclear 3–axis. The total spin $\mathbf{I}$ is given by

$$\mathbf{I} = \mathbf{R} + \mathbf{J} \tag{7.23}$$

with a corresponding projection K on the nuclear 3–axis. The magnetic moment is now defined as

$$\begin{aligned} \mu &= \frac{\langle \boldsymbol{\mu}^{op} \cdot \mathbf{I} \rangle}{I+1} \\ &= \frac{\langle \left(g_R(\mathbf{I}-\mathbf{J}) + g_\Omega \mathbf{J} \right) \cdot \mathbf{I} \rangle}{I+1} = g_R I + (g_\Omega - g_R) \frac{\langle \mathbf{I} \cdot \mathbf{J} \rangle}{I+1} \\ &= g_R I + (g_\Omega - g_R) \frac{\Omega K}{I+1} + (g_\Omega - g_R) \frac{\langle I_+ J_- + I_- J_+ \rangle}{2(I+1)} \end{aligned} \tag{7.24}$$

The last term in this expression is referred to as the Coriolis interaction, and is zero for $K = \Omega \neq 1/2$. Also, for the case of an axially symmetric nucleus $K = \Omega$, and equation (7.24) may thus be simplified

$$\mu = g_R I + \frac{K^2}{I+1}(g_K - g_R) \tag{7.25}$$

Now, following on from equation (7.22)

$$g_K \mathbf{J} = g_l \mathbf{l} + g_s \mathbf{s}$$
$$= g_l \mathbf{J} + (g_s - g_l)\mathbf{s} \qquad (7.26a)$$

so that

$$g_K K = g_l K + (g_s - g_l)\langle s_3 \rangle \qquad (7.26b)$$

where $\langle s_3 \rangle$ is the projection of the intrinsic spin onto the nuclear symmetry axis. For the special case where $I = K$, then (7.26) simplifies further to give

$$\mu = \frac{I}{I+1}(g_R + I g_K) \qquad (7.27)$$

The rotational g-factor g_R is commonly taken as $g_R \approx Z/A$ [20] .

Taking $g_R = Z/A$ and a magnetic moment of 5.43nm (from the $9/2^+$ bandheads in ^{119,121}Cs), a value of $g_s = 0.78 g_s^{free}$ may easily be deduced from equations (7.26) and (7.27), for the [404]9/2 proton orbital (for which $\langle s_3 \rangle = +1/2$). No other proton orbital near the Fermi surface in [Fig 7.15] can give rise to such a large moment.

For the case of an odd-odd nucleus, the g-factor is obtained by projecting the intrinsic proton and neutron motions separately onto the nuclear symmetry axis, with the result that

$$g_K = g_{K_p} K_p \pm g_{K_n} K_n \qquad (7.28a)$$

where

$$K = K_p \pm K_n \qquad (7.28b)$$

In this equation g_{K_p} and g_{K_n} are the same as those found from equation (7.26) for single particles. Likewise, K_p and K_n are the single particle K values.

Ekström *et al*[4] has measured the magnetic moment of the odd-odd ^{120}Cs^g ($I = 2$) to be 3.95(5)nm. This large value again indicates the presence of the proton [404]9/2 orbital. At deformations $\epsilon_2 > 0.2$, the only two neutron orbitals

near the Fermi surface which can couple to the [404]9/2 orbital to produce a state of spin 2, are [413]5/2 and [532]5/2. On the basis of comparison between experimental and theoretical magnetic moments, Ekström *et al* prefer the assignment $2^+\{p[404]9/2\ n[413]5/2\}$.

This choice of neutron orbital is supported by in-beam and decay studies of odd-neutron $^{117-121}$Xe nuclei, revealing $I = 5/2^{(+)}$ ground state spins, which have tentatively been ascribed to the [413]5/2 orbital[6,7] . In addition, the magnetic moments of ^{119}Xe and ^{121}Xe have been measured [21] to be $|\mu| =$ 0.59(6) and 0.65(3)nm respectively. These values tend to favour the [413]5/2 over the [532]5/2 assignment, for which the calculated magnetic moments are too low.

The experimental magnetic moments of the two isomers of ^{118}Cs are both found to be large, suggesting again the presence of the [404]9/2 proton orbital. The comparison between experimental and theoretical moments, calculated using equation (7.28), is shown in [Fig 7.16] for both isomers of ^{118}Cs. The solid and dashed lines correspond to the indicated Nilsson configurations, whose g-factors have been calculated with the shell parameters used above, taking $g_R = Z/A$, $g_s = 0.60 g_s^{free}$ (thick lines) and $0.78 g_s^{free}$ (thin lines).

The agreement between experiment and the above theory is clearly shows that the large [404]9/2 g-factor is the dominant factor in producing a large resultant magnetic moment. For ^{118}Cs^m, either of the neutron configurations tried could explain the measured value, and in the absence of log ft values for decay to states in ^{118}Xe, it is not possible to clearly distinguish between them.

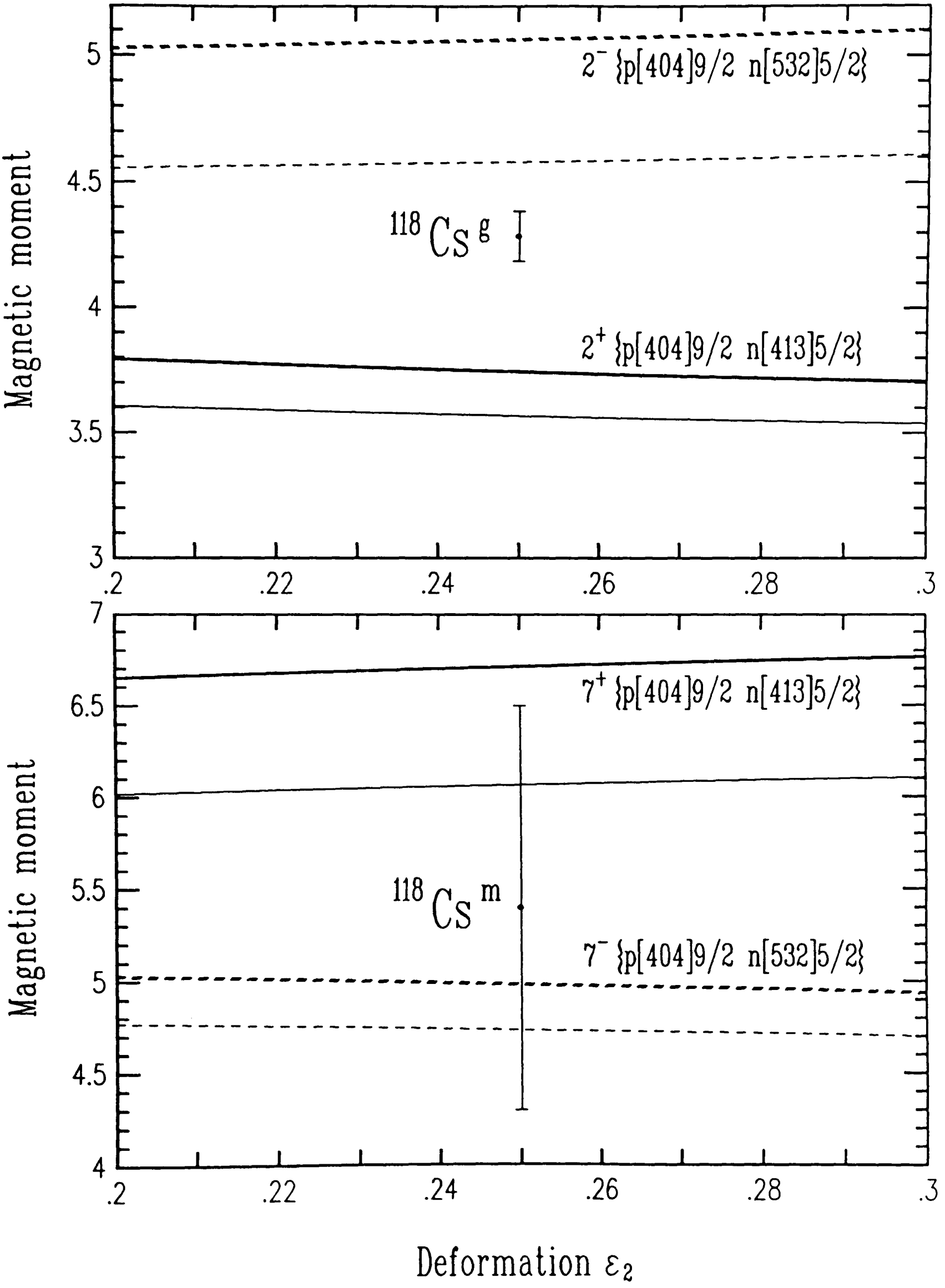

Figure 7.16. Comparison between experimental and theoretical magnetic moments for $^{118}Cs^{g}$ ($I = 2$) and $^{118}Cs^{m}$ ($I \geq 6$).

References

[1] . S.R.Reintsema, S.A.Drentje and H. de Waard,
Hyp. Int. **5**(1978)167.

[2] . T.L.Shaw, V.R.Green, C.J.Ashworth, J.Rikovska, N.J.Stone,
P.M.Walker and I.S.Grant, Phys. Rev. **C36**(1987)413.

[3] . C.Ekström, S.Ingelman, G.Wannberg, M.Skaresstad,
and the ISOLDE Collaboration, Nucl. Phys. **A293**(1977)144.

[4] . C.Ekström, G.Wannberg and J.Heinemeier,
Phys. Lett. **76B**(1978)565.

[5] . C.Thibaut, F.Touchard, S.Büttgenbach, R.Klapisch,
M. de Saint Simon, H.T.Duong, P.Jacquinot, P.Juncar,
S.Liberman, P.Pillet, J.Pinard, J.L.Vialle, A.Pesnelle
and the ISOLDE Collaboration, Nucl. Phys. **A367**(1981)1.

[6] . K.Sofia, B.N.Subba Rao and J.E.Crawford,
Phys. Rev. **C24**(1981)1615.

[7] . G.Marguier, C.Richard-Serre, J.Genevey-Rivier, M.Morgue,
A.Charvet, J.Giroux, A.Huck, A.Knipper, G.Walter
and the ISOLDE Collaboration, J. Phys. **G12**(1986)757.

[8] . P.Chowdhury, U.Garg, T.P.Sjoreen and D.B.Fossan,
Phys. Rev. **C23**(1981)733.

[9] . E. der Mateosian and A.W.Sunyar, Atomic and Nuclear Data
Tables **13**(1974)391.

E. der Mateosian and A.W.Sunyar, Atomic and Nuclear Data
Tables **13**(1974)408.

[10] . T.Yamagazi, Nuclear Data **A3**(1967)1.

[11] . R.M.Diamond, E.Matthias, J.O.Newton and F.S.Stephens, Phys. Rev. Lett. **26**(1966)1205.

[12] . J.Genevey-Rivier, A.Charvet, G.Marguier, C.Richard-Serre, J.D'Auria, A.Huck, G.Klotz, A.Knipper, G.Walter and the ISOLDE Collaboration, Nucl. Phys. **A283**(1977)45.

[13] . W.D.Hamilton, private communication (1985).

[14] . J.Kanamori, H.K.Yoshida and K.Terakura, Hyp. Int. **9**(1981)363.

[15] . H.K.Yoshida, K.Terakura and J.Kanamori, J. Phys. Soc. Japan **50**(1981)1942.

[16] . E.Klein, in Low-Temperature Nuclear Orientation, eds. N.J.Stone and H.Postma (North Holland,1987) Ch 12.

[17] . S.G.Nilsson, C.F.Tsang, A.Sobiczewski, Z.Szymański, S.Wycech, C.Gustafson, I.L.Lamm, P.Möller and B.Nilsson, Nucl. Phys. **A131**(1969)1.

[18] . U.Garg, T.P.Sjoreen and D.B.Fossan, Phys. Rev. **C19**(1979)217.

[19] . S.G.Nilsson, Dan. Matt. Fys. Medd. **29**(1955).

[20] . J.M.Irvine, in Nuclear Structure Theory, (Pergamon,1972) Ch 16.

[21] . T.L.Shaw, V.R.Green, C.J.Ashworth, J.Rikovska, N.J.Stone, P.M.Walker and I.S.Grant, Daresbury Annual Report(1985/86)47.

Appendix I

Solutions of the relaxation equations

I .1 Evaluation of the relaxation matrix

The relaxation matrix is defined in equation (2.12) to be

$$R_{mn} = \begin{cases} W_{n,m} & \text{for } n \neq m \\ -(W_{n,m+1} + W_{n,m-1}) & \text{for } n = m \end{cases} \qquad (I.1)$$

where the transition rates are defined in equation (2.8)

$$W_{m+1,m} = \frac{(E_{m+1} - E_m)}{2kC_k} \left[\frac{I(I+1) - m(m+1)}{1 - \mathrm{e}^{-(E_{m+1}-E_m)/kT_L}} \right] \qquad (I.2a)$$

$$W_{m,m+1} = \frac{(E_{m+1} - E_m)}{2kC_k} \left[\frac{I(I+1) - m(m+1)]}{\mathrm{e}^{(E_{m+1}-E_m)/kT_L} - 1} \right] \qquad (I.2b)$$

These equations make no assumptions about the sub-level energies E_m. They are valid for both $E_{m+1} > E_m$ and $E_{m+1} < E_m$, and apply also for non-equal sub-level spacings. For degenerate sub-levels, $(I.2)$ must be written as

$$W_{m+1,m} = W_{m,m+1} = \frac{T_L}{2C_k}[I(I+1) - m(m+1)] \qquad (I.3)$$

For computational purposes, it is more convenient to apply an equivalence transformation to R to yield a symmetric matrix $\mathbf{R^s}$. To do this it is first necessary to consider the relation between the upward and downward transition

probabilities. In thermal equilibrium the populations p_m and p_n will be related to each other by,

(i) the Boltzmann equilibrium condition where

$$\frac{p_n}{p_m} = \mathrm{e}^{-(E_n - E_m)/kT_L} \tag{I.4}$$

(ii) the number of upward transitions must be balanced by the number of downward transitions

$$\frac{p_n}{p_m} = \frac{W_{m,n}}{W_{n,m}} \tag{I.5}$$

From these two conditions it can be seen that

$$W_{m,n}\mathrm{e}^{-(E_m - E_n)/2kT_L} = W_{n,m}\mathrm{e}^{-(E_n - E_m)/2kT_L} \tag{I.6}$$

From this it is now easy to show that the diagonal matrix $\mathbf{D}$ with $D_{mn} = \delta_{mn}\mathrm{e}^{-E_m/2kT_L}$ will give a symmetric matrix $\mathbf{R^s} = \mathbf{D^{-1}RD}$.

$$\begin{aligned} R^s_{mn} &= \sum_{i,j} (D)^{-1}_{mi} R_{ij} D_{jn} = \sum_{i,j} \delta_{mi}\mathrm{e}^{E_m/2kT_L} R_{ij} \delta_{jn}\mathrm{e}^{-E_n/2kT_L} \\ &= R_{mn}\ \mathrm{e}^{-(E_n - E_m)/2kT_L} \\ &= W_{n,m}\mathrm{e}^{-(E_n - E_m)/2kT_L} \\ &= W_{m,n}\mathrm{e}^{-(E_m - E_n)/2kT_L} \\ &= R^s_{nm} \end{aligned} \tag{I.7}$$

The subroutine RELAX, listed in appendix *I*.4 calculates either the relaxation matrix $\mathbf{R}$, or the symmetric relaxation matrix $\mathbf{R^s}$.

I .2 Time dependent relaxation equations

I .2.1 The relaxation master equation

To reiterate, the relaxation equation to be solved is given by equation (2.11) as

$$\frac{d\mathbf{p}}{dt} = \mathbf{R}\mathbf{p} \qquad (I.8)$$

where $\mathbf{p}$ is a $(2I+1)$ column vector representing the sub-level populations and $\mathbf{R}$ is the tri-diagonal relaxation matrix.

As stated in chapter 2.3.1 the method used to solve these coupled equations is to diagonalize the relaxation matrix $\mathbf{R}$. If $\mathbf{U}$ is a matrix containing the eigenvectors of $\mathbf{R}$ (as columns) and $\mathbf{K}$ is a matrix containing the corresponding eigenvalues (with $K_{lj} = k_l\delta_{lj}$), then the eigenvalue equation is simply

$$\mathbf{RU} = \mathbf{KU} \qquad (I.9)$$

hence, provided that the matrix $\mathbf{U}$ is not singular (i.e. it has an inverse),

$$\mathbf{U}^{-1}\mathbf{RU} = \mathbf{U}^{-1}\mathbf{KU} = \mathbf{K} \qquad (I.10)$$

as $\mathbf{K}$ is diagonal.

Now if $\mathbf{p} = \mathbf{U}\mathbf{p}'$ is substituted into the master equation $(I.8)$

$$\frac{d\mathbf{p}'}{dt} = (\mathbf{U}^{-1}\mathbf{RU})\mathbf{p}' = \mathbf{K}\mathbf{p}' \qquad (I.11)$$

Again, as $\mathbf{K}$ is diagonal, the solution of this equation is now trivial with

$$\mathbf{p}'(t) = \mathbf{e}^{\mathbf{K}t}\mathbf{p}'(0) \qquad (I.12)$$

where $\mathbf{p}'(0)$ is the initial state. Now substituting back for $\mathbf{p}$ this becomes

$$\mathbf{p}(t) = \mathbf{U}\mathbf{e}^{\mathbf{K}t}\mathbf{U}^{-1}\,\mathbf{p}(0) \qquad (I.13a)$$

Since $(\mathrm{e}^{\mathbf{K}t})_{lj} = \mathrm{e}^{k_l t}\delta_{lj}$, this may be written in component form as

$$\begin{aligned} p_m(t) =& \sum_{l,i,n} U_{ml}(\mathrm{e}^{k_l t}\delta_{li})U^{-1}_{in}p_n(0) \\ =& \sum_{l} U_{ml}\mathrm{e}^{k_l t}\left(\sum_{n} U^{-1}_{ln}p_n(0)\right) \end{aligned} \tag{I.13b}$$

For computational purposes this equation can be simplified if the symmetric relaxation matrix $\mathbf{R}^s$ is diagonalized instead of $\mathbf{R}$. This is because the eigenvectors of a symmetric matrix are orthogonal. Hence, after normalization the matrix of eigenvectors $\mathbf{U}^s$ will be unitary with $(\mathbf{U}^s)^{-1} = \mathbf{U}^{s\dagger}$. Written in component form,

$$(U^s)^{-1}_{mn} = U^{s\dagger}_{mn} = U^s_{nm} \tag{I.14}$$

it is clear that the inverse of $\mathbf{U}^s$ is simply accomplished by exchange of indices.

From section *I*.1 the symmetric relaxation matrix is $\mathbf{R}^s = \mathbf{D}^{-1}\mathbf{R}\mathbf{D}$ where $\mathbf{D}$ is diagonal ($D_{mn} = \delta_{mn}\mathrm{e}^{-E_m/2kT_L} = d_m$) To see how equation (*I*.14) must be modified it is necessary to find a relationship between $\mathbf{U}$ and $\mathbf{U}^s$. This is easily derived from the eigenvalue equation (*I*.9) by substituting for $\mathbf{R}$

$$\begin{aligned} (\mathbf{D}\mathbf{R}^s\mathbf{D}^{-1})\mathbf{U} =& \mathbf{K}\mathbf{U} \\ \mathbf{R}^s(\mathbf{D}^{-1}\mathbf{U}) =& \mathbf{D}^{-1}\mathbf{K}\mathbf{U} \\ =& \mathbf{K}(\mathbf{D}^{-1}\mathbf{U}) \end{aligned} \tag{I.15}$$

This shows that $\mathbf{R}$ and $\mathbf{R}^s$ possess the same eigenvalues and their eigenvector matrices are related by $\mathbf{U} = \mathbf{D}\mathbf{U}^s$. This relation can now be used in equation (*I*.13) to give

$$\mathbf{p}(t) = \mathbf{D}\mathbf{U}^s\mathrm{e}^{\mathbf{K}t}(\mathbf{U}^s)^{-1}\mathbf{D}^{-1}\,\mathbf{p}(0) \tag{I.16a}$$

As above this may be converted to component form as follows

$$\begin{aligned} p_m(t) =& \sum_{k,l,i,j,n} d_m\delta_{mk}U_{kl}(\mathrm{e}^{k_l t}\delta_{li})(U^s)^{-1}_{ij}d^{-1}_j\delta_{jn}p_n(0) \\ =& \sum_{l,n} d_m U^s_{ml}\mathrm{e}^{k_l t}(U^s)^{-1}_{ln}d^{-1}_n p_n(0) \\ =& \sum_{l} d_m U^s_{ml}\mathrm{e}^{k_l t}\left(\sum_{n} U^s_{nl}d^{-1}_n p_n(0)\right) \end{aligned} \tag{I.16b}$$

The subroutine TRELAX, listed in appendix *I*.4, which is used to evaluate this equation, calculates the eigenvalues and eigenvectors of the symmetric relaxation matrix (supplied by RELAX) by use of the NAG library routine F02AMF.

The subroutine requires some initially specified sub-level populations $\mathbf{p}(0)$, with a corresponding source strength $n(0)$. These initial populations must be normalized such that $\sum_m p_m(0) = 1$. If no initial sub-level populations are supplied, then default values of $p_m(0) = 1/(2I+1)$ and $n(0) = 1$ are taken, corresponding to no initial orientation.

The calculated sub-level populations $p_m(t)$ are returned with the normalization condition $\sum_m p_m(t) = 1$. As outlined in chapter 2.4.2, the source strength $n(t)$ is not implicit in equation (*I*.16), but is simply calculated as an exponential decay from the initial value $n(0)$, such that $n(t) = n(0)\mathrm{e}^{-t/\tau}$. If the half-life is not specified, then the source strength is assumed to be time independent (i.e. $\tau \rightarrow \infty$).

I .2.2 The modified relaxation master equation

The modified relaxation master equation is given by (2.27) as

$$\frac{d\mathbf{p}}{dt} = (\mathbf{R}+\mathbf{T})\,\mathbf{p} + \mathbf{P}\,\mathbf{p}_\mathbf{p} \qquad (I.17)$$

The solution of this equation is very simple if the time variation of the $\mathbf{p}_\mathbf{p}$ can be neglected. If $\mathbf{p}' = \mathbf{p} + (\mathbf{R}+\mathbf{T})^{-1}\,\mathbf{p}_\mathbf{p}$ is substituted into the above equation, then

$$\begin{aligned}\frac{d\mathbf{p}'}{dt} = \frac{d\mathbf{p}}{dt} &= (\mathbf{R}+\mathbf{T})\,\mathbf{p} + \mathbf{P}\,\mathbf{p}_\mathbf{p} \\ &= (\mathbf{R}+\mathbf{T})\,\mathbf{p}' \qquad (I.18)\end{aligned}$$

For $\mathbf{T} \neq \mathbf{0}$ the matrix $(\mathbf{R}+\mathbf{T})$ is non-singular, and by analogy with equations $(I.8)$ and $(I.13)$ this may be solved to give

$$\mathbf{p}'(t) = \mathbf{U}'\mathbf{e}^{\mathbf{K}'t}\mathbf{U}'^{-1}\,\mathbf{p}'(0) \qquad (I.19)$$

where $\mathbf{U}'$ is the matrix of eigenvectors of $(\mathbf{R}+\mathbf{T})$ and $\mathbf{K}'$ is the diagonal matrix of corresponding eigenvalues. $\mathbf{U}'$ and $\mathbf{K}'$ may easily be deduced from

$$\begin{aligned}(\mathbf{R}+\mathbf{T})\mathbf{U} =& \mathbf{R}\mathbf{U}+\mathbf{T}\mathbf{U} = \mathbf{K}\mathbf{U}+\mathbf{T}\mathbf{U}\\ =& (\mathbf{K}+\mathbf{T})\mathbf{U}\end{aligned} \qquad (I.20)$$

hence, $\mathbf{U}' \equiv \mathbf{U}$ and $\mathbf{K}' \equiv (\mathbf{K}+\mathbf{T})$. Equation $(I.19)$ may now be written

$$\mathbf{p}'(t) = \mathrm{e}^{-t/\tau}\,\mathbf{U}\mathrm{e}^{\mathbf{K}t}\mathbf{U}^{-1}\,\mathbf{p}'(0) \qquad (I.21)$$

As $t \rightarrow \infty$ the sub-level populations will approach secular equilibrium values, as discussed in chapter 2.4.3. These values are found by setting $d\mathbf{p}/dt$ to zero in equation $(I.17)$

$$\mathbf{p}(\infty) = -(\mathbf{R}+\mathbf{T})^{-1}\,\mathbf{p}_{\mathbf{p}}(0) \qquad (I.22)$$

The evaluation of this equation is dealt with in the next subsection. From this it is easily seen that $\mathbf{p}'(t) = \mathbf{p}(t) - \mathbf{p}(\infty)$. Now, substituting for $\mathbf{p}'$ in equation $(I.21)$ gives

$$\mathbf{p}(t) = \mathrm{e}^{-t/\tau}\,\mathbf{U}\mathrm{e}^{\mathbf{K}t}\mathbf{U}^{-1}\,[\mathbf{p}(0) - \mathbf{p}(\infty)] + \mathbf{p}(\infty) \qquad (I.23)$$

The form of this equation is very similar to equation $(I.13)$, and by analogy with equation $(I.16)$ it may may more conveniently be written as

$$\mathbf{p}(t) = \mathrm{e}^{-t/\tau}\,\mathbf{D}\mathbf{U}^{s}\mathrm{e}^{\mathbf{K}t}(\mathbf{U}^{s})^{-1}\mathbf{D}^{-1}\,[\mathbf{p}(0) - \mathbf{p}(\infty)] + \mathbf{p}(\infty) \qquad (I.24a)$$

or in component form

$$p_m(t) = \mathrm{e}^{-t/\tau}\sum_l d_m U^s_{ml}\mathrm{e}^{k_l t}\left(\sum_n U^s_{nl} d_n^{-1}\,[p_n(0) - p_n(\infty)]\right) + p_m(\infty) \qquad (I.24b)$$

The subroutine TRELAX, listed in appendix *I*.4, is used again to evaluate this equation, as a separate option to calculating equation (*I*.16). It calculates the eigenvalues and eigenvectors of the symmetric relaxation matrix, by use of the NAG library routine F02AMF.

In the solution of the above equation, it is necessary to specify how the sub-levels are populated, which is done through the p(∞) term, defined by equation (*I*.22). The evaluation of this is dealt with in section I.3, where it is assumed that all sub-levels are equally populated (see chapter 2.4.2), and where the normalization condition $\sum_m p_m(\infty) = 1$ is adopted.

The initial sub-level populations p(0) must also be specified, with a corresponding source strength $n(0)$. These initial populations must be normalized such that $\sum_m p_m(0) = 1$, and will then be multiplied by n(0). If initial sub-levels populations are not specified, then the default value of $n(0) = 0$ is taken, corresponding to no initial source.

The sub-level populations $p_m(t)$ are then evaluated using equation (*I*.24), and the corresponding source strength is given by $n(t) = \sum_m p_m(t)$ (see chapter 2.4.2). The sub-level populations are then normalized before exit to set $\sum_m p_m(t) = 1$.

I .3 Secular equilibrium solution

For secular equilibrium (*I*.17) reduces to

$$\frac{d\mathbf{p}}{dt} = 0 = (\mathbf{R} + \mathbf{T})\,\mathbf{p} + \mathbf{q} \qquad (I.25)$$

where $\mathbf{q} \equiv \mathbf{P}\,\mathbf{p_p}$ is a constant. This may simply be solved by inversion of $(\mathbf{R}+\mathbf{T})$. However, for computational purposes, it is easier to invert a symmetric matrix, so the matrix $(\mathbf{R} + \mathbf{T})$ is first symmetrized. This is easily done using the same

equivalence transformation $(\mathbf{R}+\mathbf{T})^s = \mathbf{D}^{-1}(\mathbf{R}+\mathbf{T})\mathbf{D}$ as in appendix I.1 (where $\mathbf{D}$ is diagonal with $D_{mn} = \delta_{mn}\mathrm{e}^{-E_m/2kT_L} = d_m$) to give,

$$\begin{aligned}(R+T)^s_{mn} &= \sum_{i,j}(D)^{-1}_{mi}(R+T)_{ij}D_{jn} = \sum_{i,j}\delta_{mi}\mathrm{e}^{E_m/2kT_L}\left(R_{ij} - \frac{1}{\tau}\delta_{ij}\right)\delta_{jn}\mathrm{e}^{-E_n/2kT_L} \\ &= R_{mn}\mathrm{e}^{-(E_n-E_m)/2kT_L} - \frac{1}{\tau}\delta_{mn}) \\ &= (R^s+T)_{mn} \qquad (I.26)\end{aligned}$$

Now the solution of equation $(I.25)$ is straightforward

$$\begin{aligned}\mathbf{p}(\infty) &= -(\mathbf{R}+\mathbf{T})^{-1}\,\mathbf{q} = -\mathbf{D}[(\mathbf{R}+\mathbf{T})^s]^{-1}\mathbf{D}^{-1}\,\mathbf{q} \\ &= -\mathbf{D}(\mathbf{R}^s+\mathbf{T})^{-1}\mathbf{D}^{-1}\,\mathbf{q} \qquad (I.27a)\end{aligned}$$

This may be written in component form as

$$\begin{aligned}p_m(\infty) &= -\sum_{i,j,n} d_m\delta_{mi}(R^s+T)^{-1}_{ij}d_j^{-1}\delta_{jn}q_n \\ &= -d_m\sum_n (R^s+T)^{-1}_{mn}d_n^{-1}q_n \qquad (I.27b)\end{aligned}$$

The subroutine SECLAR listed in appendix I.4 calculates this equation, assuming that the population of the sub-levels is uniform (i.e. all q_n are equal). The matrix inversion is performed by a subroutine MATINV, which is listed in the book by Bevington [1] . The sub-level populations calculated are returned with the normalization condition $\sum_m p_m(\infty) = 1$.

I .4 Basic relaxation programs

I .4.1 The subroutine RELAX

```
C     SUBROUTINE RELAX
C
C     CALCULATES THE RELAXATION MATRIX (IN SYMMETRIC FORM IF
C     REQUIRED) ASSUMING THAT THE RELAXATION MECHANISM INVOLVES M1
C     TRANSITIONS BETWEEN ADJACENT MAGNETIC SUB-LEVELS (WHICH NEED NOT
C     BE EQUALLY SPACED)
C
C
C     DESCRIPTION OF PARAMETERS
C     XJOR   - SPIN OF ORIENTED STATE
C     BMOM   - MAGNETIC INTERACTION (IN NM.TESLA)
C     QFREQ  - QUADRUPOLE FREQUENCY (IN MHZ)
C     CKORR  - KORRINGA CONSTANT (IN KELVIN.SECONDS)
C     RECIPT - RECIPROCAL LATTICE TEMPERATURE
C     ISYMM  - IF SET TO 1 THEN THE RELAXATION MATRIX
C              IS CONSTRUCTED TO BE SYMMETRIC
C     RELMAT - RELAXATION MATRIX
C              (ILEVEL = 1 :  M'TH SUB-LEVEL
C              ILEVEL = NLEVEL : -M'TH SUB-LEVEL)
C              (TLS : DECEMBER 1984)
C
C
      SUBROUTINE RELAX(XJOR,BMOM,QFREQ,CKORR,RECIPT,ISYMM,RELMAT)
      DIMENSION ENERGY(50),Q(50),W(50),RELMAT(50,50)
C
      BOLTZK=1.38066E-23
      XNMAG=5.05082E-27
      PLANCK=6.62618E-34
      NLEVEL=2.0*XJOR+1.1
C
C     EVALUATE ENERGY LEVELS
C
      Q(1)=0.0
      W(1)=0.0
      W(NLEVEL+1)=0.0
      DO 105 ILEVEL=1,NLEVEL
      XLEVEL=ILEVEL
      XM=XJOR+1.0-XLEVEL
      ENERGY(ILEVEL)=-XM*BMOM*XNMAG/XJOR+QFREQ*1.0E6*PLANCK*
     C(XM*XM-XJOR*(XJOR+1.0)/3.0)
      IF(ILEVEL.EQ.1)GOTO 105
      TINT=(ENERGY(ILEVEL)-ENERGY(ILEVEL-1))/BOLTZK
      IF(ABS(TINT).LT.1.0E-10)GOTO 101
C
      Q(ILEVEL)=EXP(TINT*RECIPT)
      W(ILEVEL)=(-TINT)/(CKORR*(1.0-Q(ILEVEL)))
      GOTO 105
C
 101  Q(ILEVEL)=1.0
      W(ILEVEL)=1.0/(RECIPT*CKORR)
 105  CONTINUE
C
C     CONSTRUCT RELAXATION MATRIX
```

```
C
      DO 205 ILEVEL=1,NLEVEL
      XLEVEL=ILEVEL
      XM=XJOR+1.0-XLEVEL
      XMINUS=XJOR*(XJOR+1.0)-XM*(XM-1.0)
      XPLUS=XJOR*(XJOR+1.0)-XM*(XM+1.0)
C
      RELMAT(ILEVEL,ILEVEL)=-(W(ILEVEL)*Q(ILEVEL)*XPLUS+
     CW(ILEVEL+1)*XMINUS)/2.0
C
      IF(ILEVEL.EQ.NLEVEL)GOTO 205
      IF(ISYMM.NE.1)GOTO 201
C
      RELMAT(ILEVEL,ILEVEL+1)=W(ILEVEL+1)*SQRT(Q(ILEVEL+1))*XMINUS/2.0
      RELMAT(ILEVEL+1,ILEVEL)=RELMAT(ILEVEL,ILEVEL+1)
      GOTO 205
 201  RELMAT(ILEVEL,ILEVEL+1)=W(ILEVEL+1)*Q(ILEVEL+1)*XMINUS/2.0
      RELMAT(ILEVEL+1,ILEVEL)=W(ILEVEL+1)*XMINUS/2.0
C
 205  CONTINUE
      RETURN
      END
```

I .4.2 The subroutine TRELAX

```
C     SUBROUTINE TRELAX
C
C     CALCULATES SUB-LEVEL POPULATIONS AT A PARTICULAR TIME USING
C     EIGENVALUES AND EIGENVECTORS OF THE SYMMETRIC RELAXATION MATRIX
C     (HALF-LIFE CAN BE INCLUDED IF REQUIRED)
C
C     THE RELAXATION MECHANISM ASSUMES M1 TRANSITIONS
C     BETWEEN ADJACENT MAGNETIC SUB-LEVELS (WHICH NEED NOT
C     BE EQUALLY SPACED)
C
C
C     DESCRIPTION OF PARAMETERS
C     XJOR   - SPIN OF ORIENTED STATE
C     BMOM   - MAGNETIC INTERACTION (IN NM.TESLA)
C     QFREQ  - QUADRUPOLE FREQUENCY (IN MHZ)
C     CKORR  - KORRINGA CONSTANT (IN KELVIN.SECONDS)
C     RECIPT - RECIPROCAL LATTICE TEMPERATURE
C     IDECAY = 0 :  PURE RELAXATION CALCULATION IGNORING DECAY
C              1 :  RELAXATION/DECAY CALCULATION
C     HLIFE  - HALF-LIFE (IN SECONDS)
C     PO     - NORMALIZED INITIAL SUB-LEVEL POPULATIONS
C              (ZERO UNLESS SUMPO .GT. 0.0)
C     SUMPO  - SUM OF INITIAL SUB-LEVEL POPULATIONS
C     D      - MATRIX OF EIGENVALUES
C     U      - MATRIX OF EIGENVECTORS
C     IVEC   - D AND U ARE CALCULATED INTERNALLY IF IVEC=0
C              (OTHERWISE D AND U ARE SUPPLIED BY CALLING PROGRAM)
C     TIME   - TIME AT WHICH SUB-LEVEL POPULATIONS ARE TO BE
C              CALCULATED
C     PT     - NORMALIZED SUB-LEVEL POPULATIONS AT SPECIFIED TIME
C     SUMPT  - SUM OF SUB-LEVEL POPULATIONS AT SPECIFIED TIME
C              (ILEVEL = 1 :  M'TH SUB-LEVEL
C              ILEVEL = NLEVEL : -M'TH SUB-LEVEL)
```

```
C
C
C     SUBROUTINES REFERENCED :
C            RELAX(XJOR,BMOM,QFREQ,CKORR,RECIPT,ISYMM,RELMAT)
C            SECLAR(XJOR,BMOM,QFREQ,CKORR,RECIPT,HLIFE,SECPOP)
C            FO2AMF - NAG ROUTINE TO FIND EIGENVALUES AND EIGENVECTORS
C              OF A SYMMETRIC TRI-DIAGONAL MATRIX
C
C     **MODIFIED TO CALCULATE FOR LARGE TIMES (TLS : JANUARY 1986)
C     **MODIFIED TO INCLUDE SOURCE STRENGTH AND TIME = 0 PROPERLY
C     (TIME .LT. 0 ARE TREATED AS TIME = 0)
C     (TLS : APRIL 1986)
C     **MODIFIED TO CHECK FOR NEGATIVE POPULATIONS IN LOW TEMPERATURE
C     LIMIT
C     (TLS : SEPTEMBER 1986)
C
C
C
      SUBROUTINE TRELAX(XJOR,BMOM,QFREQ,CKORR,RECIPT,IDECAY,HLIFE,
     CPO,SUMPO,D,U,IVEC,TIME,PT,SUMPT,NEG)
      DOUBLE PRECISION XO2AAF,QSYMM,SUM,SUMPOP,SLEV,D,E,U,OFFSET
      DIMENSION D(*),PO(*),PT(*)
      DIMENSION ENERGY(50),E(50),RELMAT(50,50),U(50,50)
      DIMENSION P(50),PZERO(50)
C
      BOLTZK=1.38066E-23
      XNMAG=5.05082E-27
      PLANCK=6.62618E-34
      NLEVEL=2.0*XJOR+1.1
      XLAMDA=0.0
      NEG=0
      IF(IDECAY.EQ.1)XLAMDA=ALOG(2.0)/HLIFE
C
C     CALCULATE ENERGY LEVELS
C
      P(1)=1.0
      DO 105 ILEVEL=1,NLEVEL
      XLEVEL=ILEVEL
      XM=XJOR+1.0-XLEVEL
      ENERGY(ILEVEL)=-XM*BMOM*XNMAG/XJOR+QFREQ*1.0E6*PLANCK*
     C(XM*XM-XJOR*(XJOR+1.0)/3.0)
C
C     SET INITIAL POPULATIONS AND CHECK FOR TIME .LE. 0
C
      IF(SUMPO.GT.0.0)THEN
      PZERO(ILEVEL)=PO(ILEVEL)*SUMPO
      ELSE IF(IDECAY.EQ.1.AND.TIME.GT.0.0)THEN
      PZERO(ILEVEL)=0.0
      ELSE
      PZERO(ILEVEL)=1.0/(2.0*XJOR+1.0)
      ENDIF
      PT(ILEVEL)=0.0
      IF(TIME.LE.0.0)PT(ILEVEL)=PZERO(ILEVEL)
C
      IF(ILEVEL.EQ.1)GOTO 105
      P(ILEVEL)=P(ILEVEL-1)/EXP((ENERGY(ILEVEL)-ENERGY(ILEVEL-1))*
     CRECIPT/BOLTZK)
 105  CONTINUE
C
C     SET SUMMED POPULATIONS FOR TIME = 0
C
      IF(TIME.LE.0.0)THEN
      IF(SUMPO.GT.0)THEN
```

```
      SUMPT=SUMPO
      ELSE IF(IDECAY.EQ.1)THEN
      SUMPT=0.0
      ELSE
      SUMPT=1.0
      ENDIF
      RETURN
      ENDIF
C
      IF(IVEC.NE.0)GOTO 101
C
C     INITIALIZE ARRAYS
C
      E(1)=0.0D0
      DO 205 ILEVEL=1,NLEVEL
      U(ILEVEL,ILEVEL)=1.0D0
      DO 205 JLEVEL=1,NLEVEL
      IF(ILEVEL.EQ.JLEVEL)GOTO 205
      U(ILEVEL,JLEVEL)=0.0D0
 205  CONTINUE
C
C     CONSTRUCT SYMMETRIC RELAXATION MATRIX
C
      CALL RELAX(XJOR,BMOM,QFREQ,CKORR,RECIPT,1,RELMAT)
      DO 305 ILEVEL=1,NLEVEL
      D(ILEVEL)=RELMAT(ILEVEL,ILEVEL)
C
      IF(ILEVEL.EQ.NLEVEL)GOTO 305
      E(ILEVEL+1)=(RELMAT(ILEVEL,ILEVEL+1)+RELMAT(ILEVEL+1,ILEVEL))
     C/2.0
 305  CONTINUE
C
C     EVALUATE EIGENVALUES AND EIGENVECTORS
C
      IFAIL=0
      CALL F02AMF(NLEVEL,X02AAF(X),D,E,U,50,IFAIL)
C
 101  SUMPOP=0.0D0
      OFFSET=TIME*(D(1)+D(NLEVEL))/2.0D0
      IF(DABS(OFFSET)-85.0D0)302,302,301
C
C     CALCULATE EQUILIBRIUM VALUES
C
 302  IF(IDECAY.EQ.1)CALL SECLAR(XJOR,BMOM,QFREQ,CKORR,RECIPT,
     CHLIFE,PT)
      DO 405 ILEVEL=1,NLEVEL
      E(ILEVEL)=PZERO(ILEVEL)-PT(ILEVEL)
 405  CONTINUE
C
C     CALCULATE TIME DEPENDENT SUB-LEVEL POPULATIONS
C
      DO 505 ILEVEL=1,NLEVEL
      SLEV=0.0D0
      DO 605 JLEVEL=1,NLEVEL
      SUM=0.0D0
      DO 705 KLEVEL=1,NLEVEL
      QSYMM=EXP(ENERGY(KLEVEL)*RECIPT/(2.0*BOLTZK))
      SUM=SUM+U(KLEVEL,JLEVEL)*E(KLEVEL)*QSYMM
 705  CONTINUE
      QSYMM=D(JLEVEL)*TIME-OFFSET
      SLEV=SLEV+U(ILEVEL,JLEVEL)*DEXP(QSYMM)*SUM
 605  CONTINUE
      QSYMM=ENERGY(ILEVEL)*RECIPT/(2.0*BOLTZK)-OFFSET+XLAMDA*TIME
```

```
C
      IF(QSYMM-85.0D0)201,201,202
 201  QSYMM=1.0D0/DEXP(QSYMM)
      GOTO 203
 202  QSYMM=0.0D0
C
 203  SLEV=SLEV*QSYMM+PT(ILEVEL)
      SUMPOP=SUMPOP+SLEV
      PT(ILEVEL)=SLEV
 505  CONTINUE
C
C     SUMPOP IS SOURCE STRENGTH FOR IDECAY = 1 ONLY
C
      IF(IDECAY.EQ.1)THEN
      SUMPT=SUMPOP
      GOTO 303
      ELSE
      GOTO 304
      ENDIF
C
C     THERMAL EQUILIBRIUM AS TIME TENDS TO INFINITY
C
 301  IF(IDECAY.EQ.1)THEN
      CALL SECLAR(XJOR,BMOM,QFREQ,CKORR,RECIPT,HLIFE,PT)
      SUMPT=1.0
      RETURN
      ENDIF
C
C     CALCULATE POPULATIONS AND SOURCE STRENGTH FOR IDECAY = 0
C
      DO 805 ILEVEL=1,NLEVEL
      PT(ILEVEL)=P(ILEVEL)
      SUMPOP=SUMPOP+PT(ILEVEL)
 805  CONTINUE
 304  SUMPT=1.0
      IF(SUMPO.GT.0.0)SUMPT=SUMPO
      IF(ABS((ALOG(2.0)/HLIFE*TIME)).LT.85.0)THEN
      SUMPT=SUMPT*EXP(-ALOG(2.0)/HLIFE*TIME)
      ELSE
      SUMPT=0.0
      ENDIF
C
C     NORMALIZE SUB-LEVEL POPULATIONS
C
 303  DO 905 ILEVEL=1,NLEVEL
      PT(ILEVEL)=PT(ILEVEL)/SUMPOP
      IF(PT(ILEVEL).LT.0.0)NEG=NEG+1
 905  CONTINUE
      RETURN
      END
```

I .4.3 The subroutine SECLAR

```
C     SUBROUTINE SECLAR
C
C     CALCULATES SUB-LEVEL POPULATIONS FOR THE CASE
C     WHERE THE HALF-LIFE IS COMPARABLE TO THE RELAXATION
C     TIME : SECULAR EQUILIBRIUM IS ASSUMED
C
C     THE RELAXATION MECHANISM ASSUMES M1 TRANSITIONS
C     BETWEEN ADJACENT MAGNETIC SUB-LEVELS (WHICH NEED NOT
C     BE EQUALLY SPACED)
C
C
C     DESCRIPTION OF PARAMETERS
C     XJOR   - SPIN OF ORIENTED STATE
C     BMOM   - MAGNETIC INTERACTION (IN NM.TESLA)
C     QFREQ  - QUADRUPOLE FREQUENCY (IN MHZ)
C     CKORR  - KORRINGA CONSTANT (IN KELVIN.SECONDS)
C     RECIPT - RECIPROCAL LATTICE TEMPERATURE
C     HLIFE  - HALF-LIFE (IN SECONDS)
C     SECPOP - SECULAR EQUILIBRIUM POPULATIONS
C              (ILEVEL = 1 :  M'TH SUB-LEVEL
C              ILEVEL = NLEVEL : -M'TH SUB-LEVEL)
C
C     SUBROUTINES REFERENCED :
C            RELAX(XJOR,BMOM,QFREQ,CKORR,RECIPT,ISYMM,RELMAT)
C            (TLS : DECEMBER 1984)
C
C
      SUBROUTINE SECLAR(XJOR,BMOM,QFREQ,CKORR,RECIPT,HLIFE,SECPOP)
      DOUBLE PRECISION ARRAY,ALPHA,SUMPOP,SLEV,QSYMM,XNORM
      DIMENSION SECPOP(*)
      DIMENSION ENERGY(50),ALPHA(50),ARRAY(50,50),RELMAT(50,50)
C
      BOLTZK=1.38066E-23
      XNMAG=5.05082E-27
      PLANCK=6.62618E-34
      XLAMDA=ALOG(2.0)/HLIFE
      NLEVEL=2.0*XJOR+1.1
C
      DO 105 ILEVEL=1,NLEVEL
      DO 105 JLEVEL=1,NLEVEL
      ARRAY(ILEVEL,JLEVEL)=0.0D0
 105  CONTINUE
C
C     CALCULATE ENERGY LEVELS
C
      DO 205 ILEVEL=1,NLEVEL
      XLEVEL=ILEVEL
      XM=XJOR+1.0-XLEVEL
      ENERGY(ILEVEL)=-XM*BMOM*XNMAG/XJOR+QFREQ*1.0E6*PLANCK*
     C(XM*XM-XJOR*(XJOR+1.0)/3.0)
 205  CONTINUE
C
C     CONSTRUCT RELAXATION/DECAY MATRIX
C
      CALL RELAX(XJOR,BMOM,QFREQ,CKORR,RECIPT,1,RELMAT)
      DO 305 ILEVEL=1,NLEVEL
      ALPHA(ILEVEL)=RELMAT(ILEVEL,ILEVEL)-XLAMDA
 305  CONTINUE
C
C     NORMALIZE RELAXATION/DECAY MATRIX FOR INVERSION
```

```
C
      DO 405 ILEVEL=1,NLEVEL
      ARRAY(ILEVEL,ILEVEL)=-1.0D0
C
      IF(ILEVEL.EQ.NLEVEL)GOTO 405
      XNORM=DSQRT(ALPHA(ILEVEL)*ALPHA(ILEVEL+1))
C
      ARRAY(ILEVEL,ILEVEL+1)=RELMAT(ILEVEL,ILEVEL+1)/XNORM
      ARRAY(ILEVEL+1,ILEVEL)=ARRAY(ILEVEL,ILEVEL+1)
 405  CONTINUE
C
C     INVERT RELAXATION/DECAY MATRIX
C
      CALL MATINV(ARRAY,NLEVEL,DET)
      SUMPOP=0.0D0
      DO 505 ILEVEL=1,NLEVEL
      SLEV=0.0D0
C
      DO 605 JLEVEL=1,NLEVEL
      QSYMM=EXP(ENERGY(JLEVEL)*RECIPT/(2.0*BOLTZK))
      SLEV=SLEV+ARRAY(ILEVEL,JLEVEL)/DSQRT(-ALPHA(JLEVEL))*QSYMM
 605  CONTINUE
C
      QSYMM=EXP(ENERGY(ILEVEL)*RECIPT/(2.0*BOLTZK))
      SLEV=SLEV/(DSQRT(-ALPHA(ILEVEL))*QSYMM)
      SUMPOP=SUMPOP+SLEV
      SECPOP(ILEVEL)=SLEV
 505  CONTINUE
C
C     NORMALIZE SUB-LEVEL POPULATIONS
C
      DO 705 ILEVEL=1,NLEVEL
      SECPOP(ILEVEL)=SECPOP(ILEVEL)/SUMPOP
 705  CONTINUE
      RETURN
      END
```

References

[1] . P.R.Bevington, in Data reduction and error analysis for the physical sciences (McGraw-Hill,New York,1969)297.

Appendix II

Time dependent relaxation analysis

II .1 Evaluation of the integrated source strength

The technique used to observe time-dependent relaxation, described in chapters 3 and 4, is basically to implant a source for a time t_{on}, then wait a time t_{off} before implanting again, and just repeating this many times. Assuming that a sufficient number of cycles is performed, and that the implantation rate of I_o atoms/s remains constant, it is easy to see that an equilibrium will be established. This is illustrated in [Fig 4.2]. Adopting the notation used in chapter 4.5, the numbers of nuclei, n_{on}^{∞} and n_{off}^{∞}, at the start and end of an equilibrium implantation cycle will be derived, and from these, the number of nuclei $n(t)$ at any time during such a cycle may be deduced.

Due to the periodic nature of $n(t)$, it is sufficient to consider only times $0 \leq t \leq t_{on} + t_{off}$, where $t = 0$ is defined as the start of the implantation cycle. During the waiting periods, the implanted source undergoes radioactive decay, and the number of nuclei will obey the relation

$$\frac{dn}{dt} = -\frac{n}{\tau} \qquad (II.1)$$

Solving this, with the appropriate initial condition gives

$$n(t) = n_{off}^{\infty} e^{(t-t_{on})/\tau} \qquad (II.2)$$

During implantation, the source strength obeys the relation

$$\frac{dn}{dt} = I_o - \frac{n}{\tau} \qquad (II.3)$$

which has the solution

$$n(t) = n_{on}^{\infty}\, \mathrm{e}^{-t/\tau} + I_o\tau(1 - \mathrm{e}^{-t/\tau}) \qquad (II.4)$$

when the appropriate initial conditions are applied. From these two solutions, it is now easy to deduce n_{on}^{∞} and n_{off}^{∞}. At time $t = t_{on}$, equation $(II.4)$ gives

$$n_{off}^{\infty} = n_{on}^{\infty}\, \mathrm{e}^{-t_{on}/\tau} + I_o\tau(1 - \mathrm{e}^{-t_{on}/\tau}) \qquad (II.5)$$

and at time $t = t_{off}$, equation $(II.2)$ gives

$$n_{on}^{\infty} = n_{off}^{\infty}\, \mathrm{e}^{-t_{off}/\tau} \qquad (II.6)$$

Now, eliminating n_{on}^{∞} from these last two equations gives

$$n_{off}^{\infty} = I_o\tau \left(\frac{1 - \mathrm{e}^{-t_{on}/\tau}}{1 - \mathrm{e}^{-(t_{on}+t_{off})/\tau}} \right) \qquad (II.7)$$

It is now possible to write the time dependent source strength for the equilibrium cycle shown in [Fig II .1] as

$$n(t) = \begin{cases} n_{on}^{\infty}\, \mathrm{e}^{-t/\tau} + I_o\tau(1 - \mathrm{e}^{-t/\tau}) & 0 \le t \le t_{on} \\ n_{off}^{\infty}\, \mathrm{e}^{-(t-t_{on})/\tau} & t_{on} \le t \le t_{on} + t_{off} \end{cases} \qquad (II.8)$$

where n_{on}^{∞} and n_{off}^{∞} are given by equations $(II.6)$ and $(II.7)$.

In an experiment of this kind, data may be acquired between times t_1 and t_2, and an important quantity to know in the analysis of the data is the integrated source strength $\int_{t_1}^{t_2} n(t)\, dt$ for this counting period, which is given by integrating equation $(II.8)$ to give

$$\int_{t_1}^{t_2} n(t)\, dt = \begin{cases} I_o(t_2 - t_1) + (n_{on}^{\infty} - I_o\tau D(t_1, t_2) & 0 \le t_1 < t_2 \le t_{on} \\ n_{off}^{\infty}\, \mathrm{e}^{t_{on})/\tau} D(t_1, t_2) & t_{on} \le t_1 < t_2 \le t_{on} + t_{off} \end{cases} \qquad (II.9a)$$

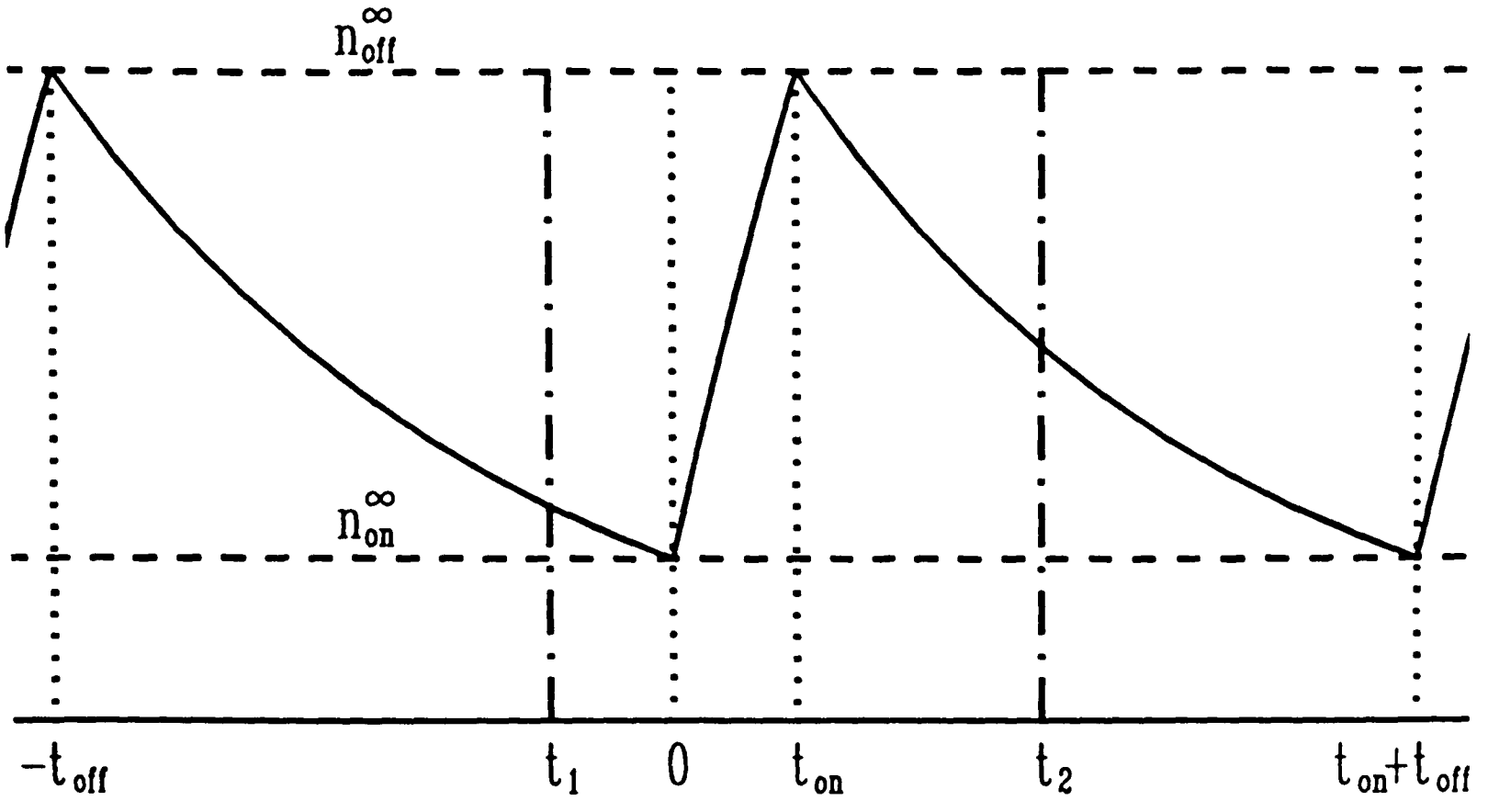

Figure II .1. Valid regions for which the integrated source strength can be calculated by HLINT. The dashed lines correspond to possible start and stop times over which time dependent effects might be observed.

where

$$D(t_1, t_2) = \mathrm{e}^{-t_1/\tau} - \mathrm{e}^{-t_2/\tau} \qquad (II.9b)$$

The possible range over which measurements may want to be made is shown in [Fig II .1] , and a subroutine HLINT has been written to calculate the integrated source strength between times t_1 and t_2, based on equation $(II.9)$, subject to the following conditions

$$-t_{off} \leq t_1 < t_2 \leq t_{on} + t_{off} \qquad (II.10)$$

If the implantation rate is supplied to HLINT, then the total number of decays will be calculated between the given integration limits. However, there are two normalization options which set, either the implantation rate (I_o), or the decay rate at the end of implantation $(n^{\infty}_{off}\tau)$, to be unity. This subroutine is listed in $II.4$.

II .2 Convergence to the equilibrium values

The method described in the last section calculates the expected source strengths in a pulsed relaxation experiment. It relies upon the fact that an equilibrium will be set up, in which the number of nuclei implanted in one cycle equals the total number that decay during the implantation and wait periods (i.e. $I_o t_{on}$ nuclei). For the concept of this equilibrium to be a useful one, it is necessary that it be established in a time short compared to the total length of the experiment. To determine how fast the source strength and the sub-level populations converge upon their equilibrium values, it is necessary to evaluate them as a function of time and the number of cycles performed.

The source strengths at the beginning and end of the i^{th} implantation are denoted by n^i_{on} and n^i_{off} respectively. Using equations $(II.2)$ and $(II.4)$, the following recursion relations may be written down

$$\begin{aligned} n^i_{off} &= n^i_{on}\, \mathrm{e}^{-t_{on}/\tau} + (1 - \mathrm{e}^{-t_{on}/\tau}) \\ n^{i+1}_{on} &= n^i_{off}\, \mathrm{e}^{-t_{off}/\tau} \end{aligned} \qquad (II.11)$$

where the initial value $n^1_{on} = 0$ is taken, and the normalization condition $I_o\tau = 1$ is also assumed. In a similar way, it is also possible to write down recursion relations for the corresponding sub-level populations $\mathbf{p}^i_{on}$ and $\mathbf{p}^i_{off}$, from equations $(I.16)$ and $(I.24)$

$$\begin{aligned} \mathbf{p}^i_{off} &= \mathrm{e}^{-t_{on}/\tau}\, \mathbf{D}\mathbf{U}^{\mathbf{s}}\mathrm{e}^{\mathbf{K}t_{on}}(\mathbf{U}^{\mathbf{s}})^{-1}\mathbf{D}^{-1}\, \left[\mathbf{p}^i_{on} - \mathbf{p}(\infty)\right] + \mathbf{p}(\infty) \\ \mathbf{p}^{i+1}_{on} &= \mathbf{D}\mathbf{U}^{\mathbf{s}}\mathrm{e}^{\mathbf{K}t_{off}}(\mathbf{U}^{\mathbf{s}})^{-1}\mathbf{D}^{-1}\, \mathbf{p}^i_{off} \end{aligned} \qquad (II.12)$$

where the initial populations $\mathbf{p}^1_{on}$ are set to zero, and $\mathbf{p}(\infty)$ are given by equation $(I.27)$.

The source strengths and sub-level populations, given by equations $(II.11)$ and $(II.12)$, can easily be calculated using the subroutine TRELAX. To investigate the speed of convergence of these parameters, a subroutine EQPOP has

been written which successively increments i, until the following convergence criteria are satisfied

$$\frac{n^{i+1}_{on,off} - n^{i}_{on,off}}{n^{i+1}_{on,off}} < 0.0001$$

$$\frac{B_2(\mathrm{p}^{i+1}_{on,off}) - B_2(\mathrm{p}^{i}_{on,off})}{B_2(\mathrm{p}^{i+1}_{on,off})} < 0.0001 \qquad (II.13)$$

where the sub-levels populations, p^{i}_{on} and p^{i}_{off}, for the i^{th} cycle, are compared with those of the next cycle through their respective orientation coefficients, $B_2(\mathrm{p}^{i}_{on,off})$ and $B_2(\mathrm{p}^{i+1}_{on,off})$.

The subroutine EQPOP, listed in $II.4$, returns the number of cycles needed to reach the above convergence criteria, along with the equilibrium sub-level populations $\mathrm{p}^{\infty}_{on,off}$ and the corresponding source strengths, $n^{\infty}_{on,off}$. The sub-level populations returned are normalized such that $\sum_m p_m = 1$.

II .3 Evaluation of time-averaged orientation coefficients

In the last section, the approach to equilibrium of both the source strength and the sub-level populations was considered. For such an equilibrium implantation/wait cycle, the integrated source strength $\int_{t_1}^{t_2} n(t)\ dt$ has been evaluated in appendix $II.1$. To complement this, it is also necessary to be able to calculate the *time-averaged* anisotropy for such a time period. As outlined in chapter 4.5.2, this can be done by evaluating the time-averaged orientation coefficient $\overline{B_\lambda}(\Delta t_{12})$, defined by

$$\overline{B_\lambda}(\Delta t_{12}) = \frac{\int_{t_1}^{t_2} B_\lambda(p_m(t))n(t)\ dt}{\int_{t_1}^{t_2} n(t)\ dt} \qquad (II.14)$$

where $n(t)$ is the source strength at time t, and the sub-level populations are *normalized* so that $\sum_m p_m(t) = 1$.

From equation (1.14), the orientation coefficient $B_\lambda(p_m(t))$ may be written as a linear combination of the time dependent sub-level populations $p_m(t)$

$$B_\lambda(p_m(t)) = \sum_{m=-I}^{I} \alpha_m^\lambda(I) p_m(t) \qquad (II.15)$$

where $\alpha_m^\lambda(I)$ is a variable depending on the oriented spin I, as well as λ and m. Combining equations $(II.14)$ and $(II.15)$ now gives

$$\begin{aligned} \overline{B_\lambda}(\Delta t_{12}) &= \frac{\int_{t_1}^{t_2} \left(\sum_m \alpha_m^\lambda(I) p_m(t)\right) n(t)\, dt}{\int_{t_1}^{t_2} n(t)\, dt} \\ &= B_\lambda(\overline{p_m}(\Delta t_{12})) \qquad (II.16a) \end{aligned}$$

where

$$\overline{p_m}(\Delta t_{12}) = \frac{\int_{t_1}^{t_2} p_m(t) n(t)\, dt}{\int_{t_1}^{t_2} n(t)\, dt} \qquad (II.16b)$$

Hence, the time-averaged orientation coefficients, $\overline{B_\lambda}(\Delta t_{12})$, can be calculated from the time-averaged sub-level populations, $\overline{p_m}(\Delta t_{12})$.

The time dependence of the sub-level populations for an equilibrium cycle may be determined using equations $(I.16)$ and $(I.24)$ to be

$$\mathbf{p}(t) = \begin{cases} \mathrm{e}^{-t/\tau}\mathbf{D}\mathbf{U}^{\mathbf{s}}\mathrm{e}^{\mathbf{K}t}(\mathbf{U}^{\mathbf{s}})^{-1}\mathbf{D}^{-1}\,[\mathbf{p}_{on}^{\infty} - \mathbf{p}(\infty)] & 0 \le t \le t_{on} \\ \quad + \mathbf{p}(\infty) & \\ \mathbf{D}\mathbf{U}^{\mathbf{s}}\mathrm{e}^{\mathbf{K}(t-t_{on})}(\mathbf{U}^{\mathbf{s}})^{-1}\mathbf{D}^{-1}\,\mathbf{p}_{off}^{\infty} & t_{on} \le t \le t_{on} + t_{off} \end{cases} \qquad (II.17)$$

where $\mathbf{p}_{on}^{\infty}$ and $\mathbf{p}_{off}^{\infty}$ can be calculated using the recursion relations $(II.12)$, described in the previous section.

A function subprogram PTI has been written to evaluate the *normalized* population of the i^{th} sub-level as a function of time (from equation $(II.17)$), multiplied by the source strength (from equation $(II.8)$), for an equilibrium cycle. Thus, $PTI = p_i(t)n(t)$, where $\sum_i p_i(t) = 1$. The equilibrium values $n_{on,off}^{\infty}$, and $\mathbf{p}_{on,off}^{\infty}$ are calculated externally (e.g. by EQPOP) and passed to PTI via a COMMON block.

In order to evaluate the integral $\int_{t_1}^{t_2} p_i(t)n(t)\ dt$, a subroutine AVPTI has been written, which uses the NAG library routine D01AJF to perform the integration. The integrand for this integration subroutine is supplied by the function PTI. Both PTI and AVPTI are listed in appendix *II*.4, and along with the subroutine HLINT, the averaged sub-level populations, $\overline{p_m}(\Delta t_{12})$, may be evaluated, from equation (*II*.16*b*).

II .4 Relaxation analysis subroutines

II .4.1 The subroutine HLINT

```
C     SUBROUTINE HLINT
C
C     CALCULATES TOTAL NUMBER OF DECAYS BETWEEN TIMES T1 AND T2
C     FOR THE CASE OF A CYCLE OF IMPLANTATION (TIMEON) AND COUNTING
C     (TIMEOF) WHERE EQUILIBRIUM HAS BEEN ESTABLISHED
C     T1 AND T2 MUST LIE BETWEEN -TIMEOF AND (TIMEON+TIMEOF)
C
C
C     DESCRIPTION OF PARAMETERS
C     RATE   - IMPLANTATION RATE (ATOMS/SECOND)
C            = 0.0 : THEN ON,OFF,TOTAL ARE SPECIFIED RELATIVE TO
C                    THE DECAY RATE FOR CONTINUOUS IMPLANTATION
C            = -1.0 :THEN ON,OFF,TOTAL ARE SPECIFIED RELATIVE TO
C                    THE DECAY RATE AT THE END OF IMPLANTATION
C     HLIFE  - HALF-LIFE (IN SECONDS)
C     TIMEON - IMPLANTATION TIME (BEAM ON)
C     TIMEOF - COUNTING TIME (BEAM OFF)
C     T1     - INITIAL TIME (TO INTEGRATE FROM)
C     T2     - FINAL TIME (TO INTEGRATE TO)
C     ON     - DECAY RATE AT T = 0
C     OFF    - DECAY RATE AT T = TIMEON
C     HLTOT  - TOTAL NUMBER OF DECAYS BETWEEN T1 AND T2
C
C     (TLS : APRIL 1986)
C
C
      SUBROUTINE HLINT(RATE,HLIFE,TIMEON,TIMEOF,T1,T2,ON,OFF,HLTOT)
      REAL*8 SUMON,SUMOFF,DTON,DTOFF,DT1,DT2,DIFF
C
      DIFF(DT1,DT2)=(DEXP(-DT1)-DEXP(-DT2))
C
C     INITIALIZE VARIABLES
C
      IF(T2.GT.(TIMEON+TIMEOF).OR.T1.GE.T2)RETURN
```

```
      HLTOT=0.0
C
      XLAMDA=ALOG(2.0)/HLIFE
      DTON=XLAMDA*TIMEON
      DTOFF=XLAMDA*TIMEOF
      DT1=XLAMDA*T1
      DT2=XLAMDA*T2
C
      IRATE=RATE
      IF(IRATE.EQ.0)THEN
      SOURCE=1.0
      SUMOFF=(1.0D0-DEXP(-DTON))/(1.0D0-DEXP(-DTON-DTOFF))/XLAMDA
      ELSE IF(IRATE.EQ.-1)THEN
      SOURCE=(1.0D0-DEXP(-DTON-DTOFF))/(1.0D0-DEXP(-DTON))
      SUMOFF=1.0D0/XLAMDA
      ELSE
      SOURCE=RATE
      SUMOFF=RATE/XLAMDA*(1.0D0-DEXP(-DTON))/(1.0D0-DEXP(-DTON-DTOFF))
      ENDIF
C
      SUMON=SUMOFF*DEXP(-DTOFF)
      OFF=SUMOFF*XLAMDA
      ON=SUMON*XLAMDA
C
C     REGION ONE
C
      IF(T1.GE.TIMEON)THEN
      HLTOT=SUMOFF*DEXP(DTON)*DIFF(DT1,DT2)
C
C     REGION TWO
C
      ELSE IF(T1.LT.TIMEON.AND.T1.GE.0.0)THEN
      IF(T2.LE.TIMEON)THEN
      HLTOT=SOURCE*(T2-T1)+(SUMON-SOURCE/XLAMDA)*DIFF(DT1,DT2)
      ELSE
      HLTOT=SOURCE*(TIMEON-T1)+(SUMON-SOURCE/XLAMDA)*DIFF(DT1,DTON)
     C+SUMOFF*DEXP(DTON)*DIFF(DTON,DT2)
      ENDIF
C
C     REGION THREE
C
      ELSE
      IF(T2.LE.0.0)THEN
      HLTOT=SUMON*DIFF(DT1,DT2)
      ELSE IF(T2.LE.TIMEON)THEN
      HLTOT=SUMON*DIFF(DT1,0.0D0)
     C+SOURCE*T2+(SUMON-SOURCE/XLAMDA)*DIFF(0.0D0,DT2)
      ELSE
      HLTOT=SUMON*DIFF(DT1,0.0D0)
     C+SOURCE*TIMEON+(SUMON-SOURCE/XLAMDA)*DIFF(0.0D0,DTON)
     C+SUMOFF*DEXP(DTON)*DIFF(DTON,DT2)
      ENDIF
      ENDIF
      RETURN
      END
```

II .4.2 The subroutine EQPOP

```
C     SUBROUTINE EQPOP
C
C     CALCULATES INITIAL SUB-LEVEL POPULATIONS FOR A CYCLE OF
C     IMPLANTATION (BEAM ON) AND COUNTING (BEAM OFF)
C
C
C     DESCRIPTION OF PARAMETERS
C     XJOR   - SPIN OF ORIENTED STATE
C     BMOM   - MAGNETIC INTERACTION (IN NM.TESLA)
C     QFREQ  - QUADRUPOLE FREQUENCY (IN MHZ)
C     CKORR  - KORRINGA CONSTANT (IN KELVIN.SECONDS)
C     RECIPT - RECIPROCAL LATTICE TEMPERATURE
C     HLIFE  - HALF-LIFE (IN SECONDS)
C     D      - MATRIX OF EIGENVALUES
C     U      - MATRIX OF EIGENVECTORS
C     TIMEON - IMPLANTATION TIME (BEAM ON)
C     TIMEOF - COUNTING TIME (BEAM ON)
C     ICYCLE .EQ. 0  ON ENTRY THEN ON EXIT IT WILL CORRESPOND TO THE
C                    NUMBER OF ITERATIONS NEEDED TO REACH EQUILIBRIUM
C     ICYCLE .GT. 0  ON ENTRY THEN ON EXIT THE VALUES ON EXIT WILL
C                    CORRESPOND TO ICYCLE ITERATIONS
C     PTON   - INITIAL SUB-LEVEL POPULATIONS FOR IMPLANTATION (BEAM ON)
C     SUMON  - SOURCE STRENGTH BEFORE IMPLANTATION (SUM OF PTON)
C     PTOFF  - INITIAL SUB-LEVEL POPULATIONS FOR COUNTING (BEAM OFF)
C     SUMOFF - SOURCE STRENGTH BEFORE COUNTING (SUM OF PTOFF)
C     IFAIL  - ZERO ON NORMAL COMPLETION (-1 IF B2 = 0)
C              (-2 IF ICYCLE = 100)
C
C     SUBROUTINES REFERENCED :
C            TRELAX(XJOR,BMOM,QFREQ,CKORR,RECIPT,IDECAY,HLIFE,PTOFF,SUMOFF,
C                   D,U,IVEC,TIME,PTON,SUMON,NEG)
C
C            (TLS : APRIL 1986)
C
C
      SUBROUTINE EQPOP(XJOR,BMOM,QFREQ,CKORR,RECIPT,HLIFE,D,U,
     CTIMEON,TIMEOF,ICYCLE,PTON,SUMON,PTOFF,SUMOFF,IFAIL)
      DOUBLE PRECISION D,U
      DIMENSION PTON(*),PTOFF(*)
      DIMENSION P(50),U(50,50),D(50)
C
C     EVALUATE THERMAL EQUILIBRIUM ORIENTATION COEFFICIENT
C
      IFAIL=0
      B2EQ=BCOEFF(2.0,XJOR,0,BMOM,QFREQ,RECIPT,P)
      IF(ABS(B2EQ).LT.1.0E-7)THEN
      IFAIL=-1
      RETURN
      ENDIF
C
C     CALCULATE EQUILIBRIUM SOURCE STRENGTHS
C
      ISTOP=-1
      IF(ICYCLE.GT.0)ISTOP=ICYCLE
      TON=ALOG(2.0)/HLIFE*TIMEON
      TOFF=ALOG(2.0)/HLIFE*TIMEOF
      SOFF=(1.0-EXP(-TON))/(1.0-EXP(-TON-TOFF))
      SON=SOFF*EXP(-TOFF)
C
C     POPULATIONS START AT ZERO FOR FIRST CYCLE
```

```
C
      NLEVEL=2.0*XJOR+1.1
      SUMON=0.0
      DO 105 ILEVEL=1,NLEVEL
      PTON(ILEVEL)=0.0
 105  CONTINUE
C
C     POPULATIONS WITH RELAXATION/DECAY (BEAM ON : T = T1 )
C
      ICYCLE=0
 101  ICYCLE=ICYCLE+1
      CALL TRELAX(XJOR,BMOM,QFREQ,CKORR,RECIPT,1,HLIFE,PTON,SUMON,
     CD,U,ICYCLE-1,TIMEON,PTOFF,SUMOFF,NEG)
C
C     POPULATIONS WITH RELAXATION ONLY (BEAM OFF : T = T1+T2 )
C
      CALL TRELAX(XJOR,BMOM,QFREQ,CKORR,RECIPT,0,HLIFE,PTOFF,SUMOFF,
     CD,U,1,TIMEOF,PTON,SUMON,NEG)
C
C     CALCULATE TIME DEPENDENT B2 VALUES (CHECK FOR CONVERGENCE)
C
      ON=BCOEFF(2.0,XJOR,1,0.0,0.0,0.0,PTON)/B2EQ
      OFF=BCOEFF(2.0,XJOR,1,0.0,0.0,0.0,PTOFF)/B2EQ
      IF((ABS(ON-ONOLD)/ON).LT.0.0001.AND.
     C(ABS(OFF-OFFOLD)/OFF).LT.0.0001.AND.
     C(ABS(SUMON-SON)/SON).LT.0.0001.AND.
     C(ABS(SUMOFF-SOFF)/SOFF).LT.0.0001)
     CRETURN
C
      IF(ICYCLE.EQ.100)THEN
      IFAIL=-2
      RETURN
      ELSE IF(ICYCLE.EQ.ISTOP)THEN
      RETURN
      ELSE
      ONOLD=ON
      OFFOLD=OFF
      GOTO 101
      ENDIF
C
      END
```

II .4.3 The subroutine PTI

```
C     FUNCTION PTI
C
C     EVALUATES SUB-LEVEL POPULATION FOR A PARTICULAR LEVEL AT A
C     PARTICULAR TIME FOR THE NAG INTEGRATION ROUTINE D01AJF
C     [REPLACES SEPOP AND TEPOP]
C     (TLS : APRIL 1986)
C
C
      FUNCTION PTI(X)
      DOUBLE PRECISION PTI,X,D(50),U(50,50)
      DIMENSION POP(50),DUMMY(1),PTON(50),PTOFF(50)
      COMMON/NAGPTI/ILEVEL,XJOR,BMOM,QFREQ,CKORR,RECIPT,JDECAY,HLIFE,D,U
      COMMON/ONOFF/IONOFF,TIMEON,TIMEOF,PTON,SUMON,PTOFF,SUMOFF
C
C     SET TIME
C
      TIME=X
C
C     CALCULATION USING SPECIFIED INITIAL SUB-LEVEL POPULATIONS
C
      IF(IONOFF.EQ.-1)THEN
C
C     BRING TIME WITHIN RANGE 0.0 TO (TIMEON+TIMEOF)
C
      TOTAL=TIMEON+TIMEOF
      IF(TIME.GE.0.0)THEN
      ISTEP=TIME/TOTAL
      ELSE
      ISTEP=TIME/TOTAL-1
      ENDIF
      TIME=TIME-ISTEP*TOTAL
C
C     CHECK WHICH REGION (IMPLANTATION OR DECAY)
C
      IF(TIME.GE.TIMEON)THEN
      TIME=TIME-TIMEON
      CALL TRELAX(XJOR,BMOM,QFREQ,CKORR,RECIPT,0,HLIFE,PTOFF,
     CSUMOFF,D,U,1,TIME,POP,SUMPOP,NEG)
      ELSE IF(TIME.GE.0.0)THEN
      CALL TRELAX(XJOR,BMOM,QFREQ,CKORR,RECIPT,1,HLIFE,PTON,
     CSUMON,D,U,1,TIME,POP,SUMPOP,NEG)
      ENDIF
      PTI=POP(ILEVEL)*SUMPOP
C
C     CALCULATION USING DEFAULT INITIAL SUB-LEVEL POPULATIONS
C
      ELSE
      CALL TRELAX(XJOR,BMOM,QFREQ,CKORR,RECIPT,JDECAY,HLIFE,DUMMY,
     C-1.0,D,U,1,TIME,POP,SUMPOP,NEG)
      PTI=POP(ILEVEL)*SUMPOP
      ENDIF
      RETURN
      END
```

II .4.4 The subroutine AVPTI

```
C     SUBROUTINE AVPTI
C
C     EVALUATES AVERAGE SUB-LEVEL POPULATION FOR A PARTICULAR LEVEL
C     BETWEEN TIMES TIME1 AND TIME2 USING THE NAG INTEGRATION
C     ROUTINE D01AJF
C     THE FUNCTION PTI(X) IS USED TO CALCULATE SUB-LEVEL POPULATION AT
C     TIME X
C     IDECAY = 0 :  PURE RELAXATION CALCULATION IGNORING DECAY
C              1 :  RELAXATION/DECAY CALCULATION
C
C     (TLS : APRIL 1986)
C
C
      SUBROUTINE AVPTI(IDECAY,TIME1,TIME2,PAV,EPAV,IFAIL)
      DOUBLE PRECISION TA,TB,EABS,EREL,PBAR,PERR,W,PTI,D(50),U(50,50)
      DIMENSION W(1000),IW(127)
      COMMON/NAGPTI/ILEVEL,XJOR,BMOM,QFREQ,CKORR,RECIPT,JDECAY,HLIFE,D,U
      EXTERNAL PTI
C
      JDECAY=IDECAY
      TA=TIME1
      TB=TIME2
      EABS=0.0D0
      EREL=1.0D-5
      IFAIL=0
C
      CALL D01AJF(PTI,TA,TB,EABS,EREL,PBAR,PERR,W,1000,IW,127,IFAIL)
C
      PAV=PBAR
      EPAV=PERR
      RETURN
      END
```